AEROFOIL SELF NOISE REDUCTION BY INNOVATIVE TRAILING EDGE TREATMENT

A thesis submitted for the degree of Doctor of Philosophy

by

Philip Charles Woodhead

College of Engineering, Design and Physical Sciences

Brunel University London

Declaration Of Authorship

I, Philip Charles Woodhead, declare that this thesis entitled 'Aerofoil Self Noise Reduction By Innovative Trailing Edge Treatment' and the work presented in it is my own and has been generated as the result of my own original research. I confirm that the following statements are true:

1. All work was done wholly while in candidature for a research degree at Brunel University London.
2. All parts of this thesis which have been previously been published work of others has been clearly stated and clearly attributed.
3. The source of all literature and research from other works used for the purpose of this thesis has always been given.
4. I have acknowledged all main sources of help.
5. Where the thesis is based on work done by myself jointly with others, I have made clear exactly what was done by others and what I have contributed myself.
6. Either none of this work has been published before submission, or parts of this work have been published as:

Conference Papers:

1. P.C. Woodhead, T.P. Chong and J.G. Wissink (2017), "Exploiting the Misalignment of the Serrated Trailing Edge for Improved Aerofoil Broadband Noise Reduction", 23rd AIAA/CEAS Aeroacoustics Conference.
2. P.C. Woodhead, T.P. Chong, P.F. Joseph and J.G. Wissink (2019), "On the Double-Rooted Trailing Edge Serration", 25th AIAA/CEAS Aeroacoustics Conference.

Signed:.....

Date:.....

Abstract

This thesis aims to develop the next level mitigation methods for the reduction of the aerofoil turbulent boundary layer trailing-edge noise (TBL-TE) self-noise radiation focusing on the add-on TE passive flow control devices in the forms of slitted and modified sawtooth geometries. The research undertaken involves experimental, numerical and analytical efforts.

The introduction of the flap angle represents an additional optimisation parameter for a modified sawtooth geometry, which is exploited for the design of serration as a periodic-function in the spanwise direction. The thesis shows that a more rapid spanwise waviness of the serration can outperform the noise reduction performance between the mid and high frequency range, while remain the same level at the low frequency, when compared to the conventional serration. The associated flow-topology is also investigated to provide some explanation for the mechanisms underpinning the broadband noise reduction.

For the first time, slit TE is found to facilitate acoustical interference between two sources that were physically displaced in the longitudinal direction. The findings successfully establish the frequency fine-tuning capability by slit TEs for the self-noise reduction. New analytical noise prediction model based on the acoustical interference mechanism is developed, which has been demonstrated to be compatible with the experimental results. The next level of improvement is achieved in the form of a hybrid device: *Double-Rooted-Trailing-Edge-Serrations* (DRooTES). The DRooTES combines the acoustical destructive interference mechanism from the slit TE, and the serration effect from the sawtooth. Both effects are found to co-exist and can be exerted constructively. The DRooTES not only demonstrates larger level of broadband noise reduction, but also establishes the frequency-tuning capability.

Finally, a Large-Eddy-Simulation was performed to investigate the detailed flow mechanisms causing the acoustical interference for the slit TE. The results help to explain some of the flow mechanisms observed in the experimental results.

Acknowledgement

I wish to express my sincere appreciation to my supervisors, Dr Jan Wissink and Dr Tze Pei Chong, for making this project a great experience. I have greatly benefited from Dr Jan Wissink's support which was invaluable in the development and advice during the numerical works.

Also, I want to thank Dr Tze Pei Chong for his insightful support, guidance and intellectual advice towards this thesis, and always having time for meetings. Without their guidance and constant help, this thesis would not have been possible.

I would like to offer my special thanks to Professor Phillip Joseph at Southampton University for his guidance and feedback in the collaboration works of the Single-Serrated, DRooTES and Slit TE project.

Special thanks to the Engineering and Physical Sciences Research Council, EPSRC, for their financial support of my PhD.

I am deeply grateful to technical staff, in particular to Kevin Robinson. His support was invaluable in the laboratories for preparing and conducting all the experiments, and his advice into the design of experimental equipment is truly appreciated.

I want to thank Shelagh Egan for the feedback of my writing which was invaluable during my PhD studies.

Finally, and most importantly, I wish to acknowledge the support and great love of my family and friends for their patience and support through difficult times during the PhD.

Contents

Nomenclature

Abbreviations

ΔPWL	Difference in Sound Power Level [dB/Hz]
ΔSPL	Difference in Sound Pressure [dB/Hz]
ACARE	Advisory Council for Aeronautics Research in Europe
AoA	Angle of Attack [degrees]
B	Baseline/ Non-Serrated
BL	Boundary Layer
CFD	Computational Fluid Dynamics
CTA	Constant Temperature Anemometer
DFS	Dual-Flapped-Straight
DNS	Direct Numerical Simulation
DRooTES	Double-Rooted-Trailing-Edge-Serration
DSGS	Dynamic Sub-Grid-Scale
EASA	European Union Aviation Safety Agency
EPN	Effective Percieved Noise
EU	European Union
EWEA	European Wind Energy Association
FFT	Fast Fourier Transform
FVM	Finite Volume Method

GW	Giga-Watts
ICAO	International Civil Aviation Authority
IFS	sIngle-Flapped-Serration
K-H	Kelvin-Helmholtz
kW	Kilo-Watts
LE	Leading Edge
LES	Large Eddy Simulation
MFS	Multi-Flapped-Serration
OAPWL	Overall PoWer Level [dB]
PIV	Particle Image Velocimetry
PSD	Power Spectra Density
PWL	Sound Power Level spectrum [dB/Hz]
RANS	Reynolds Averaged Navier Stokes
Re	Reynolds Number
RMS	Root Mean Squared
SGS	Sub-Grid-Scale
SIMPLE	Semi-Implicit Method for Pressure Linked Equations
SPL	Sound Pressure Level [dB/Hz]
SS	Straight Serration
SSF	Straight-Single-Flapped
SST	Shear Stress Transport
STENO	Serrated Trailing Edge Noise
SWS	Spanwise-Wavy-Serration
T-S	Tolmien-Schlichting

TBL-TE	Turbulent Boundary Layer Trailing Edge
TE	Trailing Edge
TKE	Turbulent Kinetic Energy
UDF	User Define Interface

Greek letters

α	angle of attack [degrees]
$\Delta\Theta$	Angle between adjacent microphones [Rad]
ΔP_r	Local Pressure Difference at Root
ΔP_t	Local Pressure Difference at Tip
Δ	Volume [m^3]
δ	Boundary Layer Thickness
δ_1	Turbulent Boundary Layer Displacement Thickness [m]
δ_2	Momentum Thickness [m]
η	Empirical Constant
η_x	Streamwise separation distance between two points
η_z	Spanwise separation distance between two points
γ	Boundary Layer Streamwise Coherence function
γ_x^2	Streamwise Coherence
γ_z^2	Spanwise Coherence
γ_{xy}^2	Coherence between root_2–root_1
$\hat{\omega}$	Phase Angle [rad/Hz]
κ	Empirical Correction Factor
λ	Wavelength [m]
λ'	Serration Spanwise Oscillation Wavelength [mm]

λ_0	Root_1–Root_2 lateral Displacement [mm]
ω	Angular Frequency [rad/Hz]
ω_0	Peak Frequency [Hz]
∂_{ij}	Kronecher delta
Φ	Angle of Serration Tip [degrees]
ϕ	Flap Angle [degrees]
ϕ_U, ϕ_L	Flap up, Flap down [degrees]
π	Pi [= 3.14159265]
Ψ_z	Spanwise Overall Coherence Level
ρ	density, [kg.m^{-3}]
ρ_{xx}	Auto-correlation
τ_A	Difference in Propagation times to the observer between sound radaition at the root of the slit and at the tip of the slit
τ_H	Time taken for the turbulent eddies to convect along the slit length
τ_{ij}	Sub-Grid Scale Reynold Stress
Θ	Polar Angle [degrees]
θ	Observer Angle
s	Standard Deviation
l	Longitudinal displace between two sources

Symbol

ΔH	Separation distance on the flat plate
λ'	Oscillation Serration Wavelength [mm]
$\mathcal{L}_{ij}$	Germano Identity
$\mathcal{W}(f)$	Sound Power integrated for the radiation angles
$\mathcal{W}_0$	Reference of Sound Power Level [= 10^{-12}]

$\overline{p}$	Kinematic Pressure
$\overline{U}, \overline{V}, \overline{W}$	Mean Velocity [ms^{-1}]
$\overline{u}_i$	Filtered (Resolved) Function
$\overline{x}$	Mean of the Sample
$A_{1,2,...}$	Polynomial Coefficients
B_1, B_2	Coefficients
b_1, b_3	Decay Constants
c_∞	Speed of Sound [= 343 ms^{-1}]
C_p	Coefficient of Pressure
C_s	Smagorinsky Constant
$c_{0\_original}$	Aerofoil Chord Length [= 0.15 m]
c_0	Overall Chord Length [m]
$E\{\cdot\}$	Expected Value Operator
f_{peak}	Peak Frequency [Hz]
$G(x, x')$	Filter Function
H'	Serration Spanwise Oscillation Amplitude [mm]
h'	Root$_1$-Root$_2$ Longitudinal Displacement [mm]
h'	root$_1$–root$_2$ longitudinal displacement
H''	root$_2$–tip longitudinal displacement [mm]
h''	longitudinal displacement between secondary root to tip for the DRooTES
$H_{1/2}$	half-length of the amplitude [m]
l_x	Streamwise Correlation Length
l_z	Spanwise Correlation Length
L_x	Separated by a Distance in Streamwise

L_y	Separated by a Distance in Vertical
L_z	Separated by a Distance in Spanwise
p	Static Pressure [Pa]
P_∞	Pressure at Freestream [Pa]
P_0	Reference Pressure [$= 20\mu$ Pa]
P_{rms}	Root Mean Squared of Pressure [Pa]
R_{xy}	Cross-Correlation Coefficient
S_1, S_2	Acoustic Radiation Source Strength Locations
$S_{\Delta prr}$	Source Strength at Root
$S_{\Delta ptt}$	Source Strength at Tip
S_{ij}	filtered strain-rate tensor
S_{pp}	Far-Field Pressure Power Spectrum Density
$T_{a,calibration}$	Ambient Temperature at Calibration [$^\circ C$]
T_a	Ambient Temperature during the Experiments [$^\circ C$]
T_{ij}	Lighthill's Stress Tensor
T_w	Temperature of the Hot-Wire Sensor Wire [$^\circ C$]
u, v, w	Instantaneous Velocity [ms^{-1}]
u', v', w'	Velocity Fluctuation [ms^{-1}]
U_∞	Freestream Velocity [ms^{-1}]
U_c	Convection Velocity [ms^{-1}]
u_{rms}, v_{rms}, w_{rms}	Root Mean Square of the Velocity Component [ms^{-1}]
V_{xx}, V_{yy}	Auto-Power Spectra Density
V_{xy}	Cross-Power Spectra Density
x^+, y^+, z^+	Wall Coordinates

x_i	Data points
x_n, y_n	Jointly stationary random processes, $-\infty < n < \infty$, $-\infty < m < \infty$
2D	Two-Dimensional
3D	Three-Dimensional
a	Width of the Slit Tip [mm]
Cov	Sample Covariance of a time series
f	Frequency [Hz]
H	Serration/Slit Amplitude, Length of Flat Plate [mm]
I	Turbulence Intensity
N	Total Number of Samples
R	Specific Gas constant for air (= 287.05 J/(kg.K))
St	Strouhal number/non-dimensional frequency
t	Time [Seconds]
u, v, w	velocity component [ms^{-1}]
Var	Sample Variance of a time series
W	Width of the Slit Root/Opening [mm]
x, y, z	Coordinate System [Streamwise, Vertical, Spanwise]
dB	decibel
ms^{-1}	metre per second
P	Pressure [Pa]
Pa	Pascal
r	Distance from Aerofoil Trailing Edge and Microphone (observer)
U	Velocity [ms^{-1}]
V	Voltage [Volts]

List of Figures

List of Tables

Chapter 1

Introduction

1.1 Wind Energy Noise

The late 20^{th} century saw the re-emergence and significant development of wind energy as a major source of world energy generation. Wind power has played a fundamental part in the history of humankind, from the transport of civilization and goods using sailing ships, to the industrialization of food production using wind mills, and most recently to energy generation [31, 119]. The earliest record of wind generated electricity occurred in 1887 by Professor James Blyth in Glasgow [31]. However, the use of fossil fuel has weakened the development and role of wind in energy generation [31, 92]. By the 1990s, the re-emergence of wind energy was starting to make a non-negligible contribution to the overall energy generation [31, 92]. This decade saw a rise in the worldwide wind energy industry and significant growth in wind energy generation capacity, with a shift to megawatts-sized wind turbines and the development of offshore wind farms [31, 92, 119]. This trend continued into the 21^{st} century in European Union (EU) countries, via government policies that focus on developing domestic sustainable energy supplies and lowering pollution emissions.

The European Commission aims to reduce emissions within the EU countries through more climate-friendly and less energy-consuming ways. A report by the European Commission [27] sets out a low-carbon economy roadmap which outlines cuts in greenhouse emissions by 2050 to 80% below 1990 levels. It also outlines targets to be achieved by 2030 and 2040 of 40% and 60% respectively, applied to all economic sectors [27]. The energy sector has the largest potential for cutting greenhouse emissions, with the view to almost eliminating carbon dioxide (CO_2) emissions by 2050 [27]. The EU suggests the replacement of fossil fuels with renewable sources

e.g. wind, solar, water and biomass or other low-emission sources. This potentially spells the end of the fossil fuel era. The main focus within this research is wind energy.

Compared to the situation in 2014, the European Wind Energy Association (EWEA) Report [28] aims, by 2030, to increase the generation of energy by a two-thirds. This scenario is expected to produce 320 Giga-watts (GW) per annum in 2030, with 79.4% from onshore and 20.6% from off-shore wind farms [28]. In 2015 under the Paris Agreement [128], government policies sought to unite all nations to jointly address the effects of climate change. For further information please refer to website [128]. The EU total wind power generated increased from about 41 GW in 2005 to 169 GW in 2017 [72]. This increase of 425% in 12 years makes it the second largest source of power within the EU and this increase is set to continue, following the targets of the European Commission and EWEA, now referred to as WindEurope [28].

The significant growth within the onshore wind farms in the EU member states would inevitably increase the aerodynamic noise pollution. It is widely known that noise pollution is essentially a form of unwanted noise that affects health and wellbeing, especially near wind farm sites. Studies have shown that wind farm noise pollution have adverse health effects resulting in annoyance, sleep disturbance and cognitive impairment [9, 81, 99, 107]. To protect the public, strict noise regulations have been implemented to both the aviation and wind energy sectors.

This thesis focuses on aeroacoustic. The two main sources of noise generated from wind turbines are mechanical and aerodynamic noise [133]. The wind turbine mechanical noise is mainly caused by the moving parts inside the gearbox and generator [110]. However, the recent development of high precision gear tooth profile designs and acoustic insulation of casings has reduced the source of mechanical noise [92, 127]. In contrast, the aerodynamic noise generated from the wind turbine blade is more difficult to reduce. To protect local settlements, maximum noise levels are currently set at 35-45 dB(A) at 350 m from the wind turbines [43]. At 500 metres (0.3 miles) the sound pressure level (SPL) drops to 38 dB [78].

In comparison to aircraft, road traffic and railway noise, wind turbine noise has a lower exposure level. However, Miedema and Voss [94] found that the issue regarding noise characteristics led to a large proportion of people finding wind turbine noise annoying. A study by Persson Waye and Agge [108] indicated that the sound characteristics described as "lapping", "swishing" and "whistling" led to different perceptions and resulted in a different sense of annoyance. The frequency region at which the descriptions "swishing" and "whistling" occurred was from 2 kHz to 4 kHz [109]. The description "lapping" referred to aerodynamically induced fluctuations and was found to be best described by specific loudness over time [108]. As a result, wind turbine companies often reduce the rotation speed of their turbines at high wind speed in order to curb

the aerodynamic noise levels so as not to exceed the prescribed limits. This practice essentially leads to a under utilisation of the available wind energy source. Reduction of noise without reducing the rotor-speed would therefore make wind energy cheaper and, hence, a more attractive alternative to fossil energy.

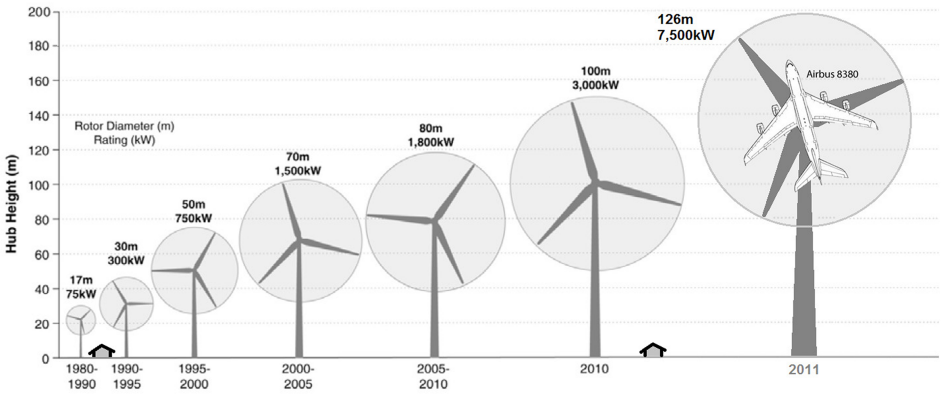

Figure 1.1: Historical trends of wind turbines size of rotor diameter in metres and wind generation capacity in kW [7]

Over the last decades, the onshore wind turbine has significantly increased wind energy production from 75 kilowatt (kW), in 1980–90, to 7,500 kW in 2011 [7]. However, the rotor diameter has increased from 17 m in 1980–90 to 126 m in 2011, shown in Figure 1.1. The influence of increasing wind turbine rotor diameter has a direct relation with noise levels [101], as seen in Figure 1.2. In quantitative terms, a further 1 dB noise reduction from current level can lead to a significant increase in wind energy production. In other words, to continue the research on wind turbine noise reduction is absolutely worthwhile and important for the promotion of clean energy.

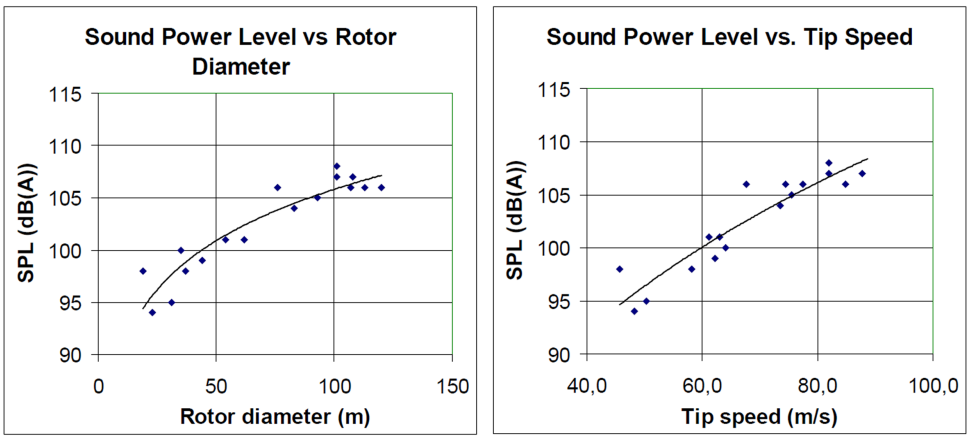

Figure 1.2: Comparison of the sound power levels (SPL) against rotor diameter and tip speeds from Oerlemans and Fuglsang [101]

Aerodynamic noise can emanate from the aerofoils' leading and trailing edges. The aerofoil noise is generated either at the leading edge of the blades, through interaction with the atmospheric turbulence, or at the TEs, where turbulence in the boundary layer develops on the blade's surface and scatters into sound [100]. For the TE noise (also commonly referred to self-noise), it remains one of the most relevant noise sources related to the aviation and wind turbine industries. A comprehensive report on the physical aerofoil self-noise mechanisms can be found in Brooks *et al.* [125].

The bio-inspired passive flow control device provides an attractive method of reducing aerodynamic noise at the TE. The sawtooth TEs, also known as serrations, were shown to be an effective passive flow control device to reduce turbulent boundary layer trailing edge (TBL-TE) noise. Studies have successfully demonstrated that sawtooth TEs can achieve noise reduction in wind tunnel experiments up to 8 dB [1, 18, 26, 36, 57, 58, 65, 76, 130]; whereas full-size wind turbine blades achieve reductions up to 3 dB [100]. Further development of the TE serration technology which will be thoroughly studied in this thesis.

1.2 Aviation Noise

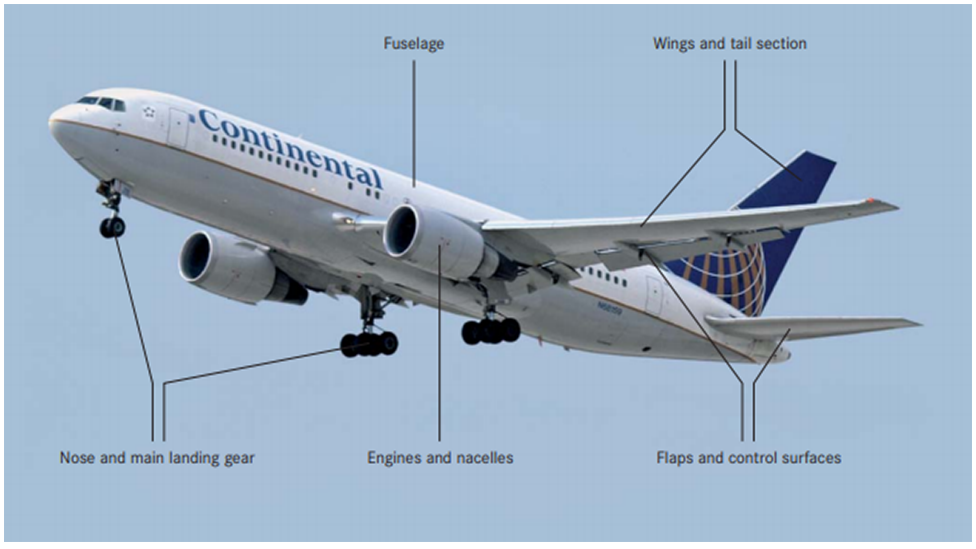

Figure 1.3: Noise source generated by modern civil aircraft from MTU Aero Engines[42]

The European Commission [27] has outlined aviation targets for aviation noise to be reduced by 65% by 2050 compared to the levels produced in 2000. However, civil aviation traffic is expected to expand worldwide between 4% and 5% annually with higher growth in the Middle East and Asia [2, 27]. In 2018, the total number of passengers carried on scheduled services rose to 4.3 billion, that was 6.4% higher than 2017 [102]. Aviation contributes to global economics

by around € 220 billion [8], providing 4.5 million jobs [27, 44]. This significant growth within the aviation industry inevitably leads to increased noise pollution around many of the busiest international airports, such as Heathrow and Gatwick within the United Kingdom.

Since the 1970s the aviation industry has seen significant jet noise reduction as a result of modifications, especially improvements in engine performance have led to lower levels of noise generation [16]. In the last decade, increased engine bypass ratios and advanced fan design have contributed to decreased levels of fan and jet noise, resulting from reduced jet exhaust velocities [16]. On the other hand, the high bypass ratios resulted in fan noise becoming the predominant noise source [57]. Also, airframe components have become a major contributor to overall aircraft noise, in particular from the landing gear and high-lift components, such as slats and flaps, shown in Figure 1.3, that are employed at take-off and landing [135]. Modern aircraft are quieter than previous generations of aircraft entering service in the 1960s, with reductions of noise levels by more than 90% [98]. The International Civil Aviation Authority (ICAO) and the Advisory Council for Aeronautics Research in Europe (ACARE) have strict regulations that are widely employed by aircraft and engine manufacturers.

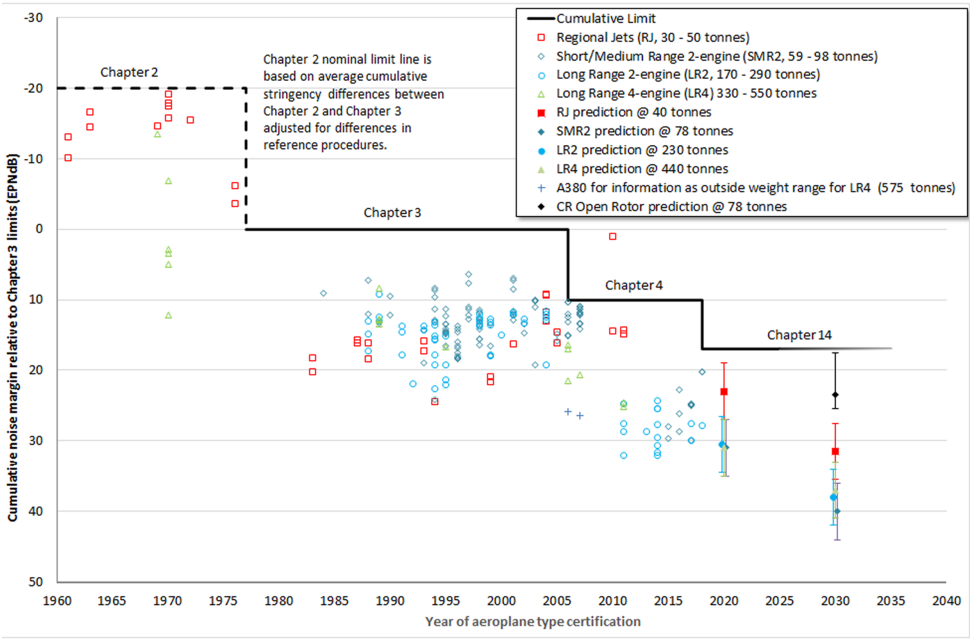

Figure 1.4: Improvement to aircraft noise performance between 1960 to 2030 from EASA report ([41] Figure 2.2)

Figure 1.4 presents the overview of aircraft development of noise technology to meet increased targets set by the European Union Aviation Safety Agency (EASA) noise certification regulations [40] over the period 1960 to 2030. EASA [41] stated that at the time of the report aircraft noise levels remained well below the limits set by the EASA certification requirements. The

EASA report [41] also outlined that noise targets for 2020 and 2030 were achievable with future development of noise technology. This opinion was based on a review of noise technology by independent experts for the ICAO performed from 2010 to 2013 [71]. However, the noise targets highlighted the need for further research into noise technology to ensure that these goals are met. ACARE [27] published a report Flightpath 2050 which outlines targets to reduce the Effective Perceived Noise (EPN) levels by 65% compared to typical new aircraft of 2000. ACARE also identified that to achieve these targets, the promotion of research and development into new low noise engine and airframe technologies is essential.

1.3 Summary

To summarise, both the aviation and wind energy sectors face significant increasing pressure to meet targets related to noise. By 2050, the aviation authority aims to reduce perceived noise by 65%, compared to typical aircrafts that went into service in 2000. Currently, the majority of aircraft noise takes place during take-off and landing; the two major noise sources are airframe and engine noise. The wind energy sector faces targets to increase its energy generation capacity to 320 GW by 2030 with the majority of wind turbines being onshore. As a result, the increase in the number of wind farms will inevitably increase aerodynamic noise pollution. However, strict noise regulations are in place, such as noise levels not to exceed 35 - 45 dB at 350 m distance [43]. As a result, wind turbine companies often reduce the rotation speed of their turbines at high wind speed in order to curb the aerodynamic noise level within the prescribed limit. Therefore, these industries are investigating new technologies such as design of low-noise aerodynamic shapes and flow control devices to reduce aerodynamic noise for wind turbine rotors, wings and high-lift devices, as well as propellers and fans. Thus, understanding aeroacoustic noise generation, in particular TE noise, and its reduction is paramount. Trailing edge noise is a form of aerofoil self-noise which occurs from the unsteady flow within the boundary layer passing over the aerofoil. This thesis focuses on the turbulent boundary layer trailing edge (TBL-TE) noise.

Currently, wind turbine companies employ sawtooth add-ons to the TE of the turbine rotors. However, further optimisation of the sawtooth devices through new noise mechanisms and geometrical parameters are yet to be investigated. As a result, this thesis focuses on the optimisation of the sawtooth passive control device to reduce aerofoil self-noise in particular TBL-TE noise.

1.4 Aims and Objectives

The aim of this research is to experimentally, analytically and numerically investigate the noise reduction mechanisms for the aerofoil self-noise, with the use of flat-plate TE devices. The findings can potentially benefit the industrial such as the aviation, wind energy sector, commercial fans, etc. In more detail, the objectives are as follows:

1. To establish the optimum geometrical configuration through single and variable flap angles.
2. To examine the effects of the flap angle, also known as misalignment, on TE noise through far-field noise and flow measurements.
3. To evaluate a new noise reduction mechanism using acoustic interference, on TE noise through multi-rooted-serrated and slit TEs via acoustic and flow measurements.
4. To investigate the flow over baseline and slit TEs and elucidate the mechanism that resulted in TE noise reduction through numerical studies.

1.5 Thesis Structure

The aim of this thesis is to provide a detailed explanation of experimental, numerical and analytic workings of the passive TE devices to reduce aerofoil TE noise. The thesis is organised into the following chapters:

Chapter 2 provides a summary of the literature into the bio-inspired passive TE devices, such as serrated and slit TEs; it outlines the fundamental theories behind aerodynamic noise; and expands into the development of key findings of bio-inspired passive TE devices to reduce TBL-TE noise – these include numerical, experimental and empirical models.

Chapter 3 describes the methodology used to perform the experimental setup and measurement techniques, such as far-field noise measurements, aerodynamic/flow visualization measurements and experimental aerofoil and test cases. It also describes the Large Eddy Simulation (LES) turbulent models used to simulate the computational models and domains.

Chapter 4 presents the results of an extensive empirical study into the noise performance of four types of sawtooth TE serrations. The influence of misalignment is investigated in order to optimize and understand the noise reductions obtained with this TE geometry. It also presents near-wake hot-wire anemometry of four misaligned sawtooth TE serrations to understand the flow mechanisms that lead to noise reduction.

Chapter 5 introduces the acoustic phase cancellation mechanism generated by two sources that were physically displaced in a longitudinal direction to reduce aerofoil TE self-noise. An extensive aeroacoustics study into the noise performance of four TEs was performed, as well as the development of a new analytical noise model based on acoustic interference. This chapter also investigates the flow structures by hot-wire anemometry used to link noise characteristics to flow mechanisms.

Chapter 6 presents the preliminary numerical study into flow mechanisms for the slit and straight TEs reported in Chapter 5. The numerical data, obtained from the LES, discusses the fluid dynamics of the slit TE that resulted in acoustic interference. This chapter also evaluates the flow field around the NACA 65-(12)10 aerofoil simulated within an open jet wind tunnel facility, and compares and validates the Reynolds Average Numerical Simulations (RANS) results against experimental results.

Chapter 7 is the final chapter and summarises the findings within this research as well as conclusions of the previous chapters.

1.6 Original contribution

The following statements highlight the original contribution of this research:

Chapter 4 - Exploiting the Misalignment of the Flat Plate Trailing Edge Devices

- An extensive experimental study investigating the flap angles, also known as misalignment, on their effects on the TE broadband self-noise radiation of an aerofoil and near wake flow field. The flap angle is the third geometrical parameter of the serration that has hitherto not been explored before. The research explored TE devices with either single or multiple flap angles, and the serration oscillation wavelength. The study investigated five individual cases, baseline, Straight-Serration (SS), sIngle-Flapped-Serration (IFS), Multi-Flapped-Serration (MFS), Split-Flapped-Serration (SFS) and Spanwise-Wavy-Serration (SWS).

- The results demonstrated that misaligned TEs produced different noise characteristics compared to the conventional TE. Furthermore, the research identified the noise spectrums that is the domain effect of flap angle.

- The next step was the oscillation flap angles in the spanwise direction. This research is the first to report SWS. The results confirmed that the SWS had similar or superior broadband noise compared to the conventional TE.

- Extensive near-wake flow measurement results provided extensive analysis on the mechanisms underpinning the noise characteristics by these TE devices.

Chapter 5 - Trailing Edge Geometrical Modification to Achieve Frequency Targeted Self-Noise Reduction by Acoustical Destructive Interference Mechanism

- Extensive experimental work exploring acoustic interference mechanism on TE self-noise, by employing phase cancellation between two sources displaced in the longitudinal direction. The study investigated four cases, baseline, single serrated, slit and a new geometry double-rooted serrated TE (DRooTES, a patent application of which is now submitted to the UK Patent office).

- The experimental results successfully demonstrated the constructive and destructive acoustical interferences by the slit TE.

- The main outcome of the slit TE is that, for the first time, it is now possible to fine-tune the frequency for the self-noise reduction. The main mechanism of noise reduction by a slit

TE is the acoustical destructive interference effect only. There is no evidence of serration effect for the slit TE.

- The next step is to combine both the acoustical destructive interference effect and the serration effect to maximise the noise reduction. This PhD work is the first to report on the use of Double Rooted Traiing Edge Serration (DRooTES). It is indeed proven to be capable of achieving both the destructive interference mechanism between the double roots of the sawtooth and the scattering mechanism employed by serrated TEs.

- Development of a new analytical noise prediction model based on phase cancellation for the slit TE, where the analytical noise trends match well with the experimental results.

- The hot-wire anemometry flow measurements provided some explanations for the flow mechanism underpinning the noise characteristics by these TE cases.

Chapter 6 - Qualitative Study of the Flow and Noise Mechanisms for a Slit Trailing Edge through CFD

- A LES study to analyse the flow mechanisms that resulted in the phase-cancellation for the slit TE. The numerical results are also used to complement the flow mechanisms seen in the experimental results in Chapter 5.

Chapter 2

Literature Review

2.1 Aerodynamic Sound

As presented in Chapter 1, noise remains the subject of interest to those aiming to understand and find solutions with regard to acoustic problems.

The earliest records of investigation into fundamental noise theory dates back to the 6^{th} century BC when Pythagoras discovered the science of acoustics by conducting experiments which involved the investigation of the properties of vibrating strings [15]. In the 4^{th} Century BC, Aristotle correctly theorised that sound waves propagate through the motion of air [15, 74]. The first modern studies of sound waves and acoustics were proposed by Galileo, in 1660s, who furthered the science of vibrations and the relationship between pitch and frequency of a sound source [5, 15]. Subsequent studies based on Galileo's fundamental theory saw rapid progression into acoustics theory. By the late 17^{th} and early 18^{th} centuries, a French physicist by the name of Sauveur researched the correlation between frequency, pitch and waves in stretched strings [5]. His work paved the way to acoustic terms used today and initially suggested the name 'acoustic' as the study of sound. In the 1650s, works by Borelli and Viviani [132] investigated the speed of sound and in 1738 the Academy of Sciences in Paris performed the earliest precise value obtained a value close to the present accepted value for the speed of sound [5]. This value was amended in 1942 (331.45 ms^{-1}) and again in 1986 to the current value of 331.29 ms^{-1} [15].

By the early 18^{th} century, the mathematical theory of waves was being researched by theoreticians. Amongst those, d'Alembert in the 1740s derived the general wave equation through the works of Taylor's mathematical theory of vibrating strings [21] and the independent works of Newton and Leibniz who each developed the theory of calculus [114]. Subsequently, Bernoulli, Euler and Lagrange advanced equations of calculus to waves through strings and air [38]. In the

early 19^{th} century, Fourier established his theorem which analysed complex periodic waves into spectral components [38]. In 1877–78, Strutt [122, 123] published numerous studies of acoustic research in two volume treatises called "The Theory of Sound". This work is taken to mark the beginning of the modern acoustic and is still referred to today.

Lighthill [85, 86] published the theory on sound generated aerodynamically in two parts, the first in 1952 and second in 1954. This could be said to mark the beginning of the subject of aeroacoustics. Lighthill's works prepared the foundation knowledge of sound generated by flow. Furthermore, he remains the most influential and useful analytical tool for the understanding and reduction of flow noise, further information can be found in Glegg and Devenport [54]. Readers should refer to Lighthill works [85, 86] for further information. A brief description of Lighthill's Acoustic Analogy follows in Section 2.1.1.

2.1.1 Lighthill's Acoustic Analogy

Sound waves in air correspond to oscillations in the pressure field. Hence, they are described by the compressible Navier-Stokes equations. Unfortunately, accurate numerical solutions that can predict the noise generated from complex geometries are computationally far too demanding to be employed in most practical situations.

Driven by the increasing need to reduce jet noise, Lighthill [85, 86] developed his "Acoustic Analogy". His inspiration arose from experiments where it was observed that oscillations, introduced acoustically at the orifice of the jet, could be significantly amplified under certain conditions. To describe this phenomenon the term "aerodynamic sound" was introduced. This sound can be defined using Lighthill's acoustic analogy, which was derived from the continuity and momentum equations that are part of the compressible Navier-Stokes equations. This analogy Lighthill's derived an inhomogeneous wave equation, known as Lighthill's wave equation:

$$\frac{\partial^2 \rho'}{\partial t^2} - c_\infty^2 \frac{\partial^2 \rho'}{\partial x_i^2} = \frac{\partial^2 T_{ij}}{\partial x_i \partial x_j} \tag{2.1}$$

where

$$T_{ij} = \rho u_i u_j - \left[(p - p_\infty) - (\rho - \rho_\infty) c_\infty^2\right] \partial_{ij} - \sigma_{ij} \tag{2.2}$$

is Lighthill's stress tensor, c_∞ is the speed of sound, ρ is the density of medium, p is the static pressure of the flow fluid, t the time of the acoustic observation at point x; u_i and u_j are velocity components, σ_{ij} is Lighthill stress tensor and δ_{ij} is the Kronecker delta. The first part of Eqn. 2.1, defines the acoustic wave propagation within a uniform medium where the speed of sound

is determined by the medium density. The second part of Eqn 2.1, is defined as source terms which include the effects that produce acoustic waves.

Lighthill's acoustic analogy, Eqn. 2.1, can be defined as wave propagating through a stationary medium at the speed of sound. The second part of Eqn. 2.1 is composed of the fluctuating forces, from a quadrupole source field, where the strength is defined by Lighthill's stress tensor. Therefore, sound waves are the resultant effect of internal stress of a fluid flow fluctuating in a uniform non-moving acoustic medium.

The formula defined in Eqn. 2.3 generates the sound pressure level (SPL) produced at point y in the flow and the observation point at x, which reduce to a point quadrupole within a volume $\mathcal{V}$ in the flow field. Therefore, where known the flow parameters define the generation of sound by a quadrupole source field from turbulence in free space.

$$p(x,t) = \frac{\partial^2}{\partial x_i \partial x_j} \int_{\mathcal{V}} \frac{T_{ij}\left(y, t - \frac{|x-y|}{c_\infty}\right)}{4\pi c_\infty^2 |x-y|} d\mathcal{V} \tag{2.3}$$

2.2 Aerofoil Self Noise

Aerofoil self-noise, also known as aerofoil TE noise, is noise radiation that results from the interaction of turbulent flow structures, present – and generated – in the boundary layer with the surface of the aerofoil and the near wake.

A study by Brook *et al.* [125] identified five mechanisms of aerofoil self-noise. These are illustrated in Figure 2.1 and defined as:

1. **Laminar Boundary Layer Instability Noise** is observed as a narrowband, tonal noise. It occurs when the viscous Tolmien-Schlichting (T-S) instability waves disturb the laminar boundary layer of an aerofoil. The formation of T-S waves generates periodic surface pressure fluctuations which scatter at the TE. As a result, acoustic pressure waves of tonal instability noise are produced. Three aeroacoustics feedback models were proposed by Arbey and Bataille [6], Desquesnes *et al.* [39], Tam [124]. Each of these feedback models observes the wake propagation upstream to the region of instability in the boundary layer that effectively amplify them. The overall effect results in an amplified tonal noise. For further information please refer to citations. However, T-S waves are not the only mechanism responsible for the tonal generation. Alternatively, the presence of a separation bubble near the TE is assumed where the separated boundary layer undergoes a Kelvin-Helmholtz (K-H) instability leading to the periodic shedding of rolls of recirculating flow

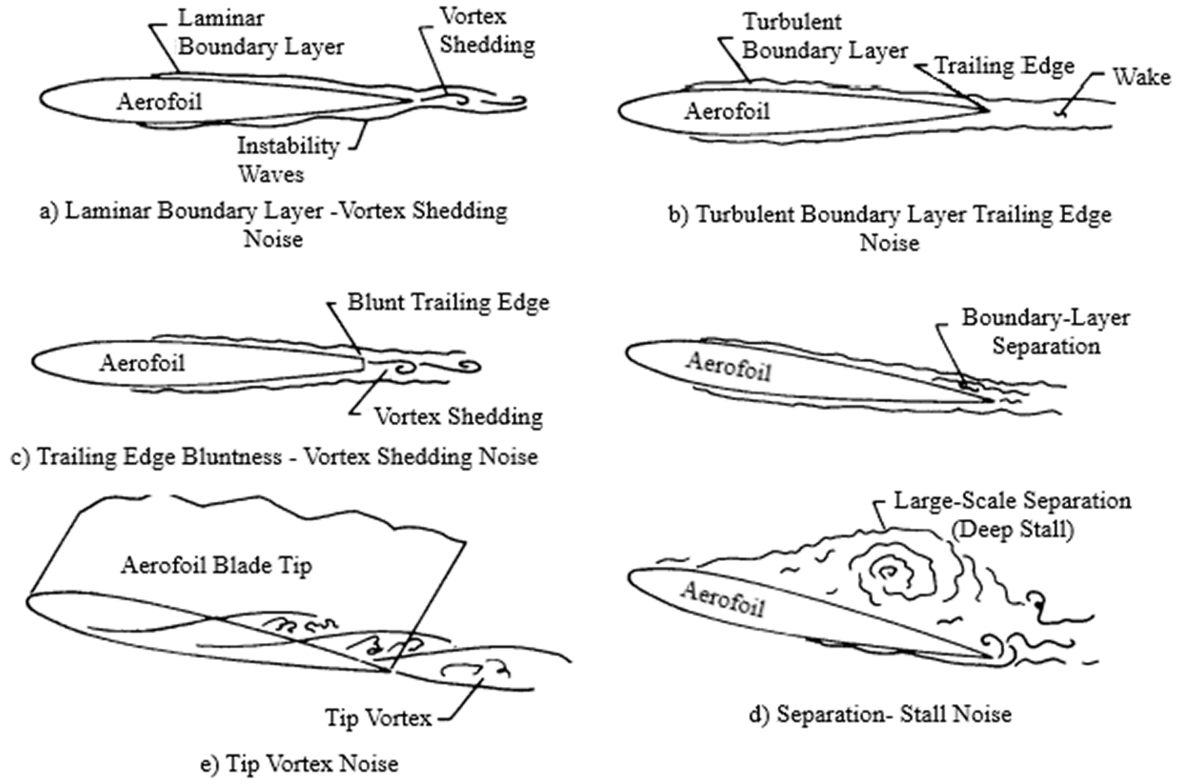

Figure 2.1: Aerofoil self-noise mechanisms based on Brooks *et al.* [19], where a) Laminar Boundary Layer - Vortex Shedding Noise, b) TBL-TE Noise, c) Trailing Edge Bluntness - Vortex Shedding Noise d) Separation - Stall Noise and e) Tip Vortex Noise. (Adapted from Brooks *et al.* [19])

(vortices) that typically have a low pressure in the interior. The K-H instability is likely to be seeded by the T-S waves originating upstream and, hence, acts as an amplifier.

2. **Turbulent Boundary Layer – TE Noise**, TBL-TE noise, is observed as a prominent source of broadband noise across a wide range of frequencies for attached boundary layer flow. This noise source occurs at high Reynolds numbers where turbulence develops in the aerofoil boundary layer, formed by eddies of various sizes and energies. The turbulent boundary layer is formed of broadband spectrum surface pressure frequencies, as these unsteady structure, describe by the Navier Stoke equations, scatter at the TE into acoustic waves with a broadband nature.

3. **Blunt TE noise – TE Bluntness** is observed as vortex shedding noise. The noise is characteristic of a tonal nature and is identifiable by a distinct broadband peak superimposed on the frequency spectrum. In the case of a turbulent boundary layer, the audible bluntness noise dominates as a distinct noise over the broadband noise. The vortex shed-

ding noise occurs at regions with small separation occurring at the aerofoil blunt TE or bluff body; this promotes the formulation of von Karman style vortex streets in the wake. This formulation results in the periodic pressure fluctuation near the TE which gives rise to tonal noise characteristics. The ratio at which bluntness noise is generated for cases usually occurs at a ratio higher than $\epsilon/\delta^* = 0.3$, where δ^* is the boundary layer thickness and ϵ is the bluntness in mm.

4. **Separation – Stall Noise** is observed at high angle of attack, AoA, where the aerofoil produces its maximum lift resulting in flow separation. As a result, a large recirculation bubble of highly unsteady flow creates broadband noise; studies have reported a noise increase up to 10 dB [48]. Paterson *et al.* [106] investigated Brooks' proposal of the difference between lightly separated flow and deep stall origin noise source. He suggested that for lightly separated flow, the dominating noise source would originate from the TE, whereas aerofoil undergoing deep stall would originate from the chord.

5. **Tip Noise – Tip Vortex Formation Noise** is generated at the tip of the blade where local separation of the flow occurs. This results in strong streamwise coherent vortex formation at the tip of the blade which has a rapid rotating core. As a consequence, these structures have a negative effect on both the aerodynamic and acoustic performances. Brooks and Marcolini [125] successfully quantified the noise source of tip vortex formation; furthermore they examined the acoustic radiation of two- and three-dimensional aerofoil models at various conditions.

This research focuses on the TBL-TE noise. The TBL-TE noise has received significant development and attention in research. The first scientist was Powell [111] in 1959, who published an experimental and analytical study of TE noise. Subsequent fundamental works have been presented by Ffowics Williams and Hall [46], Chase [24], Lighthill [86] and Curle [35].

Brooks *et al.* [125] compiled extensive aerofoil TE noise results for a NACA 0012 aerofoil. Subsequently, Brooks and Hodgson [19] measured surface pressure spectra which were analysed to predict far-field noise radiation. Analytical radiation models for interaction of a turbulent boundary layer with a semi-infinite rigid flat plate at 0° incidence angle in subsonic flow were proposed by Amiet [3], Howe [65, 69], Ffowcs-Williams and Hall [46], Crighton and Leppington [33].

During the 1970s, several noise prediction models for the TE were developed and based on three different approaches, according to Howe [68]:

1. Approach based on Lighthill's acoustic analogy [86]. The following models have been

developed by Ffowcs Williams and Hall [46]; Crighton and Leppington [33]; Crighton [33]; Levine [84] and Howe [64, 66, 67].

2. Approach based on the solution of special problems derived by linearized hydroacoustic equations: Crighton [34]; Jones [75]; Crighton and Leppington [32]; Morgan [97]; Chase [24, 25]; Chandiramani [23]; Davis [37] and Amiet [4].

3. Ad hoc methods.

The common examples for the prediction of TE noise are expressed in the works of Amiet [4] and Howe [68]. Their models, which differed in the way the aerodynamic near field was linked to the acoustic radiation, reached similar conclusions. In fact, both methods showed that the sound which radiated in the far field adhered to the velocity power law of U^5 for the pressure density spectrum, as initially suggested by Ffowcs-Williams and Hall [46]. Amiet [4] and Howe [65, 69] models are valid for acoustic wavelengths smaller than the aerofoil chord and are based on the semi-infinite flat plate assumptions. Here should be noted that Amiet's model [4] is valid for all subsonic flows, while Howe's model [69] is valid only for very low Mach numbers.

2.3 Aerofoil Trailing Edge Noise Reduction

Since the 1970s significant research has been performed on aerofoil TE noise reduction, mainly through either experimental, numerical, or analytical works.

2.3.1 Biomimetics and Trailing Edge Treatments

The development of new ideas and engineering of new technology is regularly based on biomimicry from nature. The science of biomimetics or biomimicry is defined as the study and development of systems that mimic biological systems as a model for the function of biological mechanisms. In the context of this research, the inspiration was found in the silent flight of the owl as an attractive method to achieve aerodynamic noise reduction.

Graham [56], in 1934, was the first to investigate silent flight of the owl and to identify the three main characteristics which gave the owl the characteristics of silent flight. Further investigations by Kroeger [82] in the early 1970s formed part of a programme of research into novel designs for quieter aircraft. More recently, Lilley [87], Bachmann and Klan [14] further investigated this topic. The in-depth study by Graham [56] identified the wavy comb-type leading edges, more commonly known as serrations, the periodic fringe type TEs and a downy, fibrous upper surface of the wing. The structure of the wing shows that millions of years of evolution of these features

enable the owl to generate silent flight within the maximum hearing range of its prey, typically mice and voles, at least at frequencies between 2 kHz and 20 kHz. Bachmann [14] presented detailed pictures of the feature found on the leading edge and TE of the wing structure shown in Figure 2.2 .

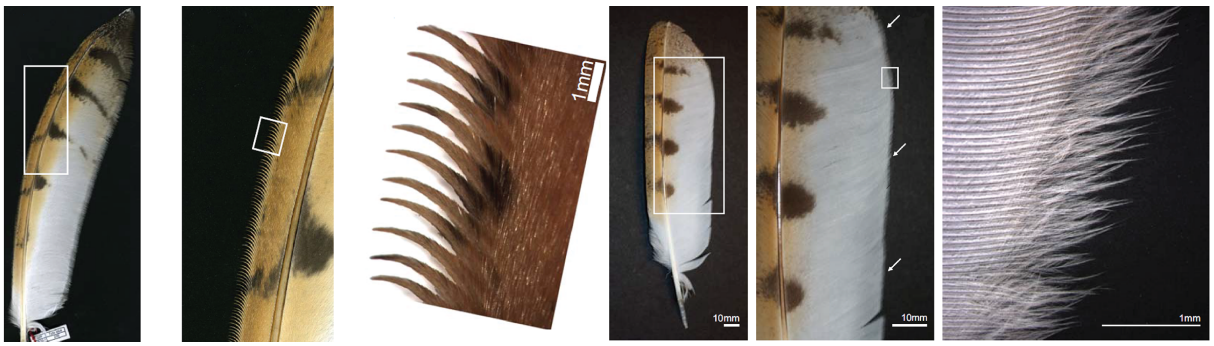

Figure 2.2: Serrations at the outer vane (left) and fringes at the inner vane (right) from barn owl feathers with magnifications (Adapted from Bachmann [14])

The owl has superior aerodynamic efficiency through its unique wing features. Kroeger [82] and Lilley [87] identified that the leading-edge serrations delayed the separation of the flow at a very steep flight path with an incidence angle of 24° at low Reynold number (1.5×10^5), when approaching its prey. In comparison, conventional aircraft wings exhibit flow detachment near the leading edge, followed by stall at these steep angles of attack. Kroeger [82] and Lilley [87] explained that each serration generates vortices and enables the boundary layer to remain attached even as the wing dynamic approaches stall. They found the addition of the serrations provided noise reductions up to approximately 20 dB. The effects of removing the leading edge comb from the owl wing resulted in the owl flight becoming unstable and as noisy as any other bird's. The fringes found at the TE of the wing caused mixing of the upper and lower boundary layers and reduced scattering by the edge discontinuity. Lilley [87] stated that TE fringes on their own resulted in reduction of 6 dB to 7 dB compared with noise measurements on a bird of similar size and mass.

The fibres of the fluffy fibrous feathers found on the surface of the upper wing and around the claws of the owl have a length scale just a little larger than the size of the Kolmogorov eddies. Lilley [87] stated that the very low noise at frequencies above 2 kHz, related to the turbulent energy of the boundary layer was absorbed by the fibrous feathers, causing a bypass dissipation mechanism. A study by Geyer *et al.* [53], conducted flyover noise measurements of three types of birds, owls, harris hawks and common kestrels. They found that the owl had superior noise characteristics at the mid-to-high frequency range.

2.3.2 Trailing Edge Serration

The bio-inspired passive flow control represents an attractive method to achieve aerodynamic noise reduction. The use of serrations is shown to be one of the most effective passive devices to reduce the TE noise of aerofoils. Also, this passive treatment came in several configurations, such as the slit [57], brush [47, 62, 63], wavy [69], M-shaped [80, 115] and sawtooth serration TE [18, 58, 70, 100, 130]. The focus of this study is on the sawtooth serration and slit TE.

A. Trailing Edge Serration - Noise

The application of TE serration has successfully demonstrated reduction in TE noise for wind tunnel experiments up to 8 dB, Dassen *et al.* [36]; Parchen *et al.* [105]; Gruber [57]; Chong; Liu [88]; Chong and Vathylakis [26]; and Thomareis and Papadakis [126]. In addition, full-size wind turbine blades have achieved reductions up to 3 dB through the works of Oerlemans *et al.* [100], Hagg *et al.* [60], Braun *et al.* [18], Schepers *et al.* [118], amongst others. The wind tunnel studies focused on two types of implementation of serrations:

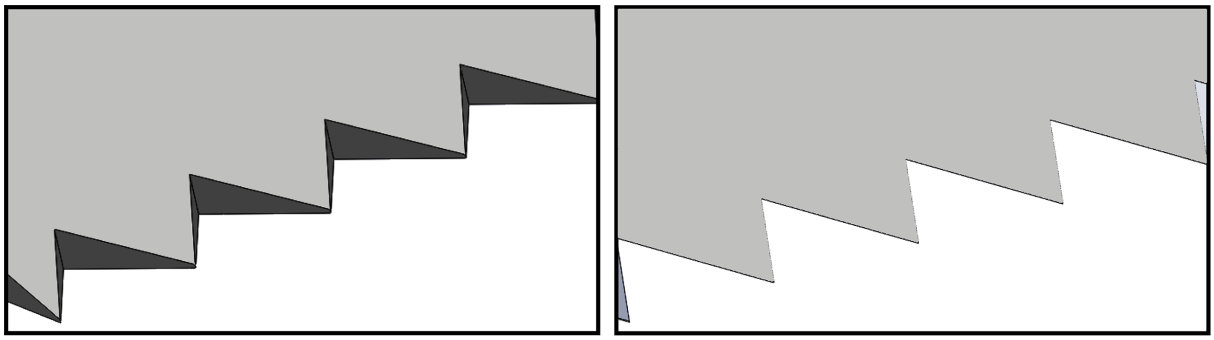

Figure 2.3: Two types of approaches of serrated TEs: a) Cut-in Serrations; and b) Flat Plate Insertion Serrations

1. Cut-in type serrations, whereby the wedges are cut into the aerofoil, illustrated in Figure 2.3a).

2. Flat plate serration attached to un-modified aerofoil, illustrated in Figure 2.3b).

The focus of this study is on the add-on flat-plate device attached to an un-modified aerofoil.

In additional to the aforementioned experimental works, analytical models were developed to predict noise reductions achieved by TE serrations. Howe [65] developed a theoretical expression of the potential noise reductions by a serrated sawtooth TE for a low Mach number flow. Howe

derived an analytical model for the prediction of TE noise over a flat plate with a serrated TE. The theoretical model stipulates that the serrated inclination angle must be less than 45° to the freestream direction to be effective in the noise reduction at frequencies $\omega H_{1/2}/U_\infty \ll 1$, where $H_{1/2}$ is the half-length of the sawtooth and U_∞ is the freestream velocity. It was also stated that the dimension of the serration must be of the same order as the turbulent boundary layer thickness δ near the TE. The studies by Braun *et al.* [18], Oerlemans [100], Gruber *et al.* [57], Moreau and Doolan [96], Chong *et al.* [26] found that the predicted noise reduction was an overestimation of those predicted by the Howe's model. Recently, Lyu *et al.* [91] developed a theoretical model for the prediction of sound radiated by serrated TEs. The new model provides a better prediction of noise generated by serrated TEs, which is underpinned by the mechanism of the destructive interference on the scattered pressure field.

The STENO (Serrated TE NOise) research project (Dassen *et al.* [36], Braun *et al.* [18]) as well as Oerlemans [100] aimed to verify whether the noise reduction performance due to TE serrations that was found on a 2D aerofoil in a wind tunnel was also applicable to a 3D full scale wind turbine. The study investigated the effects of TE serrations to wind turbine blades to evaluate the effects of length, position, and orientation of the serrations on acoustic performance. Dassen *et al.* [36] performed wind tunnel investigation of aerofoil TE noise reduction using eight aerofoils and six flat plate configurations of 250 mm chord length with different geometries. They observed acoustic reduction up to 10 dB at 1 kHz $< f <$ 6 kHz for serrated flat plates, in comparison to the serrated aerofoils which exhibited reductions up to 8 dB. The serrations on the TEs of a flat plate only yielded no a reduction in noise of no more than 2 dB when different configurations were implemented, illustrated in Figure 2.4. However, an increase in flap angle or misalignment of the sawtooth of 15° to the main flow direction, resulted in an increase in high frequency noise. Braun *et al.* [18], carried out small-scale experiments as part of the STENO research project. They found that serrations were effective at low frequencies with reduction up to 2 dB, where the opposite was true with noise increase at high frequencies and also at high angles of attack.

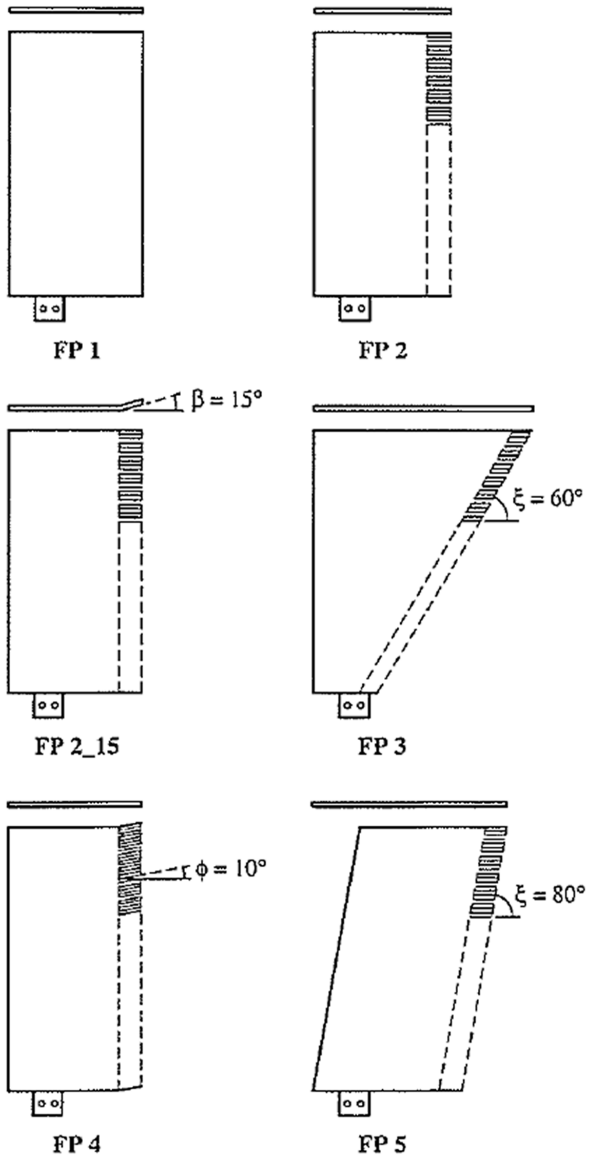

Figure 2.4: A study of serrated flat plates (From Dassen *et al.* [36] Figure 3)

Parchen *et al.* [105], in 1999, performed a comparison between experimental results obtained using serrated TEs and Howe's theory. They examined serrations applied to both wind-tunnel-scale and full-scale wind turbines, where broadband noise reductions were observed of up to 6 dB. Furthermore, the measurements confirmed that the prediction based on Howe's theoretical model was much larger than the measured noise results. Parchen *et al.* [105] also identified that noise increase for the full-scale wind turbine was exhibited for misaligned serrations to the freestream flow direction. Subsequently, Gruber [57] demonstrated that additional noise was seen at all angles of attack.

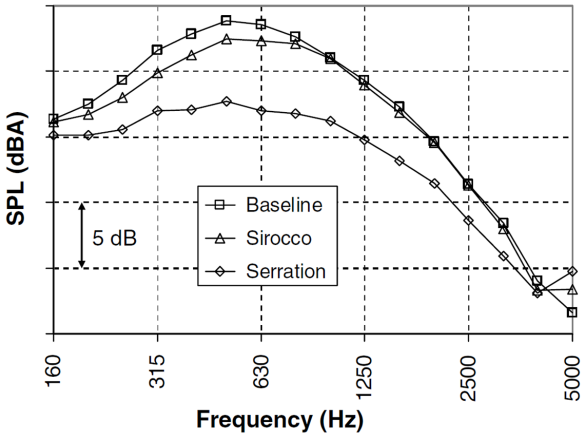

Figure 2.5: Average noise reduction of the far-field third octave band sound measurements upwind on a clean blade performed on a full scale wind turbine using conventional blade, Sirocco (optimised) blade and add-on TE serrations. (From Oerlemans *et al.* [100] Figure 13)

Oerlemans *et al.* [100] conducted experiments on a full scale three bladed wind turbine, of 94 m diameter, using serrations and shape optimization to reduce TE noise. Oerlemans *et al.* [100] examined three blades: NACA 64418, commonly used in wind turbines, as a reference blade, a blade with optimized shape and a blade with add-on serrations. They observed that the optimized aerofoil showed an overall TE noise reduction of 3.2 dB and a maximum reduction of 5 dB up to $f < 1$ kHz. In comparison, the serrations produced a further reduction of about 2 to 3 dB and an increase in high frequency noise. Oerlemans *et al.* [100] stated that the high frequency noise increase was a result of the misalignment of the serrations with the flow direction.

Most of the wind tunnel-based research investigating serrated TEs were performed on either a high camber aerofoil NACA65-1210 or on symmetrical aerofoils such as NACA 0012. The focus of this study is on the NACA65-(12)10 aerofoil. Gruber [57] examined sawtooth TEs in a series of experiments to investigate two common serration parameters: serration amplitude and serration wavelength. It goes without saying that Gruber's research provides a wealth of information on serration design. He observed the following characteristics:

1. Self-noise reduction occurs for non-dimensional frequencies $f\delta/U_\infty < 1$, and non-dimensional serration amplitudes $h/\delta > 0.25$, where δ is boundary layer thickness, f is frequency (Hz) and U_∞ is freestream velocity. Enhancement in noise reduction occurred with larger serrations and smaller serration wavelengths. In contrast, at $f\delta/U_\infty > 1$ observed noise increase at high frequencies.

2. For $H/\delta < 0.25$, the serration became ineffective with the turbulent eddies passing over the serration surface. Gruber *et al.* [57] suggested that the serration amplitude should be

twice the boundary layer thickness $H \approx 2\delta$ thus the serration amplitude would correlate to the larger turbulent structures within the boundary layer.

3. The serration edge angle, defined as a ratio between serration amplitude and serration wavelength H/λ, led to noise reduction when increased. However, the effects of serration edge angle had an upper limit.

4. Increase in high frequency noise was suggested to be the result of the cross-flow between the serrations.

The investigation into the effects of misalignment has been addressed by Dassen *et al.* [36] who concluded a loss of the noise reduction performance of the serration. Furthermore, several studies suggested misalignment to be the cause of high-frequency noise. Prior to this study, very few have considered this as a research parameter. Instead, flap angles often have been defined as a side-effect of the serration installation to aerofoil, especially those with large camber. However, a recent study by Vathylakis *et al.* [130] and Arce León *et al.* [1] investigated the effects of misalignment to serrated TEs. They artificially bent their sawtooth serration to facilitate a controlled "flap angle". Arce León *et al.* [1] investigated the flow and noise characteristics of a NACA 0018 with sawtooth TE. They reported that negative flap angles (flap-down) could degrade the level of broadband noise reduction in comparison to the straight serrations, or even produce higher noise level than the baseline, straight TE case. Such noise increase is usually accompanied by the presence of high turbulence intensity in the wake.

The most common geometrical variables describing a serration are traditionally the serration amplitude and wavelength. Whilst keeping these variables constant, Vathylakis *et al.* [130] investigated the sensitivity of the aerofoil broadband noise reduction to a third geometrical variable – serration flap angle – which could be regarded as a form of serration misalignment. Several flap angles, ϕ, were investigated: $\phi = \pm 5^\circ, \pm 10^\circ, \pm 15^\circ$, where the flap angle at $\phi = 0^\circ$ was treated as the reference. They found that certain serration flap angles further improved the level of broadband noise reduction. In particular, the flap-up positions were generally found to achieve higher level of broadband noise reduction than the flap-down positions. The most optimum flap-up angle was at $\phi = +5^\circ$, where it outperformed the non-flap angle cases from mid-to-high frequencies. The -5° flap-down angle represented the worst performer amongst all the non-zero flap angle cases because of the consistent noise increase throughout the whole range of frequency. Nevertheless, the largest flap-down angle at $\phi = -15^\circ$ produced almost the identical level of broadband noise reduction as the non-flap angle case.

B. Trailing Edge Serration - Flow Characteristics

Various aerodynamic studies of flow over an aerofoil with serrations at the TE were carried out. Here, the focus was on wake development, flow motion at the surface and the effect of spacing between serrations. These flow measurements included hot-wire anemometry, Particle Image Velocimetry (PIV) and surface pressure measurements.

Geiger [50] studied two serrated TEs, with amplitudes $H = 12.7$ mm and $H = 25.4$ mm, respectively, to observe the changes in blade steady loading and the wake behind the serrated TEs. The steady loading data was obtained using static pressure taps distributed over the aerofoil surface. Geiger [50] stated that the serrated case compared to the non-serrated case showed a variation smaller than 9% over the whole aerofoil body, with almost non-existent changes in steady loading at the aerofoil TE in comparison to the straight TE. From the hotwire measurements, that were conducted of the mean and unsteady velocity within the wake, the following observations were made:

1. The presence of serrated TE increased wake thickness. In fact, the larger the serration amplitude, the greater the wake thickness.

2. That increasing the serration amplitude led to a reduction in the maximum velocity deficit at the wake centreline.

3. The serrated TE observed increased mixing of the turbulent flow due to increased vorticity. However, reduced levels of turbulence kinetic energy (TKE) were observed for serration when $x/c > 1$, where c is the chord length and x is the downstream location with aerofoil TE being $x = 0$, in comparison to the straight TE.

4. The serrated TE case found the rate of decay at the wake centre line increased at the serration tip and reduced at the root of the sawtooth when compared to the baseline case. In addition, the serrated TE case with larger serration amplitude observed increase rate of decay.

5. The serrated TEs was found to have higher redistribution rate of the wake, in comparison to the baseline. Furthermore, it was found that downstream of the serration tip were more effective at redistributing the wake, whilst, downstream of the serration roots were found to be the least effective. He also indicated that increase of serration amplitude further improved the redistribution rates within the wake.

6. At the tip of serrated TE observation of the production of TKE was superior.

Chong and Vathylakis [26] performed several experimental techniques to study the effect of a turbulent boundary layer convecting over the serrated TE on a flat plate. They observed a strong correlation between the time-averaged heat-transfer and pressure measurements that indicated the presence of convective pressure-driven vortical structures which formed near the edge of the serration, as well as the tip region. They suggested that the presence of the vortical structures was a contributor to the efficiency of broadband self-noise reduction, due to the redistribution of the shear stress, momentum transport and turbulent, along the oblique edges and tips of the serrations. They also found that the mechanism that resulted in reduction of the self-noise radiation was inconsequential to the variation in the wall pressure power spectra density (PSD) and the spanwise coherence.

Several studies were performed by the aeroacoustics team from TU Delft University investigating the acoustics and flow-field via experiment and/or computational method [1, 10–13, 83, 89, 113, 131].

An experimental study of the three-dimensional flow-field of a turbulent boundary layer convecting over a serrated TE was examined by Avallone *et al.* [11] They performed time-resolved tomographic PIV on a NACA 0018 aerofoil with a serrated TE mounted in an open jet wind tunnel at an AoA of 4°. The boundary layer upstream of the serrations exhibited a moderate effect on the turbulent boundary layer for the mean velocity and turbulent fluctuation, which agreed with the study of Gruber *et al.* [59]. The flow pattern, downstream of the serrations, became significantly complex for the serrated TE, in comparison to the straight TE, with the formulation of counter-rotating streamwise vortical structures along the oblique edge. Avallone *et al.* [11] suggested that the formulation of the vortical structures along the oblique edges were the result of the pressure gradient between the two sides of the aerofoil. In addition, observation of streamwise-oriented vortices, described as a 'funneling motion', were found in the air gaps between the serrations. These structures caused a secondary effect, by funnelling the incoming flow which distorted the serration effective angle. This phenomenon was also reported by Chong and Vathylakis [26] who suggested that this distortion could contribute to the way broadband noise was scattered along the oblique edges. They evaluated the time average streamwise velocity component at the serration surface that showed the flow approaching the serration drawn into the serration gaps, which concluded in a funnelling effect. Furthermore, acceleration of the streamwise velocity was observed near the tips of the serrations; this caused a thinning effect on the boundary layer and an increase of the spanwise correlation length. This was also confirmed by Jones and Sandberg [76] and more recently by Van der Velden *et al.* [131].

Arce León *et al.* [1] utilised the stereoscopic PIV to study the effects of serration flap angle and aerofoil incidence on the flow. They observed the effect of the secondary flow established on the suction and pressure sides of the serrated TE. The results showed the additional formation of streamwise vortex pairs in the cross-flow plane, which also reported by Avallone *et al.* [11]. The relationship between these vortices and the serrations with flap angles was found to be stronger than the relationship between the vortices and the aerofoil incidence angle. At zero aerofoil incidence and serration flap angles the mean flow behaviour near the serration adhered closely to Howe's assumptions of a reduced acoustic scattering efficiency in the presence of oblique edges. Streamlines at the serrated TE were observed to align with the edge of the serrations on the suction side. In contrast, the opposite occurred on the pressure side with the streamlines tending to become normal to the edge of the serrations.

Juknevicius and Chong [77] performed an experimental study into flow mechanisms with add-on sawtooth serrations which led to TE broadband noise reduction. They traced the temporal spatial development of an artificially generated synthetic turbulent boundary layer across straight and serrated TEs of a NACA 0008 aerofoil. They established that the upstream boundary layer was not significantly altered by the presence of the serrations. This was also reported by Avallone *et al.* [11]. However, they observed existence of time dependent secondary flow at the serrations and into the near wake, where vortical structures formed, aligned with the oblique edge, which significantly altered the flow patterns. Furthermore, they identified that the highest noise reduction for the serrations were at the time of instance where the presence of secondary flow was observed. They concluded that the noise reduction was linked to reduced levels of wall-normal velocity fluctuations close to the surface of the serrations, as a result of the vortical structures. These structures lowered the intensity of turbulence interaction with the serration surfaces and edges, thus reducing the levels of radiated noise. At the near wake region, the high momentum anticlockwise vortical structure was formed at the tip. This vortical structure transferred velocity fluctuation from a transverse to a spanwise direction, thereby causing an increase in the anisotropic level of the turbulence at the serrations.

C. Trailing Edge - Numerical

Numerical methods can provide additional information of the flow dynamics near the (serrated) TE. Some numerical methods use empirical models for an effective prediction of the far-field noise levels, such as Amiet [4], Ffowcs Williams [46], Lighthill [86] and Curle [35]. However, to work properly these empirical models require experimental inputs. Over the last decade, due to the increase in computational power available to the research community, numerical simulations of

aerofoil flow characteristics and noise prediction has become increasingly important. To date, the majority of the numerical analyses have been performed using Reynold Average Numerical Simulation (RANS), Large Eddy Simulation (LES), Direct Numerical Simulations (DNS) or Lattice Boltzmann method to investigate the flow-field, and more recently, noise prediction/ acoustic emissions.

Sandberg and Sandham [117], Sandberg and Jones [116] and Jones and Sandberg [76] conducted DNS of turbulent flow at moderate Reynolds numbers past NACA 0006 and NACA 0012 aerofoils at different angles of incidence. They investigated several mechanisms of aerofoil sound generation to identify potential sources of noise and studied the application and accuracy of Amiet's theory to predict far-field sound using computed hydrodynamic DNS data. In addition, Jones and Sandberg [76] examined the effects of TE serrations on aerofoil TE noise generation.

Jones and Sandberg [76] performed DNS of the flow around a NACA 0012 aerofoil with and without serrated TEs. The numerical simulation was performed at Re = 50,000, corresponding to Mach number of 0.4, at a geometrical AoA of 5°. They investigated two types of serration amplitude based on boundary layer thickness where the short and longer serrations were δ and 2δ respectively. They observed a broadband noise reduction between 6 to 10 dB, where the longer serrated TE exhibited a greater noise reduction across a larger frequency bandwidth. In contrast, the shorter serrated TE results showed an increase in noise at high frequencies. They found that the TE directivity was unaffected by the TE serrations, whereas the boundary layer properties and the spanwise correlation lengths were slightly affected. Furthermore, the formulation of horse-shoe vortices were observed behind the serrations which resulted in a faster mixing of the turbulence in the aerofoil wake.

2.3.3 Alternative Periodic Trailing Edges

Examples of alternative periodic TEs are the so-called brush and slit TEs. A fibre-type (brush) TE consists of one single row of propylene fibres and was introduced by Herr [62, 63] as a method of reducing TE noise. Herr [62] measured broadband noise reduction on both a NACA 0012 aerofoil and a flat plate. Vortex shedding tonal noise was observed from the blunt baseline TE. The use of the brushes resulted in the suppression of the narrowband tonal noise. It also resulted in reduction of broadband TBL-TE noise up to 9 dB.

Herr [63] stated that the noise reduction depended on the brush geometry rather than the flow characteristics, where the following features were important:

1. A spacing between adjacent brushes of the order of the viscous sublayer thickness produced maximum broadband noise reduction, whereas an increase in spacing to 0.1 mm degraded the broadband noise reduction capability by about 5 dB.

2. The length of the brushes was found to be a critical parameter and needs to be larger than the boundary thickness from δ to 2δ.

3. The thickest diameter brush type resulted in the largest noise reductions.

4. Broadband noise reduction occurred between $0.02 \leq St \leq 0.2$. However, at $St > 0.2$ noise increase was observed which was close to the non-audible frequency range.

A similar study by Finez *et al.* [47] investigated brushed TE treatments on a NACA 65-(12)10 aerofoil, where a reduction in noise of 3 dB between 600 Hz to 2 kHz was observed. They also observed recirculation bubble noise near the leading edge, which dominated the noise emission at higher frequencies. It was observed that the spanwise pressure based on the correlation length was reduced to almost 25%, which might have resulted in the 1.3 dB noise reduction measured in the far-field. However, the large discrepancies between Herr's and Finez's studies of the noise reduction suggest a strong sensitivity with regards to the way in which the brushed TE treatments were implemented. To obtain noise reduction, both studies confirmed that brushes must have a larger length than the boundary layer thickness, and that a minimal separation distance between brushes is required.

Ortmann [103] investigated aerodynamic effects of adding slits and brushes to an aerofoil TE. It was observed that compared to the slits, the TE brushes offered significant noise benefits but adversely affected the aerodynamic performance.

Gruber [57] assessed the slit TE noise performance to reduce aerofoil TE self-noise. He considered three geometrical parameters: slit amplitude, H, slit width, d_2, and distance between adjacent slits, d_1. Gruber [57] observed the following:

1. The largest slit amplitude produced greater broadband PWL reductions of up to 2 dB, whereas the smaller slit amplitude only provided insignificant noise reduction. The sound emission of the largest slit amplitude was most effective at low freestream velocities; in contrast, at $U_\infty > 40$ ms^{-1} increased broadband noise was observed

2. Noise reduction only occurred at slit amplitude, H, corresponding to certain fraction of the boundary layer thickness, $H > \delta$.

3. Reducing the d_1 greatly increased the maximum broadband noise reduction for slit amplitude and freestream, however, at the expense of increased high frequency noise.

4. At high frequencies reduction in noise was observed with increase of d_2. It was shown that $d_2 = 0.5$ mm and $d_2 = 1$ mm exhibited noise increase up to 5 dB and up to 2 dB respectively.

2.3.4 Summary

In the literature it has been shown that bio-inspired passive flow control devices provide an attractive method for reducing aerodynamic noise reduction. In particular, the bio-inspired saw-tooth serration has received significant scientific attention via wind tunnel and full-size wind turbine experimental research, as well as numerical and analytical works. Studies have shown that, from an aeroacoustics perspective, trailing edge serrations offer considerable benefits. However, usually these benefits were accompanied by a consistent increase in high frequency noise levels. This increase was assumed to be caused by either the cross-flow in between the serrations or by the misalignment of the serrations. However, it was suggested by Vathylakis et al. [130] that the application of trailing edge misalignment could further improve the level of broadband noise reduction. To date, the effects of serration misalignment, or "flap angle", are not fully understood. In the literature review also studies were identified that concern the application of serrations at the trailing edge with periodic variation of depth and width. Hardly any studies were found that consider either applications of slits at the trailing or make use of alternative acoustic mechanisms to reduce trailing edge noise.

Chapter 3

Experimental Facilities, Instrumentation and Computational Methods

3.1 Aero-acoustic Open Jet Wind Tunnel Facility

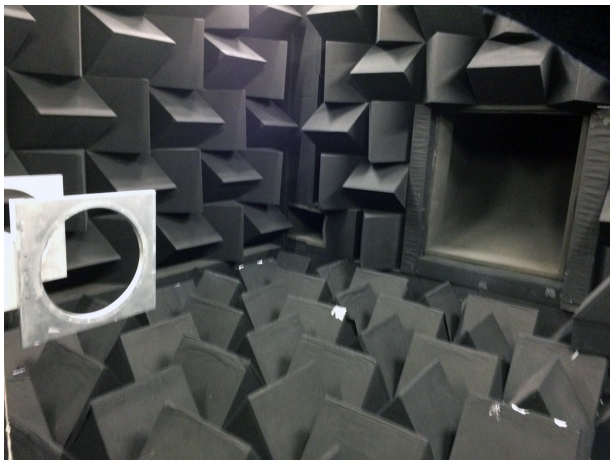

Figure 3.1: Aero-Acoustic facility at Brunel University London with open jet wind tunnel within an anechoic chamber

Far-field noise and flow visualisation measurements were performed in the aero-acoustics facility at Brunel University London, which consists of an open jet wind tunnel within an anechoic chamber of 4 m $\times$ 5 m $\times$ 3.4 m. The open jet nozzle dimension is 0.3 m $\times$ 0.1 m (width $\times$ height). As shown in Figure 3.1, The anechoic chamber is lined across the floor, walls and ceiling with acoustically treated triangular foam blocks to reduce the reflection of acoustic waves. A

far-field polar array that could be adjusted in the streamwise direction was positioned directly above the centreline of the exit of the open jet nozzle. For further information regarding the aero-acoustic facility see Vathylakis, Chong and Kim [129].

The open jet wind tunnel nozzle has an aspect ratio of 25 with the inlet dimension being 0.867 m × 0.867 m to an outlet, as previous stated above, of 0.1 m × 0.3 m. The open jet wind tunnel has an operational capacity of up to $U_\infty = 80$ ms^{-1} and features a low turbulence intensity between $I = 0.1\%$ and $I = 0.2\%$ at $U_\infty = 20$ ms^{-1} and $U_\infty = 30$ ms^{-1}, respectively. The background noise (without aerofoil, but with side plates) is largely attributed to the open jet noise, which is very low in comparison to the aerofoil self-noise level produced at the identical flow speeds, refer to Figure 4.1 in Sec. 3.3.1.

The aerofoil body is held by two side (wall) plates mounted to the nozzle lips at the exit of the open jet wind tunnel nozzle. The side walls comprise three parts, outer side walls, inner side plate and side plate clamps. The outer side walls were manufactured from aluminium alloy and are attached flush to the nozzle lips which also hold a circular Perspex plate. The inner circular Perspex side plates allows rotational movement to be able to vary the AoA, $-20° < \alpha < 20°$, of the test section. The test section is held between two 3D printed half profiles plates which clamps the test model.

3.2 Design of the NACA65-(12)10 camber aerofoil

x-coordinate displacement in mm										
	1	2	3	4	5	6	7	8	9	10
Pressure Side	2.5	10	15	20	30	40	50	70	90	110
Suction Side	2.5	7.5	12.5	20	30	40	50	70	90	110

Table 3.1: x-coordinate displacement of the surface pressure taps on the pressure and suction surfaces of the NACA 65-(12)10 aerofoil.

Research was conducted on the NACA65-(12)10 cambered aerofoil. This particular NACA 65-(12)10 cambered aerofoil was previously used at the Institute of Sound and Vibration Research (ISVR) at the University of Southampton [57] and most recently at Brunel University London [130]. The NACA 65-(12)10 cambered aerofoil consisted of two parts: a main aluminium alloy body and a detachable TE. The main body was manufactured from solid aluminium alloy with ten pressure taps, with hole diameters of 0.5 mm, across the upper and lower surfaces at positions

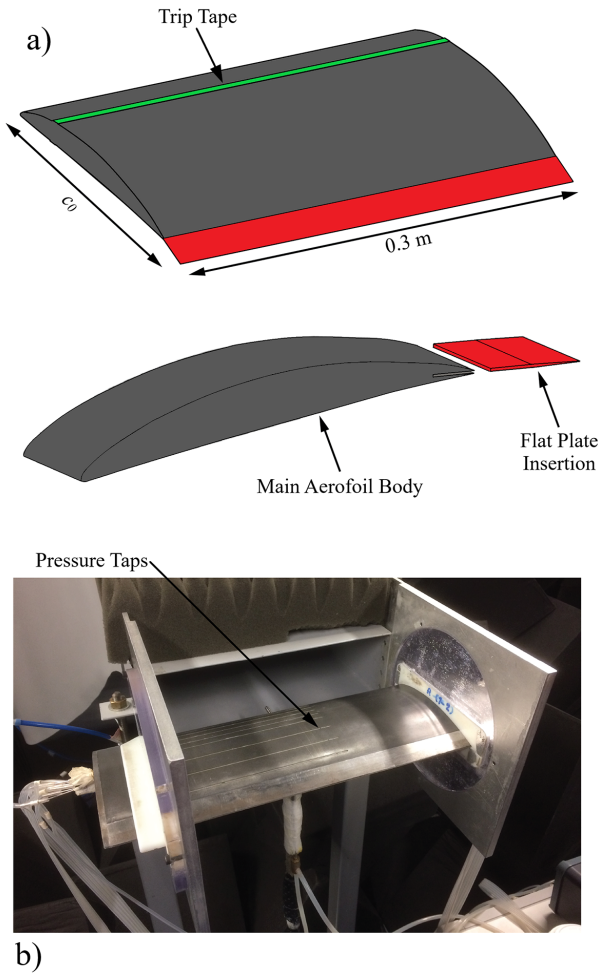

Figure 3.2: a) Three-dimensional representation with explode view of the NACA 65-(12)10 cambered aerofoil with the main aluminium alloy body and detachable TE. b) Actual experimental aerofoil mounted in the aeroacoustics facility wind tunnel.

stated in Table 3.1 and a 0.8 mm slot along the rear end. This allowed the insertion of a flat plate into the rear end of the main body. The main body had a chord-length of 0.14 m, excluding the flat-plate TE, and a span-wise length of 0.45 m.

The aerofoils with the misaligned serrated TE and the double-rooted serration had different chord-lengths to achieve the same wetted surface area for the baseline and serrated cases. The misaligned TE aerofoil had a chord-length of 0.16 m for the baseline add-on and 0.175 m for the serration cases. The double-rooted serration aerofoils had various chord-lengths ranging from 0.145 to 0.175 m. Two tripping strips, made of coarse sandpaper, were applied at $x/C = 0.2$ to both the upper and lower surfaces of the aerofoil to ensure tripping of the boundary layer into turbulent flow. These strips had a coarseness of 50, thickness of 0.95 mm and width of 10 mm. The coordinates system adopted within this thesis, in relation to the TE cases, is defined as follows: streamwise – x, vertical – y, and spanwise – z.

3.3 Design of the Add-on Flat Plate Trailing Edges

This section covers in detail the design criteria of the add-on flat plate TE cases for the misaligned (flap angle) straight, serrated and double-rooted serrations TEs. The following sub-sections illustrate and describe the geometrical parameters applied to each add-on TE device.

3.3.1 Misaligned Trailing Edge

This section describes the geometric parameters of the misaligned serrated TE flat plate case. The research studied five serration cases: Baseline, Straight-Serration (SS), Single-Straight-Flapped (SSF), Dual-Flapped-Straight (DFS), Individual-Flapped-Serration (IFS), Multi-Flapped-Serration (MFS), Split-Flapped-Serration (SFS) and Spanwise-Wavy-Serration (SWS). These acronyms are applied throughout this thesis and readers can refer to Figure 3.3 for the schematics illustrating these flat plate insertion cases. Readers should noted that straight refers to non-serrated TE. The geometric parameters of the cases are defined as the serration amplitude (H), serration wavelength (λ), flap angle (ϕ), serration span wise oscillation amplitude (H') and serration span wise oscillation wavelength (λ'). The serration amplitude and serration wavelength were kept at $H = 30$ mm and $\lambda = 3.3$ mm respectively, following a previous study by Vathylakis *et al.* [130]. The insertion of the flat plate TEs had approximately 0.8 mm thickness. The non-zero flap angle TE cases were manufactured with the desired flap angles of $\phi = \pm 5°$, $\pm 10°$ and $\pm 15°$, and $\lambda' = 15$ mm, 30 mm and 45 mm and $H' = 2.6$ mm, 5.3 mm and 8.0 mm. Note that ϕ_U and ϕ_L denote the flap-up and flap-down angles, respectively.

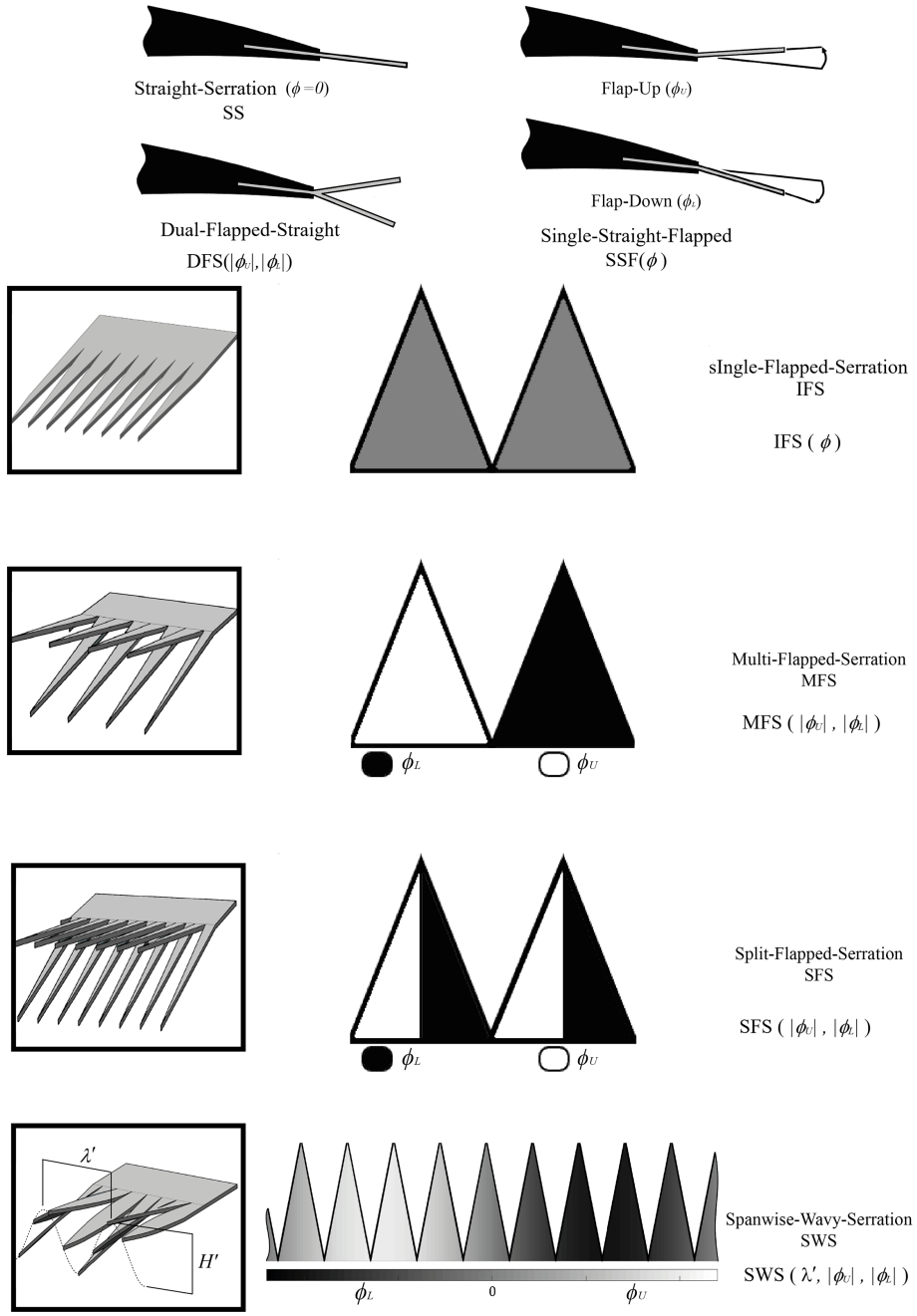

Figure 3.3: Geometric parameters of the serrated and non-serrated misalignment TE add-on for the NACA 65-(12)10: amplitude (H), wavelength (λ), flap angles (ϕ), oscillation serration amplitude (H') and oscillation serration wavelength (λ').

3.3.2 Single-Serration, DRooTES and Slit Trailing Edges

Figure 3.4 illustrates the geometric parameters of the TE flat plate cases. These are defined as the serration amplitude (H), serration wavelength (λ), root-root longitudinal displacement (h'), root-tip longitudinal displacement (h''), angle of the serration tip (Φ) and lateral-displacement serration roots (λ_0). Unless otherwise stated, the root-root longitudinal displacement (h') and

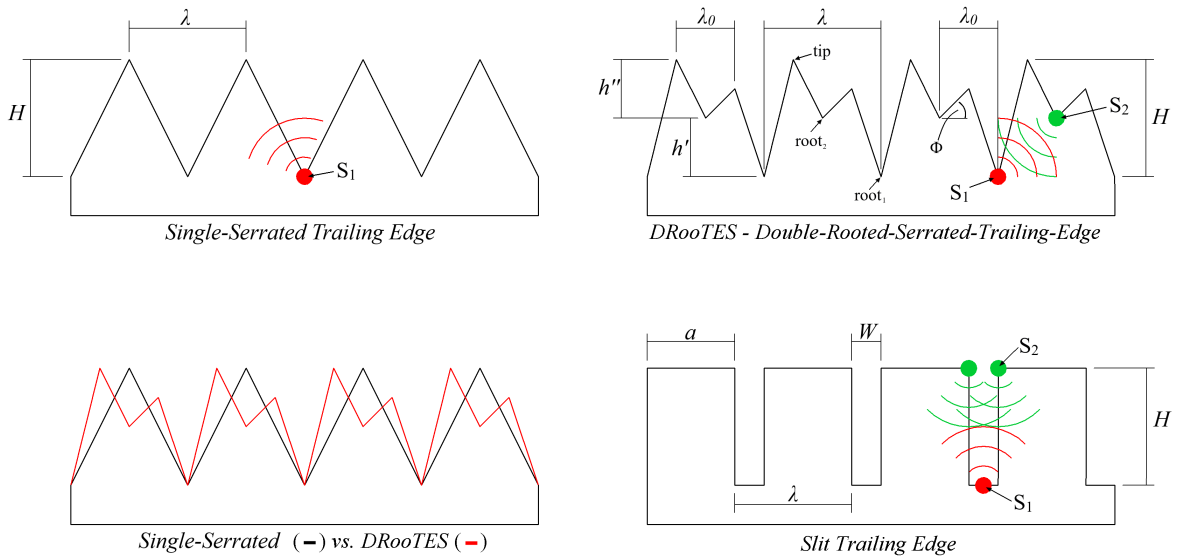

Figure 3.4: Geometric parameters of the Single-Serrated, DRooTES and Slit TE add-on for the NACA65-(12)10: amplitude (H), wavelength (λ), root-root longitudinal displacement of DRooTES (h'), root-tip longitudinal displacement of DRooTES (h''), angle of the serration tip (Φ), root-root lateral displacement of DRooTES (λ_0), width of slit tip (a) and width of slit root (W).

root-root lateral displacement (λ_0) are half the amplitude (H) and wavelength (λ) respectively. The present study investigated four cases: baseline, Single-Serration, DRooTES and Slit. The readers are advised to refer to Figure 3.4 for the schematics illustrating these cases.

A 0.8 mm slot along the rear end of the main aerofoil body allows for the insertion of a 0.8 mm thickness flat plate TE. The ranges of the serration amplitude (H) and the wavelength (λ) of the Slit, Single-Serrations and DRooTES were 5 mm $\leq H \leq$ 30 mm with intervals of 5 mm, and 3 mm $\leq \lambda \leq$ 35 mm respectively. The root-root lateral displacements and angles of the serration tips of the DRooTES were 1.5 mm $\leq \lambda_0 \leq$ 4.5 mm with an interval of 1.5 mm and $0° \leq \Phi \leq 84.3°$. The baseline TE was half the amplitude of the serrated case, to ensure similar wetted surface area for both Single-Serration and DRooTES.

3.4 Experimental Methodology

3.4.1 Far-field Noise Measurements

The aero-acoustic far-field noise measurements were performed with eight ½ inch G.R.A.S 46AE condenser microphones, shown in Figure 3.5. The polar array was mounted to the ceiling

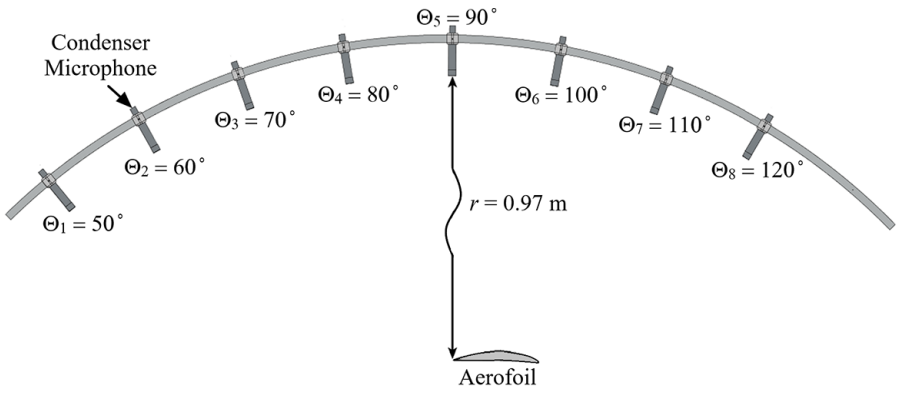

Figure 3.5: Schematic of the far-field polar array illustrated the eight $\frac{1}{2}$ inch G.R.A.S 46AE condenser microphones positioned at the TE of the aerofoil at $r = 0.97$ m, and polar angles between $50° < \Theta < 120°$ intervals of $\Theta < 10°$.

of the anechoic chamber with rails which allowed adjustment of the position of the polar array. The array was constructed of an extruded square aluminium rod in the shape of an arc with a radius of $r = 0.97$ m, which was hung by two threaded rods covered in acoustic foam. The condenser microphones were held by 3D printed microphone holders which were positioned at $50° < \Theta < 120°$ intervals of 10°, where Θ was polar angle, with the microphone with $\Theta = 90°$ positioned directly above the aerofoil TE.

The acoustic measurements were acquired using a 16-bit analogue-digital card manufactured by National Instruments. The noise was recorded at a sampling frequency of 40 kHz with a sampling time of 20 seconds, unless stated otherwise. The data were windowed and the Power Spectral Density (PSD) of 1 Hz bandwidth was computed from a 1024 point Fast Fourier Transforma (FFT) and a 50% overlap time. The far-field noise measurements for all TE cases were performed at various freestream velocities between $U_\infty = 20$ ms^{-1} and $U_\infty = 60$ ms^{-1} at $\theta = 0°$.

Microphone calibration was performed across all eight condenser microphones using G.R.A.S. pistonphone, sound calibrated 42AB, at 1 kHz and 114 dB was sampled. The sample of each microphone was converted to Volt/Pascal.

The Sound Pressure Level is denoted as SPL and given by the following equation:

$$\text{SPL} = 20 \log_{10} \left(\frac{P_{rms}}{P_0} \right) \tag{3.1}$$

where P_{rms} is the root mean square of the pressure fluctuation and $P_0 = 20$ μPa is the pressure reference.

The Sound Power Level, PWL, can be thought of as cylindrical spreading waves emanating from the TE, that is radiated per unit span for a range of angles $\Theta_1 < \Theta < \Theta_8$. The PWL is given by the following equations:

$$\mathcal{W}(f) = \frac{2\pi \int S_{pp}(f,\Theta)\Delta\Theta}{\rho c_\infty} \tag{3.2}$$

$$\text{PWL} = 10\log_{10}\left(\frac{\mathcal{W}(f)}{\mathcal{W}_0}\right) \tag{3.3}$$

where S_{pp} is the far-field pressure power spectrum density at a polar angle Θ, where $\Delta\Theta = 10^\circ \times \frac{\pi}{180}$ is the angle between adjacent microphones in radians, and $\mathcal{W}(f)$ is the sound power integrated for the radiation angles from Θ_1 to Θ_8. The polar angles of the polar array ranged from $\Theta_1 = 50^\circ$ to $\Theta_8 = 120^\circ$ with intervals of 10°, $\mathcal{W}_0 = 10^{-12}$ W, and $c_\infty = 343$ ms^{-1} is the speed of sound for air.

The OverAll sound PoWer Level (OAPWL) of the aerofoil self-noise can be defined by:

$$\text{OAPWL} = 10\log_{10}\left[\frac{\int_f \mathcal{W}(f)df}{\mathcal{W}_0}\right]. \tag{3.4}$$

3.4.2 Hot-wire Anemometry

Hotwire anemometry was conducted to obtain flow velocity measurements within the boundary layer and near-field wake. These measurements were performed with several types of miniature DANTEC hot-wire probes.

The single wire hot-wire probe were mounted to the 4 mm diameter probe support and cross (X) wire hot-wire probe were mounted to the 6 mm diameter probe support. Both the single and X wire probes had wire dimensions of 5 μm diameter and were 1.25 mm long. The hot-wire probes were used to measure fluctuations within the flow with an over-heat ratio set at 1.8. The hot-wire signals were digitised by a 12-bit A/D convector (ADCPCI) at a sampling frequency of 20 kHz for the TSI ThermoPro, and most recently, for the DANTEC StreamFlow, the hot-wire signals were digitised by a 16-bit A/D convector unit at a similar sampling frequency of 20 kHz. Both systems used the DANTEC Dynamic Multichannel Constant Temperature Anemometer (CTA) 54N80. The CTA allowed adjustment to the voltage offset and gain of the hot-wire signal to the A/D. The hot-wire readings were recorded through ThermoPro software by TSI Inc. and most recently through DANTEC StreamFlow. The hot-wire probes were mounted on a three-dimensional traverse mechanism with a resolution of 0.01 mm in all directions.

The calibration of the hot-wire probes were performed within the aero-acoustic facility on the open jet wind tunnel. The probe was positioned aligned to the flow direction at the centre of the exit of the wind tunnel nozzle. Prior to calibration, adjustment to the voltage signal was carried out through the CTA by varying the gain and offset to ensure a significant difference between lowest and largest velocities. Once a suitable difference in voltage was achieved, several velocity readings from 0 ms^{-1} to 140% of the maximum velocity were obtained using ThermoPro software.

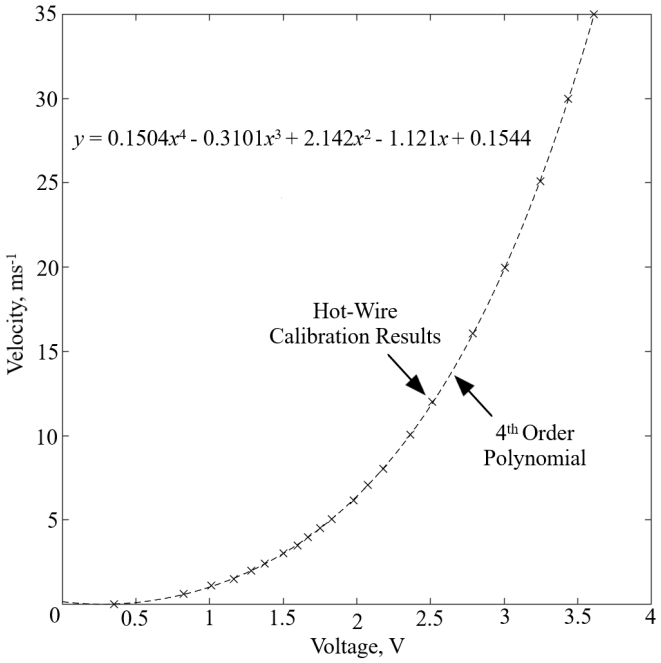

Figure 3.6: Example of a calibration curve obtained by correlated by 4^{th} order polynomial curve

A typical calibration curve, shown in Figure 3.6, is obtained by fitting a polynomial

$$U = A_1 \mathrm{V}^n + A_2 \mathrm{V}^{n-1} + \cdots + A_n \mathrm{V}^1 + A_{(n+1)} \tag{3.5}$$

where V is the voltage of the hot-wire signal, n is order of the polynomial, typically between 3^{rd} and 5^{th} order, and A_1, A_2 and A_{n+1} are the polynomial coefficients obtained for the best fit. Alternatively, the calibration curve is obtained by Kings Law defined as:

$$E^2 = B_1 + B_2 U^n \tag{3.6}$$

where B_1 and B_2 are coefficients, U is velocity and E is voltage of the hot-wire signals. At $U =$ 0 ms^{-1}, E^2 will equal A, referring to the intercept on the y-axis. The value of n is obtained by variation in order to achieve the best fit as shown in Figure 3.7.

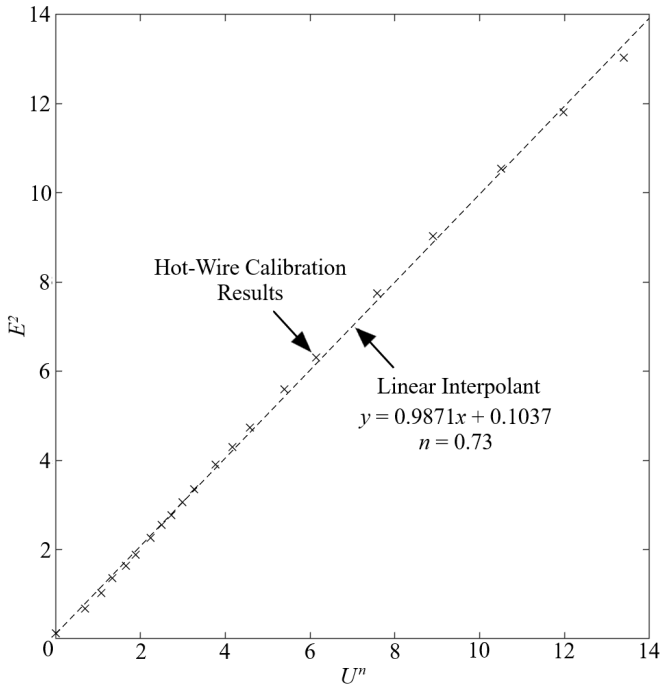

Figure 3.7: Example of a calibration curve obtained by Kings Law method.

An analytical correction method was applied to the post-analysis to account for variation in ambient temperature during experimental measurements. The analytical correction method is defined by

$$\mathrm{V}_{(w,corrected)} = \mathrm{V}_w \cdot \left(\frac{(T_w - T_a)}{(T_w - T_{(a,calibrated)}} \right)^{0.5} \tag{3.7}$$

where T_w is the temperature of the hot-wire sensor wire, T_a and $T_{a,calibration}$ are the ambient temperature during the experiments and the ambient temperature at calibration, respectively.

The following equations were used to calculate individual parameters from the hot-wire anemometry experimental measurements. The decomposition of the velocity of the hot-wire anemometry experimental measurements is defined as

$$u' = u - \overline{U}, \tag{3.8}$$

where u' is the velocity fluctuation, $\overline{U}$ is the mean velocity and u is the instantaneous velocity.

The mean velocity, $\overline{U}$, of the hot-wire signal is defined as

$$\overline{U} = \sum_{(i=1)}^{N} (u) \cdot N^{-1} \tag{3.9}$$

where N is the total number of samples and u is the instantaneous velocity obtained by the

hot-wire experimental measurements.

The root mean square (rms) of the velocity, u_{rms}, also known as the standard deviation, is defined by

$$u_{rms} = \sqrt{\overline{u'^2}} = \sqrt{\sum_{i=1}^{N}(u_i - \overline{U})^2 \cdot N^{-1}} \tag{3.10}$$

the turbulence intensity, I, is defined as

$$I = \frac{\sqrt{\overline{u'^2}}}{U_\infty}, \tag{3.11}$$

and the magnitude squared coherence, γ_i, is defined as

$$\gamma_i^2(f) = \frac{|V_{xy}(f)|^2}{V_{xx}(f)V_{yy}(f)}, i = x, z, \tag{3.12}$$

where the functions $V_{xx}(f)$ and $V_{yy}(f)$ are the auto power spectra densities, and $P_{xy}(f)$ is the cross power spectra density between stationary and non-stationary hotwire signals of x and y respectively.

The cross-correlation sequence is defined as:

$$R_{xy}(m) = E\{x_{(n+m)}y_n^*\}E\{x_n y_{n-m}^*\}, \tag{3.13}$$

where x_n and y_n are jointly stationary random processes, $-\infty < n < \infty$, $-\infty < m < \infty$, and $E\{\cdot\}$ is the expected-value operator.

The autocorrelation is defined as:

$$\rho_{xx}\Big(u(t), u(t+\Delta t)\Big) = \frac{Cov\Big(u(t), u(t+\Delta t)\Big)}{\sqrt{(Var\Big(u(t)\Big)Var\Big(u(t+\Delta t)\Big)}}, \tag{3.14}$$

$$Cov\Big(u(t), u(t+\Delta t)\Big) = \frac{\sum\Big(u(t) - \overline{u(t)}\Big)\Big(u(t+\Delta t) - \overline{u(t+\Delta t)}\Big)}{N-1}, \tag{3.15}$$

$$Var\Big(u(t)\Big) = \frac{\sum\Big(u(t) - \overline{u(t)}\Big)^2}{N-1}, \tag{3.16}$$

where Cov is the sample covariance of a time series, Var is the sample variance of a time series and N is the sample size.

3.4.3 Static Pressure Distribution

Measurements were performed in the open jet wind tunnel in the aero-acoustic facility to obtain the pressure distribution of the NACA65-(12)10 aerofoil, at an AoA of 0° and $U_\infty = 24$ ms^{-1}. A Pitot static tube was used to obtain the freestream pressure P_∞ as well as the surface static pressure at eight locations along the pressure and suction sides of the aerofoil. The differences between the static pressures were measured with the Furness FCO510 digital micro-manometer. A Furness control pressure scanner was used to change between the static pressure taps on the aerofoil. The FCO510 digital micro-manometer has a built-in data logger which can measure at a rate of 1 Hz (1 reading per second). A total of 20 reading per location were taken in order to obtain averages. The static pressure coefficient was calculated using the following equation:

$$C_p = \frac{\left(P - P_\infty\right)}{\left(\frac{1}{2}\rho_\infty U_\infty^2\right)} \rightarrow C_p = \frac{\Delta P}{\left(\frac{1}{2}\rho_\infty U_\infty^2\right)} \tag{3.17}$$

$$\rho_\infty = \frac{P_\infty}{RT} \tag{3.18}$$

where C_p is the static pressure coefficient, P is the static pressure at the pressure tap, P_∞ is the pressure at freestream, ρ is density of air and U_∞ is the freestream velocity.

Standard Deviation, s quantifying the uncertainty within the experiment results is defined by

$$s = \sqrt{\frac{1}{n-1}\sum_{i=1}^{n}(x_i - \overline{x})^2} \tag{3.19}$$

where n is the sample size, x_i are the data points and $\overline{x}$ is the mean of the sample.

3.5 Computational Detail/Framework

This section describes the computational methods used to carry out and analyse the results of the numerical simulations of the flow over the experimental NACA 65-(12)10 cambered aerofoil. The main aim of these simulations was to understand the flow characteristics at the TE. All the computational investigations were performed at a geometrical AoA of 0°, which is identical to the experimental AoA, and freestream velocities of $U_\infty = 24$ ms^{-1} and $U_\infty = 30$ ms^{-1} for 2D and 3D simulations respectively.

3.5.1 Equations and Numerical Solution Procedure

The LES of the flow around the NACA 65-(12)10 cambered aerofoil with passive TE device was performed using the LES with Dynamic Smagorinsky model on ANSYS Fluent.

The LES employs an implicit filter method, which is a universally used approach within LES. The implicit filtered system applies the filtered Navier-Stokes equations and the Sub-Grid-Scale (SGS) stresses with the desired spatial discretization. Therefore, this method can act as an effective filter with a finite support of the computational mesh and with the low-pass characteristics of the discrete differentiating operators. Thus, a direct association of the computed velocity field with the filtered velocity can be observed. For further information please refer to Lund [90].

The LES code employs a computational scheme that solves the implicitly filtered incompressible Navier-Stokes equations, consisting of continuity and momentum equations, for the resolved velocity $\overline{u_i}$, and the resolved (kinematic) pressure $\overline{p}$:

$$\frac{\partial \overline{u}_i}{\partial x_i} = 0 \tag{3.20}$$

$$\frac{\partial \overline{u}_i}{\partial t} + \frac{\partial \overline{u}_i \overline{u}_j}{\partial x_j} = -\frac{\partial \overline{p}}{\partial x_j} + \frac{\partial \left(2\nu \overline{S}_{ij}\right)}{\partial x_j} - \frac{\partial \tau_{ij}}{\partial x_j} \tag{3.21}$$

where ν is the molecular viscosity and the filtered strain-rate tensor is defined by $S_{ij} = \frac{1}{2}\left(\frac{\partial \overline{u}_i}{\partial x_j} + \frac{\partial \overline{u}_j}{\partial x_i}\right)$.

The SGS Reynold stress, or subfilter-scale model, is given by:

$$\tau_{ij} = \overline{u_i u_j} - \overline{u_i}\,\overline{u_j}. \tag{3.22}$$

Since in general $\overline{u_i u_j} \neq \overline{u_i}\,\overline{u_j}$, the SGS Reynolds stress τ_{ij} will need to be modelled.

The SGS Reynolds stress contains local averages of the small-scale field. Therefore, models for it should be based on the local velocity field or, perhaps, on the past history of the local field. The latter can be accomplished by using a model that solves partial differential equations to obtain the parameters needed to determine the SGS Reynolds stress. The SGS is the outcome from the unresolved filtered parameters by the numerical grid, and their modelling which is discussed in Sec. 3.5.2.

In the LES, the low-pass filter function consists of a combination of implicit filtering by the grid volume, defined by the FVM (Finite Volume Method), with filter width Δ, and the discretization scheme, which also tends to act as a filter. The implicit filter employed acts as a localised spatial average of the instantaneous velocity and pressure fields. The resolved scales of motion are those that are larger than the cut-off scale which is defined by the filter width Δ. The unresolved scales or SGS are the components of the instantaneous flow that are smaller than the cut-off scale. The effects of the SGS components on the resolved scales of motion needs to be modelled. In general, the filtering operation can be expressed by

$$\overline{u}_i(x) = \int G(x, x')u_i(x')dx' \tag{3.23}$$

where $G(x, x')$ is the filter function, $\overline{u_i}(x'))$ is the filtered (resolved) function and $u_i(x')$ is the unfiltered (original) function.

The LES uses body-fitted, curvilinear grids and a cell-centred FVM. The underlying numerical algorithm consisted of an implicit solution of the Poisson equation for the pressure correction, using the Semi-Implicit Method for Pressure Linked Equations (SIMPLE). The equations were solved by marching in time with a Second Order Implicit algorithm. The mass conservation was converged to a residual of 10^{-6} and velocities were updated after each Second Order Implicit.

3.5.2 Sub-Grid-Scale Modelling

The procedure and limitation of two SGS models of the eddy-viscosity type, the Smagorinsky and the Dynamic model, are presented below.

A. Smagorinsky

In 1963 Smagorinsky [121] developed the earliest and most used subgrid scale model, based on an eddy viscosity assumption to model the SGS Reynolds' stresses. All eddy viscosity models are based on the principal effects of the subgrid scale Reynold stress which increases transport and dissipation. These phenomena were similar to the effects of viscosity in laminar flows, thus it is reasonable to assume the model as:

$$\tau_{ij} - \frac{1}{3}\delta_{ij}\tau_{kk} = -2\nu\overline{S}_{ij}, \tag{3.24}$$

where the SGS eddy viscosity can be derived by dimensional arguments and is given by

$$\begin{aligned} \nu_t &= C_s^2\rho\Delta^2|\overline{S}|, \\ \overline{S} &= \sqrt{2\overline{S}_{ij}\overline{S}_{ij}} \end{aligned} \tag{3.25}$$

where $\Delta = (\Delta x\Delta y\Delta z)^{\frac{1}{3}}$ is the filter width and the Smagorinsky constant, C_s, is a model parameter to be determined. Theories have provided estimates of the parameters. These methods apply only to isotropic turbulence where they all agree that $C_s \approx 0.2$. However, C_s is not a universal constant but may be a function of Reynolds number and/or other non-dimensional parameters and may also differ for different flows.

The reader should note that the Smagorinsky model is relatively successful as an SGS eddy viscosity model, but it is not without its problems. These problems are discussed later in Sec. 3.5.2.B.

B. Dynamic Model

An alternative SGS model was proposed by Germano *et al.* [52]. This model is best known as the Dynamic SGS (DSGS) model. The DSGS model is based on Smagorinsky's model but adopts a dynamic model to alter C_s in space and time.

The procedure followed in the DSGS model is as follows: The LES is perform on a relatively fine grid, where we assume that the results are an exact representation of the velocity field. Therefore, the following procedure can be used to estimate the SGS model parameter. The velocity field $\overline{u}_i$ i is filtered, using a test filter width that is larger than the implicit filter width used in the LES performed on the fine grid. Using this larger filter width, a large-scale filtered velocity field $\overline{\overline{u_i}}$ is obtained. The difference between the two fields determines the SGS velocity field which this contains the unresolved scales of the second simulation with the larger filter width.

Similar to the Smagorinsky model, the SGS Reynolds stress tensor produced by the implicit grid filter field reads:

$$\tau_{ij} = \overline{u_i u_j} - \overline{u_i}\,\overline{u_j}. \tag{3.26}$$

Similarly, the SGS Reynolds stress tensor that is produced by the large test filter is given by:

$$\mathcal{T}_{ij} = \overline{\overline{u_i u_j}} - \overline{\overline{u_i}}\,\overline{\overline{u_j}}. \tag{3.27}$$

These two terms can be compared to test the quality of the model in a direct way. Furthermore, it can be used to calculate the value of the model parameter C_s. The two Reynolds stress terms are related by the Germano identity given by:

$$\mathcal{L}_{ij} = \mathcal{T}_{ij} - \overline{\tau_{ij}}, \tag{3.28}$$

where

$$\mathcal{L}_{ij} = \overline{\overline{u_i}\,\overline{u_j}} - \overline{\overline{u_i}}\,\overline{\overline{u_j}}, \tag{3.29}$$

is the resolved turbulent stress. The Germano identity is used to calculate dynamically the local values for C_s by applying the Smagorinsky model to both Reynold stress terms, T_{ij} and τ_{ij}. The anisotropic part of $\mathcal{L}_{ij}$ is represented as:

$$\mathcal{L}_{ij} - \frac{\delta_{ij}\mathcal{L}_{kk}}{3} = -2C_s M_{ij} \tag{3.30}$$

where

$$M_{ij} = (\overline{\Delta})^2 |\overline{\overline{S}}| \overline{\overline{S}}_{ij} - (\Delta)^2 \overline{(|\overline{S}| \overline{S}_{ij})}. \tag{3.31}$$

Subsequently, C_s is computed as

$$C_s^2 = -\frac{1}{2} \frac{\mathcal{L}_{kl} \overline{S}_{kl}}{M_{ij} \overline{S}_{ij}}. \tag{3.32}$$

A modification by Lilley [87] proposed to employ a least squares procedure for the calculation of the model parameter

$$C_s^2 = -\frac{1}{2} \frac{\mathcal{L}_{kl} M_{kl}}{M_{ij} M_{ij}}. \tag{3.33}$$

This procedure is carried out at every spatial point and time step. The value of C_s is then applied to the SGS model of the LES equation. This produces a form of self-consistent SGS model. Readers should be aware that two assumptions are made with this model.

1. The same value parameters are applied to both the actual LES grid and to the LES carried out using the test filter.

2. The parameter C_s is independent of the location.

For further information please refer to Germano *et al.* [52].

The DSGS model provides the following benefits in comparison to the Smagorinsky model, according to Ferziger and Perić [45]:

1. The Smagorinsky model parameter remains constant. However, it requires smaller values in the shear flow than the isotropic turbulence. In comparison, the dynamic model automatically changes the model parameter within these regions.

2. The dynamic model reduces the parameter at the near wall region. Whereas, the Smagorinsky model parameter necessitates to be even smaller for the near wall regions, to compensate for eddy viscosity.

3. Defining the length scale for anisotropic grids/filters remains challenging, especially when analysing the dynamic model. In fact, the parameter tends to change to offset any errors in the length scale.

The DSGS model offers significant improvements to Smagorinsky model, however it is not without its difficulties. The dynamic model generates an eddy viscosity that is can vary wildly both in space and time. Eddy viscosity can also become negative, which is a result of so-called backscatter (transport of kinetic energy from small to large scales, in contrast to the usual net energy transport from large to small scales.). However, a negative viscosity during an extended time can cause numerical instability. To counter this, negative eddy viscosities are clipped so that $\mu_t + \mu \leq 0$, and/or averaging of eddy viscosity in space (in directions where the flow is homogeneous) or time is employed.

The LES used the Dynamic Smagorinsky model with the modification of Lilley [87]. In the absence of homogeneous flow directions, a running average in time was employed to obtain a stable eddy viscosity.

3.5.3 Computational Domain, Grid and Boundary Conditions

A. Computational Domain, Grid and Boundary Conditions

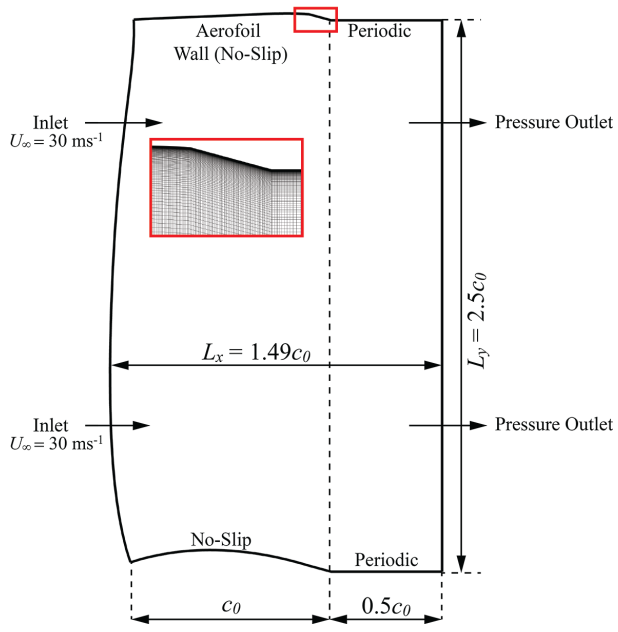

Figure 3.8: Computational domain and grid for LES at Re = 308,670.

Figure 3.8 presents the spanwise cross-section of an open jet configuration for the baseline and slit TE cases. The inlet and outlet were located on the left- and right-hand sides of the domain

respectively, separated by a distance of $L_x = 1.49c_0$, where c_0 was the aerofoil chord-length of c_0 =0.155 m. The inlet plane was positioned at $0.1c_0$, where the inlet boundary condition imposed a uniform flow at Re = 308,670 based on the aerofoil chord-length and the flow speed. The outlet was defined as pressure outlet with zero pressure gradient, and the length of the outflow area was $0.5c_0$. As illustrated in Figure 3.8, the pressure and suction surfaces of the aerofoil, where the surfaces were separated by a distance of $L_y = 2.48c_0$, were located on the upper and lower surfaces of the domain. The periodic boundaries were located between the TE and the outlet, along the upper and lower boundaries of the computational domain. The span-wise extent of the domain was $L_z = 0.019c_0$ and the periodic boundary conditions were employed at these boundaries. Readers should note that the computational domain described above was adopted to all the simulation cases for the LES simulations. The coordinate system used in relation to the domain was defined as follows: streamwise (x), vertical (y) and spanwise (z).

The geometric configuration of the numerical TE cases based on the experimental setup in Sec. 3.3.2. The numerical study investigated two cases: baseline and slit TEs. Readers are advised to refer to Figure 3.4 for the schematics definition illustrating these cases. The slit amplitude and wavelength of the slit were $H = 15$ mm and $\lambda = 3$ mm with a tip and root width being $a = 2.7$ mm and $W = 0.3$ mm respectively. The baseline TE was kept at the same amplitude as the slit to ensure similar flow conditions. In addition, the transition point similar to the experimental setup was defined at 20% of the chord length to ensure transition from laminar to turbulent flow. The transition point was modelled as a vortex generator at 30° to the flow direction with a height of $y^+ = 16$ illustrated in Figure 3.9 .

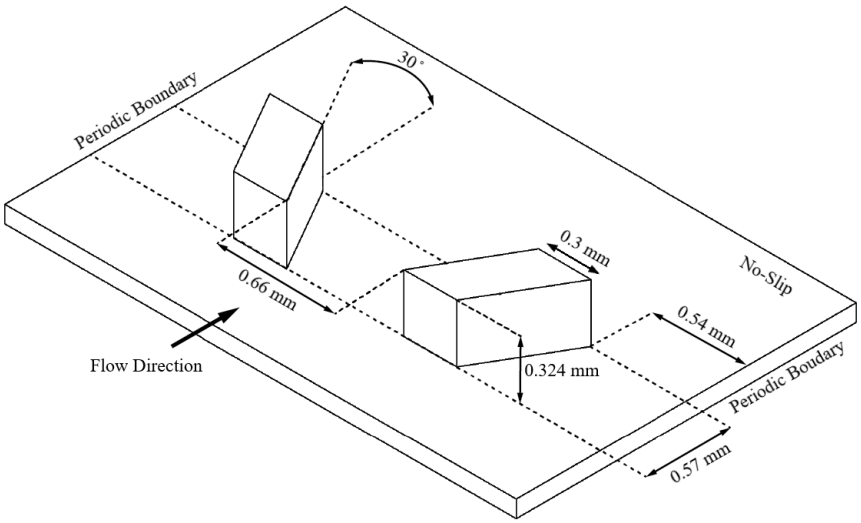

Figure 3.9: Topology of the vortex generators on the surface of the aerofoil

The grid generation employed near-orthogonal grid close to the blade surfaces, where at the wall-normal grid size $\Delta y^+ = 2$ and at streamwise grid size $\Delta x^+ = 26$. In the spanwise direction a grid size $\Delta z^+ = 8 - 17$ was employed. The terms x^+,$y^+$and z^+ were defined as wall coordinates. The grid consisted of $577 \times 282 \times 39$ nodes in the streamwise, pitchwise and spanwise directions respectively.

Given the near-wall resolution of the mesh given above, with a y^+ value small enough to accurately resolve the viscous sublayer combined with relatively small x^+ and z^+ values, the quality of mesh was deemed to provide an adequate resolution of the boundary layers around the aerofoil as well as a good resolution of the larger scales in the free-stream. A direct comparison to experimental results showed (even though the inflow conditions were not exactly matching) very similar boundary layer profiles. It is well-known that a mesh-refinement study for an LES is not useful as such a simulation is per definition grid-dependent. The only important criterion is that the numerical solution can adequately reproduce experimental results. Once this is achieved the LES results can be used to study flow patterns and flow dynamics at all locations in the computational domain. These results can then be used to further explain experimental observations. The ensure a time-accurate solution, a Courant number of 0.92 was employed to ensure that the timestep $\Delta t = 8 \times 10^{-6}$ was sufficiently small.

Chapter 4

Exploiting the Misalignment of the Flat Plate Trailing Edge Devices

4.1 Introduction

The reduction of TE noise for various types of sawtooth serrations has been successfully demonstrated in wind tunnel experiments. It was reported that broadband noise reduction values achieved up to 8 dB within wind tunnel experiments. Also, reduction of TE noise has been witnessed through the addition of serrations on a real size wind turbine blade shown by Oerlemans *et al.* [100]. They observed noise reduction on the wind turbine blade up to 3 dB. However, simultaneously also increases in high frequency noise were observed when a serrated TE was applied. Oerlemans *et al.* [100] and Dassen *et al.* [36] proposed that misalignment (flap angle) of the serrated TEs was the cause for the increase of high frequency noise, as the serrations were misaligned with the flow in the wake of the aerofoil. An alternative theory was suggested by Gruber [57] stating that the large increase in high frequency noise was a result of crossflow between the serrations.

Vathylakis *et al.* [130] and Arce León *et al.* [1] artificially bent their sawtooth serrations in order to facilitate a controlled flap angle. Arce León *et al.* [1] performed flow and acoustic measurements of the characteristics of a NACA 0018 aerofoil with sawtooth TEs. They reported that negative flap angles (flap down) could degrade the level of broadband noise reduction in comparison to the SSs, or even produce higher noise levels than the baseline, straight TE case. Such a noise increase is usually accompanied by the presence of high turbulence intensity in the wake. They also utilised stereoscopic PIV to study the of effects serration flap angles and aerofoil incidence angle and to investigate the influence of the secondary flow established on the suction

and pressure sides of the serrated TEs. The results showed the additional formation of streamwise vortex pairs in the crossflow plane. They observed a strong relationship between the vortices and serrations with flap angles rather than with the aerofoil incidence angle. At zero aerofoil incidence and serration flap angles the mean flow behaviour near the serrations adhered closely to Howe's assumptions of the reduced acoustic scattering efficiency at the presence of oblique edges. Observation of streamlines at the TE tended to align with the edge of the serrations on the suction side. In contrast, the opposite occurred on the pressure side with the streamlines tending to become normal at the edge of the serrations.

The most common geometrical variables describing a serration are traditionally the serration amplitude and wavelength. Whilst keeping these variables constant, Vathylakis *et al.* [130] investigated the sensitivity of the aerofoil broadband noise reduction to a third geometrical variable – the serration flap angle - which could be regarded as a form of serration misalignment. Several flap angles were investigated: $\pm 5°, \pm 10°, \pm 15°$, where the flap angle at $0°$ was treated as the reference. They found that certain serration flap angles further improved the level of broadband noise reduction. In particular, flap-up positions were generally found to achieve higher levels of broadband noise reduction than flap-down positions. The optimum flap-up angle was at $+5°$, where it outperformed the non-flap angle case from mid-to-high frequencies. However, the $-5°$ flap-down angle represented the worst performer amongst all the non-zero flap angle cases because of the consistent noise increase throughout the whole range of frequencies. Nevertheless, the largest flap-down angle at $-15°$ produced almost an identical level of broadband noise reduction as the non-flap angle case.

The literature has shown significant benefits of TE serrations from the aeroacoustics perspective. However, most studies also observed a consistent increase in the high frequency noise levels [18, 36, 58, 76, 100, 134]. Several studies have suggested that the possible reasons for this increase in high frequency noise are related to the crossflow within the trough of the serrations [57], or the misalignment of the serrations [36, 100]. However, the results from Vathylakis *et al.* [130] suggest that the concept of misalignment of the serrations at the TE could be carefully exploited to further improve the level of the broadband noise reduction. This chapter explores the effects of the periodic and out-of-phase serration misalignment. In particular, three new combinations of the serration geometries are investigated:

- Multi-Flapped-Serration (MFS)
- Split-Flapped-Serration (SFS)
- Spanwise-Wavy-Serration (SWS).

4.2 Experimental Setup

The following sub-sections describe the experimental setup and analysis techniques used within this research, which are similar to those of the previous study by Vathylakis *et al.* [130].

4.2.1 Design of the NACA65-(12)10 cambered aerofoil with Flapped Serrated Trailing Edges

The experiment was conducted on a NACA65-(12)10 cambered aerofoil at Brunel University London aero-acoustic facility, please refer to Sec. 3.2. The NACA65-(12)10 aerofoil had a chord length of 0.16 m and 0.175 m for baseline and serration cases respectively and a span-wise length of 0.45 m. To achieve the same wetted surface area for the baseline and serrated cases, different chord lengths were used. The detachable TEs were 3D-printed with a printing resolution of 100 microns (0.01mm) for all the cases.

In Sec. 3.3.1 Figure 3.3 displays the geometric parameters of the misaligned TE flat plate cases. These are defined as the serration amplitude (H), serration wavelength (λ), flap angle (ϕ), serration spanwise oscillation amplitude (H') and serration spanwise oscillation wavelength (λ'). In a previous study by Vathylakis *et al.* [130], the serration amplitude and serration wavelength were kept at $H = 30$ mm and $\lambda = 3.3$ mm respectively. The un-serrated, baseline TE was half the serration amplitude (i.e. $H = 15$ mm), which would produce the same wetted surface area for both serrated and baseline cases. The current research studies five serration cases: Baseline, Straight-Serration (SS), sIngle-Flapped-Serration (IFS), Multi-Flapped-Serration (MFS), Split-Flapped-Serration (SFS) and Spanwise-Wavy-Serration (SWS). These acronyms are used throughout this study, and the readers can refer to Figure 3.3 for the schematics illustrating these serration cases. The coordinate system adopted in relation to these serration cases is defined as follows: streamwise (x), vertical (y) and spanwise (z).

In this work the main aerofoil body had a 0.8 mm slot along the rear end, which allowed the insertion of the flat plate TEs of about 0.8 mm thickness. The non-zero flap angle TE cases were manufactured with the desired flap angle of $\phi = \pm 5°, \pm 10°$ and $\pm 15°$, and $\lambda' = 15$ mm, 30 mm and 45 mm and $H' = 2.6$ mm, 5.3 mm and 8.0 mm. Note that ϕ_U and ϕ_L denote the flap-up and flap-down angles respectively. Coarse sandpaper strips were applied to both the upper and lower surfaces at $x/C = 0.2$ of the aerofoil to trip the boundary layer into a turbulent boundary layer. Note that C is the aerofoil chord. The coarse sandpaper had a thickness of 0.95 mm and width of 10 mm.

4.2.2 Wind Tunnel Facilities and Instrumentation

This section describes the wind tunnel facilities and instrumentation set up for the far-field acoustic and flow measurements, which were both performed in the aeroacoustic facility at Brunel University London. Unless otherwise stated, all the far-field noise measurements, as well as the flow measurements, were performed at $U_\infty = 24$ ms^{-1}. The open jet wind tunnel can produce very low turbulence intensity of $I = 0.1\%$ – 0.2% between $U_\infty = 10$ ms^{-1} and $U_\infty = 30$ ms^{-1}. The background noise (without the presence of the aerofoil, but with the side-plate) is largely contributed by the low subsonic jet noise, which is very low in comparison to the aerofoil self-noise level produced at the identical flow speed. All the far-field noise and flow measurements were performed at a geometric AoA $\theta = 0°$.

4.2.3 Far-Field Noise Measurements

The far-field noise measurements were performed with eight 1/2 -inch condenser microphones. The 1/2-inch condenser microphone positioned at a polar angle of $\Theta = 90°$ was located at the mid-span of the aerofoil and at $r = 0.97$ m above the TE. The data were acquired using a 16-bit analogue-digital card manufactured by National Instrument. The sampling frequency was 40 kHz with a sampling time of 20 seconds. The data were windowed and the PSD of 1 Hz bandwidth was computed from a 1024-point FFT and a 50% overlap time. As stated in Section 2.2, noise measurements were performed for all the TE cases at $U_\infty = 24$ ms^{-1}.

4.2.4 Near-Field Flow Measurements

The near-field wake measurements were performed with a DANTEC miniature single hot wire straight probe (55P11). The probe was mounted parallel to the flow and was positioned at 1 mm from the serration peaks. The hot wire measured the fluctuation and mean velocity of the aerofoil wake with an over-heat ratio set at 1.8. The hot wire signals were digitised by a 12-bit A/D convector (ADCPCI) at a sampling frequency of 20 kHz, through a DANTEC Dynamic Multichannel CTA 54N80. The hot wire readings were recorded through ThermoPro software by TSI Inc. The hot wire probe was mounted to a two-dimensional traverse mechanism with a resolution of 0.01 mm in both directions. For all the serrated TE cases, the flow measurements produced a series of two-dimensional wake profiles in the y–z plane at $x = 1$ mm downstream of the peak of the serration. The streamwise flow measurements produced a series of two-dimensional wake profiles in the x-y plane at exponentially increasing intervals with size up to 50 mm. For the baseline case, the wake measurements were at $x = 1$ mm downstream of the TE.

For the baseline, SS, SFS and MFS cases, the resolution in the y-direction was typically 0.25 mm in order to account for the large velocity gradient in the viscous sublayer region, but the resolution was gradually relaxed when moving towards the freestream region. The resolution in the z-direction was consistent at 0.33 mm for a total distance of 9.9 mm. This meant that the spanwise measurements covered four serration peaks and three serration troughs, and the SWS case covered one spanwise wavelength $\lambda' = 15$ mm.

4.3 Results and Discussion

The experimental noise results of the TE serrations (SS, IFS, MFS, SFS and SWS), as well as of the baseline at $U_\infty = 24$ ms^{-1} are presented in Section 3.1. Section 3.2 discusses the flow in the near-wake produced by the above TE devices.

4.3.1 Noise Measurements

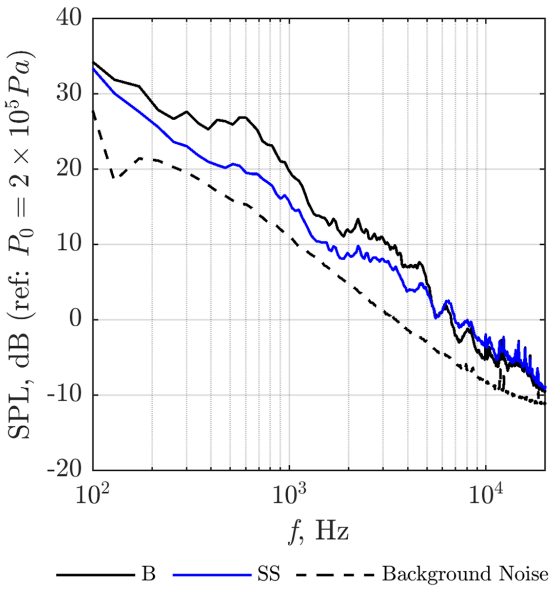

Figure 4.1: Comparison of the SPL, dB, of the baseline, SS and background noise at $H = 30$ mm, $\lambda = 3.3$mm and $U_\infty = 24$ ms^{-1}.

A comparison of the aerofoil self-noise against the background noise of the open jet wind tunnel is presented in Figure 4.1. Similar to the study by Vathylakis *et al.* [130], who used the same facility, the background noise from the freestream flow (i.e. without the aerofoil) was shown to be significantly lower than the quiet self-noise produced by the aerofoil with SS. It is worth mentioning that the SPL spectrum produced by the SS TE case was lower than that produced by the baseline case over a significant portion of the low-to-mid frequency region. However,

noise increase occurred for $f > 6$ kHz. The same characteristics of the self-noise radiation by the SS-type TE shown here were also reported in the previous studies by Oerlemans *et al.* [100], Gruber *et al.* [57], Vathylakis *et al.* [130], Acre León *et al.* [1], and Dassen *et al.* [36].

4.3.2 Comparison of the SSF at various flap angle (ϕ)

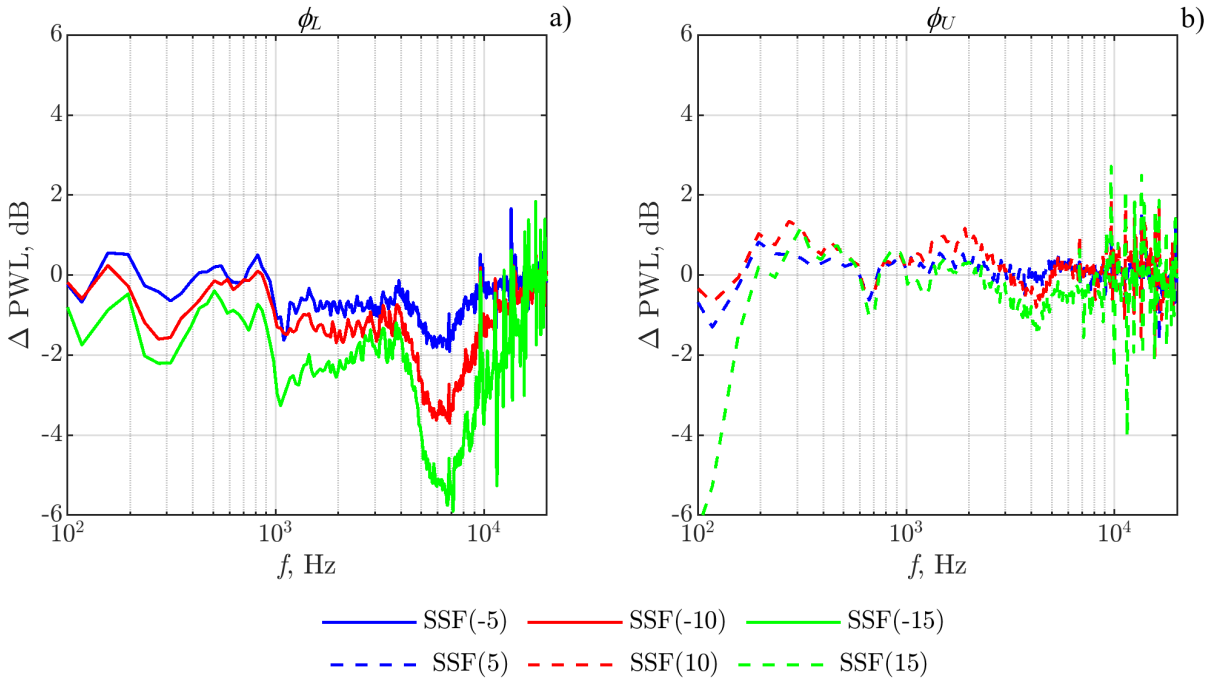

Figure 4.2: Comparison of ΔPWL, dB, between baseline and non-serrated flapped, SFS(ϕ), TEs at $-15° \leq \phi \leq 15°$, $H = 30$ mm and $U_\infty = 24$ ms^{-1}.

Figure 4.2 shows the sensitivity of the broadband radiation to the single straight (non-serrated) Flapped (SSF) TEs at various flap angles $-15° < \phi < 15°$. ΔPWL is defined as the difference in the sound power level, as a function of frequency, between the baseline and SSF TEs: $\Delta\text{PWL}(f) = \text{PWL}_B(f) - \text{PWL}_{SSF,SS,\text{ or }IFS}(f)$. Readers should note that a positive value of ΔPWL represents noise reduction and the opposite is true for noise increase. This definition also applies to the other serrated TE cases within this chapter. For the $\text{PWL}_{SSForIFS}$ case, the ϕ_U and ϕ_L denote the flap-up and flap-down angles respectively, readers should refer to the schematic illustrated in Figure 3.3.

The results in Figure 4.2 demonstrate that ϕ_U cases exhibited a similar acoustic performance across all frequencies, with the exception for $f < 200$ Hz where the SSF(15) resulted in an increase of 6 dB. This suggested that the flap angle dominated the noise characteristics for $f < 200$ Hz. Furthermore, the positive flap angles did not affect the high frequencies, $f > 7$ kHz,

which suggests that the flap angle effect was not dominant within this frequency range. The best case was at $\phi_U = 10°$ with a reduction across the frequency spectrum, whereas the worst case was at $\phi_U = 15°$. In contrast, the ϕ_L showed a significant degradation in the acoustic performance across all frequencies in comparison to the baseline. In particular, the effects of negative flap angle on the high frequencies region, $f > 4$ kHz, was significant. The best case amongst all the flap down cases was $|\phi_L| = 5°$ with (across the frequency range) noise reductions up to 0.5 dB and noise increases up to 2 dB. The worst case was $|\phi_L| = 15°$ with no noise reductions but noise increases up to 6 dB. Therefore, the flap angles at the TE had a significant effect on the acoustic performance of the aerofoil self-noise.

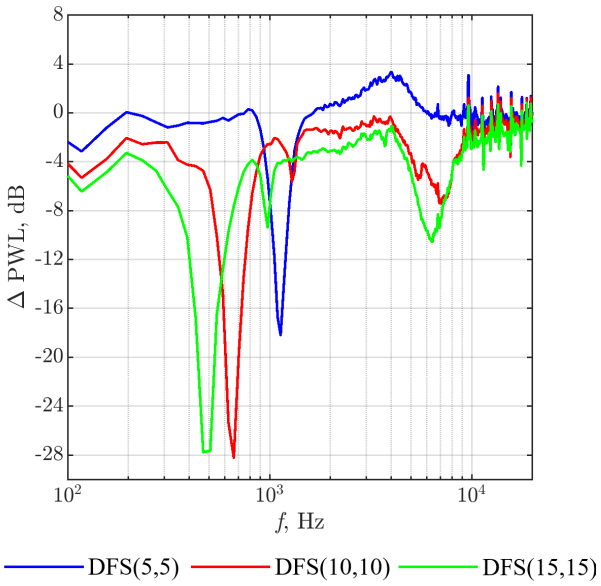

Figure 4.3: Comparison of the ΔPWL, dB, between baseline and Dual-Flapped-Straight, DFS($|\phi_U|, |\phi_L|$), TEs at various flap angles, $\phi_U = \phi_L$, $H = 30$ mm and $U_\infty = 24$ ms^{-1}.

Figure 4.3 presents the sensitivity of the broadband noise reduction of the baseline TE with DFS flap angle, $\phi_U = \phi_L$. The results showed that the effect of the DFS acted as a form of blunt TE which resulted in vortex shedding from the blunt TE; this was confirmed by the tonal noise increase up to 27.5 dB. Furthermore, periodic tonal noise was observed for each case shown in Figure 4.3. For the DFS flap angle of $\phi_U = \phi_L = 5°$, noise reductions between 2 kHz and 7 kHz of up to 3 dB were found, where other cases exhibited no noise reduction. The overall effects of the DFS produced a further degradation of the acoustic performance in comparison to the SSF; however, the flap up configuration offered additional benefits to the high frequencies, 2 kHz $< f <$ 7 kHz at the lowest flap angles, $\phi_U = \phi_L = 5°$.

4.3.3 Noise Spectra Serration Amplitude (H)

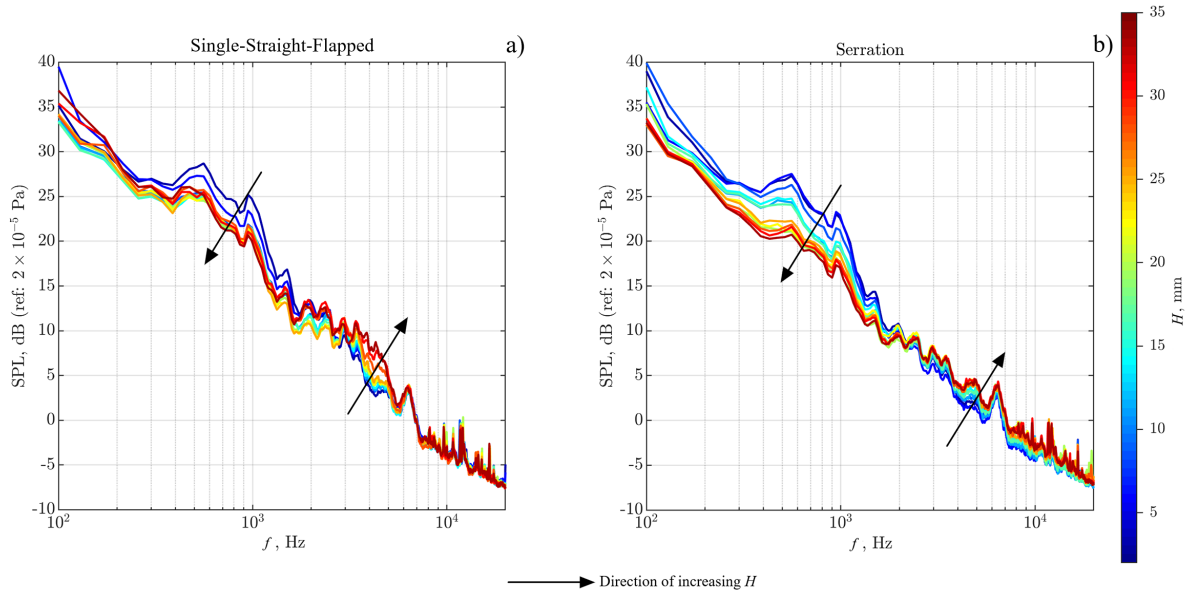

Figure 4.4: Comparison of the noise spectra, SPL dB, of serrated and non-serrated TE at different length of flat plates, H, for: (a) SSF TE, and (b) SS TE with serration wavelength of $\lambda = 3.3$ mm. The SSF and SS noise denoted spectra for 2 mm $\leq H \leq$ 35 mm. The flow conditions were $U_\infty = 24$ ms^{-1} and $\theta = 0°$. (From Vathylakis *et al.* [130] Figure 4)

Figure 4.4 presents the sensitivity of the sound power spectra of the baseline and the SS TE at various amplitudes, 2 mm $< H <$ 35 mm. Readers should note that Vathylakis *et al.* [130] used the same experimental equipment and facility as the one used in the present study. Figure 4.4a) shows that for the baseline an increase in length of the flat plate insert has significant benefits at reducing aerofoil self-noise for 250 Hz $< f <$ 2.5 kHz. Furthermore, the level of broadband noise reduction for this frequency range was strongly linked to the increase in H. However, for the frequency region of 2.5 kHz $< f <$ 5 kHz, a degradation of noise was observed as H was increased. The SSs observed similar trends to the baseline, where the best results were obtained for the largest amplitude of $H = 35$ mm, while the opposite was true for the smallest amplitude of $H = 2$ mm. Broadband noise reduction was obtained for 100 Hz $< f <$ 2.5 kHz and high frequency noise increases where obtained for $f >$ 2.5 kHz. Interestingly, the noise performance of both the baseline and SS TEs was found to eventually plateau when further increasing the length of the flat plate, H. This study found that the SS TE at $H = 30$ mm was the best configuration due to its superior noise performance in the low-to-mid frequency range which is important for real life applications.

4.3.4 Noise spectra of the IFS

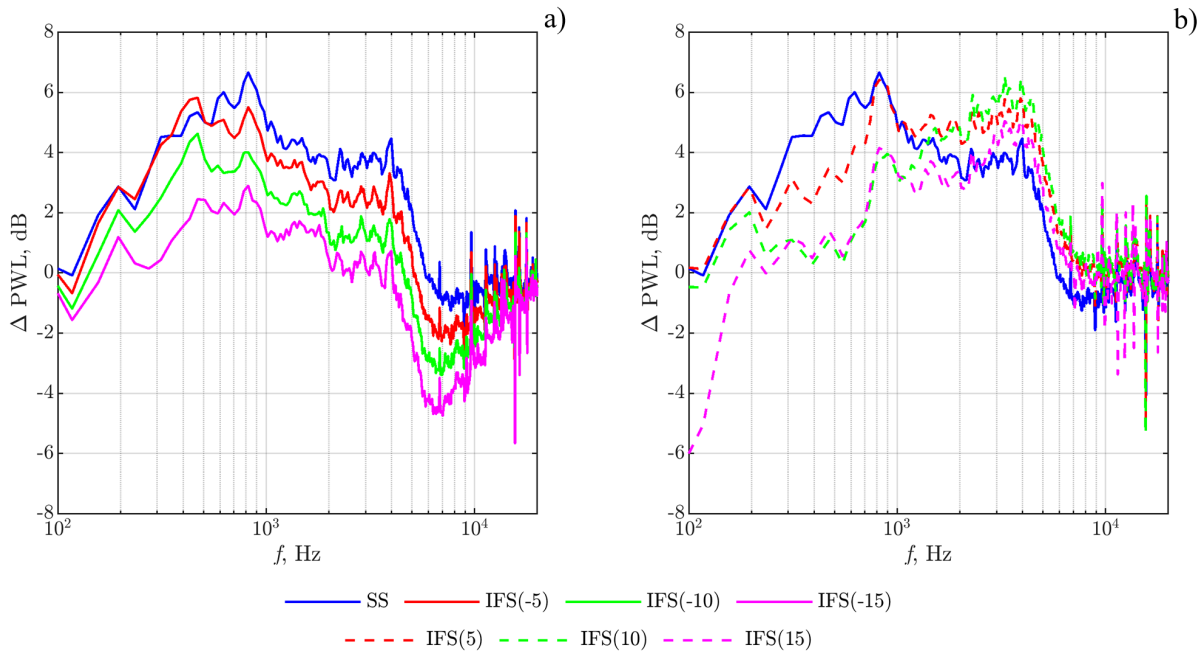

Figure 4.5: Comparison of the ΔPWL, dB, for the Baseline, SS and IFS(ϕ) (different ϕ_U and ϕ_L) TEs where (a) at $\phi \leq 15°$ and (b) $-15° \leq \phi$. $H = 30$ mm, $\lambda = 3.3$ mm and $U_\infty = 24$ ms^{-1}.

Figure 4.5 shows the sensitivities of the broadband noise radiation to the SS and IFS-type TEs. The results follow largely the same trends as observed previously by Vathylakis *et al.* [130]. Figure 4.5a clearly demonstrates that the levels of broadband noise reduction (ΔPWL) achieved by all the IFS flap-down TEs were inferior to those achieved by the conventional SS TEs. The larger the flap-down angle of the serration, the lower the ΔPWL. Moreover, larger flap-down angle also caused higher levels of noise increases in the high frequency region, $f > 4$ kHz. On the other hand, the IFS flap-up configurations produced a more positive outlook in comparison to the SS TEs (Figure 4.5b. The ΔPWL achieved by the IFS flap-up configurations was generally lower than that achieved by the SS TEs for $f < 1.5$ kHz. However, above this frequency band, all the IFS flap-down TEs outperformed the SS TEs. For example, the ΔPWL ($f = 4.5$ kHz) achieved by the IFS $\phi_U = 10°$ and the SS TEs were 6.2 dB and 4.2 dB respectively. In addition, all the IFS for flap-up configurations produced lower levels of negative ΔPWL (i.e. noise increases over the baseline TE) than those produced by the SS TEs. Overall, the most promising option for the IFS flap-up configuration was the $\phi_U = 5°$ case. The consistently high levels of ΔPWL at $f > 1.5$ kHz achieved by this type of configuration warranted further efforts to improve the noise performance at $f < 1.5$ kHz by exploiting different concepts of serration misalignment.

4.3.5 Comparison of the noise spectra of the IFS to SSF

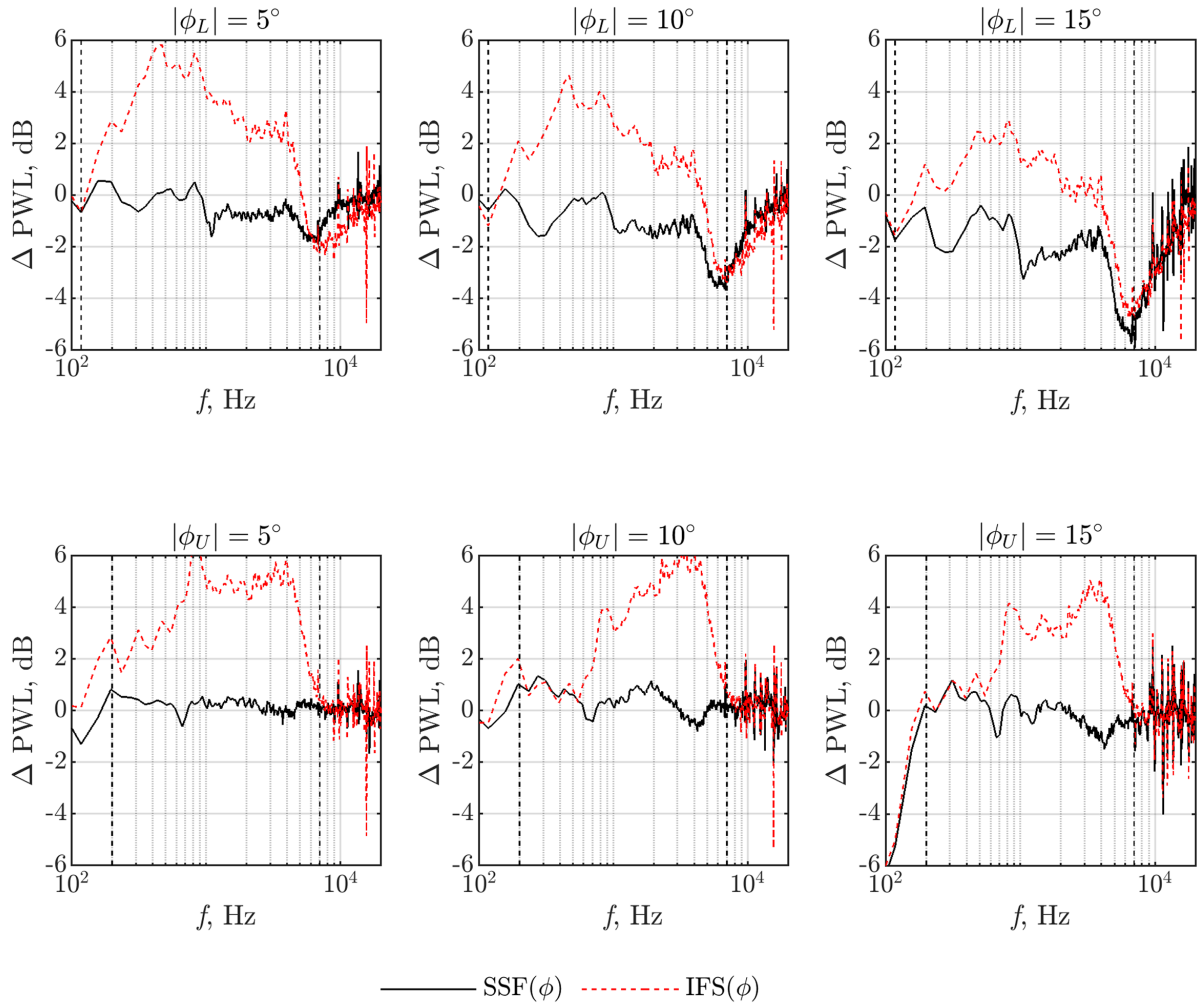

Figure 4.6: Comparison of the ΔPWL, dB, between serrated and non-serrated flapped TE, IFS(ϕ) and SSF(ϕ) respectively, at different flap angles, $-15° < \phi < 15°$, where black and red lines represent the SSF and IFS, respectively, identifying the regional effects of misalignment.

Figure 4.6 shows a comparison of the broadband noise reduction of the IFS compared to the SSF. The results demonstrated similar noise characteristics at the same flap angles for the serrated and non-serrated cases. At low frequencies, the positive flap angles $\phi_U = 10°$ and $\phi_U = 15°$ exhibited a collapse of the sound pressure level results for $f < 500$ Hz; at high frequencies similar results were seen for $f > 7$ kHz for both positive and negative flap angles. This was due to the dominant effect of the flap angle. For negative flap angles, noise reduction was noted for $f > 117.2$ Hz, which suggests that the flap angle effect was not as dominant within this frequency range as observed for the positive flap angle. Readers should note that in these frequency ranges, where the flap effect was dominant, the addition of the serrations had little to no influence on the noise performance, with the exception of frequencies in the range between

200 Hz $< f <$ 7 kHz. Therefore, the flow study in Sec. 4.4 only evaluates results for the 200 Hz $< f <$ 7 kHz frequency range for IFS cases in order to understand the effects of serrations on misalignment.

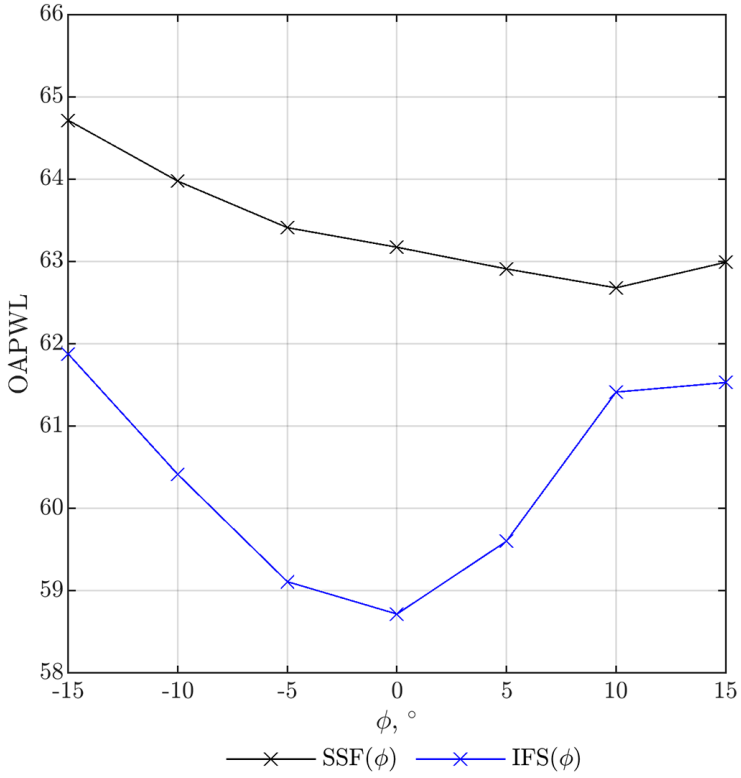

Figure 4.7: Comparison of the OAPWL integrated between 200 Hz $< f <$ 7 kHz of the SSF(ϕ) and IFS(ϕ) at various flap angles (ϕ) at $U_\infty = 24$ ms^{-1}.

Figure 4.7 presents a comparison of the OAPWL, for 200 Hz $< f <$ 7 kHz, for SSF and IFS TEs with various flap angles. The results clearly showed that the addition of serrations to the TEs significantly enhanced the overall acoustic performance for all flap angles. However, the SSF TEs confirmed that flap angle influenced the OAPWL of the aerofoil self-noise. The change in the OAPWL could be explained by the influence of the flap angles at the TE on the flow and blade loading across the main aerofoil body, in particular this was true for positive flap angles. Both the SSF and IFS had an optimal flap angle case which occurred at $\phi = 0°$ and $\phi = 10°$ for IFS and SSF, respectively. The SSF exhibited a linear OAPWL between flap angles of $-10° < \phi < -5°$. The worst case was found at the largest $\phi = -15°$ for both the SSF and IFS cases. Positive and negative flap angles on the SSF and IFS had a degrading effect on the OAPWL of the aerofoil self-noise. Furthermore, it has been confirmed by Vathylakis *et al.* [130] that flap angles have a significant effect on TE noise.

4.3.6 Noise spectra of the MFS

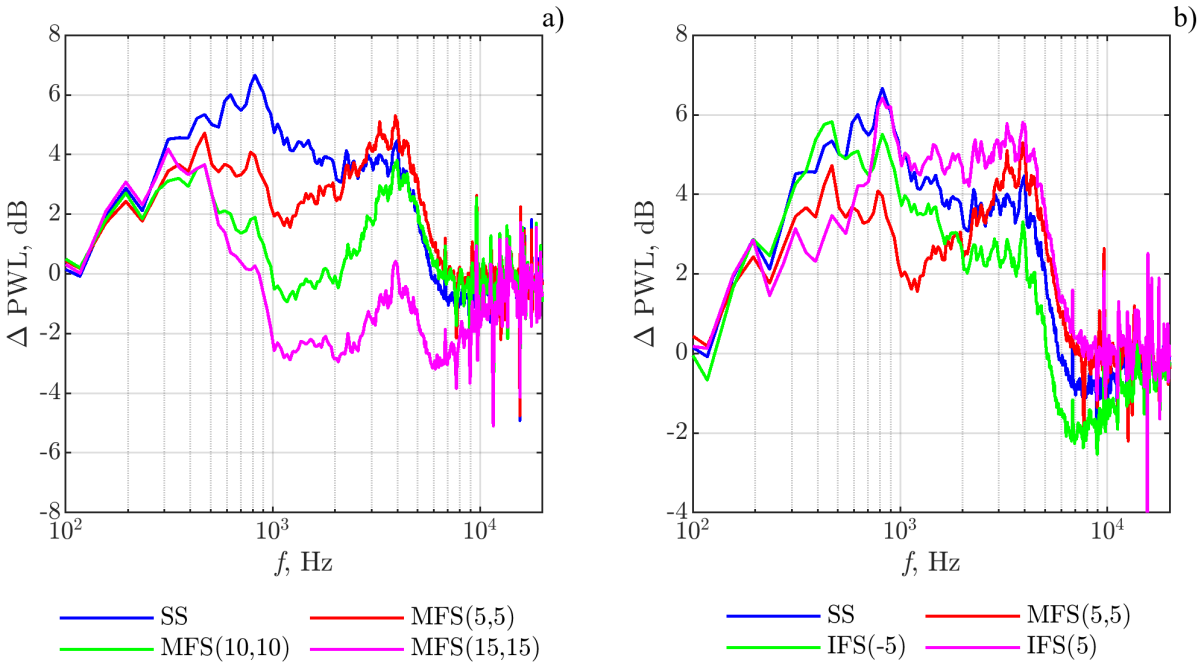

Figure 4.8: Comparison of the (a) ΔPWL, dB, between SS and MFS($|\phi_U|, |\phi_L|$) TEs with $|\phi_U| = |\phi_L| = 5°, 10°$&$15°$ and (b) ΔPWL, dB, between the SS, IFS(ϕ) at $\phi = \pm 5°$ and MFS($|\phi_U|, |\phi_L|$) TEs at $|\phi_U|, |\phi_L| = 5°$, where $H = 30$ mm, $\lambda = 3.3$ mm and $U_\infty = 24$ ms^{-1}.

Figure 4.8 shows the sensitivities of the broadband noise radiation to the SS and MFS-type TEs. For the MFS presented in Figure 4.8a), $|\phi_U|$ is equal to $|\phi_L|$ and the ΔPWL spectra show that the best performer amongst the MFS TEs was for $|\phi_U| = |\phi_U| = 5°$. The overall acoustic performance reduced with increases in both $|\phi_U|$ and $|\phi_L|$. For $f < 200$ Hz and $f > 7$ kHz, the broadband noise radiation levels of the MFS matched the trends seen in Sec. 4.3.5 and it can be concluded that for these frequencies the flap angle effect was dominant. When comparing the IFS(5) and IFS(-5) configurations to the MFS(5,5), and the SS (i.e. $|\phi_U| = |\phi_L| = 0°$) TEs in Figure 4.8b), the following was observed:

- For $f < 600$ Hz, the ΔPWL achieved by the MFS was superior to its IFS(5) counterpart, but worse than the values obtained for the SS and IFS(-5) TEs.
- For 600 Hz $< f <$ 2.8 kHz, there was a degradation in ΔPWL for the MFS in comparison to the SS and IFS TEs. This degradation in ΔPWL only occurred for the MFS and was a result of the tonal vortex shedding noise mimicking the blunt TE phenomenon, which was also seen in Figure 4.3 for the dual-flapped baseline. However, it was demonstrated that the addition of the sawtooth suppressed the tonal noise from the vortex shedding in

comparison to the broadband radiation levels seen in Figure 4.3.

- At $f = 2.5$ kHz, the noise reduction achieved by the MFS TE overtook and outperformed the SS TE noise reduction.
- For 2.8 kHz $< f <$ 6.7 kHz, the MFS consistently outperformed the IFS and SS TEs and achieved a higher ΔPWL. The largest noise reduction was achieved by the MFS case with ΔPWL = 6 dB at $f = 4.6$ kHz.
- For $f >$ 6.7 kHz, both the IFS(-5) and the SS TEs experienced negative levels of ΔPWL (i.e. noise increase). However, the MFS and IFS(5) averaged at ΔPWL ≈ 0 throughout this high frequency region.

Therefore, we can conclude that the noise spectra for low frequencies, $f <$ 500 Hz, and high frequencies, $f >$ 7 kHz, were influenced solely by the effect of flap angles and not by any flow dynamics related to the sawtooth at the TEs. This implies that between 500 Hz to 7 kHz the noise characterisitics were the result of the serrations, however, contamination by vortex shedding was observed between 800 Hz and 2 kHz due to the presence of multiple flap angles in both negative and positive directions.

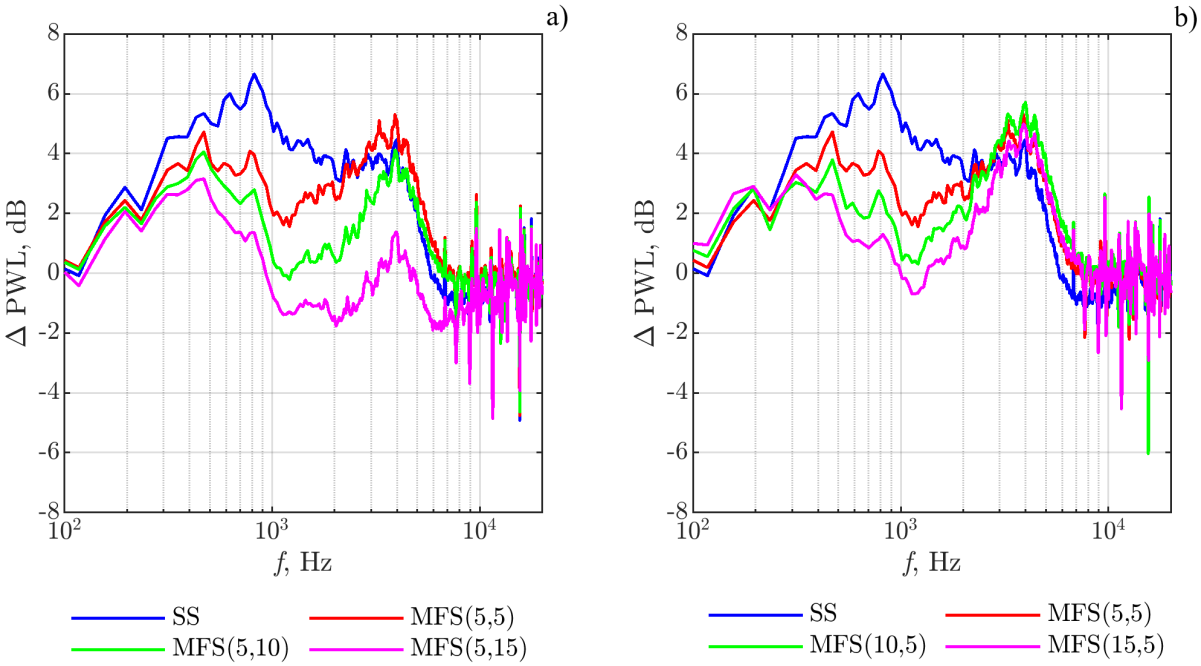

Figure 4.9: Comparison of the ΔPWL produced by SS and MFS($|\phi_U|, |\phi_L|$) TEs for: (a) $|\phi_U| = 5°$, $|\phi_L| = 5°$, 10° & 15°, and (b) $|\phi_U| = 5°$, 10° & 15°, $|\phi_L| = 5°$, at $U_\infty = 24$ ms^{-1}.

The MFS flap angles $|\phi_U|$ and $|\phi_L|$ have been shown to be advantageous when both were at 5°. The next investigation is to examine the ΔPWL spectra when $|\phi_U| = 5°$ and $5° < |\phi_L| < 15°$.

As shown in Figure 4.9a), the results were consistent with the IFS TEs results in Figure 4.5b) in that increasing the flap-down angle caused a degradation of the noise reduction performance. On the other hand, for the ΔPWL spectra achieved by the MFS TEs with $5° < |\phi_U| < 15°$ and $|\phi_L| = 5°$ in Figure 4.9b:

- For $f < 500$ Hz, the noise spectra collapsed, demonstrating evidence that the flap angle had a dominant effect on the broadband noise radiation.

- For 800 Hz $< f <$ 2 – 2.8 kHz, there was a degradation in ΔPWL for the MFS compared to the SS TEs. As previously established in Sec. 4.3.6, vortex shedding was present for the MFS cases. The higher the $|\phi_L|$, the greater the level of degradation in the ΔPWL as compared to $|\phi_U|$. The increase in $|\phi_L|$ could lead to an increased leakage of flow between the serrations, which increased broadband noise.

- For 2.8 kHz $< f <$ 6.7 kHz, a collapse of the ΔPWL curves was demonstrated regardless of the value of $|\phi_U|$. This phenomenon was also consistent with the results obtained for corresponding IFS TEs shown in Figure 4.5b. Similarly, at different $|\phi_L|$, comparable ΔPWL curve trends were noted which suggested that the effect of flap angle was dominant within this frequency range. Most importantly, and perhaps also counter-intuitively, it seemed that having a small flap-down $|\phi_L|$ angle on an MFS configuration actually improved the range of $|\phi_U|$ under which higher ΔPWL could be achieved. This indicated that the influence of flap angle had degrading properties for broadband noise radiation, consistent with the $|\phi_L|$ IFS results in Figure 4.5a. It also implied that setting a small $|\phi_L|$ on the MFS configuration could be beneficial.

- For $f >$ 6.7 kHz, all the MFS TEs averaged at ΔPWL ≈ 0 throughout this high frequency region. Again, this is consistent with the observations made in Figure 4.5 and Figure 4.7 and proved that the noise performance in this frequency range was directly influenced by flap angle.

Overall, the results presented in this sub-section suggested that it was possible to fine-tune both the $|\phi_U|$ and $|\phi_L|$ of an MFS TE to improve the ΔPWL level. The results indicated that a small $|\phi_L|$ was beneficial. It has also been shown that the noise improvement achieved by multi-flapped cases was versatile across the frequency range $f <$ 200 – 500 Hz and for $f >$ 2 kHz. Furthermore, the performance of MFS TEs was adversly influenced by vortex shedding for 800 Hz to 2 kHz, but was suppressed by the addition of serrations.

4.3.7 Noise spectra of the Split-Flapped-Serration (SFS)

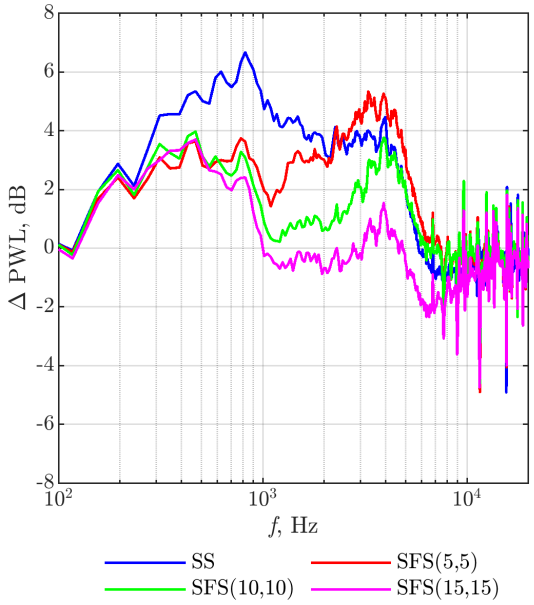

Figure 4.10: Comparison of the ΔPWL produced by the baseline, SS and SFS($|\phi_U| = |\phi_L|$) TEs, at $|\phi_U| = |\phi_L| = 5°, 10°$ & $15°$ and $U_\infty = 24$ ms^{-1}.

Figures 4.10 show the sensitivities of the broadband noise radiation to the SS and SFS-type TEs. Generally speaking, the noise charactristics and trends discussed in Sec. 4.3.6 for the MFS TEs were largely applicable to the SFS TEs. In particular, the noise characteristics for f $<$ 200 Hz and f $>$ 7 kHz were dependent on the flap angle effect and there was tonal vortex shedding between 800 Hz and 2 kHz. However, the absolute level of ΔPWL achieved by the SFS TE was generally larger than the MFS TE, as shown in Figure 4.16. For example, the MFS $|\phi_U| = |\phi_L| = 5°$ TE achieved a ΔPWL = 3.6 dB at f = 500 Hz. At the same frequency, the ΔPWL of 4.7dB was achieved by the SFS TE with $|\phi_U| = |\phi_L| = 5°$The advantages of the SFS TEs over the MFS were further manifested when comparing the SFS and the MFS both with $|\phi_U| = |\phi_L| = 15°$ (Figure 4.10 vs. Figure 4.8a respectively).

The ΔPWL spectra for the SFS TE with $|\phi_U| = 5°$ and $5° \leq |\phi_L| \leq 15°$re shown in Figure 4.11a. Figure 4.11b shows the ΔPWL spectra for the SFS TE with $\phi_L = 5°$ and $5° \leq |\phi_U| \leq 15°$. The noise characteristics and trends were again similar to the MFS TEs (compare Figure 4.8 and Figure 4.9), although in many instances the SFS TEs achieved a higher ΔPWL than the MFS.

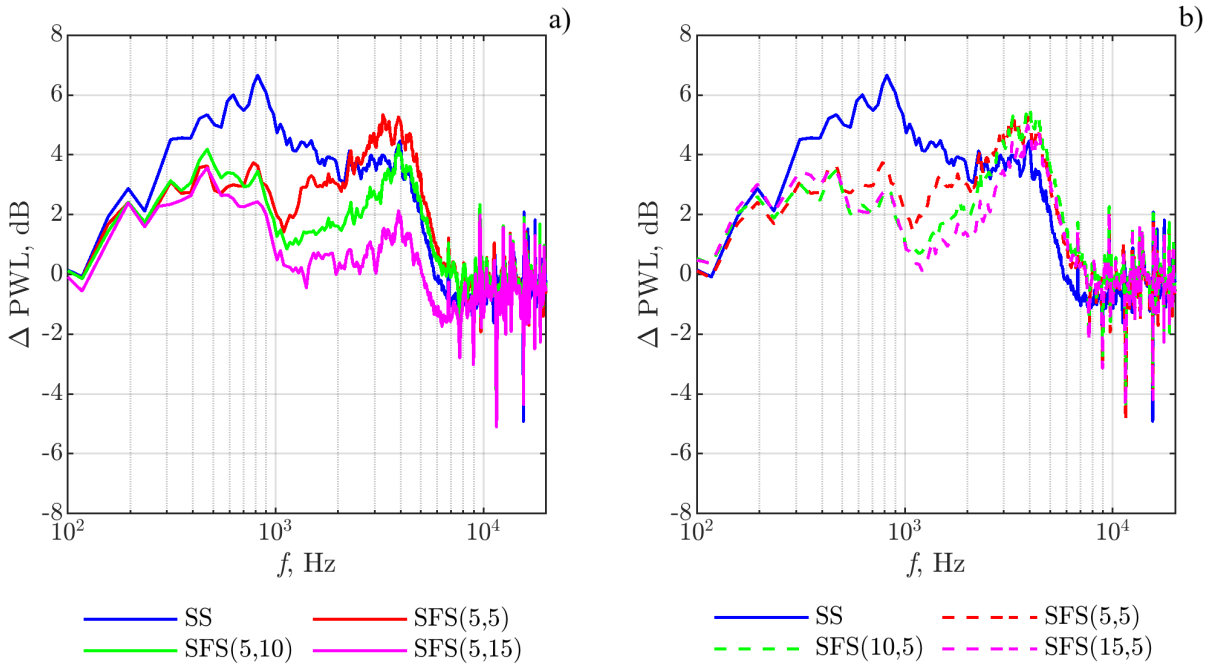

Figure 4.11: Comparison of the ΔPWL produced by the SS and SFS($|\phi_U|, |\phi_L|$) TEs for: (a) $|\phi_U| = 5°$, $|\phi_L| = 5°$, 10° & 15°, and (b) $|\phi_U| = 5°$, 10° & 15°, $|\phi_L| = 5°$ and $U_\infty = 24$ ms^{-1}.

4.3.8 Noise spectra of the Spanwise-Wavy-Serration (SWS)

Up to this point, the best candidate for the low-noise TE device was the SFS. However, just like the MFS and IFS counterparts, a drop in the ΔPWL was obtained due to vortex shedding between 800 Hz $< f <$ 2 kHz when compared to the conventional serration of the SS TE (note that the stated frequency range was averaged across the scatter of the available dataset). The IFS, MFS and SFS TE devices all featured a common characteristic in that the rate of change of the flap angle across the spanwise direction $d\phi/dz$, was either zero (IFS) or very large (MFS and SFS). It was assumed that a more gentle value of the $d\phi/dz$ might reduce the excessive strain of the secondary flow near the TE, and this represented another optimisation parameter for the out-of-phase TE serration discussed here. Figure 4.12 shows the sensitivities of the broadband noise radiation to the SS and SWS-type TEs of different λ', but all with $|\phi_U| = |\phi_L| = 10°$. Figure 4.12 demonstrates that for 800 Hz $< f <$ 2 kHz the noise performance suffered by vortex shedding for the MFS and SFS TEs, which disappeared for the SWS TE. However, the ΔPWL achieved by the SWS TE at the high frequencies was generally lower than that achieved by the MFS and SFS. For example, the largest ΔPWL for 2 kHz $< f <$ 7 kHz achieved by both the MFS and the SFS with $|\phi_U| = |\phi_L| = 5°$ was 6 dB. However, the corresponding ΔPWL achieved by the SWS with the λ'= 15 mm, $|\phi_U| = |\phi_L| = 5°$ TE was 5 dB. Overall, there was also not much variation in the acoustic performance obtained for the different values of λ'. It was found

that the $\lambda' = 15$ mm case performed better than the larger λ' cases. Figure 4.12 compares the ΔPWL spectra produced by the SS and SWS TEs. The SWS TEs had the same $\lambda' = 45$ mm, but with $5^\circ \leq |\phi_U|, |\phi_L| \leq 15^\circ$ Note that in this sub-section both $|\phi_U|$ and $|\phi_L|$ for the SWS TEs were kept the same. It can be demonstrated that the overall acoustic performance of the SWS TE was reduced when the flap angles increased. Based on the observations in Figure 4.12 and Figure 4.13, the best reduction in the broadband noise level for the SWS TE was therefore associated with both small ϕ and λ'.

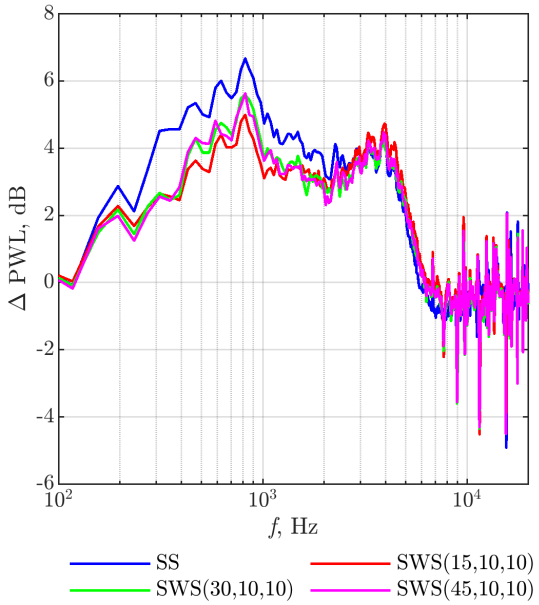

Figure 4.12: Comparison between the baseline, SS and SWS$(\lambda', 10, 10)$ TEs for $\lambda' = 15$, 30 & 40 mm, at $U_\infty = 24$ ms^{-1}.

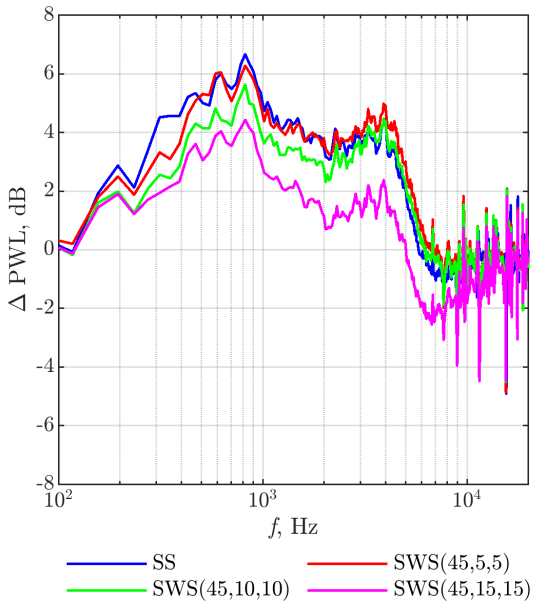

Figure 4.13: Comparison of the ΔPWL produced by the SS and SWS(45, $|\phi_U|$, $|\phi_L|$) TEs for $|\phi_U| = |\phi_L| = 5°$, 10° & 15°, at $U_\infty = 24$ ms^{-1}.

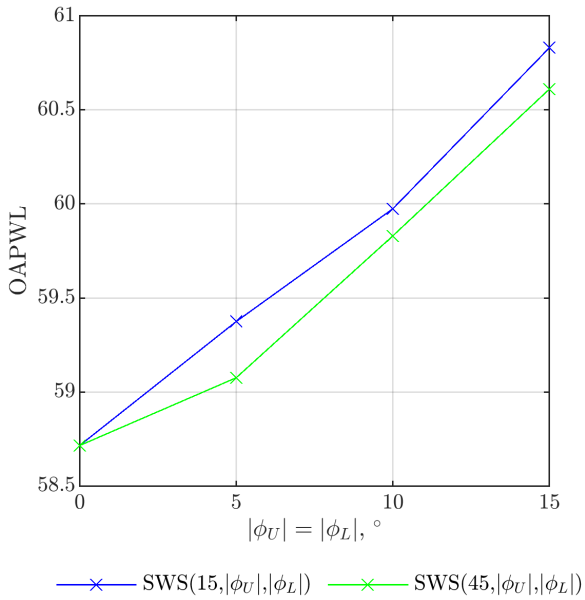

Figure 4.14: Comparison of the OAPWL integrated between 200 Hz $\leq f \leq$ 7 kHz produced by SWS(λ', $|\phi_U|$, $|\phi_L|$) TEs with $\lambda' = 15$ mm and 45 mm combined with $|\phi_U| = |\phi_L| = 5°$, 10° & 15° at $U_\infty = 24$ ms^{-1}.

Figure 4.14 presents the OAPWL of the SWS TEs at different oscillation wavelengths and flap angles for frequencies in the range of 200 Hz to 7 kHz. The results clearly show the same outcomes regarding oscillation wavelengths as previously obtained in Figure 4.10, where insufficient differences between each case at different flap angles achieved a ΔOAPWL = 0.25 dB. The effect

of increasing the flap angles significantly degraded the OAPWL performance in comparison to the non-flapped serrations at $\phi = 0°$ with a difference of 1 dB at the largest flap angle.

4.3.9 Comparison of all the trailing edge devices for their noise performances

A summary of the acoustic performance of the four TE devices, SS, MFS, SFS and SWS, is shown in Figure 4.15. It is evident that all the "misaligned" TEs (MFS, SFS and SWS) produced different noise characteristics compared to the conventional SS TEs. The MFS and SFS TEs produced largely similar ΔPWL spectra, although the SFS achieved slightly larger levels of the ΔPWL. For $f < 2.4$ kHz, both the MFS and SFS TEs still achieved noise reductions over the baseline TEs, but the level of noise reduction was lower in comparison with the conventional SS TE. However, between 2.4 kHz $< f <$ 6.7 kHz, a reverse situation occurred where they significantly outperformed the SS TE. For $f > 6.7$ kHz, where both the IFS and SS TEs experienced negative levels of ΔPWL (i.e. noise increase), both the MFS and IFS TEs averaged at ΔPWL ≈ 0 throughout this high frequency region. For the SWS TE, an opposite trend was observed. Unlike the MFS and SFS TEs, the SWS TE produced the same level of ΔPWL as the SS TE across the frequency range of $f < 2.4$ kHz. Between 2.4 kHz $< f <$ 6.7 kHz, the SWS TE still outperformed the SS TE, but the level of ΔPWL it achieved was now lower than that of the MFS and SFS TEs. For $f > 6.7$ kHz, the SWS began to experience negative ΔPWL, indicating a noise increase over the baseline TE. However, this increase in noise level in the high frequency range was still lower than that of the SS TE.

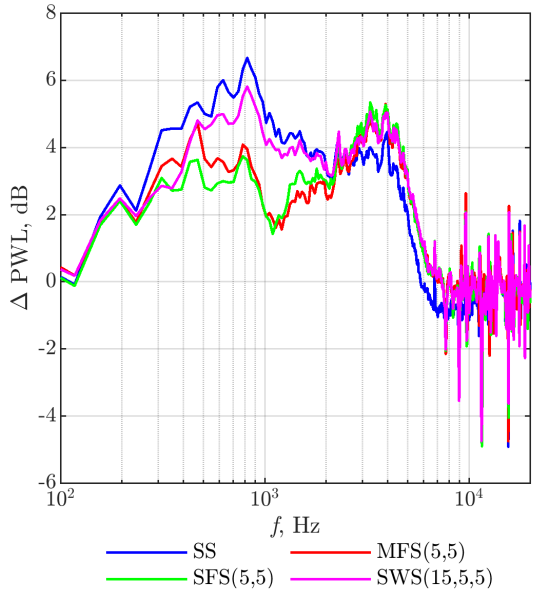

Figure 4.15: Comparison of the ΔPWL, dB, spectra achieved by the SS, MFS($|\phi_U|, |\phi_L|$), SFS($|\phi_U|, |\phi_L|$) and SWS($\lambda', |\phi_U|, |\phi_L|$) TEs at $\lambda' = 15$ mm $|\phi_U| = |\phi_L| = 5°$ and $U_\infty = 24$ ms^{-1}.

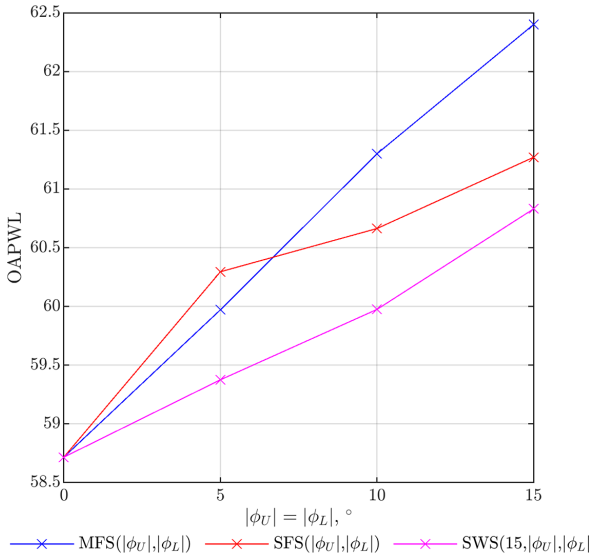

Figure 4.16: Comparison of the OAPWL integrated from 200 Hz to 7 kHz for the MFS($|\phi_U|, |\phi_L|$), SFS($|\phi_U|, |\phi_L|$) and SWS($\lambda', |\phi_U|, |\phi_L|$) where $\lambda' = 15$ mm and $|\phi_U| = |\phi_L| = 5°$, 10° & 15° at $U_\infty = 24$ ms^{-1}.

The comparison of the OAPWL obtained with the MFS, SFS and SWS TEs is shown in Figure 4.16. The OAPWL evaluated the frequency range between 200 Hz to 7 kHz. It was found that the effects of flap angle degraded the acoustic performance of the serrated TE in comparison to the SS TE. Amongst all the TE cases, the best performer was SWS. In contrast, the worst

cases were the SFS TE at $|\phi_U| = |\phi_L| = 5°$ and the MFS TE cases at the larger flap angles. The addition of dual-flap and a wavy pattern at the TE significantly reduced the effects of noise increase caused by flap angles, in comparison to the OAPWL of the IFS cases, seen in Figure 4.15.

4.4 Near Wake Flow Study

This section investigates the near wake and the wake development downstream of the serrated and baseline TEs. The baseline and serrated TEs were investigated at 1 mm downstream of the TE (TE) in the x-y and y-z planes. The experiments were performed in the open-jet aeroacoustic wind tunnel using a cross hot-wire probe for the baseline and IFS cases; and a single hot-wire probe for the baseline, SS, MFS with $|\phi_U = |\phi_L| = 5°$ SFS with $|\phi_U = |\phi_L| = 5°$ and SWS with $\lambda' = 15$ mm, $|\phi_U = |\phi_L| = 5°$.

4.4.1 Cross-section of Near Wake Baseline

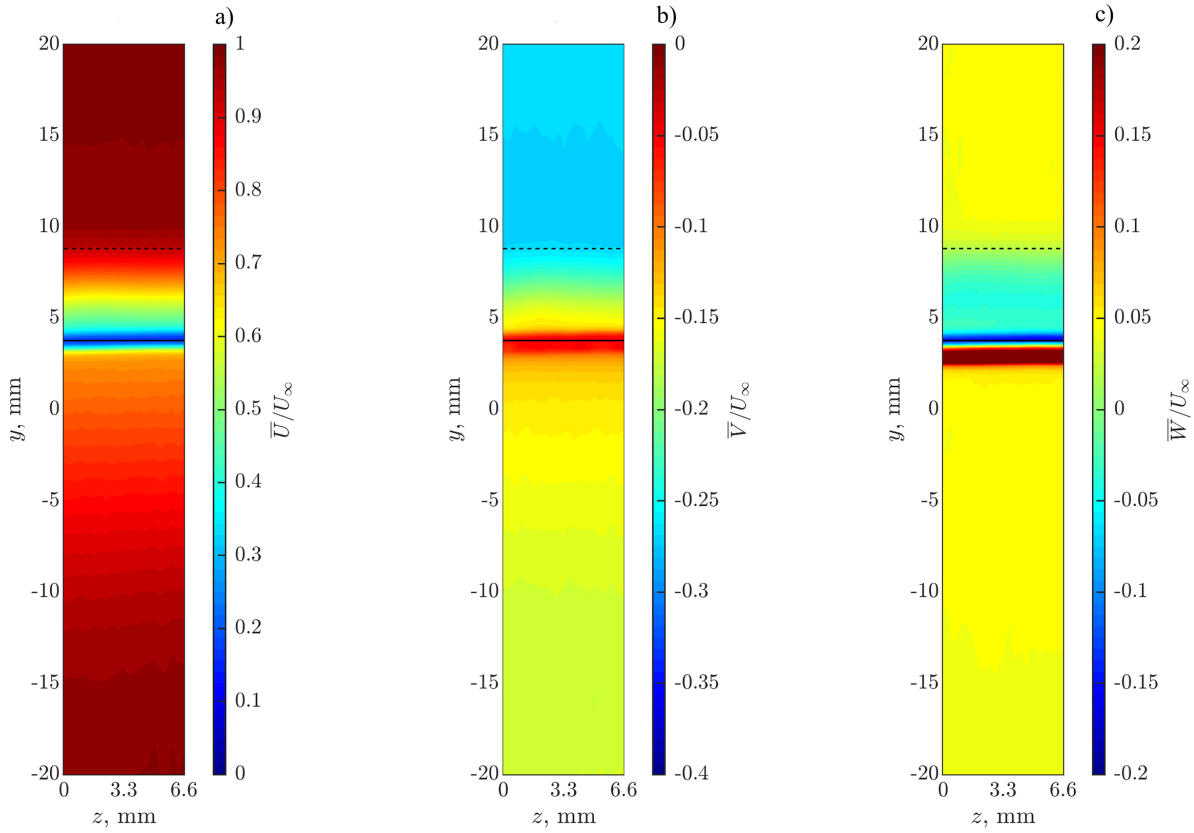

Figure 4.17: Mean velocity contour maps in the y-z plane 1mm downstream of the baseline TE at $U_\infty = 24$ ms^{-1}, where (-) and (- -) identify the locations of the TE and the TE slot of the main aerofoil body, respectively.

The near wake profile is presented in Figure 4.17 of the y-z plane in the u, v and w velocity components. The results showed that the mean flow in the spanwise direction was uniform for all velocity components. In Figure 4.17a, the u velocity component illustrated that the boundary layer on the suction side exhibited a lower flow velocity in comparison to the pressure surface. Vathylakis *et al.* [130] suggested that this was the result of the original design of the NACA 65-(12)10 laminar aerofoil. Furthermore, a leading edge transition bubble was found on the pressure surface, as discussed in Sec. 6.3.1. As a result, the pressure surface experienced higher levels of mixing in comparison to the suction surface, which led to a more fully developed turbulent boundary layer. Figure 4.17b) shows that the upper freestream, $y > 10$ mm, was more negative in comparison to the lower freestream, $y < 12.5$ mm. This was a result of the overall aerofoil geometry and TE which deflected the overall flow downward. In Figure 4.17c) the w-component

shows that the dominant flow tended to the right on the suction surface with the opposite being true on the pressure side.

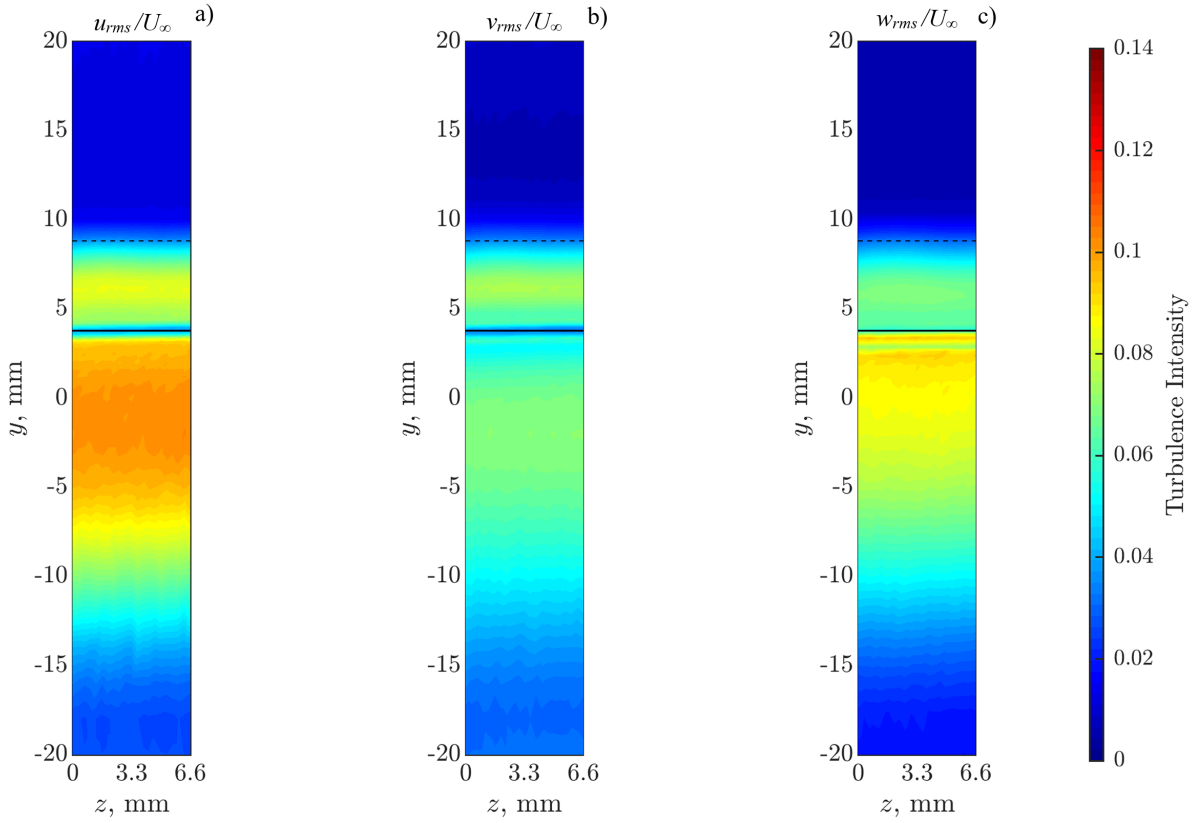

Figure 4.18: Turbulent Intensity contour maps in the y-z plane 1mm downstream of the baseline TE at $U_\infty = 24$ ms^{-1}, where (-) and (- -) identify the locations of the TE and the TE slot of the main aerofoil body, respectively.

Figure 4.18 presents the turbulent intensity contour maps of the baseline in the y-z plane for various velocity components. Figure 4.18a) shows that the thickness of the turbulent wake part on the pressure side ($y < 0$) was significantly larger than the wake part on the suction side ($y > 0$). A study by Vathylakis *et al.* [130] observed similar trends and suggested that the original design of the NACA 65-(12)10 laminar aerofoil resulted in this difference in the wake. Since the thickest part of the NACA 65-(12)10 was located at a considerable distance downstream of the leading edge, the growth of the boundary layer on the suction side experienced an acceleration as a result of a strongly favourable pressure gradient over the first half of the aerofoil. Beyond the thickest part of the aerofoil, an adverse pressure gradient took over where the flow decelerated towards the TE. In comparison, the pressure side was largely flat but exhibited a constant expansion angle. The adverse streamwise pressure gradient along the entire pressure side encouraged a considerable thickening of the boundary layer by the time it reached the TE. In addition, a separation bubble

at the leading-edge on the pressure side induced an early transition to turbulence which resulted in a wake-like flow to form along the pressure surface of the aerofoil.

From Figure 4.18, there is little variation in the turbulence intensity level across the spanwise distance for the baseline TE. Note that $y = 0$ identifies the TE location. The near wake was characterised by low turbulence intensity levels near the TE as it was related to the viscous, inner part of the upstream boundary layers on both the suction and pressure sides. The maximum turbulence intensity levels were achieved at an intermediate vertical distance which was largely associated with the upstream buffer layer of the boundary layer. Finally, the turbulence intensity gradually reduced to very low levels in the freestream.

4.4.2 Straight Serration (SS) Trailing Edge

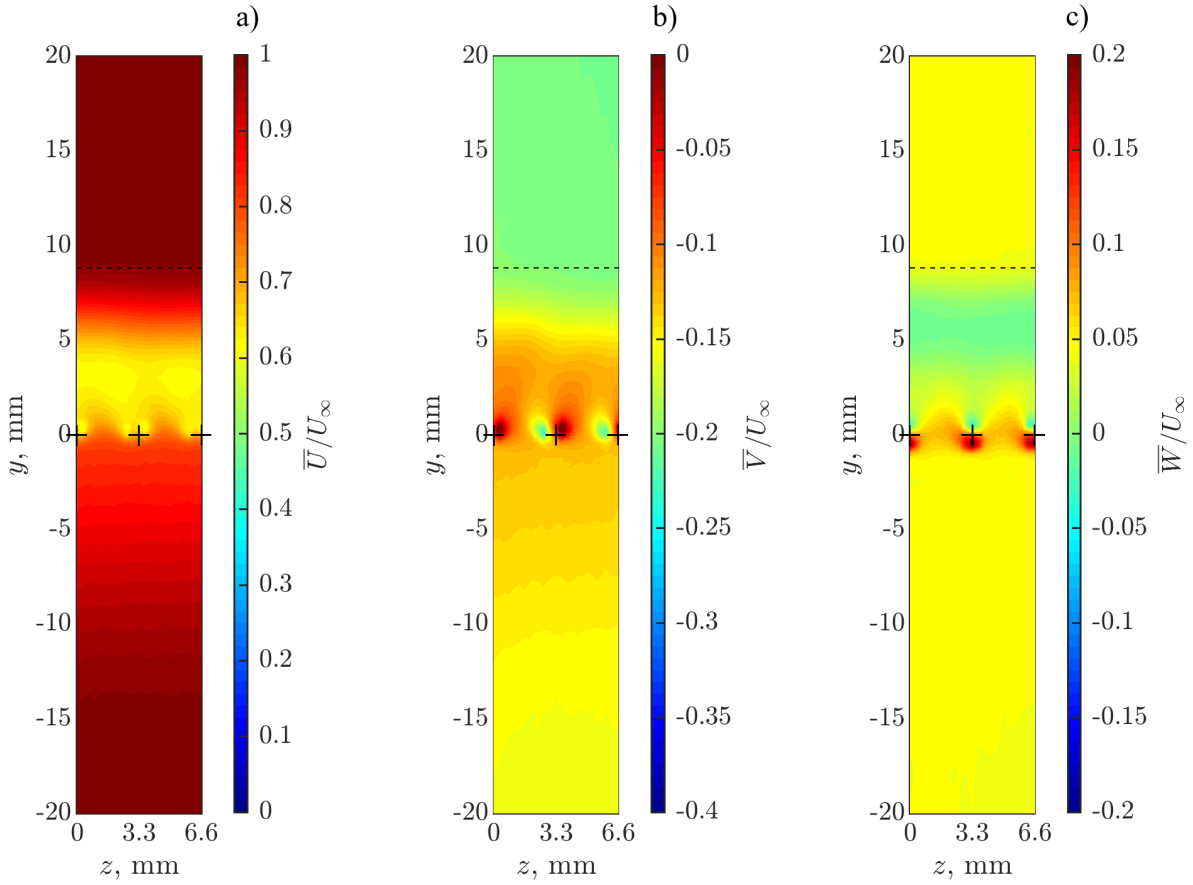

Figure 4.19: Mean non-dimensional velocity contour maps in the y-z plane 1mm downstream of the SS TE at $U_\infty = 24$ ms^{-1}, where (-) and (- -) identify the locations of the TE and the TE slot of the main aerofoil body, respectively.

Figure 4.19 displays the mean velocity in the u, v and w components for the SS TE. The influence of the serration confirmed the observation of a leakage/crossflow mechanism seen in-between

the sawteeth, because of the pressure difference between the suction and pressure surfaces. Studies investigating serrated TEs observed similar outcomes [1]. Furthermore, the v- and w- velocity components showed that the tips of the serration generated anti-clockwise vortices. The direction of rotations matched the trends of the w-velocity component seen on the baseline case. The phenomenon of the vortex structure could be the result of the influence of the crossflow resulting in the transfer of energy to the secondary flow structures on the sawteeth and the generation of the structure itself.

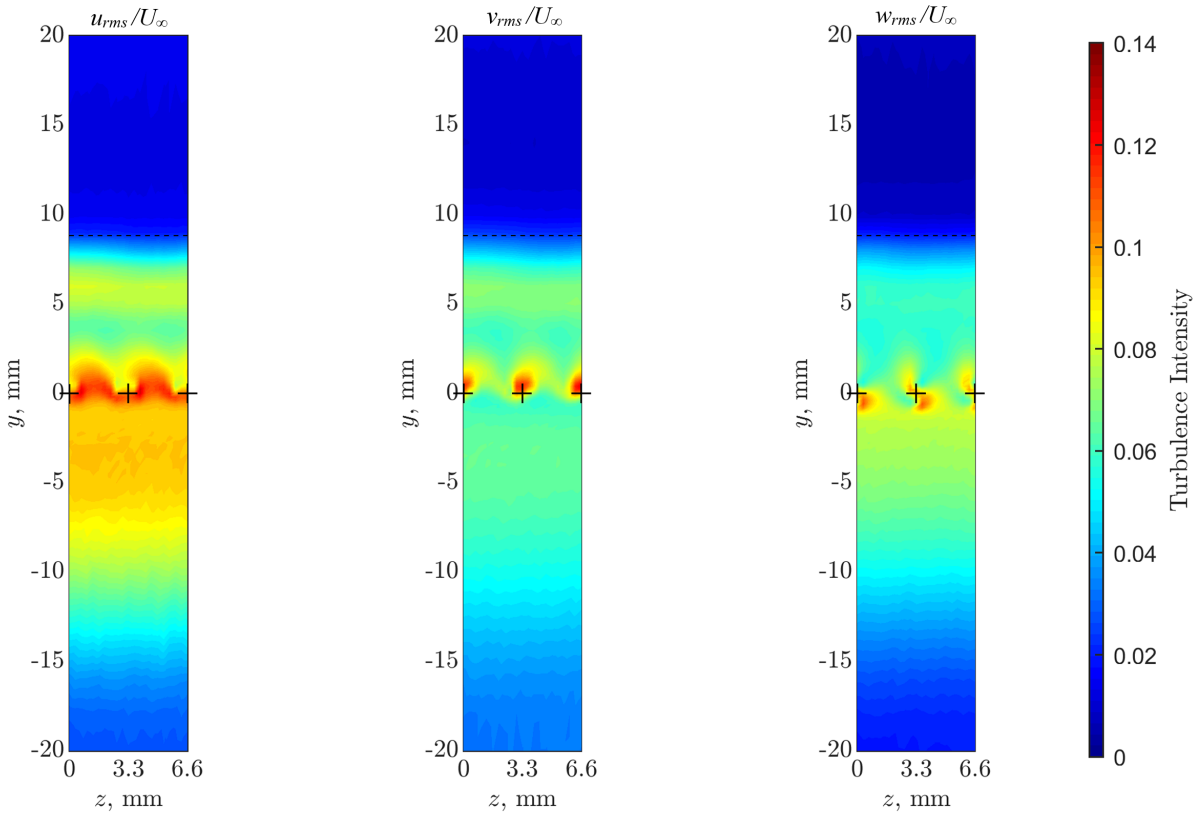

Figure 4.20: Turbulent Intensity contour maps in the y-z plane 1mm downstream of the SS TE at $U_\infty = 24$ ms^{-1}, where (-) and (- -) identify the locations of the TE and the TE slot of the main aerofoil body, respectively.

Figure 4.20 shows the turbulent intensity contour maps for the SS at $U_\infty = 24$ ms^{-1}. As can be seen in the u component, crossflow/leakage led to an increased turbulent intensity between the serration tips from the pressure surface to the suction surface. Furthermore, the presence of the crossflow resulted in a reduction in the pressure side wake width in comparison to the baseline of about 4 mm. Also, vortical structures emanated from the tips of the serrations, where high intensity was observed on the suction side of the serrations of the v-component and a quadrant

of high and low intensity was seen in the w-component. The crossflow induced an increase in the strength of the vortex's turbulent intensity in the v- and w-components at the tip of the serrations. As suggested in Figure 4.19, the leakage/crossflow could have potentially transferred energy within the wake into the vertical and spanwise components resulting in the high intensity of the secondary flow structures. A study by Juknevicius *et al.* [77] observed similar trends for the serrated TE.

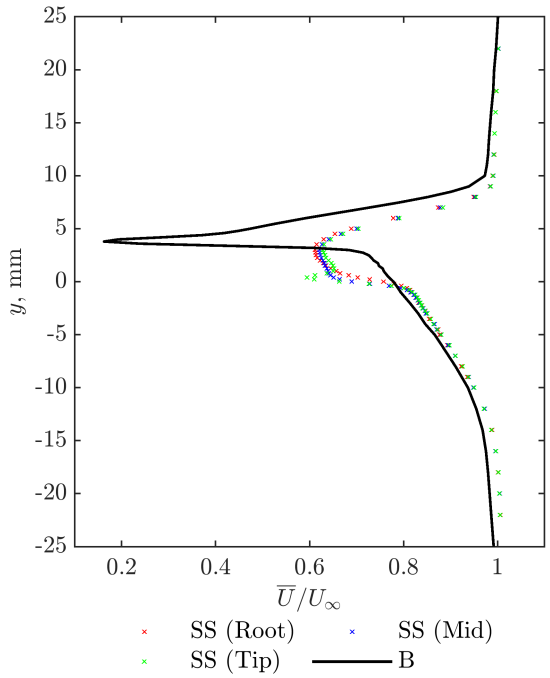

Figure 4.21: Comparison of the non-dimensional mean u velocity near wake profile for the B (-) and SS (x) TEs at various locations in the spanwise direction, and $U_\infty = 24$ ms^{-1}.

The non-dimensional mean velocity near wake profile for the baseline and SSs are shown in Figure 4.21. The results clearly show that the baseline exhibited a significant deflection at the tip, up to U/U_∞ =0.15, in comparison to the SS which was observed up to U/U_∞ =0.6. Similar observations were made by Geiger [50]. The difference in the boundary layer at the tip could have been a result of the energy transfer from the crossflow to the flow on the suction side boundary layer. In addition, at the tip of the serration a secondary flow structure was observed due to the inflection pattern at $0 < y < 3$ mm. This secondary flow structure could have been a K-H instability, or pressure driven vortices as suggested by Chong and Vathylakis [26]. At the root and mid locations, the wake profile showed less deflection of the non-dimensional velocity in comparison to the tip locations. This was thought to be due to crossflow-induced mixing in the flow at the near wake and the fact that the wake was slightly more developed downstream of the serration roots compared to the situation downstream of the serration tips.

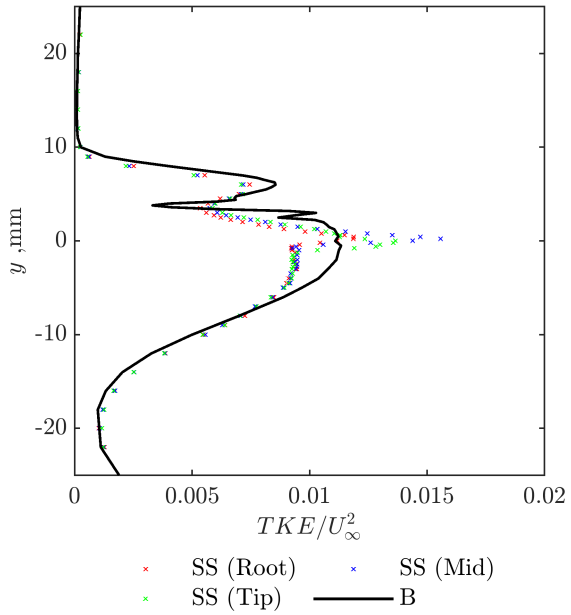

Figure 4.22: Comparison of the non-dimensional TKE near wake profile for the B (-) and SS (x) TEs at various locations in the spanwise direction, and $U_\infty = 24$ ms^{-1}.

The non-dimensional TKE of the near wake of the baseline and SS TE cases is shown in Figure 4.22. The results show that the TKE produced by the baseline TE was significantly larger than for the SS TE, except at the centreline of the serrated TE where it had larger TKE for all locations with values up to 0.016. For the baseline TE case two regions of high TKE on both sides of the aerofoil were found, due to the production of TKE from the mean shear stress originating from the upper and lower boundary layers. These presence of these regions of high TKE in case baseline suggested that a significant amount of acoustic emission was related to vorticity (shear) generated at the surfaces of the aerofoil. For the SS TE, significant increases in TKE at the serrations corresponded to production of TKE in regions of high shear stress within the flow which correlated to the secondary flow structures, as seen in Figure 4.20. The significant increase in TKE at the tip of the serrations was the result of flow (vortical) structures transferring kinetic energy from the crossflow into the secondary flow on the suction side of the TE. Therefore, the highest TKE, corresponding to peaks of shear-stress, suggested that acoustic radiation was emitted predominantly from the centreline of the serrated TE and to a lesser extent from the suction and pressure sides' wake.

4.4.3 Single Flapped Serration (IFS)

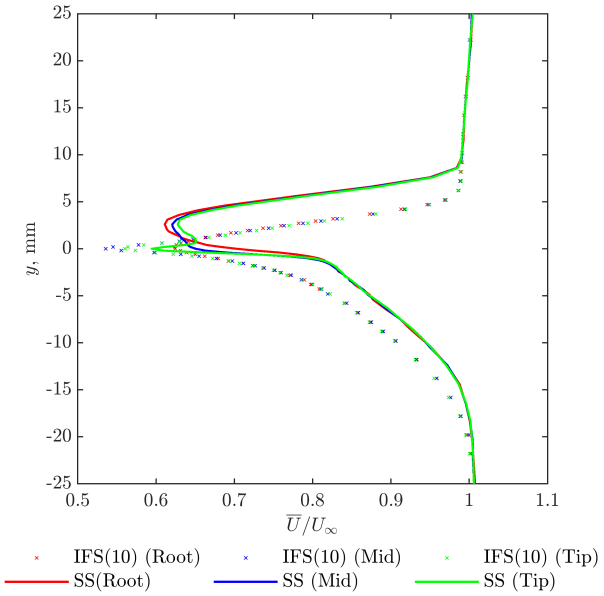

Figure 4.23: Comparison of the non-dimensional mean u velocity near wake profile for the SS (-) and IFS (x) TEs at various locations in the spanwise direction, and $U_\infty = 24$ ms^{-1}.

Figure 4.23 shows the non-dimensional mean velocity for the SS and IFS(10) at various locations across the TE. The influence of the positive flap angle had an insignificant effect on the flow characteristics compared to the SS TE. It could be said that the IFS with $|\phi_U| = 10$ exhibited similar near wake flow characteristics to the baseline TE, seen in Figure 4.21. However, the slowing of the flow within the wake at the mid and tip locations was less, while at the root a similar reduction in flow was obtained in comparison to the SS TE. Furthermore, the secondary flow structure, or inflection profile, observed for the SS TE was not found for the IFS(10).

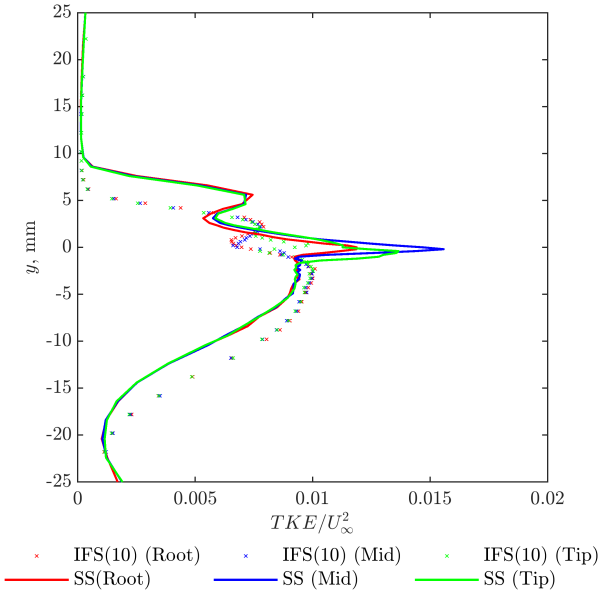

Figure 4.24: Comparison of the non-dimensional TKE near wake profile for the SS (-) and IFS (x) TEs at various locations in the spanwise direction, and $U_\infty = 24$ ms^{-1}.

The non-dimensional TKE at various locations across the SS and the IFS(10) TEs is shown in Figure 4.24. Increasing the flap angle up caused an increase in the TKE across the near wake region in comparison to the SS TE. The highest TKE for IFS(10) was observed in two equally high peaks at the tip of the serration and at the pressure side of the wake. In addition, a high TKE peak can also be seen on the suction side. These peaks originate from the production of TKE from mean shear stress within the secondary flow structures formed on the suction side of the serrations and the highly mixing velocity flow within the boundary layer. At the root and mid locations, the TKE levels were similar across the entire near wake. It could be suggested that the lack of crossflow in Figures 4.25 and 4.26 had a significant effect on the production of TKE at the TE, which could be a possible reason for the favourable acoustic performance at mid-to-high frequencies, seen in Figure 4.5.

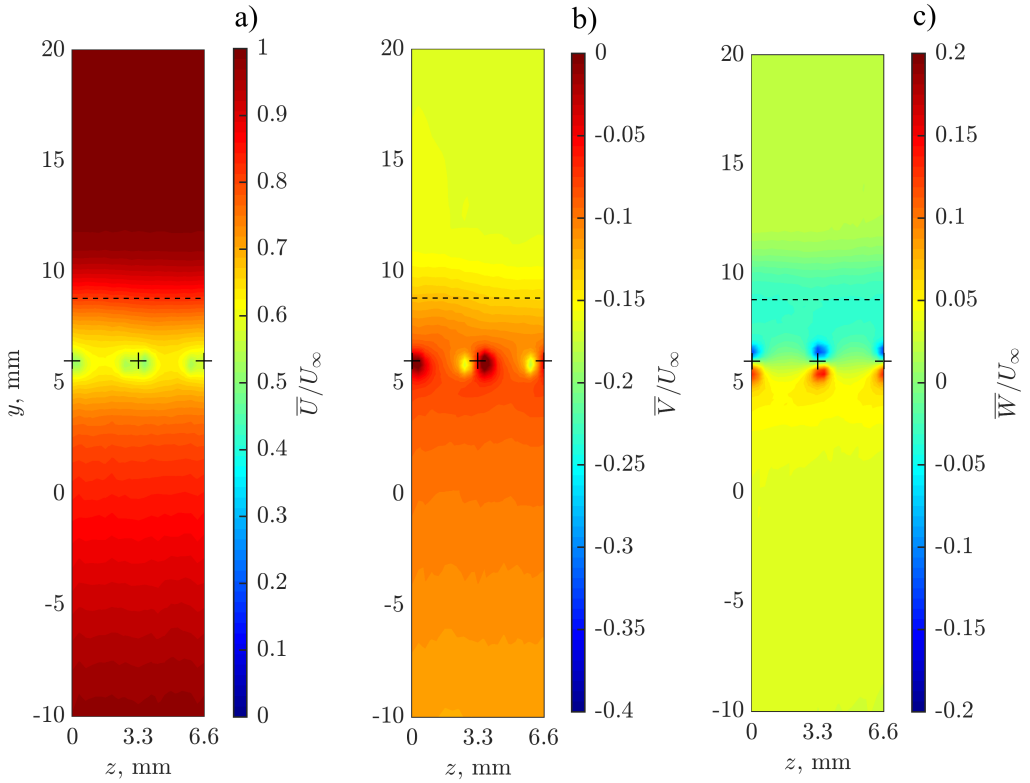

Figure 4.25: Non-dimensional mean velocity contour maps in the y-z plane at 1 mm from TE of the near wake profile for the IFS(10), where serration tips are represented as (+) and (- -) refers to the slot at the TE of the main aerofoil body at $U_\infty = 24$ ms^{-1}.

Figure 4.25 presents the mean velocity in the y-z plane at 1 mm downstream of the serrated TE. Figure 4.25a) shows that the positive flap angle led to the flow becoming more uniform around the serration, yet, at the tips of the serrations an additional slowing occurred on either side of the tip. Furthermore, the u-component exhibited no evidence of crossflow/leakage between the sawteeth. Therefore, it could be suggested that the strength of the crossflow/leakage along the serrations strongly depends on the flap angle. However, the influence of crossflow could still have been present at the root of the serrations, but in this case, the vertical velocity component was negligibly small at the TE. Furthermore, the influence of a positive flap angle at the TE had a significant effect on the flow upstream by altering the blade loading and pressure gradients. In Figures 4.25b) and 4.25c), the v- and w- velocity components are shown. Anti-clockwise rotating vortical structures can be seen emanating from the tips of the serrations. However, the strength of the individual velocity components was similar in comparison to the situation for the SS TE.

This suggests that the anti-clockwise rotation remained at a similar angular velocity independent of the flap angle.

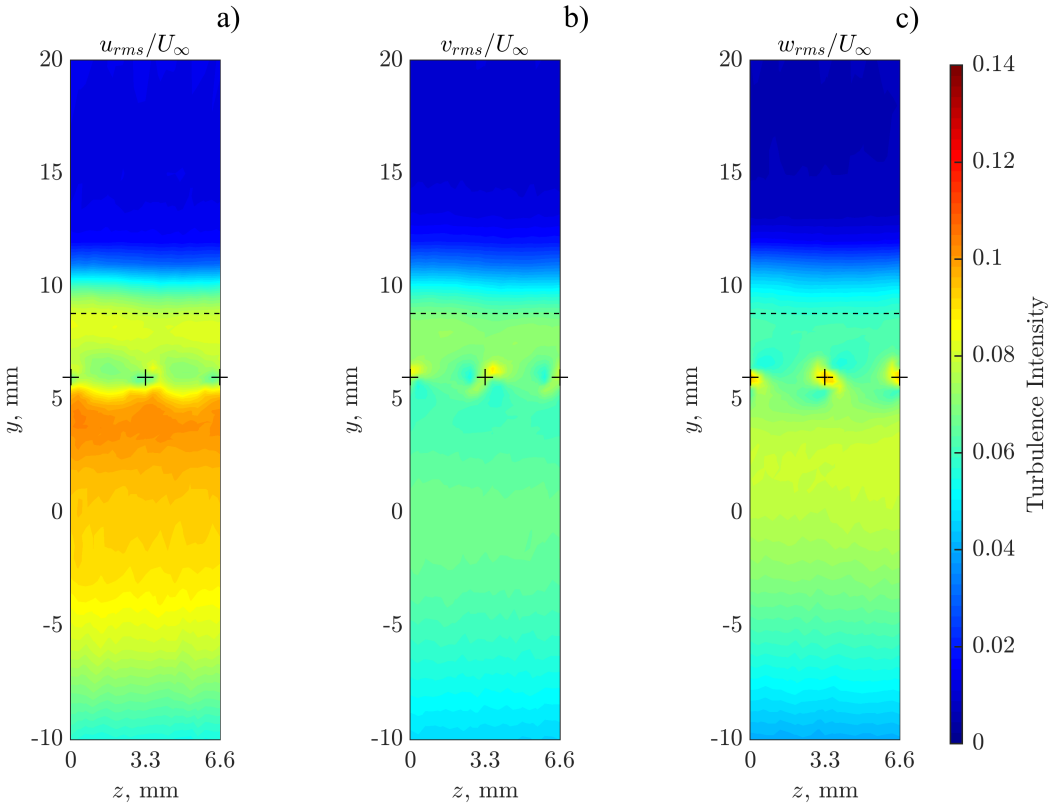

Figure 4.26: Turbulent Intensity contour maps in the y-z plane at 1 mm from TE of the near wake profile for the IFS(10), where serration tips are represented as (+) and (- -) refers to the slot at the TE of the main aerofoil body at $U_\infty = 24$ ms^{-1}.

Figure 4.26 presents the turbulent intensity in the near wake regions of the IFS with $|\phi_U| = 10$ of various velocity components. The first major observation was the reduction in crossflow between the serrations in the U- component, with a significant reduction in the turbulent intensity between the serrations. Furthermore, a higher turbulent intensity was seen on the suction and pressure surfaces in comparison to the non-flap serrations. In the V- and W- components, there was evidence of anti-clockwise vortices, however, the strength of the vortices was significantly reduced in comparison to the IFS with $|\phi_U| = 0°$. The main reason for the reduction in the vortices' strength was the significant reduction in the crossflow between the serrations, (that results in the formation of secondary flow/vortical structures) which would be related to the

transferring of energy from the u component to the v and w components within the secondary structure occurring along the serrations.

4.4.4 Negative Flapped Serration

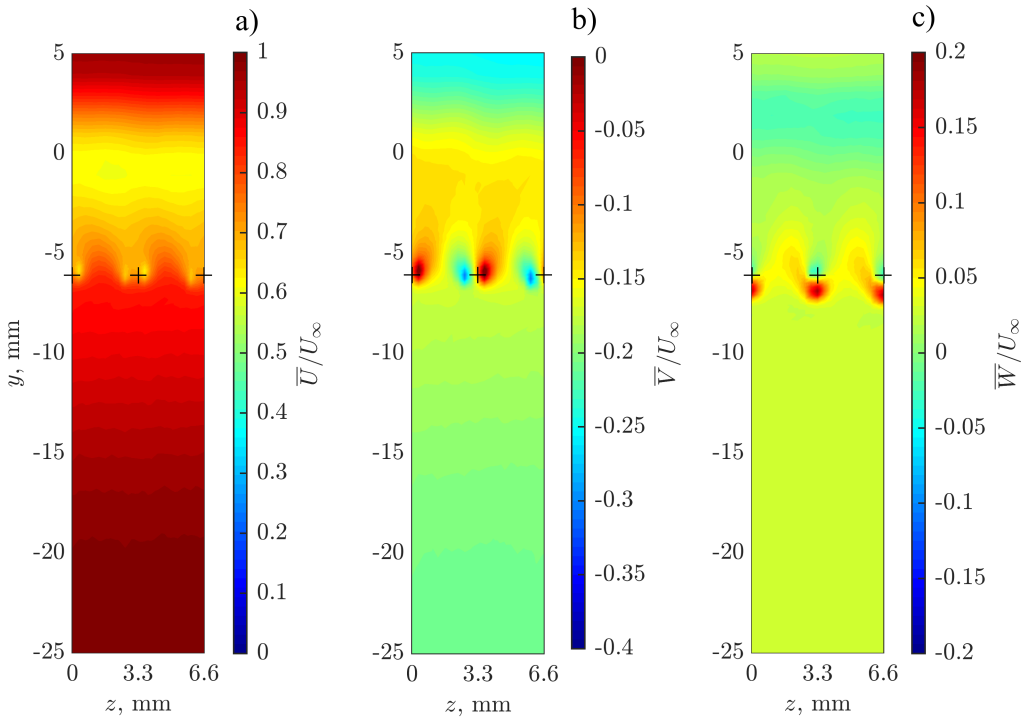

Figure 4.27: Non-dimensional mean velocity contour maps in the y-z plane at 1 mm from TE of the near wake profile for the IFS(-10), where serration tips are represented as (+) and (- -) refers to the slot at the TE of the main aerofoil body at $U_\infty = 24$ ms^{-1}.

Figure 4.27 shows contours of the mean velocity components in the y-z plane of the IFS with $|\phi_L| = 10°$. The results show a significant increase in the u-components between the serrations as a result of the crossflow in comparison to the other IFS TE cases. From the v- and w-components it can be seen that the strength of the anti-clockwise vortices located around the tips of the serrations remained comparable to the IFS cases. The later observation further confirms that the flap angle largely determines the strength of the crossflow/leakage along the serrations. Furthermore, the angular velocity of the vortices was found to be independent of flap angle.

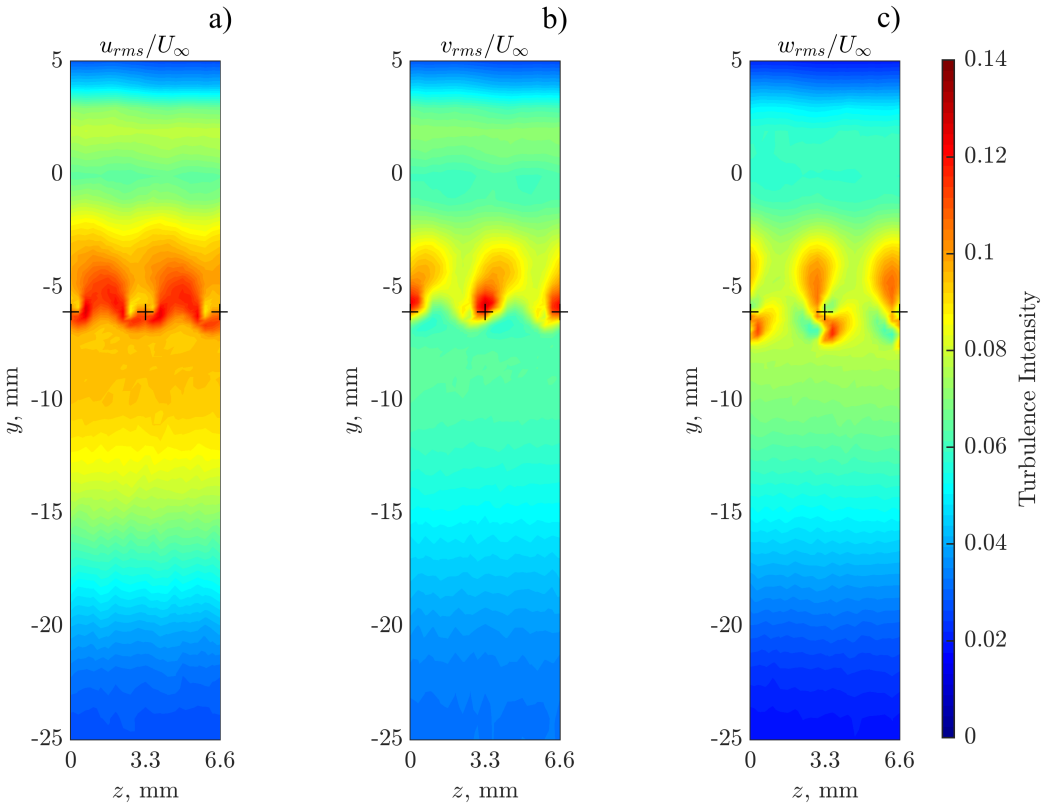

Figure 4.28: Turbulent Intensity contour maps in the y-z plane at 1 mm from TE of the near wake profile for the IFS(-10), where serration tips are represented as (+) and (- -) refers to the slot at the TE of the main aerofoil body at $U_\infty = 24$ ms^{-1}.

The turbulent intensity in the near wake regions for the IFS with $|\phi_L| = 10°$ in the y-z plane is shown in Figure 4.28. The negative IFS caused a large pressure difference between the two sides of the aerofoil, which resulted in a significant injection of turbulent fluctuations in-between the serrations, which is clearly visible in the u-component of the turbulent intensity. This crossflow caused a significant reduction in size of the pressure side wake in comparison to the other IFS and baseline TE cases. Yet, the crossflow was significantly stronger in comparison to the other IFS cases. Therefore, this could have outweighed the benefits of the reduction to the pressure side wake width leading to further acoustic radiation on the suction side. For the v - and w - components, the intensity of the vortices, seen in Figures 4.28b) and 4.28c), increased in strength at the tips of the serrations and extended further into the upper boundary layer of the suction surfaces. In the w - component, four quadrants of alternately high and low intensity could be seen to have greater strength compared to the non-flapped serrations. The increased strength of the tip vortices could have been a result of the crossflow injecting energy into the flow structures on the suction surface. The effect of increased vortex strength could have promoted the break-up

of turbulent eddy structures within the wake, but potentially also resulted in increased acoustic radiation.

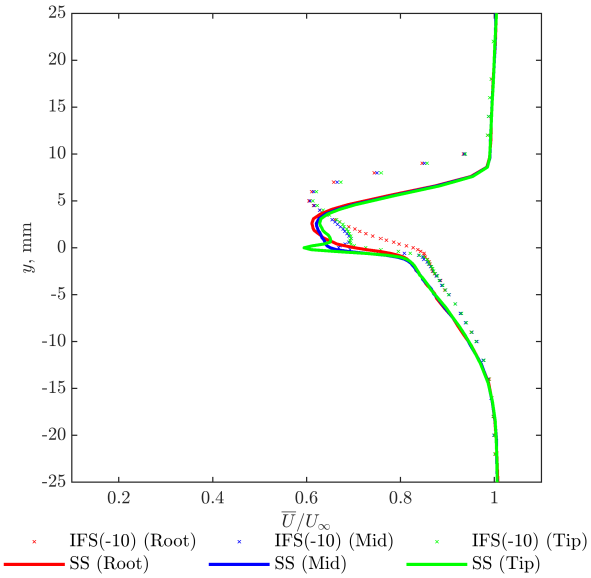

Figure 4.29: Comparison of the non-dimensional mean u velocity near wake profile at 1 mm for the SS (-) and IFS(-10) (x) TEs at various locations in the spanwise direction, and $U_\infty = 24$ ms^{-1}.

Figure 4.29 presents the non-dimensional mean u-velocity in the near wake profile for the SS and the IFS(-10) TE cases. The influence of negative IFS flap angle had a minor effect on the maximum wake deficit, $\overline{U}/U_\infty = 0.605$, to the freestream compared to other IFS cases. Furthermore, the results presented evidence of a large inflection profile on the suction side due to the presence of strong secondary flow structure at the mid and tip locations. On the pressure side, the influence of negative flap angle on the near surface flow was found to result in a thinner wake-like boundary layer flow at the tip in comparison to the SS TE case. As previously suggested, the influence of the pressure imbalance between the two sides of the aerofoil led to a reduction in boundary layer thickness on the pressure surface.

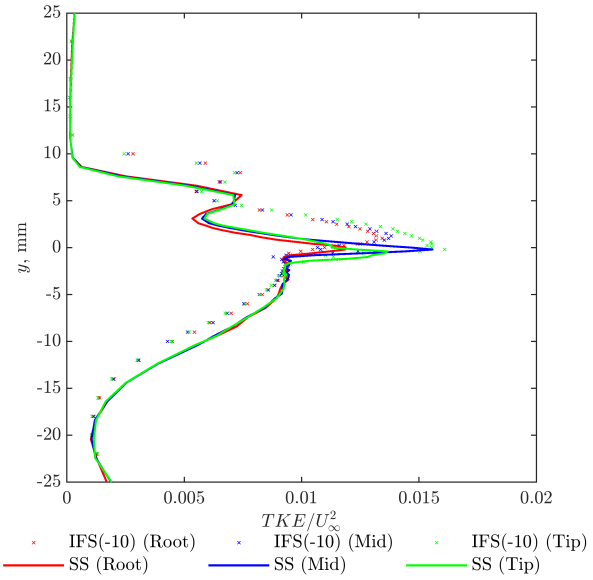

Figure 4.30: Comparison of the non-dimensional TKE near wake profile at 1 mm for the SS (-) and IFS(-10) (x) TEs at various locations in the spanwise direction, and $U_\infty = 24$ ms^{-1}.

In Figure 4.30 the effect of IFS and SS TEs on the non-dimensional TKE distribution was evaluated at three different spanwise locations, downstream of 1) the root 2) the middle between root and tip and 3) the tip. An increase in the negative flap angle was found to result in a reduction in TKE in the pressure side wake. However, the opposite was true for the suction side, where the TKE reached higher levels across all three locations compared to the SS TE case. Furthermore, the TKE distribution suggested that the negative flap angle led the suction side flow to be displaced upwards. This feature that can be seen in Figure 4.30, matched the general trend found that negative flap angles tend to increase the cross flow strength (see Figure 4.28). The increased crossflow resulted in additional production of TKE, due to the presence of high shear stress, through the interaction between crossflow and the secondary flow structures generated along the serrations. The presence of this crossflow-induced shear, resulting in the production of TKE could explain the observed increase in acoustic radiation.

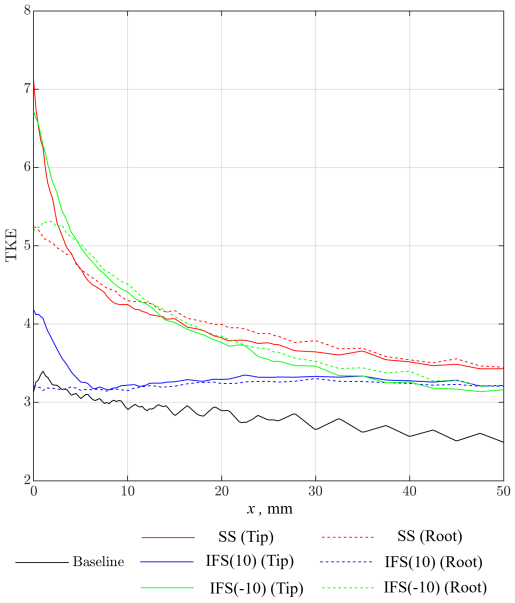

Figure 4.31: Comparison of the dissipation of the TKE downstream of the TE at the tip and root locations defined as solid and dashed lines, respectively, for the baseline, SS and IFS(ϕ) TEs where $\phi = 10°$ & $-10°$.

So far, it was found that misalignment had a significant effect on the near-wake characteristics with different flow mechanisms being observed for the IFS cases. The next investigation, shown in Figure 4.31, examined the TKE dissipation downstream of the TE downstream of either the tip or root locations. The first major observation was seen for SS and IFS(-10) producing the highest levels, TKE = 7.1, compared to the IFS (10) which produced TKE = 4.2. At the downstream locations, the TKE downstream of the tip of the IFS(10) dissipated rapidly to similar levels as the root TKE by $x = 5$ mm. It was then followed by the IFS(-10) at $x = 35$ mm. However, at $x = 35$ mm, the SS produced the largest TKE level in comparison to other IFS cases. Therefore, the results showed that the TKE emitted from the tips of the TEs were greater in comparison to the root locations. Readers should note that all readings were taken at the same spanwise location, 1 mm downstream from the tip. Therefore, it would be expected that the TKE downstream of the roots has dissipated more than the TKE downstream of the tips. For the IFS(10) no changes were observed in the downstream TKE, whereas the SS and the IFS(-10) produced increased values of TKE of 5.2 and 5.3 respectively, which dissipated downstream to TKE levels similar to the IFS(10).

4.4.5 Comparison of PSD

The next investigation evaluated the PSD of the near-wake flow of the baseline and the IFS cases. It was established in Sec. 4.3.5. that the effect of flap angle was dominant across specific frequencies which meant the benefits of the add-on serrated TE were limited. This sub-section assessed the energy within the near-wake flow for frequency regions with 500 Hz $< f <$ 2 kHz across all velocity components. The assessment of the energy within the near-wake flow for specific frequency region is defined by:

$$\Omega_i = \int_{f_1}^{f_2} V_{ii}(f)df, i = x, y, z, \tag{4.1}$$

where $V_{ii}(f)$ is the auto-power spectra density measured by the hot-wire probe of the velocity fluctuations. The index, $i = x, y$ and z are to differentiate the velocity fluctuation in the u, v and w components, respectively.

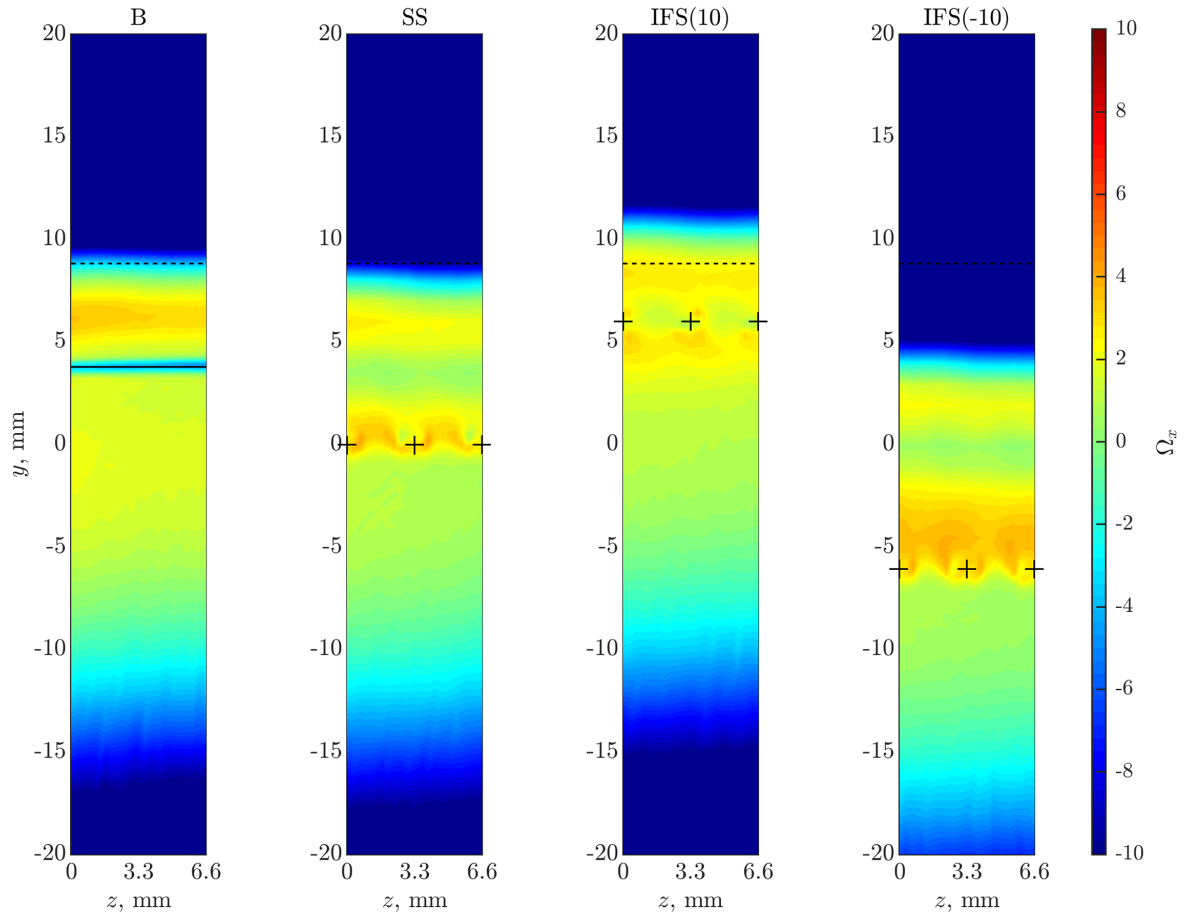

Figure 4.32: Ω_x contour maps in the y-z plane at 1 mm from the TE for the baseline, SS and IFS(ϕ) TEs where $\phi = 10°$ & $-10°$ TEs, integrated between 500 Hz $< f <$ 7 kHz in the u-component.

A comparison of the baseline and IFS TEs for the PSD was integrated at 500 Hz to 7 kHz, as shown in Figure 4.32. The first major observations were seen for the SS and IFS(-10) TEs where a reduction in the PSD was noted on the pressure side wake and suction side buffer layer, in comparison to the baseline TE. It is suggested that the reduction in the PSD levels was linked to the crossflow mechanism between the sawteeth, which enabled the transfer of energy of the u-component to the secondary flow structures formed on the serrations. In contrast, little to no crossflow was seen for the IFS(10) TE where a high concentration of energy surrounded the serrations on the suction and pressure surfaces. The IFS(-10) TE was highly effective at reducing the size of the wake and intensity on the pressure side. However, the strength of the crossflow resulted in a cross-contamination by the transfer of energy towards the suction side of the aerofoil which resulted into a degradation of the acoustic performance.

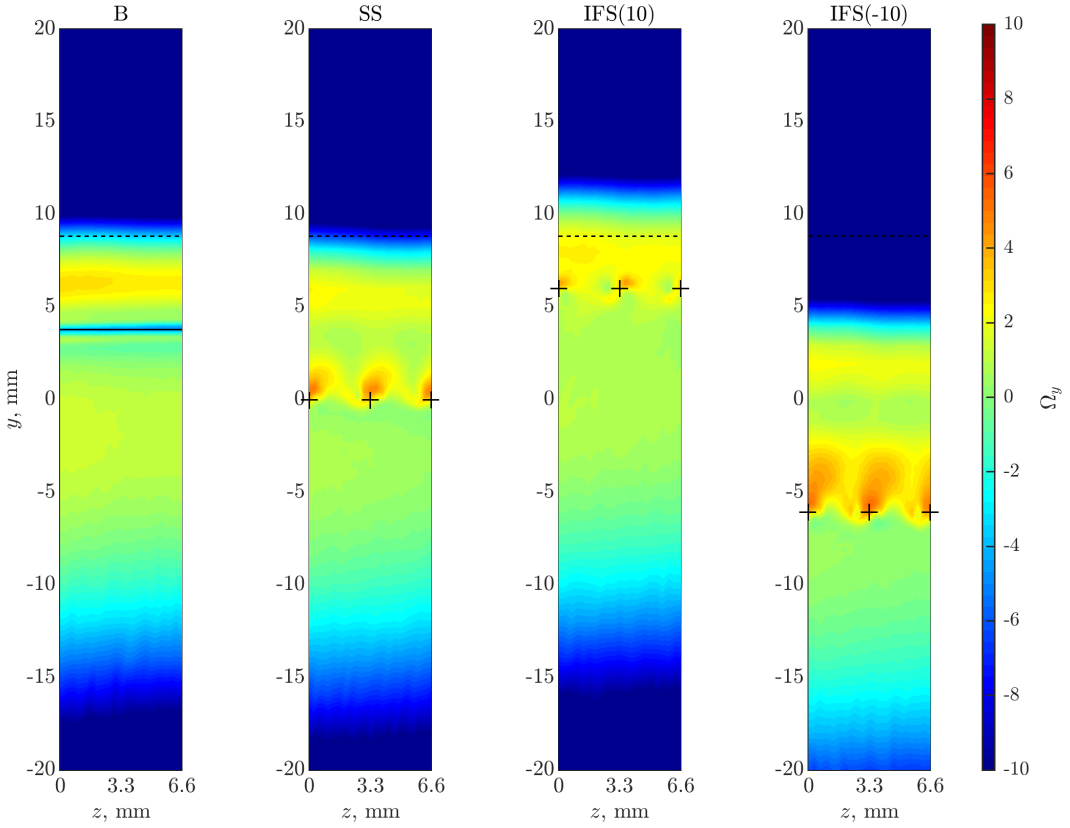

Figure 4.33: Ω_y contour maps in the y-z plane at 1 mm from the TE for the baseline, SS and IFS(ϕ) TEs where $\phi = 10°\& -10°$ TEs, integrated between 500 Hz $< f <$ 7 kHz in the v-component.

Figures 4.33 and 4.34 evaluate the PSD of the v and w velocity components of the baseline and IFS cases at various flap angles integrated over 500 Hz to 7 kHz. Generally speaking, the

PSD characteristics and trends discussed in Figure 4.32 for the baseline and IFS TEs were largely applicable also to the PSD of the v and w components. The similarities are a reduction in the thickness of the pressure side wake of the IFS cases and a reduction in the PSD levels within the pressure and suction side wakes. Figures 4.31 and 4.32 show a highly localised energy intensity above the tips of the serrations of the IFS cases. As suggested in Figure 4.32, the reduction in the PSD levels within the wake was linked to the crossflow between the sawteeth. The resultant effect is the transfer of energy from the u component through the crossflow to either the v or w components within the secondary flow structures formed on the serrations. The strength of the crossflow influenced the intensity of the PSD at the tips for the v and w components, shown in Figures 4.33 and 4.34. Furthermore, the intensity of the energy at the tips had a strong correlation with the broadband noise, where the largest reduction in noise was seen for IFS(10), with the lowest intensity in the v and w components. In contrast, the largest noise increase was for IFS(-10), with the highest intensity in the v and w components.

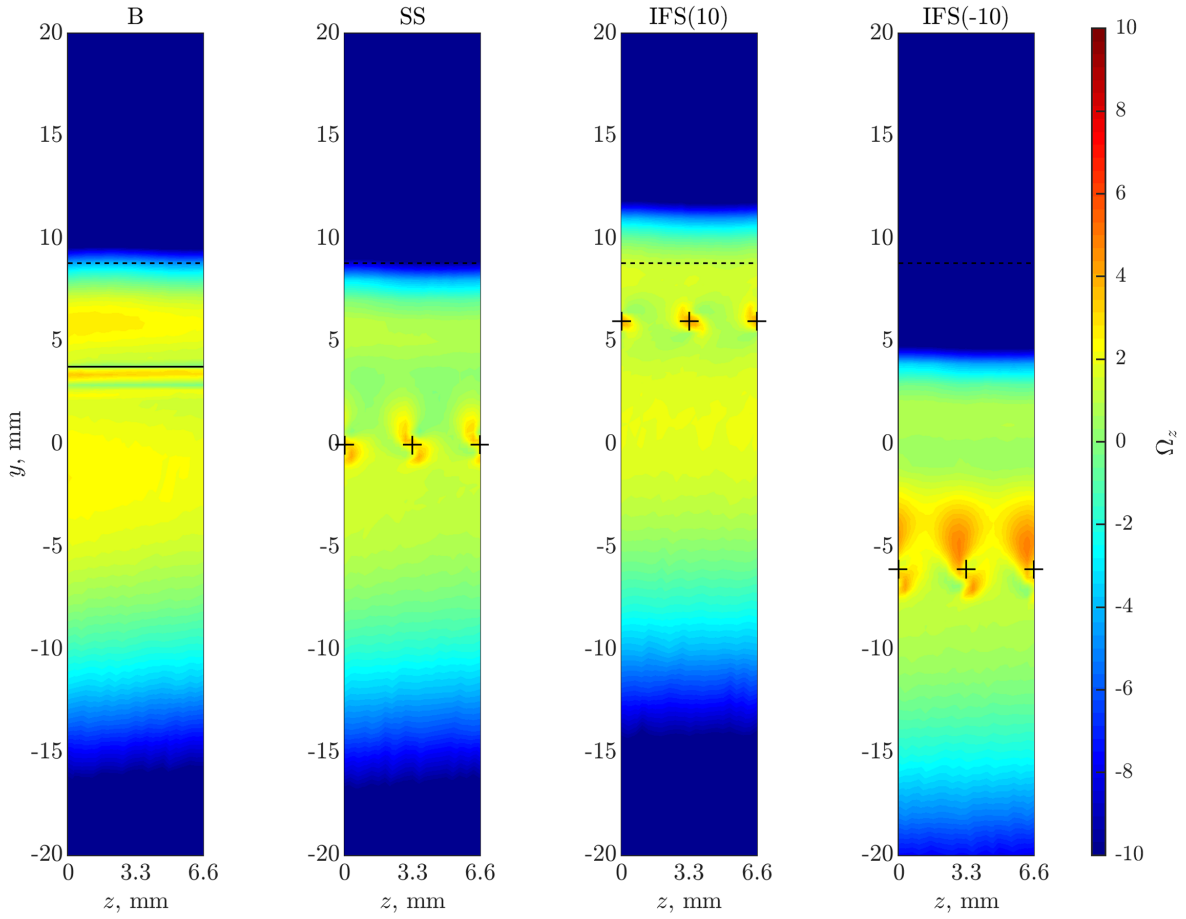

Figure 4.34: Ω_z contour maps in the y-z plane at 1 mm from the TE for the baseline, SS and IFS(ϕ) TEs where $\phi = 10°$ & $-10°$ TEs, integrated between 500 Hz $< f <$ 7 kHz in the w-component.

4.4.6 Optimal Configurations

The following figures present the wake flow across the serrated and baseline TEs at 1 mm downstream of the TE in the y-z plane. These measurements were performed using a single hot-wire probe. The baseline, SS, MFS(10,10), SFS(10,10) and SWS(15,10,10) were investigated. The serration amplitudes for the IFS, MFS, SFS and SWS were the same at $H = 30$ mm. In order to follow the standard practice of matching the same wetted area, the length of the flat plate insert of the baseline TE was chosen as $H = 15$ mm. This meant that during the changeover of the different TE devices, the hot wire probe always remained at 1 mm from the TE.

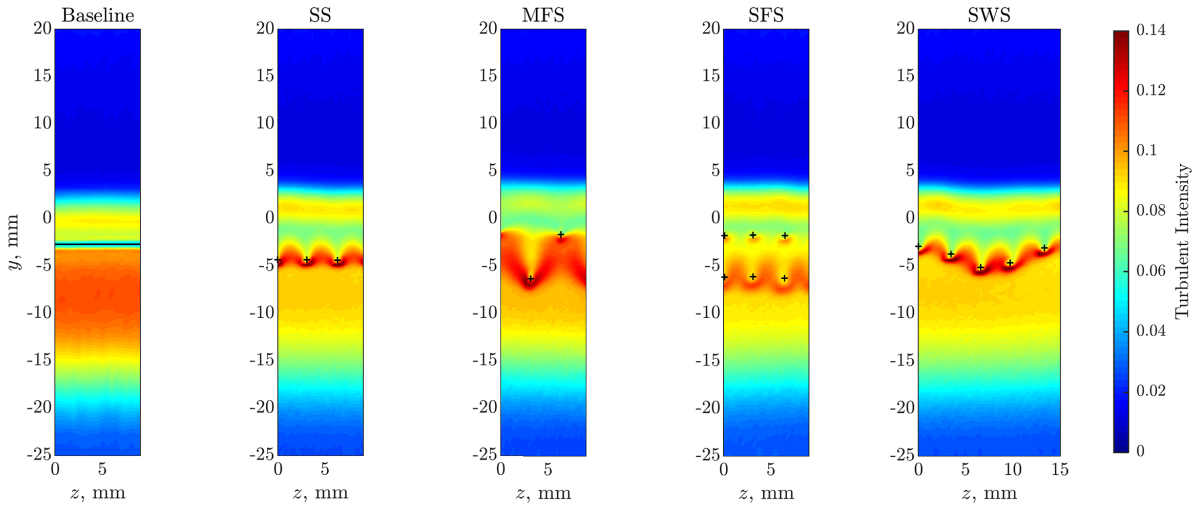

Figure 4.35: Turbulence intensity contour maps in the y–z plane at 1 mm from the TE for the baseline, SS, MFS($|\phi_U|, |\phi_L|$), SFS($|\phi_U|, |\phi_L|$), and SWS($\lambda', |\phi_U|, |\phi_L|$) TEs, where $\lambda' = 15$ mm and $|\phi_U|, |\phi_L| = 10°$, at U = 24 ms^{-1}

The turbulence intensity, I, (u_{rms}/U_∞) contour maps are presented in Figure 4.35. Based on the above arrangement, one would expect that the "width" of the turbulent wake region for the baseline TE, which can be identified from the turbulence intensity contours to some extent, would be smaller than the turbulent wake width somewhere in between the serration peak and trough for the serrated case. Interestingly, this was not the case. Instead the y–z turbulence intensity contour maps produced by the SS TE exhibited the following:

- Thickening of the turbulent wake on the suction side but thinning on the pressure side. The overall width of the turbulent wake, however, remained roughly the same compared to the baseline TE case.
- The turbulent intensity region within the pressure side wake is reduced in comparison to the baseline, due to crossflow from pressure side to suction side.
- The dominant turbulence intensity region associated with the suction side buffer layer was displaced upwards.
- The presence of an ∩ - shaped high turbulence intensity structure at every sawtooth gap.
- High turbulence intensity on the pressure side at the serration peak region, as a result of the transfer of energy to secondary flow structures on the serrations.

Combining the five points above, a first explanation of the mechanism for the broadband noise reduction by the conventional SS TE can be attempted: That is, the sawtooth gap represents a

leakage mechanism drawing flow from the pressure side to the suction side through the sawtooth gaps. The fluid-structure interaction between the crossflow and the serrations then increases the local turbulence level and inevitably produced an extraneous noise (i.e. in the frequency band 200 Hz $< f <$ 7 kHz). However, the crossflow components could also trigger a global displacement of the turbulent wake and the upstream boundary layer, such that the dominant turbulence production mechanism on the suction side is now distanced from the wall. At the same time, a homogeneous buffer layer on the pressure side is absent, partly due to the entrainment of the crossflow component at the sawtooth gap as manifested in the y–z contour map in Figure 4.35. As a result, the mechanism for the turbulent broadband noise radiation by the baseline TE was significantly disrupted by the SS TE, which then led to a reduction in the broadband noise.

For the MFS TE, the flap-up sawteeth seemed able to compartmentalise the suction side buffer layer into individual cell structures. This compartmentalisation of the buffer layer could be the result of the flap up sawteeth altering the flow characteristics (i.e. change in pressure gradients and overall blade loading). This may provide a further broadband noise reduction as manifested in Figures 4.7 and 4.8. On the other hand, the turbulent wake within the flap-up and flap-down sawteeth could be explained by the combination of the crossflow component and separated flow (due to the presence of the flap angle) resulting in vortex shedding. The SFS TE results could indeed support this hypothesis because the turbulence intensity level in the turbulent wake region between the flap-up and flap-down sawteeth became even less significant due to a similar, if more complex, flow field.

The y–z turbulence intensity contour map produced by the SWS TE is shown in Figure 4.35. Overall, all the characteristics described in points 1–5 above pertaining to the SS TE are also applicable to the SWS TE, except that the individual $\cap$ structures were now skewed according to the angle of orientation of the corresponding sawtooth. These flow features may explain how the noise performance for the SWS TE was not significantly different to the SS TE performance at the low-to-mid as well as the very high frequency ranges (see Figure 4.9b). Figure 4.35d shows a compartmentalisation of the buffer layer on the suction side by the SWS TE, which was suggested as a result of the positive flap angle altering the flow condition upstream.

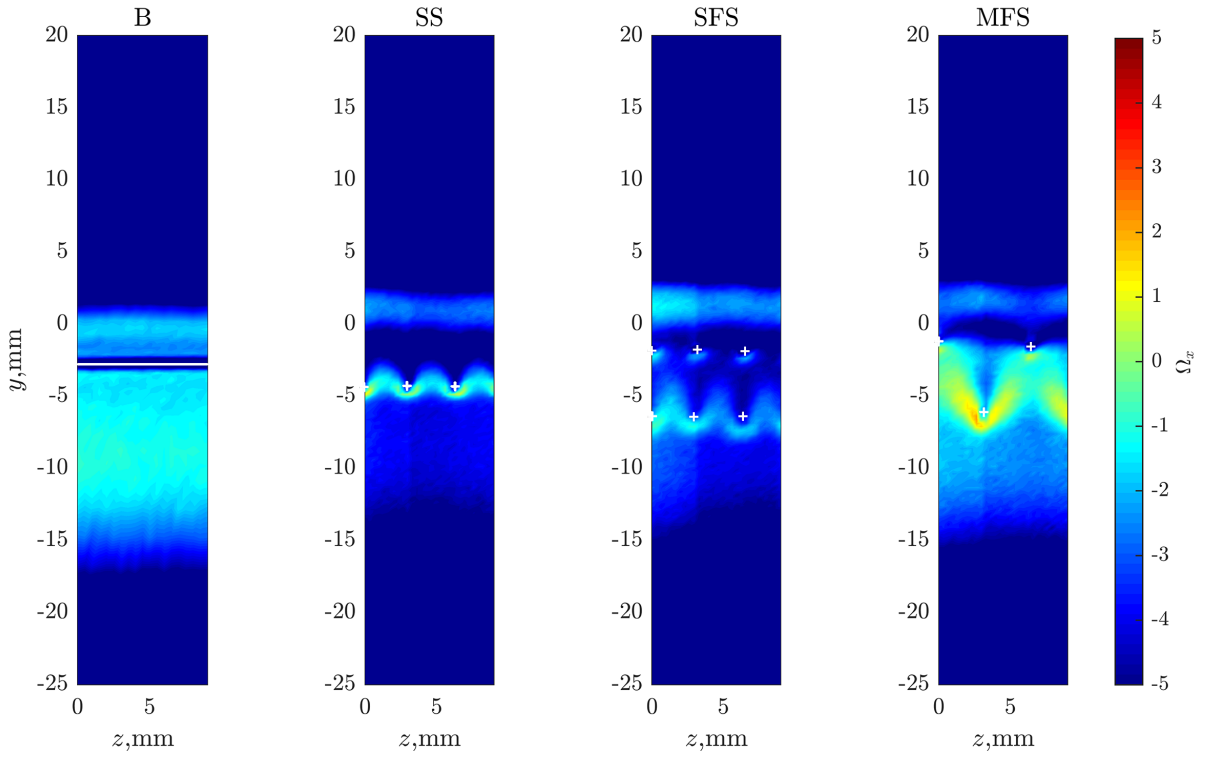

Figure 4.36: Ω_x contour maps in the y-z plane at 1 mm from the TE for the baseline, SS, SFS($|\phi_U|, |\phi_L|$) and MFS($|\phi_U|, |\phi_L|$) TEs where $|\phi_U| = |\phi_L| = 10°$ TEs, integrated between 500 Hz $< f <$ 800 Hz in the u-component.

Figure 4.36 presents a comparison of the turbulent energy for the baseline, SS, SFS and MFS TEs integrated at 500 Hz $< f <$ 800 Hz. The results for the baseline TE showed that significant levels of turbulent energy were observed on the pressure and suction sides. In contrast, the serrated case exhibited significant reduction in the intensity of turbulent energy within the pressure and suction sides but formed high PSD within the serration air gaps, corresponding to the crossflow and buffer layer. Furthermore, the PSD levels of the SS significantly reduced in comparison to other cases, which matched the trends observed in Figure 4.15.

The SFS and MFS TEs results showed similar patterns to the SS TE with reductions in the intensity of the turbulent energy in the pressure and suction side wakes in comparison to the baseline. However, high PSD levels were found at the negative flap angle, corresponding to the presence of crossflow between the serrations. On the other hand, the flap up serrations displayed a reduction of turbulent energy around the serrations, in particular for the SFS cases. Therefore, only the negative flap angle significantly increased the noise generated at this frequency range in comparison to the non-flapped and positive flap angles. Furthermore, based on Figure 4.36, the MFS produced the highest PSD followed by the SFS, while the SS TE producing the lowest

PSD. These results were confirmed by the noise spectra results seen in Figure 4.15.

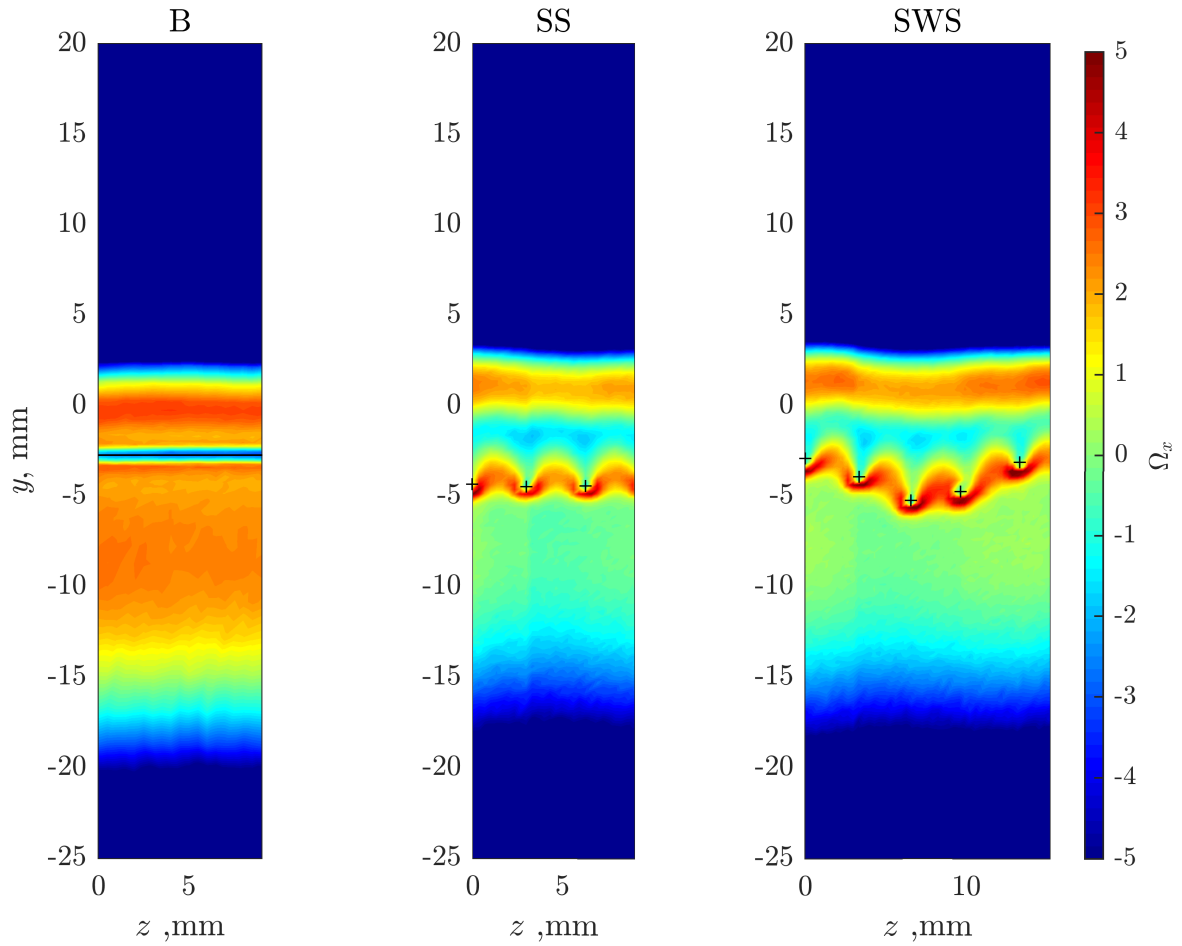

Figure 4.37: Ω_x contour maps in the y-z plane at 1 mm from the TE for the baseline, SS and SWS($\lambda', |\phi_U|, |\phi_L|$) TEs where $\lambda' = 15$ mm, $|\phi_U| = |\phi_L| = 10°$ TEs, integrated between 500 Hz $< f <$ 800 Hz in the u-component.

Figure 4.37 show contours of the turbulent energy in the y-z plane at 1 mm downstream of the TE for the baseline, SS and SWS TEs integrated over 500 Hz $< f <$ 2 kHz. The results show that the baseline TE exhibited higher levels of turbulent energy within the wake on the pressure side and the buffer layer on the suction side, in comparison to the serrated TE cases. In contrast, in the SS case a significant reduction in the turbulent energy on the pressure side and above the serration on the suction side was observed. This is suggested to be the result of the crossflow mechanism, transferring energy from the pressure side flow into the secondary flow structures formed on the serrations. Furthermore, this could explain the high intensity of the PSD seen around and in between the serrations and within the displaced buffer layer. Interestingly, also regions of reduced PSD levels could be observed between the serrations and the buffer layer.

Generally speaking, the flow characteristics of the SWS TE, shown in Figure 4.37c), were very similar to the SS TE results and the features discussed for the SS were also applicable to the SWS case. However, as previously observed for other cases within this chapter, the flap angle had a significant effect on the noise and flow characteristics. In particular, the negative flap angle of the SWS TE exhibited increased levels of turbulent energy formed below and in between the serrations in comparison to the SS TE. Also, the positive flap angles increased the PSD levels within the pressure side wake and between the serrations and buffer layer where the SS displayed a reduction in PSD levels. Therefore, this phenomenon indicates the loss in acoustic performance for 500 Hz $< f <$ 2 kHz for SWS TE in comparison to the SS TE results.

4.5 Summary

This chapter presents an experimental study using flow and noise measurements to evaluate the effects of adding a flap with variable flap angles at the TE of a NACA 65-(12)10 aerofoil. Several combinations of TE devices with straight and serrated TEs were tested at various flap angles: $\pm 5°, \pm 10°, \pm 15°$ and compared to the zero flap angle case as a reference. The experimental investigation examined freestream velocities, U_∞ between 20 ms^{-1} and 60 ms^{-1}, where the serration amplitude and wavelength were kept at $H = 30$ mm and $\lambda = 3.3$ mm respectively.

The misaligned TE cases exhibited different noise characteristics to the conventional TE geometries. The positive flap angle IFS TE cases were outperformed by the SS TE cases for broadband noise at low-to-mid frequencies, however, at mid-to-high frequencies the IFS cases proved to be superior. At negative flap angles, IFS was outperformed by the SS TE across all frequencies. The best flap angle configuration was IFS for both positive and negative flap angles of $\pm 5°$. For the MFS and SFS cases the broadband noise reduction degraded at low-to-mid frequencies in comparison to the SS TE. However, at mid-to-high frequencies both cases outperformed the SS TE. The SWS TE at low-to-mid frequencies exhibited similar broadband noise reduction as the SS TE. At mid-to-high frequencies, the SWS cases produced further noise reduction in comparison to the SS TE, yet, the noise reduction achieved was less than that of MFS and SFS cases.

The acoustic measurements established that the dominant effect of flap angle for all misaligned cases concerned noise characteristics for $f <$ 500 Hz and $f >$ 7 kHz. It was confirmed that misalignment was the result of high frequencies noise, especially for negative flap angles. Also, it was concluded that the sawtooth geometry affected the broadband noise between 500 Hz $< f <$ 7 kHz. At 2 kHz $< f <$ 7 kHz noise reduction was achieved by using a positive flap angle,

which altered the flow conditions upstream of the TE, such as the blade loading. These noise characteristics were seen for the largest serration wavelength and largest oscillation wavelength for the SWS cases.

Flow measurements confirmed the presence of crossflow between the serrations as a result of the pressure imbalance between both sides of the aerofoil. Furthermore, the strength of the crossflow was altered by flap angles with the highest strength seen for the largest negative flap angle, while opposite was true for positive flap angles.

Chapter 5

Trailing Edge Geometrical Modification to Achieve Frequency Targeted Self-Noise Reduction by Acoustical Destructive Interference Mechanism

5.1 Introduction

The bio-inspired passive flow control device provides an attractive method of reducing aerofoil noise radiated at the leading edge and trailing edge, respectively. Leading edge undulations, taking inspiration from the Humpback whale flipper on one hand, have been shown to be able to delay or sometimes completely suppress large-scale boundary layer separation [26, 61, 73, 95, 120]. In the aeroacoustics community, the inspiration mainly comes from the owl's wing. By utilising a serration pattern on aerofoil's leading edge, turbulence–leading-edge interaction noise can be reduced significantly over a relatively large frequency band [17, 26]. Kim *et al.* [79], whose numerical works aim to investigate the mechanism through aerofoil interaction of turbulence mean flow, found a decorrelation between the surface pressure fluctuations on the serrated leading edge and the far-field spectra. For a straight leading edge, the correlation would have been much stronger. Furthermore, they observed that noise reduction at the mid-to-high frequency range is the result of phase interference between the peak (tip) of the sawtooth and mid regions of the oblique edge.

The establishment of phase interference at various noise source regions for an aerofoil with a serrated leading edge provides a new foundation to achieve the next level of aerodynamic

noise reduction. Chaitanya and Joseph [22] explored an alternative profile of slit leading edge that can produce compact sources at both ends of the slit, i.e. opening and root. Essentially, incoming freestream turbulence eddies of a characteristic integral-length scale reaches the slit opening and then scatters into noise through the leading edge turbulence interaction mechanism. On the basis that the turbulent eddies are frozen and continue to propagate downstream, a second interaction noise scattering process will occur at the slit root. As a result, the same hydrodynamic disturbances will undergo acoustical scattering twice at the different spatial and temporal domains. Chaitanya and Joseph [22] successfully validated the destructive interference mechanism in the reduction of turbulence–leading edge interaction noise, when the most effective cancellation of the acoustic pressure waves is underpinned by the phase angle between the two sources equalling to π. This exploitation leads Chaitanya and Joseph [22] to achieve leading edge noise reductions of almost 18 dB at freestream velocity of 40 ms^{-1} using an optimised slit configuration. To put this in context, a conventional sawtooth leading edge profile with the same overall geometrical amplitude can only achieve up to 7 dB noise reduction [22]. In a numerical study, Cannard *et al.* [20] observed two highly localised low- and high-pressure distribution at the tip (front edge) and root (back-edge) of the slit, respectively. In comparison to the front edge, the back-edge of the slit exhibited significant higher-pressure fluctuation which contributed to the far-field noise reduction. The result of this acoustic radiation from the front and back edges can be emitted at a range of angles resulting in these regions interfere destructively, thus improving noise reduction. The works by Cannard *et al.* [20] thus provide a detailed dynamic of fluid-acoustic interaction to complement Chaitanya and Joseph original innovation. In essence, a small modification to the leading edge is already enough to achieve a significant reduction of the broadband interaction noise.

Another prominent noise source for an aerofoil is the TBL-TE noise. Similarly, sawtooth TE has shown to be a successful passive flow control device to reduce this particular type of noise. This has been reported by several other research studies. Van der Velden *et al.* [131] performed a numerical study to establish the relationship between the far-field noise and the flow-field on a NACA 0018 aerofoil with serrated TEs. They observed that the intensity of the surface pressure fluctuations vary across the streamwise direction and most of the low-frequency noise is generated at the roots of the serrations. Moreover, they suggested that two statistical parameters, the edge-oriented correlation length and convection velocity, are influential for both the intensity and frequency range of the noise reduction. They postulated that acoustical interference mechanism due to the scattered pressure waves along the oblique edge exists, and this is responsible for the broadband noise reduction by a single-serrated TE. However, unlike the aforementioned

slit leading edge case where the phase angle between two scattering sources are controllable, acoustical interference for a single-serrated TE is random and no optimal phase angle can be established. In other words, there is no frequency targeting capability for a single-serrated TE.

The establishment of controllable acoustic interference between different scattering sources for a TE, and the enhancement of the level of self-noise reduction, are the motivations of this chapter. This chapter focuses on the experimental study into the characteristics and mechanisms of acoustic interferences optimised for the turbulent TE broadband noise by two types of TE modification: a slit TE and a Double-Rooted Trailing Edge Serration (DRooTES). Conventional single-serrated TE is also included in the analysis. The fundamental theory that underpins this work is based on the interference in wave theory, similar to that of the leading edge case described earlier. As a generic term, the following equation is applied to determine the phase angle, $\hat{\omega}$, defined as:

$$\hat{\omega} = \frac{\omega \cdot l}{U_\infty} \tag{5.1}$$

$$\omega = 2\pi f \tag{5.2}$$

where ω is the angular frequency, f is the frequency, l is the longitudinal displacement between the two sources and U_∞ is the freestream velocity. A perfect destructive interference should occur when acoustic radiation from two coherent sources, S_1 and S_2, are 180° out-of-phase. Note that the l is essentially the h' for the DRooTES, and H for the slit TE, as shown in Figure 5.1. The relevant phase difference (or phase angle) can be expressed as $n\pi$, where n = 1, 3, 5, and so on. This results in the cancellation of the acoustic radiation. In contrast, a perfect constructive interference occurs when the acoustic radiation is in-phase between the two sources (i.e. when n = 2, 4, 6, and so on), which results in the amplification of the acoustic radiation to the far field. To summarise:

$$\frac{2\pi f H}{U_\infty} = n\pi \tag{5.3}$$

$$St = \frac{fH}{U_\infty} = \frac{1}{2}n \begin{cases} n = 1, 3, 5, ... & \text{for destructive interference} \\ n = 2, 4, 6, ... & \text{for constructive interference} \end{cases} \tag{5.4}$$

where St is known as the Strouhal number, which demonstrates that the respective values of the non-dimensional frequency at which the destructive acoustic interference occurs at 0.5, 1.5, 2.5 and so on, and the constructive acoustic interference occurs at 1, 2, 3 and so on. A strong

feature in Eqn. 5.3 is that, under a particular incoming velocity, the value of l dictates the frequency characterised by the destructive interference (as well as the constructive interference). In other words, for the first time, it is now possible to fine-tune a desired frequency to achieve the maximum level of noise reduction by TE geometrical modification.

5.2 Definition of the trailing edge add-ons, experimental setup and data analysis techniques

The NACA 65-(12)10 cambered aerofoil is the same one used for the study in the previous chapter 4. Similarly, it has a 0.8 mm slot at the rear, which is to facilitate insertion of detachable, laser-cut flat plate of 0.8 mm thickness that can either be the baseline sharp TE, slit TE, single-serrated TE or DRooTES. When the TE flat plate insert is included, the overall chord-length of the aerofoil ranges from $c_0 = 0.1425$ m to $c_0 = 0.170$ m. Comparison between the unmodified and modified TEs is largely based on the principle of similar wetted surface area. A coarse sandpaper was applied to the upper and lower surfaces at $x/c_{0\_original} = 0.2$, $c_{0\_original} = 0.15$ m, to ensure the boundary layers will be fully tripped to turbulent. The sandpaper strip has a width of 10 mm and a thickness of 0.95 mm.

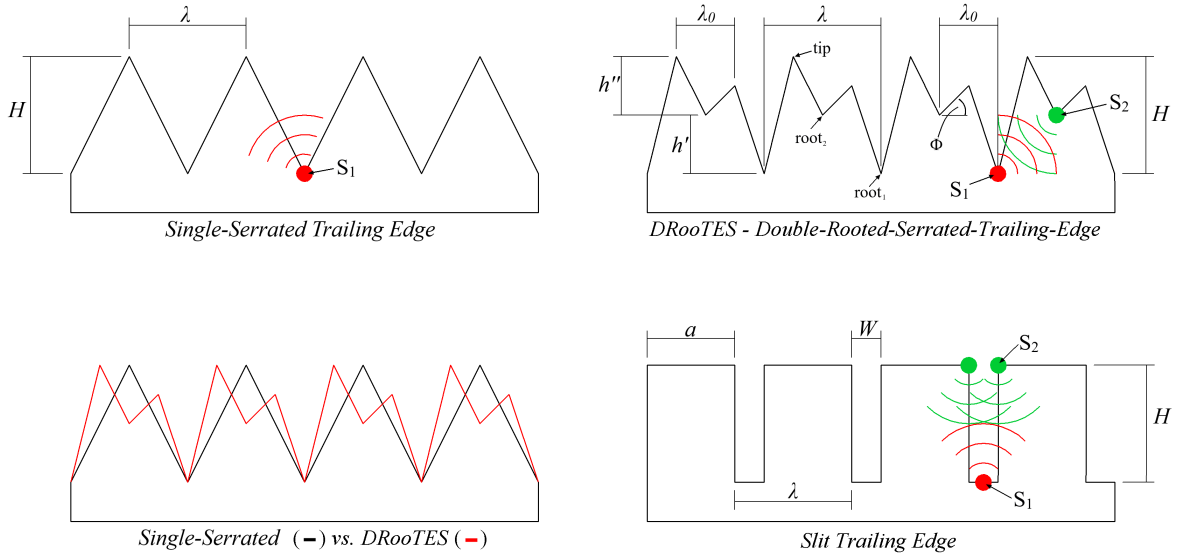

Figure 5.1: Geometric parameters of the Single-serrated TE, DRooTES and Slit TE for the NACA65-(12)10.

Figure 5.1 illustrates the geometric parameters of the TE flat plate cases. For a single-serrated TE, the main parameters are the serration amplitude (H), and serration wavelength (λ). The amplitude H in this case refers to the distance between the root and tip of the serration. For the

DRooTES, the amplitude H is made up of the root$_1$–root$_2$ longitudinal displacement (h'), and root$_2$–tip longitudinal displacement (h''). The same definition of serration wavelength (λ) is retained for the DRooTES, but a further description of the lateral-displacement of root$_1$–root$_2$ (λ_0) is added. Unless otherwise stated, the root$_1$–root$_2$ longitudinal displacement (h') and root$_1$–root$_2$ lateral displacement (λ_0) are half the amplitude (H) and wavelength (λ), respectively. Another geometrical parameter that is unique for the DRooTES is the angle of serration tip (Φ), where the value can dictate the level of symmetry between the "chipped" sawteeth. It is worth reminding that the single-serrated TE and DRooTES that have the same H and λ are compatible in terms of the wetted surface area, which is illustrated in Figure 5.1. Finally, for a slit TE, the symbols H and λ refer to the longitudinal distance between the slit opening and root, and lateral displacement between slits, respectively. In addition, the width of the slit root/opening is defined as W, and the counterpart between each gaps is defined as a, resulting in $\lambda = W + a$.

The ranges of serration amplitude (H) and wavelength (λ) of the single-serrated TE, DRooTES and slit TE investigated in this study are 5 mm $\leq H \leq$ 30 mm intervals of 5 mm, and 3 mm $\leq \lambda \leq$ 35 mm, respectively. For the DRooTES, two scenarios are included:

$$\textbf{Scenario 1: } (h' + h'') = H, \text{ where } h' = h'', \text{ and } 5 \text{ mm} \leq H \leq 30 \text{ mm}$$
$$\rightarrow 2.5 \text{ mm} \leq (h' = h'') \leq 15 \text{ mm}$$
$$\textbf{Scenario 2: } (h' + h'') = H, \text{ where } h' \neq h'', \text{ and } H = 30 \text{ mm only}$$
$$\rightarrow (h', h'') = (5 \text{ mm}, 25 \text{ mm}), (10 \text{ mm}, 20 \text{ mm}) \ldots (25 \text{ mm}, 5 \text{ mm})$$

In addition, the root$_1$–root$_2$ lateral displacement and angle of the serration tip of the DRooTES are 1.5 mm $\leq \lambda_0 \leq$ 4.5 mm interval of 1.5 mm, and $0° \leq \Phi \leq 84.3°$, respectively. For the slit TE, the same ranges of H and λ as above are retained, and the range slit tip and root width are 0.15 mm $\leq a \leq$ 1.5 mm and 1.5 mm $\leq W \leq$ 29.85 mm respectively.

When analysing the acoustic far field, it is important to define the appropriate "baseline" TE against each of the single-serrated TE, DRooTES and slit TE. The baseline TE is taken as $1/2H$ against the single-serrated TE and DRooTES, both of which with a full H, to ensure a similar wetted surface area. As a first assumption, comparison between the baseline and slit TEs could be made under the same H. Furthermore, the $1/2H$ criterion for the baseline TE will not be applicable to the slit TE in terms of achieving the same wetted surface area. Nonetheless, it is also important to ensure some consistencies amongst the TE add-ons tested in this study. Furthermore, as will be shown later in the result section, the far field radiation of the aerofoil with the baseline TE is found to be insensitive to the Therefore, the $1/2H$ criterion is retained as the baseline counterpart for the slit TE.

The far-field noise measurements were also conducted in the acoustic facility using the far-field polar array at Brunel University London. The microphones were positioned at $50^\circ \leq \Theta \leq 120^\circ$ intervals of 10° with the $\Theta = 90^\circ$ microphone corresponds to the mid-span of the aerofoil and at 0.97 m above the TE. The sampling frequency was 40 kHz with a sampling time of 20 seconds. The data were windowed and the PSD of 1 Hz bandwidth was computed from a 1024 points FFT and a 50% overlap time. This refers to a frequency resolution of 39 Hz for the spectra. Noise measurements were taken at freestream velocities between $U_\infty = 20$ ms^{-1} and 60 ms^{-1}. The Sound Power Level, PWL, can be calculated with an assumption of cylindrical spreading of acoustic waves from the TE. Radiated per unit span in the range of angles $\Theta_1 < \Theta < \Theta_8$, the PWL can be represented by the following equations:

$$\mathcal{W}(f) = \frac{2\pi \int S_{pp}(f,\Theta)\Delta\Theta}{\rho c_\infty}, \Theta_1 < \Theta < \Theta_8, \tag{5.5}$$

$$\text{PWL} = 10\log_{10}\left(\frac{\mathcal{W}(f)}{\mathcal{W}_0}\right) \tag{5.6}$$

where S_{pp} is the far-field pressure power spectrum density at a polar angle Θ, $\Delta\Theta = 10^\circ \times \frac{\pi}{180}$ is the angle between adjacent microphones in radians, and $\mathcal{W}(f)$ is the sound power integrated for the radiation angles from Θ_1 to Θ_8. The polar angles of the condenser microphone was from $\Theta_1 = 50^\circ$ to $\Theta_8 = 120^\circ$ intervals of 10°, $\mathcal{W}_0 = 10^{-12}$ W, and c_∞ is the speed of sound.

In the investigation of the flow field, unsteady velocity measurements were conducted at freestream velocity of $U_\infty = 30$ ms^{-1}, corresponding to Re $= 3.108 \times 10^5$. Similar to the previous chapter, the hot wire anemometry is the main flow-diagnostic tool. More details about the hot wire anemometry setup can be found in Chapter 3. Figure 5.2 explains the velocity measurements in the forms of boundary layer and two-point cross-correlation and coherence. Note that, unlike in the acoustical test, the baseline TE is the same amplitude as the single-serrated, DRooTES and slit TEs in the flow field study. Boundary layer measurements were taken in the x-y plane where the probe was positioned at 0.1 mm, corresponding to $y^+ = 6.67$ from the surface of the flat plate TE. The measurements were only performed for the baseline and slit TEs with the same amplitude at three identical locations downstream at the root (x/c_0 =0.903), mid (x/c_0 =0.952) and tip (x/c_0 =0.998). Note that the orientation of the hot wire probe in the boundary layer measurement is adjusted such that the hot wire is parallel to the wall surface, which could achieve an initial resolution in the y-direction of 0.01 mm in order to account for the large velocity gradient with the boundary layer profile. The boundary layer measurements at the three locations, as indicated in Figure 5.2, were performed at both the suction and pressure sides of the aerofoil.

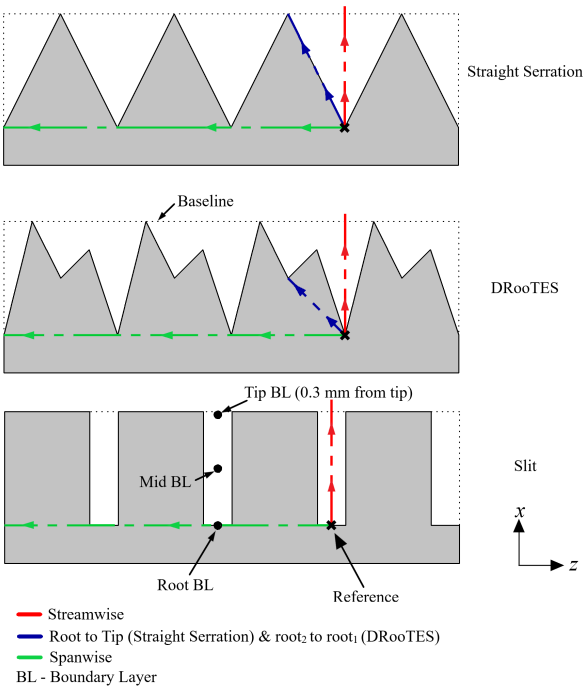

Figure 5.2: Schematic of the unsteady velocity measurements that were taken for the baseline, straight-serration, DRooTES and slit TEs.

Coherence and cross-correlation measurements were taken in an x and z plane as shown in Figure 5.2. Unlike in the boundary layer measurement, the probes were re-orientated such that the hot wires are perpendicular to the wall surface. The mid-point of the hot wire was positioned at approximately 0.725 mm from the wall surface, corresponding to $y^+ = 48.4$. The coherence and cross-correlation measurements have a reference point, also referred to as the fix-point, which is located at the root of the single-serrated, DRooTES and slit TEs, as shown in Figure 5.2. The corresponding reference-point is also the same for the baseline TE. A stationary-probe was positioned at the reference point, and a traversing-probe was positioned in line at the closest distance between the hot-wire probes at $\Delta z = 0.5$ mm. The unsteady velocity measurements were taken in the streamwise and/or spanwise direction by the traverse mount probe, as indicated in Figure 5.2. The closest distance when the two probes met is about 0.5 mm. Note that the possible thermal interference when the probes are the closest against each other will not affect the coherence and cross-correlation results. These two-point measurements were conducted on both the suction and pressure sides of the aerofoil.

The post-analysis of the unsteady streamwise velocity focused on the evaluation of the coherence and cross-correlation. The coherence examines the "similarity" between two points in a frequency domain, which is defined as:

$$\gamma_i^2(f) = \frac{|V_{xy}(f)|^2}{V_{xx}(f)V_{yy}(f)},\ i = x, z \tag{5.7}$$

where $V_{xy}(f)$ is the cross-power spectra density between the stationary and non-stationary velocity fluctuations measured by the hot-wire probes, and $V_{xx}(f)$ and $V_{yy}(f)$ is the auto-power spectra density of the stationary and non-stationary velocity fluctuations, respectively. The index $i = x$ and z is to differentiate the coherence in the streamwise and spanwise directions, respectively. The cross-correlation examines the time lag of two signals, which is defined as:

$$R_{xy}(m) = E\{x_{n+m}\, y_n^*\} E\{x_n y_{n-m}^*\}, \tag{5.8}$$

where x_n and y_n are the jointly stationary random processes, $-\infty < n < \infty$, $-\infty < m < \infty$, and $E\{\cdot\}$ is the expected value operator.

5.3 Results and Discussion

5.3.1 Characteristics of the baseline aerofoil noise radiation

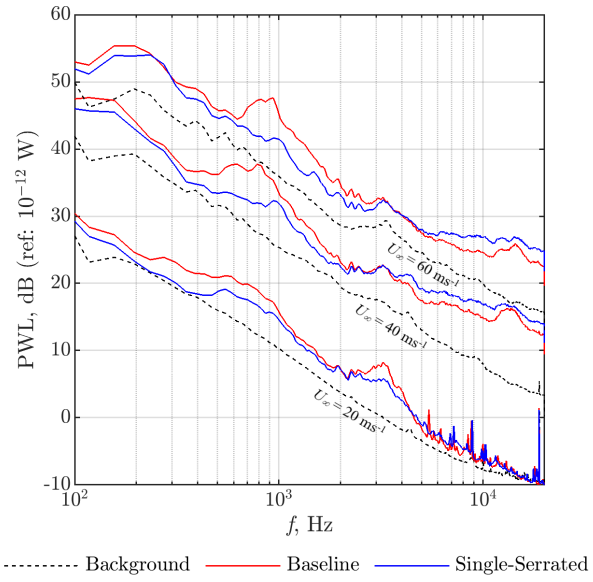

Figure 5.3: Comparison of the PWL, dB between the baseline TE ($H = 15$ mm), straight-serrated TE ($H = 30$ mm and $\lambda = 3$ mm), and background noise at $U_\infty = 20$, 40 and 60 ms^{-1}.

Comparison of the Sound Power Level (PWL) between the background noise (mostly the jet noise), the baseline and straight-serration aerofoil is shown in Figure 5.3. Similar to the results presented by Vathylakis *et al.* [129], the background noise is quieter than the aerofoil self-noise across a large range of frequency. This enables a meaningful quantification of the level of noise reduction achieved by the TE add-on. For example, in Figure 5.3, the straight-serration can demonstrate noise reduction up to 6 dB across the low-to-mid frequencies, $f = 100$ Hz to $f = 2$ kHz, in comparison to the baseline TE. However, at the mid-to-high frequencies, $f > 2$ kHz, in some cases the straight-serration produces higher broadband noise levels than the baseline TE. The same outcomes regarding the noise reduction at the low-to-mid frequencies and noise increases at the mid-to-high frequencies are also reported by Gruber [57] and Vathylakis *et al.* [130].

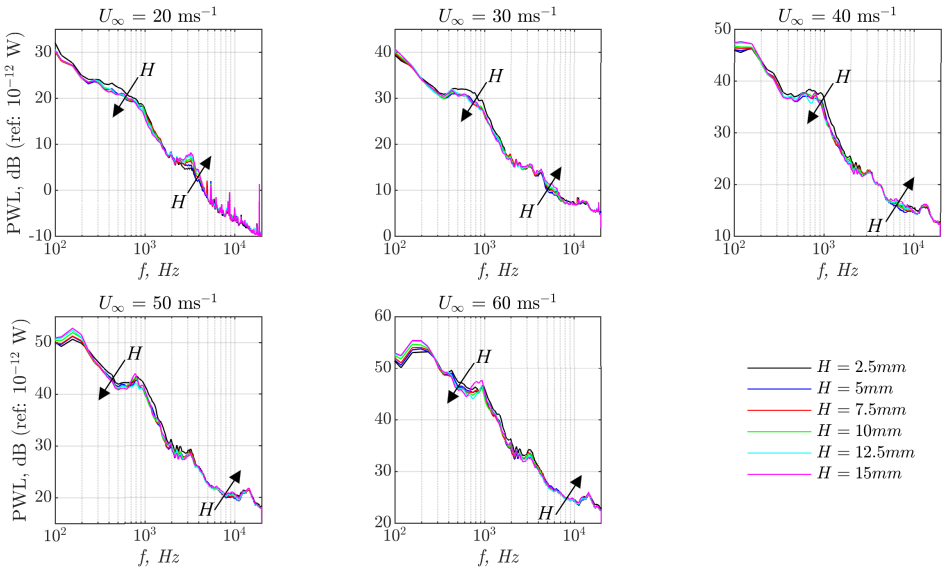

Figure 5.4: Comparison of the PWL, dB, of baseline TE noise at different amplitude 2.5 mm $\leq H \leq$ 15 mm at 20 ms^{-1} $\leq U_\infty \leq$ 60 ms^{-1}.

A study is performed to establish the effect of the flat plate length, H, for the baseline TE, on the aerofoil self-noise radiation. Figure 5.4 presents the PWL spectra of the baseline TEs at different inflow velocities: 20 ms^{-1} $\leq U_\infty \leq$ 60 ms^{-1}, when the H is varied between $H = 2.5$ mm and $H = 15$ mm, at intervals of $H = 2.5$ mm. The results clearly demonstrate that the addition of the add-on flat plates (no serration) can already achieve broadband noise reduction up to 3 dB at all inflow velocities investigated here across the low-to-mid frequency region. Generally speaking, the larger the flat plate length, H, the lower level of the broadband noise radiation at this frequency range. However, the trend reverses at the mid-to-high frequency region. As the H increases, the larger level of broadband noise radiation can be observed. Both trends described

above are also reported by Vathylakis *et al.* [130].

Self-noise radiation can be a function of the boundary layer properties near the flat plate TE. However, as one would expect the edge boundary layer to become thicker when H increases, the increase in size of the largest eddy scale in the boundary layer would normally translate into increase of noise level at low-to-mid frequency and reduction in the mid-to-high frequency noise levels. This reasoning, however, contradicts the measured noise spectra in Figure 5.4. This implies that the change in noise characteristics simply by adding straight flat plate could be caused by the alteration in the blade loading. The boundary layers at the suction and pressure sides may not respond in the same way to the change in the overall blade loading. Therefore, it is possible that the combined eddy size from the suction and pressure sides at the vicinity of the TE is actually smaller as the H increases.

Another observation related to Figure 5.4 is the interplay between the freestream velocity, U_∞, and the radiated acoustic frequency, f, for a baseline TE. The figure shows as U_∞ increases, the frequency range at which noise increase and/or reduction occurs also increases. Therefore, the results confirm the hydrodynamic origin of the radiated noise at the frequency range of interest, which will be formed as the basis for comparison with the single-serrated, slit and DRooTES to be discussed next.

5.3.2 Single-Serrated Trailing Edge

Noise performance by the single-serrated trailing edge

A. Variation in the serration amplitude (H)

Before an in-depth discussion on the slit and DRooTES TEs, it is necessary to establish and discuss the noise performances of the straight-serrated TEs first. Figure 5.5 shows the PWL of the radiated noise spectra pertaining to the single-serrated TEs of different H, but all with a fixed serration wavelength $\lambda = 3$ mm. True to the entire inflow velocity range investigated here, the radiated noise by the single-serrated TE reduces as the serration amplitude H, increases. The largest $H = 30$ mm represents the most promising option for the straight-serration at low-to-mid frequencies, whereas the $H = 5$ mm is not desirable within the same frequency region. However, a straight-serration with a large H will also result in an increase in the broadband noise radiation at the mid-to-high frequencies. The noise performance trends in the low-to-mid, and mid-to-high frequency are exactly similar to the baseline case (see Figure 5.4), although the sensitivity of the noise radiation to the flat plate amplitude is greater for the serration case. Noise increase by the serrations at mid-to-high frequency is also reported by Gruber [57], Acre León *et al.*

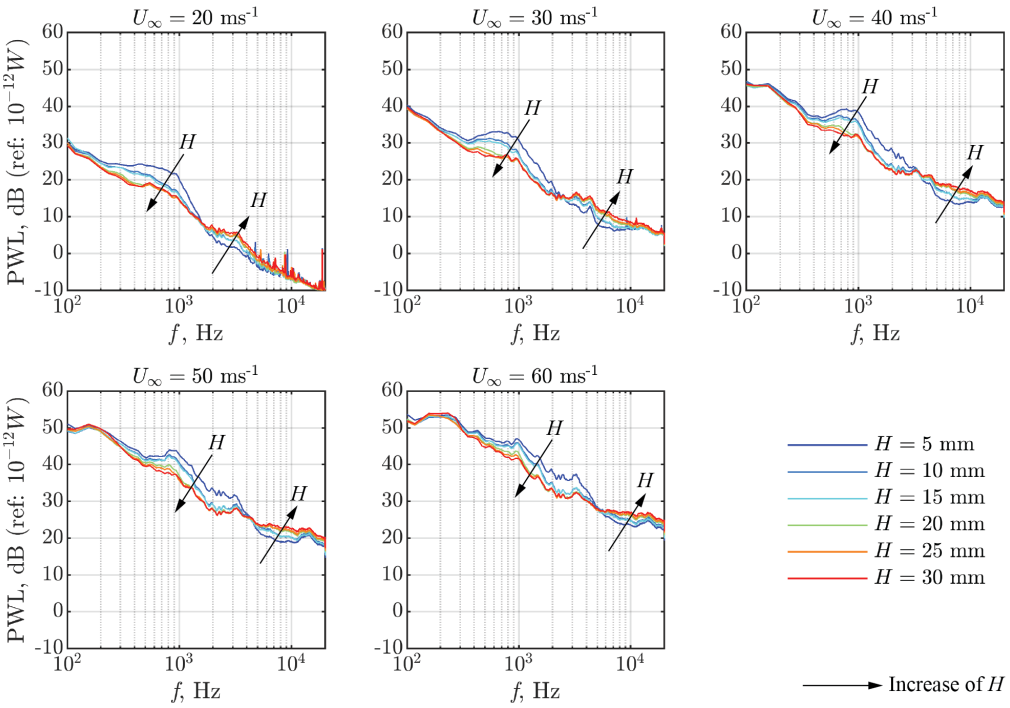

Figure 5.5: Comparison of the PWL, dB, for the single-serrated TEs of different H and $\lambda = 3$ mm at 20 ms^{-1} $\leq U_\infty \leq$ 60 ms^{-1}.

[1], Vathylakis *et al.* [130], Oerlemans *et al.* [100] and Woodhead *et al.* [134]. Furthermore, Oerlemans *et al.* [100] and Dassen *et al.* [36] suggest that the increase in high frequency noise is a result of the misalignment of the serrations with respect to the incoming mainstream flow angle, which will result in the cross-flow between the serrations. The resulting fluid-structure interaction then leads to the increase in high-frequency noise. The single-serrated TE with $H =$ 30 mm produces the greatest level of noise in the high-frequency range, whereas the opposite is true for the smallest H that produces the lowest level of noise.

B. Variation in the serration wavelength (λ)

After establishing earlier that a large serration amplitude, H, is favourable for broadband noise reduction, Figure 5.6 presents the acoustic spectra for the single-serrated TEs, all of which have a constant serration amplitude $H = 30$ mm, but with different serration wavelengths, λ. The results clearly show that at low-to-mid frequency ($f < 2.5$ kHz.) the one that performs the best is the smallest $\lambda = 3$ mm, with reduction up to 6 dB. As the serration wavelength increases, the level of noise radiation at this frequency range also increases. The one with the largest wavelength, $\lambda = 35$ mm represents the worst performance amongst the different serration wavelength. At mid-to-high frequencies, $f > 2.5$ kHz, an opposite trend emerges. The smaller

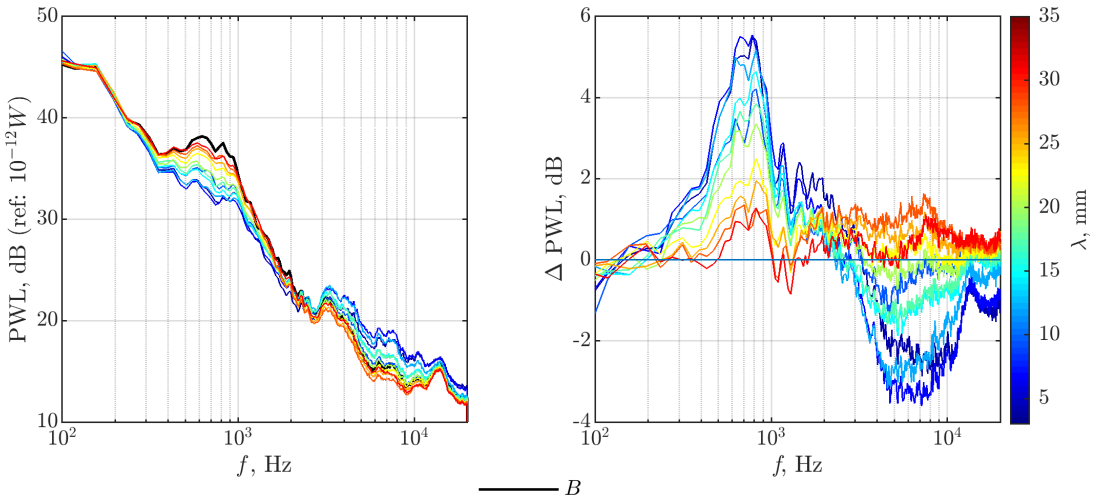

Figure 5.6: Comparison of the single-serrated TE at different λ with a constant H = 30 mm for: (a) PWL, dB and (b) ΔPWL, dB. U_∞ = 40 ms^{-1}.

serration wavelength tends to radiate larger level of noise than the baseline TE, up to ΔPWL = –4 dB. In contrast, noise radiation by the largest serration wavelength is even lower than the baseline TE, achieving noise reduction up to ΔPWL = 2 dB. As a reminder, ΔPWL is defined as the difference between sound power levels, as a function of frequency, between the baseline and either the single-serrated, slit or DRooTES TEs. Therefore a positive value of ΔPWL represents reduction in noise level, and the opposite is true for a negative value of ΔPWL that denotes noise level increases.

Thus, the following conclusion can be drawn: a smaller serration wavelength offers significant benefits at reducing noise level at low-to-mid frequencies, while a larger serration wavelength is desirable to reduce noise levels at mid-to-high frequencies. The results in Figure 5.6 follow largely the same trend as Gruber [57]. The different sensitivities of the noise radiation with respect to the λ between the low-to-mid and mid-to-high frequencies mean that there should be an intermediate configuration of the single-serrated TE where the ΔPWL remains positive (i.e. noise reduction) throughout the frequency range. Indeed, this is the case when λ is around 15 mm.

C. Quantification of the noise reduction in non-dimensional frequency – effect of the *H*

Figure 5.7 presents the difference in the sound power level ΔPWL between the baseline and single-serrated TEs in a non-dimensional frequency, $St = {}^{fH}/_{U_\infty}$, where St is the Strouhal number. In the context of adopting H as the scaling factor, the results demonstrate that the noise

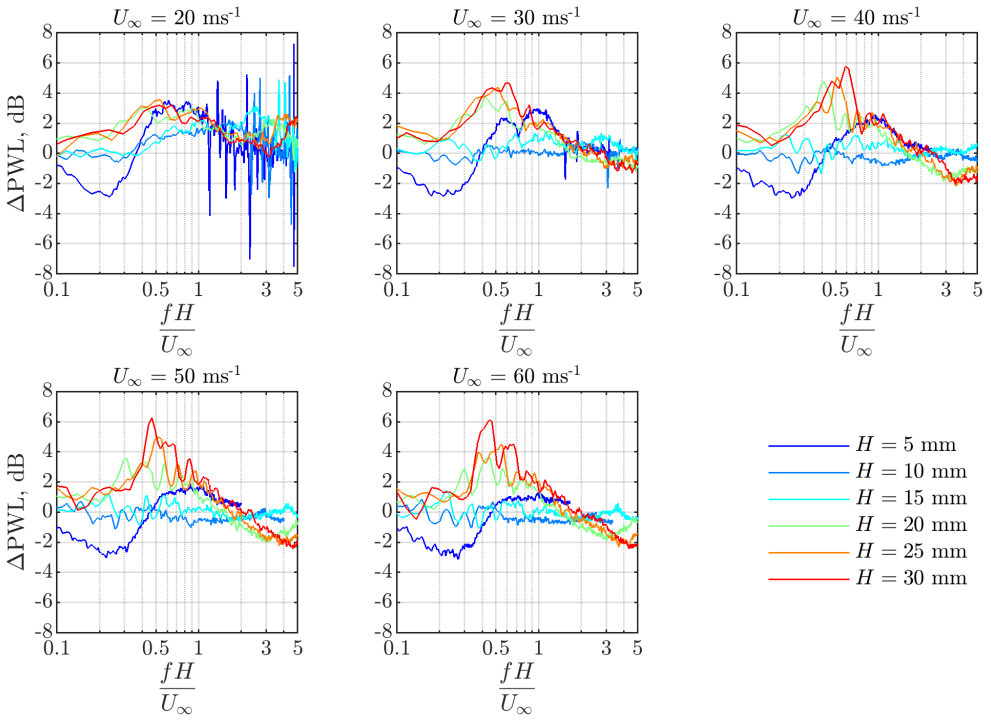

Figure 5.7: Comparison of the ΔPWL, dB, between the baseline and single-serrated TEs at λ = 3 mm and 20 ms^{-1} $\leq U_\infty \leq$ 60 ms^{-1} on the non-dimensional frequency.

reduction achieved by the single-serrated TE has no relationship with the phase cancellation (or destructive interference) between the serration tip and root. This is demonstrated by the discrepancy of various peaks ΔPWL scattered over a wide range of non-dimensional frequencies, between St = 0.6 and 1, at different H. Furthermore, at U_∞ = 20 ms^{-1}, the single-serrated TE exhibits no distinctive maximum noise reduction peaks.

Figure 5.8 shows the contour maps of the ΔPWL against f and H achieved by the single-serrated TE at various U_∞. The results demonstrate that noise reduction achieved by the single-serrated TE cannot be characterised by the non-dimensional frequencies, shown by the black lines representing St = 0.5. It is worth noting that the majority of the broadband noise reduction achieved by the single-serrated TE occurs at $H \geq$ 20 mm. Therefore, the noise reduction mechanism by the destructive interference, as described in Eqn. 5.3, cannot be applied to the single-serrated TE. In other words, the sawtooth tip is unlikely to be a noise source.

Flow field analysis of the single-serrated TE

Figure 5.9 present the streamwise coherence, calculated by Eqn. 5.7, for the single-serrated TE of H = 15 mm and λ = 3 mm between the root and downstream locations along the

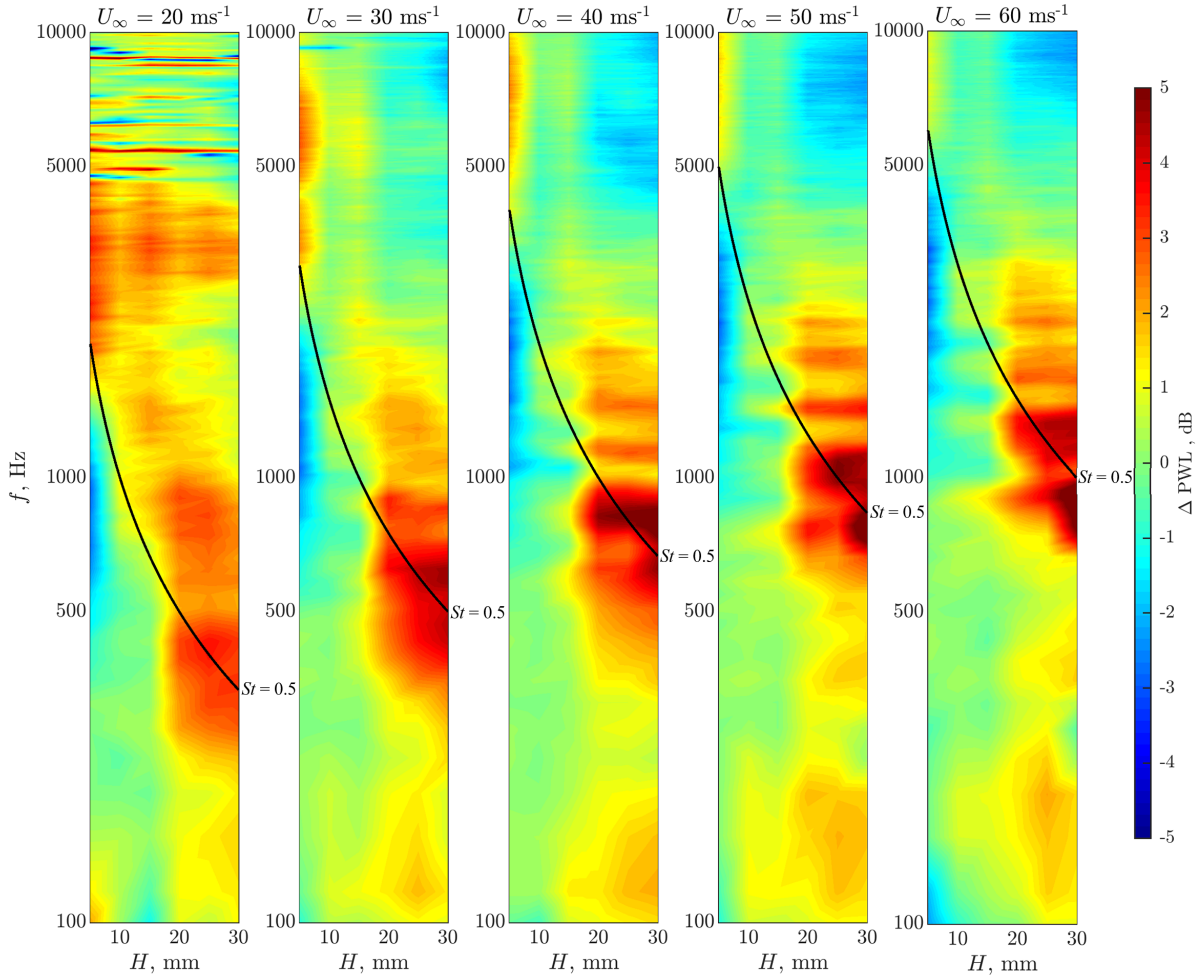

Figure 5.8: Contour maps of the ΔPWL, dB, between the baseline and single-serrated TEs in the domains of H and f, at 20 ms^{-1} $\leq U_\infty \leq$ 60 ms^{-1}. The serration all has the same λ = 3 mm.

oblique edge of the serration on the pressure and suction surfaces (represented by the blue line in Figure 5.2). The corresponding streamwise coherence for the baseline TE are also included for comparison. The figure is split into a number of sub-figures, each represents the variation of coherences pertaining to a particular ΔH, which is defined as the longitudinal distance between the serration root and a point in the oblique edge. The following summarises the observation in Figure 5.9:

1. When ΔH is small, a reasonably large level of the coherence can be observed at low frequency, which will then decay to zero as the frequency increases. This is true for both the baseline and single-serrated TEs.

   (a) The coherence levels at the pressure side are usually larger than those on the suction side. This is true for both the baseline and single-serrated TEs.

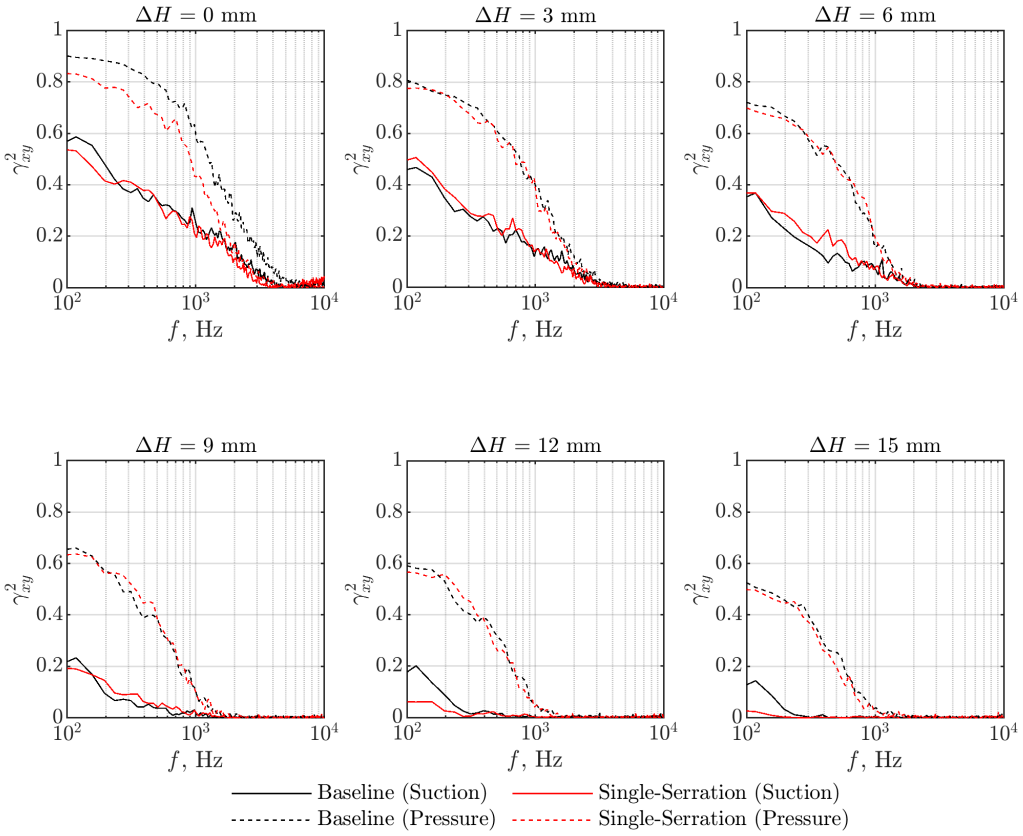

Figure 5.9: Comparison between the baseline and single-serrated TEs for the coherence, γ^2_{xy}, in the streamwise direction between root to tip where H = 15 mm and λ = 3 mm, at U_∞ = 30 ms^{-1}.

(b) The coherence levels attained by the single-serrated TE, at both the suction and pressure sides, are generally lower than that those attained by the baseline TE.

2. As ΔH increases, the overall level of the coherence decreases. It also reaches zero level faster in the frequency domain.

(a) Similarly, the coherence levels at the pressure side are usually larger than those on the suction side. In extreme cases, such as the coherence between the root–tip (i.e. ΔH = 14 mm) of the single-serrated TE at the suction side, there is almost a complete loss in coherence across the presented frequency range.

(b) The difference in the coherence level between the baseline and single-serrated TEs is becoming less.

When $\Delta H = 0$, the coherence level should be unity across the entire f. When ΔH is non-zero, only the larger scale turbulent eddies (much larger than the ΔH) can still attain high

coherence level. However, the coherence level will exhibit an exponential decay with increasing f in conjunction with the smaller scale turbulent eddies at high frequency. Considering the same cascade of turbulent eddy scales, but this time subjected to a larger displacement between the reference point and the traverse point, i.e. larger ΔH, the overall coherence level will dissipate as well. The larger coherence level at the pressure side is due to the larger turbulent boundary layer thickness developed there. The above descriptions should explain most of the phenomena observed in Figure 5.9. In addition, the results also paint a preliminary picture of the change in turbulent eddies when a single-serrated TE is introduced. For both the suction and pressure sides, and the $\Delta H = 0.5$ mm case, the single-serration exhibits weakened coherence strength compared to the baseline case at most of the frequency. By $\Delta H = 6$ mm, the baseline and straight-serration begin to exhibit similar coherence level across the entire frequency for both the pressure and suction side. At $\Delta H = 15$ mm, the coherence on the suction side was seen to be completely dissipated for the single-serrated TE, although very low coherence level of about 0.1 can still be seen at low frequency $100 < f < 200$ Hz for the baseline TE. The coherence results for the single-serrated TE suggest a faster break-up and dissipation of the turbulent eddies across the oblique edge of the serration. This is caused by the geometrical features of the serration which have been shown to change significantly the flow characteristics at the TE. Furthermore, as far as the suction side is concerned, the lack of any coherence between the root and tip of the single-serrated TE confirms that there is no acoustical interference between them.

Using the same raw data, a cross-correlation analysis using Eqn. 5.8 can be conducted in the time domain. Figure 5.10 presents the contour maps of the cross-correlation coefficient R_{xy} as a function of ΔH and time lag on both the pressure and suction sides. The gradient of the dominant R_{xy} in each graph represents the convection velocity of the characteristic eddies, U_c. The results are summarised in Table 5.1. For the baseline TE, the convection velocity for the turbulent eddies at the suction and pressure sides are 57% and 86% of the local freestream velocities, respectively. However, for the single-serrated TE, the convection rate at the suction side decreases to 45%, whilst at the pressure side, the convection rate even surpasses the local freestream velocity to 90%. This, perhaps, is in line with Chong and Vathylakis [26], who hypothesise that the secondary flow structure in a form of pressure-driven vortices at the sawtooth edges would entail an accelerated flow at the pressure side, and a decrease in velocity at the suction side due to the formation of the streamwise vortices.

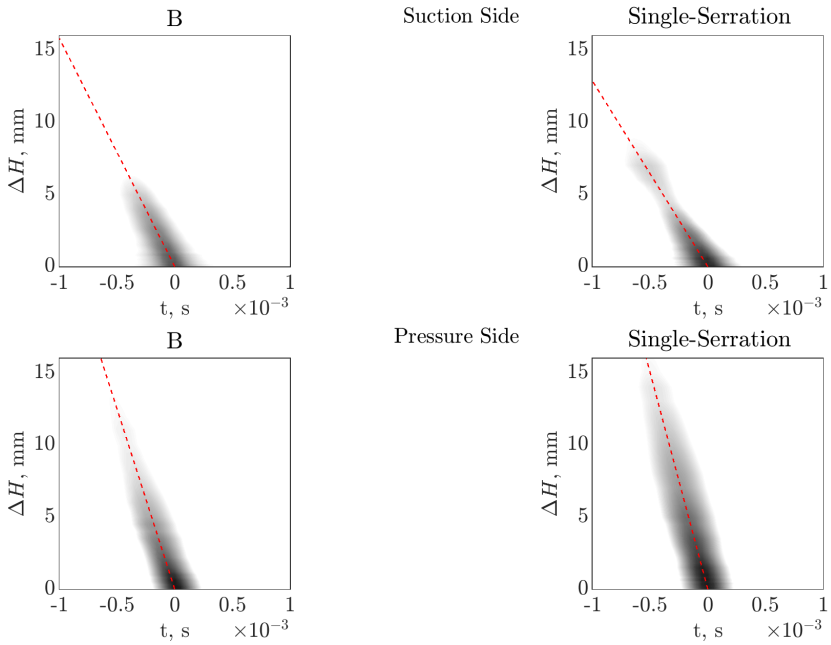

Figure 5.10: Comparison between the baseline and single-serrated TEs for the cross-correlation coefficients, R_{xy}, in the streamwise direction between root to tip where $H = 15$ mm and $\lambda = 3$ mm, at $U_\infty = 30$ ms^{-1}.

		U_c/U_∞
baseline	Pressure	0.86
	Suction	0.57
Single-serrated	Pressure	0.9
	Suction	0.45

Table 5.1: Results of the hydrodynamic disturbances convection velocity, U_c, for the baseline and single-serrated TEs on the pressure and suction sides.

The variation in the spanwise variation of coherence is also investigated here. Note that the measurement location is in accordance to the green lines depicted in Figure 5.2, i.e. they all correspond to the spanwise correlation length scale at the root region of the single-serrated, slit and DRooTES TEs, and the same location for the baseline TE. According to Amiet [4], the spanwise correlation length, l_z is one of the main components for the radiation of aerofoil self-noise into far field. The l_z can be determined from the coherence function $\sqrt{\gamma_z^2}$ of a hydrodynamic quantity over the span of the aerofoil near the TE, i.e.

$$l_z(f) = \int_0^\infty \gamma_z(\eta_z, f) d\eta_z \tag{5.9}$$

where η_z is the spanwise separation distance between two points. The original hydrodynamic quantities refers to the wall pressure fluctuations. However, this particular quantity is not available in the current study. The l_z is also difficult to be determined experimentally by the wall pressure fluctuations in the context of Eqn. 5.9. Instead, the boundary layer velocity fluctuation is used to calculate the l_z. Figure 5.11 (a) shows the l_z as a function of frequency for the baseline, single-serrated, slit and DRooTES TEs when $U_\infty = 30$ ms^{-1}. At the suction side of the aerofoil, the l_z between the baseline and single-serrated TEs are very similar at $f > 200$ Hz, despite the baseline counterpart would attain larger level of l_z at lower frequency. At the pressure side, the decays of the l_z with respect to the frequency are similar amongst the baseline, single-serrated, slit and DRooTES TEs, but the slit TE attains a larger values of l_z at $f < 2$ kHz. This implies that the incoming turbulent eddies have already been affected differently at the root region of the slit TE compared to others. The implication of which will be discussed in the later sections. Figure 5.11 (b) shows the decay of the frequency-integrated coherence in the spanwise direction. Again, with the exception of the slit TE, the other TEs are quite similar to each other.

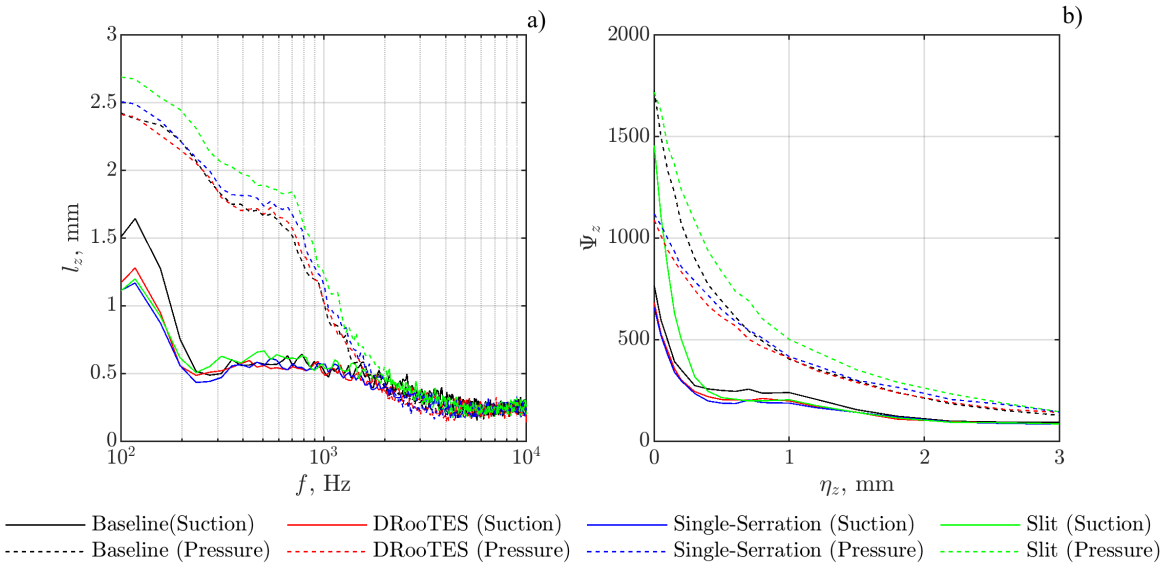

Figure 5.11: Comparison of the (a) spanwise correlation length scale l_z, and (b) spanwise overall coherence level Ψ_z , between the baseline, single-straight, slit and DRooTES TEs where $H = 15$ mm, $\lambda = 3$ mm, $W = 0.3$ mm at $U_\infty = 30$ ms^{-1}. Note that the measurement location is in accordance to the green lines depicted in Figure 5.2.

5.3.3 Slit Trailing Edge

Noise performance by the slit TE

A. Variation in the slit amplitude (H)

This section will examine the effect of slit TE on the broadband noise radiation, and most importantly, to determine whether the destructive interference mechanism in accordance to Eqn. 5.3 can be executed by the slit TE design. Figure 5.12 presents a comparison of the sensitivity of slit TEs at various H subjected to different inflow velocities, U_∞. The results clearly show that the slit TE can achieve significant level of broadband noise reduction. This is quite unprecedented because, to the best knowledge of the author, there is no documentation in the literature thus far that reports broadband self-noise reduction by a slit-typed TE.

The results are presented in this section. The section covers the noise measurements obtained by the baseline, Single-Serrations DRooTES and Slit TEs at U_∞ between 20 ms^{-1} and 60 ms^{-1}, with an interval of 10 ms^{-1}, at $\theta = 0°$.

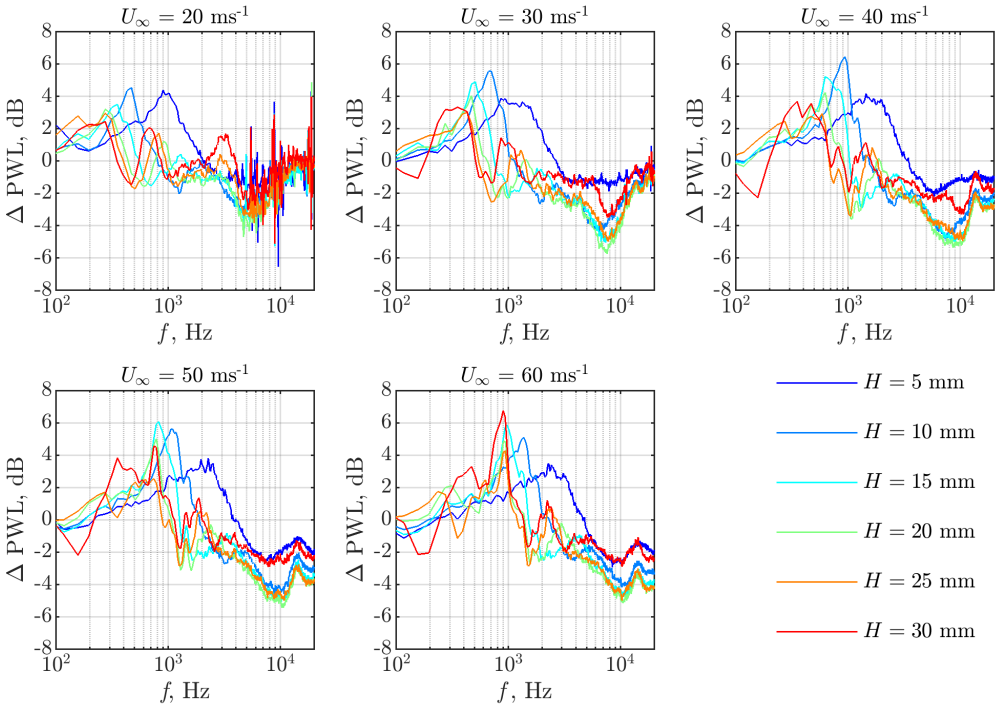

Figure 5.12: Comparison of the ΔPWL, dB, between the baseline and slit TEs at $\lambda = 3$ mm, $W = 0.3$ mm and 20 ms^{-1} $\leq U_\infty \leq$ 60 ms^{-1}.

Based on the results in Figure 5.12, the largest level of noise reduction (ΔPWL $\sim$ 7 dB) by the slit TE is noted at the low-to-mid frequency range. In contrast, noise increase can also be

observed at the mid-to-high frequencies (ΔPWL ∼ –5 dB). This particular trend is similar to the single-serrated TE discussed previously. In addition, distinctive peaks of noise reduction level ΔPWL achieved by the individual slit TEs appear not to follow a trend of slit amplitude H across various U_∞. Rather, the frequency pertaining to these ΔPWL peaks, f_{peak}, would follow the below relationships:

1. $f \propto U_\infty$
2. $f \propto \frac{1}{H}$

The first relationship is caused by the hydrodynamic origin of the radiated self-noise, where a certain type of the Strouhal number dependency is expected. The second relationship is very unique, and is not observed in the single-serrated TE case. This prompts the following question: *can f_{peak} be decided by the slit amplitude, H?*

B. Quantification of the noise reduction in non-dimensional frequency – effect of the *H*

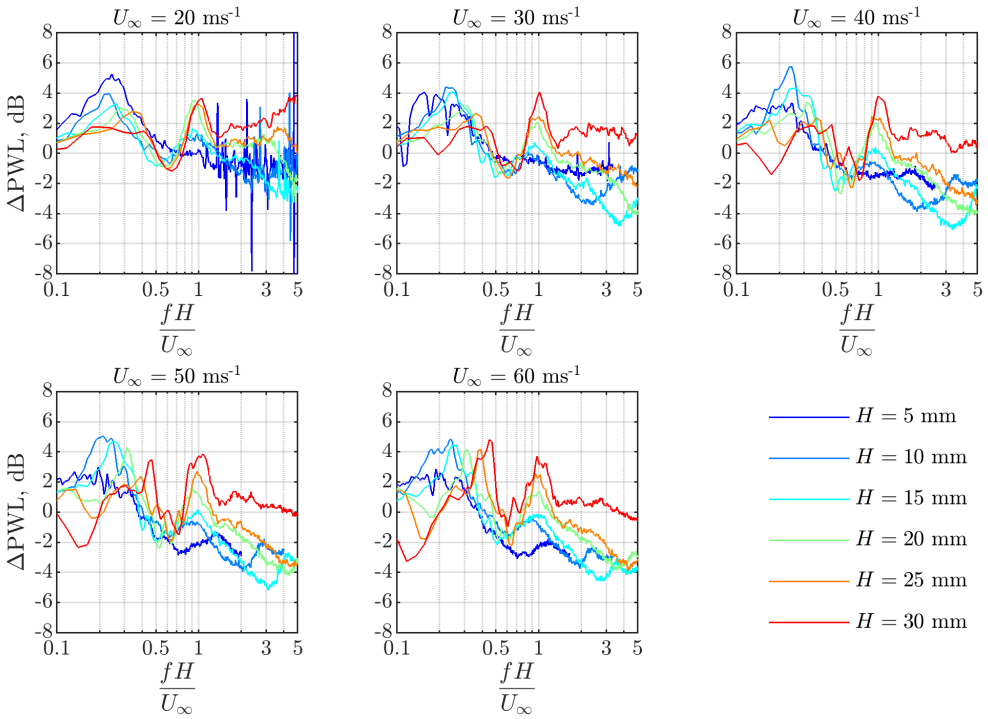

Figure 5.13: Comparison of the ΔPWL, dB, between the baseline and slit TEs at λ = 3 mm, W = 0.3 mm and 20 ms^{-1} ≤ U_∞ ≤ 60 ms^{-1} on the non-dimensional frequency.

Non-dimensionalising the frequency against the broadband noise reduction by the slit TE could be a first step to answer the question posted in the previous section. Figure 5.13 compares the ΔPWL by the slit TEs of $5 \leq H \leq 30$ mm, all fixed at $\lambda = 3$ mm, $W = 0.3$ mm and subjected to 20 ms^{-1} $\leq U_\infty \leq$ 60 ms^{-1} when the non-dimensional frequency is defined as $St = \frac{fH}{U_\infty}$. The ΔPWL spectra in Figure 5.4 all exhibit a similar trend: two peaks and a trough. The first peak takes place at around $St \approx 0.3$ for almost the entire slit amplitudes H (except for the $U_\infty = 60$ ms^{-1}, where a slight fluctuation of Strouhal number can be seen). The second peak occurs at $St \approx 0.9$—1, while the trough occurs in between the peaks, at $St \approx 0.6$. Setting aside for the time-being the numerical accuracy of these Strouhal number representations, the collapses in the first and second peaks, as well as the trough, already indicate the dominance of the acoustical destructive and constructive mechanisms in the slit TE.

In theory, a perfect acoustical destructive interference occurs when the acoustic radiations are at 180° out-of-phase between two sources, resulting in cancellation of the acoustic radiation. This is illustrated in Figure 5.1 which showcases the initial hypothesis of destructive interference between two sources at the root and tip of the slit TE. This means that the non-dimensional frequency for the first destructive interference, defined in Eqn. 5.3, should be equal to 0.5. However, as discussed earlier, the first peak ΔPWL takes place at around $St \approx 0.3$, which deviates quite a bit with respect to the theoretical Strouhal number $St = 0.5$ pertaining to the 180° out of phase cancellation between the two sources (root and tip). As already mentioned, all the peaks ΔPWL pertaining to the slit configurations are followed by a significant dip in ΔPWL (noise increase) at $St \approx 0.6$, which is caused by the constructive interference (360° phase angle) between the sources of the slit TEs. A second destructive interference occurs at $St \approx 0.9$-–1. Three factors that potentially affect the value of the non-dimensional frequency are:

1. Turbulent eddies scatter into pressure waves in close proximity to the roots, not exactly at the root, which can affect the "true" longitudinal displacement between roots and tips of the slit, i.e. the H.

2. Incorrect use of the inflow velocity U_∞ as the scaling factor for the Strouhal number. Rather, the turbulent eddies convection velocity should be adopted.

3. An additional factor affecting the convection speed of the turbulent eddies due to the presence of secondary flows (e.g. the cross-flow within the slit). More detailed discussion on this flow phenomenon is documented later in this chapter, as well as in Chapter 6.

The first factor can be considered as minor, but the second and third factors are likely to be significant. Further investigation has been conducted, and the outcomes will be discussed in Section 5.3.3.

C. Variation in the slit wavelength (λ), but with constant width of slit root (W)

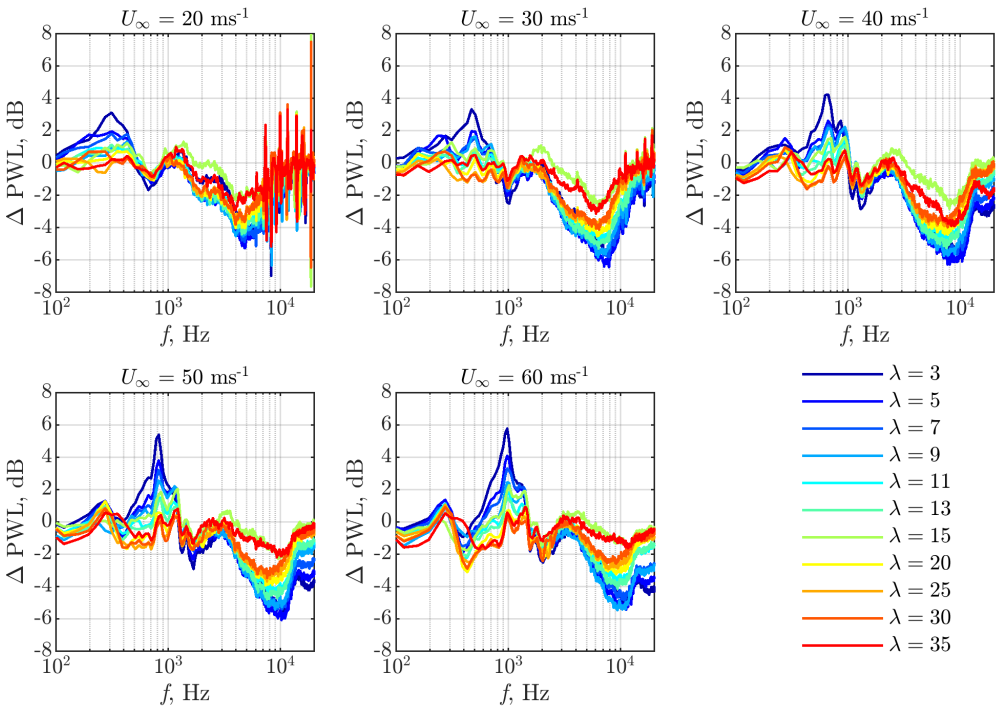

Figure 5.14: Comparison of the ΔPWL, dB, between the baseline and slit TEs at $W = 0.3$ mm, $H = 15$ mm and $20 \leq U_\infty \leq 60$ ms^{-1}.

This section investigates the effect of the slit wavelength, λ to the radiated far field noise. Figure 5.14 presents the ΔPWL spectra produced by slit TEs of 3 mm $\leq \lambda \leq$ 35 mm, with a fixed slit width, $W = 0.3$ mm, and $H = 30$ mm. No attempt is made to non-dimensionalise the frequency by the slit amplitude as per the previous practice because the H is constant. Due to the fixed value of the W, essentially, λ measures the number of slits per unit span. The smaller the value of λ, the more number of slits exists per unit span, and vice versa. The results clearly demonstrate that λ plays a significant role in the noise characteristics of the slit TEs. In what follows, the terms "low-to-mid" and "mid-to-high" do not refer to a specific frequency range, as they will shift simultaneously when the inflow velocity increases. Rather, they are qualitative terms simply used to differentiate a specific pattern and characteristic in the ΔPWL spectra. Amongst all the slit TEs, the most optimal configuration for the low-to-mid frequency region relates to the $\lambda = 3$ mm case where the level of noise reduction improves with the inflow velocity,

from 3 dB (20 ms^{-1}), to 4.2 dB (40 ms^{-1}) and then 6 dB (60 ms^{-1}). This is a significant departure from the conventional serrated TE where the level of broadband noise reduction is generally found to deteriorate with the inflow velocity. When λ increases (i.e. less number of slits per unit span), the level of noise reduction at the same frequency region becomes less prominent. This feature is generally the same for all the inflow velocities investigated here. The slit TE with the smallest $\lambda = 3$ mm, which is the quietest at the low-to-mid frequency range, undergoes a reversal at the mid-to-high frequency range by producing the largest noise increase up to 6.5 dB. In what follows, the mechanisms underpinning the ΔPWL behaviours at the "low-to-mid" and "mid-to-high" frequency ranges, respectively, will be discussed next.

At $U_\infty = 30$ ms^{-1}, the "low-to-mid" frequency region refers to $300 < f < 800$ Hz. Under the same range of frequency, the spanwise correlation length scale l_z for the slit TE is approximately 0.6212 mm (see in Figure 5.11a). As discussed previously, the l_z is an important hydrodynamic parameter for the radiation of self-noise. When the spanwise spacing between the slits, λ is small enough to fit multiple slits within a spanwise correlation length scale of the turbulent eddies, this greatly increases the number of the acoustical scattering points for the execution of the destructive interference at multiple points. As a result, a much-improved noise reduction performance can be achieved. Accordingly, if the spanwise spacing between the slits is too large, i.e. λ is large, the noise reduction performance will deteriorate due to the lower number of scatter points to facilitate the destructive interaction mechanism, and the returning to a straight TE (i.e. baseline) noise characteristic where the ΔPWL $\rightarrow 0$. A question was posted at the end of subsection A: *can f_{peak} be decided by the slit amplitude, H?* The results in Figure 5.14, though not directly answer the question, do provide another perspective whereby variation in the slit wavelength λ can only manipulate the level of the ΔPWL, but not the f_{peak}. This corroborates with the establishment so far that the main mechanism of destructive interference is responsible for the noise reduction for a slit TE. Although not shown here, when Figure 5.14 is re-plotted in a non-dimensional frequency $St = \frac{fH}{U_\infty}$, the ΔPWL peaks correspond to the destructive interference occur at $St = 0.36$ and 1.05, and the ΔPWL troughs by the constructive interference at $St = 0.75$ for all cases. Interestingly, the effect of the acoustic interference mechanism is still observable at the largest λ cases, although it is also significantly weakened in comparison to the smallest λ cases.

A slit TE with a small λ, in what used to be a favourable configuration at the "low-to-mid" frequency region, can abruptly become prone to incurring significant noise increase at the "mid-to-high" frequency region. The underpinning mechanism is related to the cross-flow across the slit from the pressure side to the suction side. This flow phenomenon has been demonstrated

in detailed from the numerical study in Chapter 6. With the slit width, W relatively small in this case, significant fluid-structure interaction between the cross-flow and the slit edges will produce the extraneous high frequency noise. This is analogous to blowing across a hair comb perpendicularly, where the larger number of the fringes/slits it contains, i.e. small λ, the higher level of the high frequency noise it produces.

D. Variation in the width of slit root (W), but with constant slit wavelength (λ)

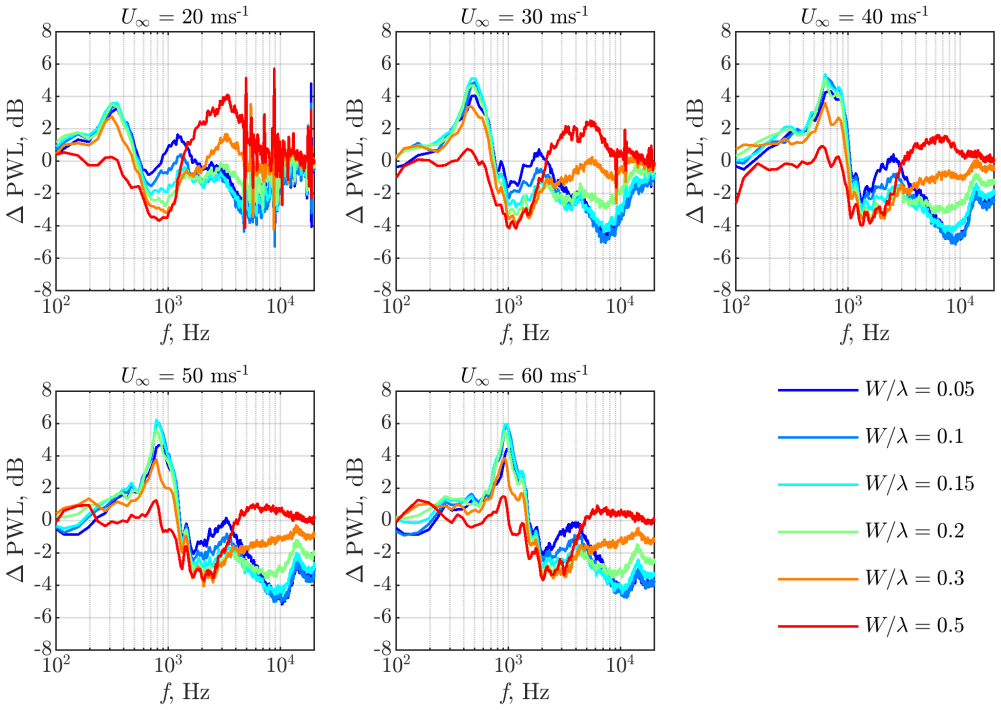

Figure 5.15: Comparison of the ΔPWL, dB, between the baseline and slit TEs at λ = 3 mm, H = 15 mm and 20 ms^{-1} $\leq U_\infty \leq$ 60 ms^{-1}.

This section will investigate the exclusive effect of the width of the slit root, W to the self-noise radiation of the slit TE. Figure 5.15 presents a comparison of the ΔPWL spectra for the slit TEs at different aspect ratios W/λ, where λ was kept constant at 3 mm. The slit amplitude H is 15 mm. The results clearly demonstrate that W/λ is the most optimal between 0.1 and 0.2 at the low-to-mid frequency region across all the inflow velocities. Amongst all the cases, the best performer is $W/\lambda = 0.15$ with reduction up to 6 dB. Below this optimal range, it is thought that the slit width is too small to be an effective scatter source for the incoming turbulent eddies. Within the optimal range, the slit width geometry will become more compatible with the spanwise correlation length scale of the turbulent eddies, resulting in an increase in the source

strength between the root and tip. Above the optimal range, the widened slit width at the root region slowly reverts to a straight TE noise mechanism, which in turn diminishes the noise reduction capability. When Figure 5.15 is re-plotted in a non-dimensional frequency $St = \frac{fH}{U_\infty}$ (not shown here), the ΔPWL peaks correspond to the destructive interference occur at St = 0.25 and 1, and the ΔPWL troughs by the constructive interference at $St = 0.5$ for all cases. This again demonstrates that the frequency targeting capability for the noise reduction by the acoustical destructive interference mechanism is only governed by the H, and is insensitive to λ and W.

Despite not achieving meaningful noise reduction at the low-to-mid frequency region by the largest $^W/\lambda = 0.5$ slit TE, it is the only configuration that is immune from the noise increase at the mid-to-high frequencies. In fact, it can even achieve a slight broadband noise reduction up to 4 dB at low U_∞. The smaller $^W/\lambda$ configurations that are otherwise effective at the low-to-mid frequency range now become the opposite at the mid-to-high frequency range, as they can produce quite significant noise increase. Considering that the noise mechanism of this frequency region is related to the cross-flow dynamics from the pressure side to the suction side (Chapter 6), the observation discussed above provides a hint that, under the same number of slits (i.e. λ is a constant), the contributing role of the cross-flow in the high frequency noise diminishes when W increases.

Based on the results presented thus far, the following statements can be summarised:

1. Small $^W/\lambda$ configuration (between 0.1 and 0.2) is desirable for broadband noise reduction at the low-to-mid frequency. This is to avoid the slit width becoming too compatible with the spanwise integral length scale of the turbulent eddies in the case of large $^W/\lambda$ configuration.

2. Large $^W/\lambda$ configuration is desirable to avoid noise increase at high frequency. As will be demonstrated in Chapter 6, the cross-flow is induced by the upward velocity components near the inner edges of the slit, Note that these upward velocity components will eventually form a pair of streamwise vortices at the suction side. When W is large, the expectation is that the induced velocity for the cross-flow across the slit will be weakened, thus minimises the high frequency noise radiation.

Flow field analysis of the slit trailing edge

After presenting all the noise characteristics pertaining to the slit TEs in the previous sections, the dominant effect of the acoustical interference mechanism (both destructive and constructive) in the noise radiation have been demonstrated. A simple analytical noise model based on this

mechanism has been developed in this study, where it can predict the f_{peak} accurately for various slit configurations. The detailed discussion will be provided in Section 5.3.3. Before that, it is necessary to resolve and reconcile the issue left in Section 5.3.3.B, i.e. the disparity of the theoretical and experimentally-observed non-dimensional frequencies St pertaining to the destructive and constructive interferences, respectively. More specifically, theoretical values of St = 0.5, 1.5, etc. for the destructive interference are observed in the experiment to be St = 0.3, 0.9, etc. Similarly, theoretical value of St = 1.0 for the constructive interference is observed in the experiment to be St = 0.6.

So far, the St is defined as $\frac{fH}{U_\infty}$. In Section 5.3.3.B, question was asked whether the blanket use of the inflow velocity U_∞ as the scaling factor for the Strouhal number is appropriate. The presence of a secondary flow structure at the suction side of the slit TE, and its possible interaction with the turbulent boundary layer, further raises question on the validity of such simple substitution. After all, the phase difference between the scattering at the two source locations, i.e. the slit root and tip, is dictated by the passing of the wall-bounded turbulent eddies, instead of the inviscid potential flow. These turbulent eddies should also contain a sufficient level of streamwise coherence as a priori for the destructive interference to be executed effectively. Therefore, the turbulent eddies convection velocity should be adopted in the definition of the Strouhal number St. To be more precise, the turbulent eddies convection velocity should take into account the possible interaction between the turbulent boundary layer and the secondary flow structures. In what follows, the analysis will be divided into three sub-sections to investigate the A) streamwise coherence at the slit proximity, B) boundary layer characteristics at the slit root, mid and tip regions, and C) the convection velocity of the turbulent eddies from the root to tip (baseline and slit TEs).

A. Streamwise coherence at the slit proximity

The measurement technique for the streamwise coherence γ_x^2 has already been discussed in Section 5.2. As a reminder, a reference "stationary" hot wire probe is fixed at the root region, while the "traversing" hot wire probe will move downstream in a straight line resulting in a streamwise distance of η_x (illustrated by the red line in Figure 5.2). The closet separation between the two hot wire probes is 0.5 mm, where the largest γ_x^2 value is measured. In this study, the streamwise coherence measurements were performed at the suction and pressure sides for both the baseline and slit TEs, who share the same H at 15 mm. In addition, the slit TE has a wavelength λ = 3mm. The inflow velocity is set at U_∞ = 30 ms^{-1}. It should be emphasised that the presentation of the coherence function using the fluctuating velocity within the boundary

layer is entire valid for the investigation of the acoustical interference mechanism.

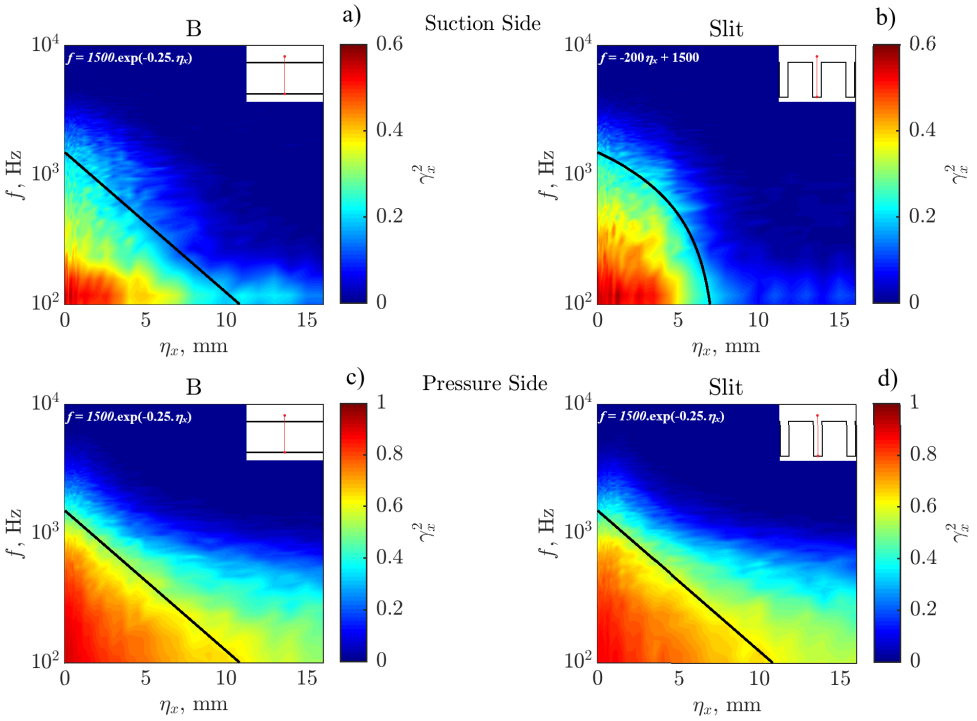

Figure 5.16: Comparison between the baseline and slit TEs for the γ_x^2 (streamwise coherence) where $H = 15$ mm and $\lambda = 3$ mm, at $U_\infty = 30$ ms $^{-1}$.

Figure 5.16 compares the γ_x^2 as a function of f and η_x, between the baseline and slit TEs at both the suction and pressure sides. In general, the coherence level is greater, and has an overall larger footprint in the f and η_x domains at the pressure side. This is due to the larger integral length scale of the turbulent eddies at the pressure side where the turbulent boundary layer is several times thicker than that on the suction side. For the baseline aerofoil, the results clearly show that the turbulent boundary layer has a prominent coherence at the low-to-mid frequency range, 100 Hz $< f <$ 3 kHz, for both the suction and pressure sides when $\eta_x \to 0$. Very low level of γ_x^2 is observed at higher frequency, which might indicate a limitation on the destructive interference mechanism on the very high frequency noise targeting. On the suction side, as the η_x increases, the γ_x^2 will undergo a global exponential decay in the frequency against the streamwise distance, $f \sim \mathrm{e}^{-0.25\,\eta_x}$, as indicated in the figure (note the use of logarithm scale at the ordinate of the figure). According to the exponential curve, there should be negligible γ_x^2 level for $f \geq 100$ Hz when $\eta_x \geq 10$ mm. Interestingly, remnants of the γ_x^2 at very low frequency ($\sim$ 100–200 Hz) extends up to $\eta_x = 15$ mm, i.e. the location of the TE. On the pressure side, the decay rate of the turbulent eddies is also very similar to the suction side. At the TE, i.e. at $\eta_x = 15$ mm, γ_x^2

as high as 0.45 is achieved at $f \approx 700$ Hz. Significant footprint of the γ_x^2 can still be found at $\eta_x > 15$ mm.

For the slit TE, a somewhat different picture is observed at the suction side. The decay of the γ_x^2 can no longer be adequately described by an exponential function, where a linear decay function becomes more appropriate at $f = -200\eta_x + c$, where c is a constant. The core level of the γ_x^2 at $\eta_x < 5$ mm is evidently extended to a larger frequency range in comparison to the baseline TE. This illustrates that the cascading scales of the turbulent eddy at close proximity to the slit root region have deviated from the otherwise nominal turbulent boundary layer. A further anomaly is observed for the abrupt end of the γ_x^2 footprint at the entire frequency range when $\eta_x < 7.5$ mm, i.e. at the mid region of the slit. It is obvious that the presence of the cross flow (from the pressure side to the suction side), and the ensuing formation of a pair of secondary flow structures in the form of counter-rotating streamwise vortices, are responsible for the change in the γ_x^2 behaviours for the slit TE at the suction side. An important physics of these pressure-driven streamwise vortices, which will be comprehensively discussed in the numerical study in Chapter 6, and in the experimental boundary layer analysis in the sub-section 5.3.3.B, is their uplifting away from the wall when propagating towards the slit tip. The stationary and traversing hot wire probes used for the coherence measurement both have sensing length of approximately 1.25 mm. At the slit root region, where the streamwise vortices are still relatively close to the suction side wall surface (see Figure 6.11 in Chapter 6), signals measured by the probes would be dominated by the dynamics of these streamwise vortices. This explains the change in the γ_x^2 behaviours at low level of η_x. As the η_x becomes larger, these streamwise vortices will be lifted up, and in the process transporting the turbulent kinetic energy away from the wall surface (see Figure 6.13 in Chapter 6), beyond the sensing element of both the hot wire probes. This could explain the rapid decay of the γ_x^2 on the suction side of the slit TE. Because the turbulent kinetic energy is no longer at close proximity to the wall surface when reaching the slit tip, one might question the effectiveness of the acoustical interference mechanism on the suction side. On the other hand, the γ_x^2 characteristics at the pressure side of the slit TE is very similar to that of the baseline counterpart. This suggests that the turbulent boundary layer is not affected significantly by the slit, as evident in the boundary layer profiles to be presented in the sub-section 5.3.3.B. Most importantly, scattering of pressure waves at the slit root and tip, respectively, is expected to be in coherent at the pressure side to execute the acoustical interference mechanism.

B. Boundary layer characteristics at the slit root, mid and tip regions

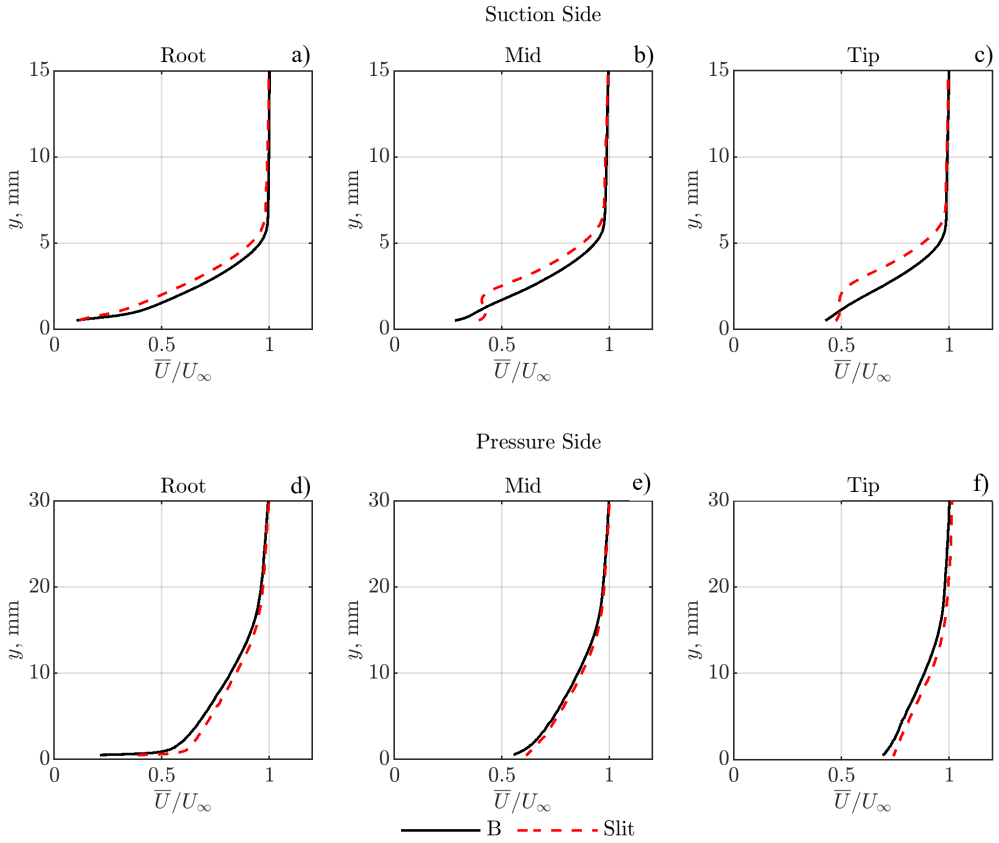

Figure 5.17: Comparison of the mean velocity profiles for the baseline and slit TEs at three downstream locations: root, mid and tip on the suction and pressure surfaces where $H = 15$ mm and $\lambda = 3$ mm, at $U_\infty = 30$ ms^{-1}.

The next investigation, Figure 5.17, is to examine the effects of the mean velocity boundary layer profile for the baseline and slit TEs at various locations near the TE: root ($x/c_0 = 0.91$), mid ($x/c_0 = 0.95$), and tip ($x/c_0 = 1$). Table 5.2 presents the measured boundary layer parameters corresponding to the above locations for both the baseline and slit TEs. On the suction side of the root region, the boundary layer profile pertaining to the slit TE begins to show a less stable characteristic than the baseline TE at the exact same location. This condition quickly deteriorates at the mid and tip regions for the slit TE. In what would otherwise be the turbulent boundary layer profiles as far as the baseline case is concerned, the mid and tip locations of the slit TE are now showing inflection points. As will be shown in Chapter 6, the inflectional profile is the result of the coalescence of the vertically displaced (pressure side to suction side through the slit) secondary flow structures and the local turbulent boundary layer. The flow dynamics

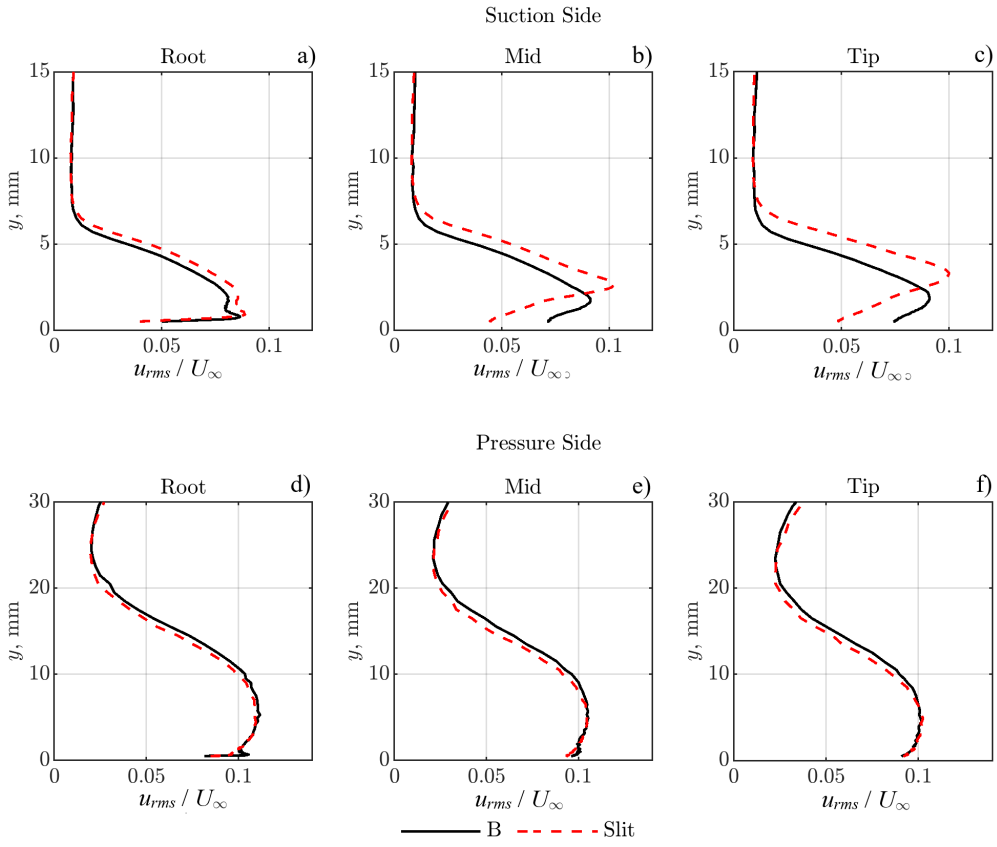

Figure 5.18: Comparison of the non-dimensional velocity fluctuation (turbulence intensity, I) between the baseline and Slit TEs for: a), b), c) suction side and d), e), f) pressure side at U_∞ = 30 ms^{-1}.

can be further examined from the turbulence intensity profile, which is shown in Figure 5.18. For the root location on the suction side, the slit has an overall 1% higher level in turbulence intensity than the baseline across much of the boundary layer profile (from the near wall maxima until the freestream). Here, the turbulence maxima for the slit TE is slightly above the baseline counterpart. This upward tendency is exacerbated in the mid and root regions, where the upward displacement of the turbulence maxima is increased by a further 3 mm in the z direction. In addition, the turbulence level of the maxima is also elevated from 8% (baseline) to 11%. These turbulence maxima by the slit TE is only slightly higher than the inflectional point appearing in the mean boundary layer profile (see Figure 5.19). Because of the upward displacement of the turbulence maxima, the near wall turbulence intensity for the slit TE is relieved. In their efforts to reduce the TE broadband noise, Gerhard et al. [51] utilised the active flow control of wall blowing technique to manipulate the turbulent boundary layer. They observe an upward displacement of the turbulence maxima, as well as a slightly lower turbulence intensity at the

near wall region. This manipulated flow field is similar to the current case of the slit TE at the suction side. To some extents, it would be interesting to find out whether a passive slit TE can replicate the wall blowing effect in TE broadband noise reduction. This is not pursued in the current thesis.

On the pressure side, the boundary layer mean velocity profiles for both the baseline and slit TEs are significantly different in comparison to the suction side. Although at a geometrical AoA of zero degree, the level of pressure gradients experienced by both sides of the aerofoil are already markedly different due to the highly cambered configuration. The pressure side turbulent boundary layer is several times thicker than that developed on the suction side, thus illustrates the much greater level of the adverse pressure gradient experienced at the pressure side. At the root region, the near wall velocity excess for the slit TE is greater than the baseline profile. This might be due to the local acceleration of the leakage flow from the pressure side to the suction side. However, when proceeds to the mid and tip regions for the slit TE, the near wall velocity excess (in comparison with the baseline boundary layer profiles) becomes deficit. Cross-examination with the turbulence intensity profiles in Figure 5.18 shows that the turbulence intensity level for the slit TE at the tip region is greater than the baseline profile. Based on the available experimental data, it is difficult to draw a concrete conclusion of the underlying mechanism that causes such a development in the mean and turbulent velocity profiles at the pressure side of the slit TE. Nevertheless, it is worth pointing out that the effects observed on the suction side of secondary flow structure are not evident on the pressure side (e.g. no inflection profile is observed throughout the flow field at the pressure side of the slit TE). The flow dynamics at the pressure side of the slit TE should instead be regarded as the feeder for the secondary flow structures at the suction side. This, however, will be re-visited in Chapter 6 when the numerical flow results are analysed.

The dynamics of the secondary flow structures at the suction side can also be examined for their spectral characteristics. Figure 5.19 presents the contours of PSD of the fluctuating velocity within the boundary layer at the root ($x/c_0 = 0.91$), mid ($x/c_0 = 0.95$), and tip ($x/c_0 = 1$) for the baseline and slit TEs. On the suction side of the baseline TE, the dominant spectral feature of the turbulent boundary layer is up to $z = 5$ mm at the entire frequencies across the root, mid and tip locations. The most dominant PSD levels, shown by the black bold line in the figure, are found at the low-to-mid frequencies, $0.1 < f < 1$ kHz. In comparison, at the root of the slit TE, the most dominant PSD (shown by the filled yellow contour) encompasses a similar frequency–spatial domain as the baseline TE. However, at the mid location the most dominant PSD is elevated to 2.5 mm $\leq z \leq$ 4.5 mm. This upward trend continues until the tip location

Suction Side					
		Boundary Layer Thickness (δ)	Displacement Thickness (δ_1)	Momentum Thickness (δ_2)	Shape Factor
baseline	Root	7.5 mm	1.51	0.81	1.85
	Mid	7.5 mm	1.63	0.92	1.75
	Tip	7.5 mm	1.34	0.86	1.57
Slit	Root	7.5 mm	1.89	0.94	2.00
	Mid	7.5 mm	2.02	1.10	1.83
	Tip	7.5 mm	1.86	1.10	1.69
Pressure Side					
baseline	Root	30 mm	4.12	2.98	1.38
	Mid	30 mm	3.35	2.57	1.30
	Tip	30 mm	2.56	2.10	1.22
Slit	Root	30 mm	3.48	2.65	1.31
	Mid	30 mm	2.99	2.35	1.27
	Tip	30 mm	3.48	2.65	1.31

Table 5.2: Comparison the pressure and suction sides boundary layer parameters at various locations downstream of the baseline and Slit TE.

where the most dominant PSD is now at 3.0 mm $\leq z \leq$ 4.5 mm. One important observation is that the frequency range pertaining to these elevated dominant PSD in the slit TE at the mid and tip is markedly similar to those of produced by the baseline TE ($0.1 < f < 1$ kHz). This suggests that the turbulence maxima in Figure 5.18 for the slit TE at the suction side are originated from the near wall turbulence. The vertical displacement of the turbulence maxima is caused by the cross flow through the slit. Their turbulence level can be further enhanced by the instability mechanism of the inflectional point at close proximity. On the pressure side, both the baseline and slit's most dominant PSD are observed up to $z = 13$ mm across the low-to-mid frequencies, $100 < f < 700$ Hz. Generally, the spectral characteristics of the baseline and slit TEs at the pressure side are similar.

C. The convection velocities of the turbulent eddies from the root to tip (baseline and slit TEs)

As discussed in Section 5.3.3.B, the first peak of ΔPWL for the noise reduction is found to occur at around Strouhal number $St \approx 0.3$ in the experiment, which deviates quite a bit with respect to the theoretical value $St = 0.5$. Three possible factors have been proposed that could cause such a deviation. The first factor is related to the true scattering location of the turbulent

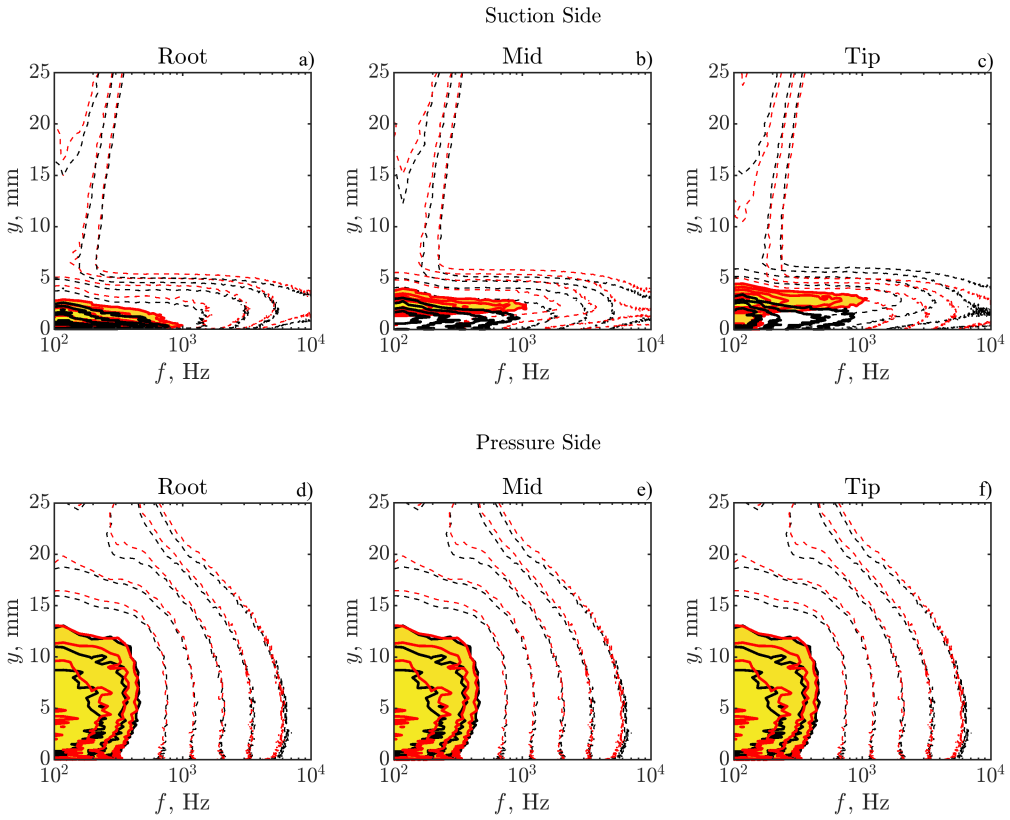

Figure 5.19: Comparison of the PSD for baseline (–) and Slit (–) TE at various location across the TE where fill (yellow region) for Slit and black bold line for baseline represents a specific PSD values; at $U_\infty = 30$ ms^{-1}; where baseline ($H = 15$ mm) and Slit ($H = 15$ mm, $W = 0.3$ mm and $\lambda = 3$ mm).

sources, while the second and third factors are related to the correct use of the velocity scale in the Strouhal number definition. In particular, the convection of the turbulent eddies should instead be used rather than the freestream velocity. This section aims to measure the convection velocity of the dominant turbulent eddies from the root and tip of the slit TE, on both the suction and pressure sides. The data used for this analysis is the same one used for the streamwise coherence study described earlier, but the analysis is performed at the time domain by calculating the cross-correlation coefficients between the velocity measured by the stationary hot wire probe (at the root location) and the traversing hot wire probe. The results are plotted in Figure 5.20 for both the baseline and slit TEs, each split into presentation for the suction and pressure sides. An arbitrary threshold is applied to separate the dominant cross-correlation coefficients from the non-dominant ones. The exact value of the threshold is not important as it will not affect the main purpose of this exercise, which is to calculate the gradient (i.e. the convection velocity U_c)

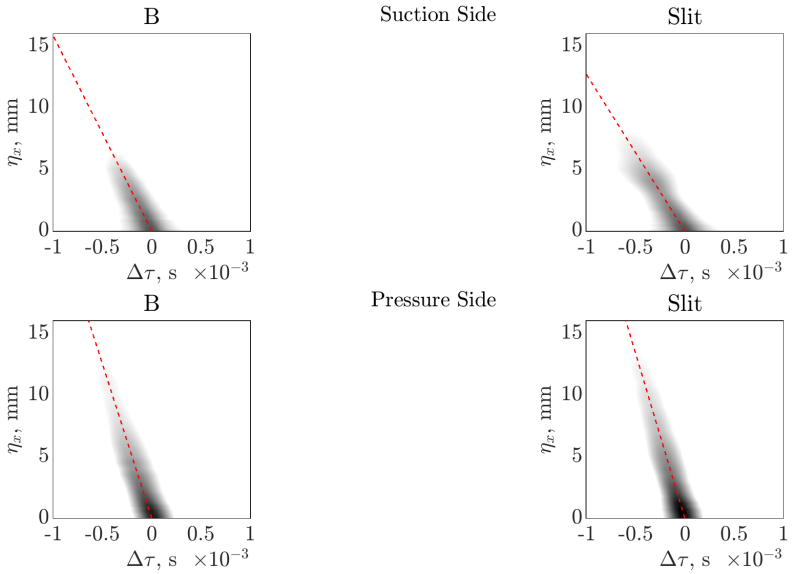

Figure 5.20: Cross-Correlation between the stationary and traverse in the downstream to obtain the convection velocity within the boundary layer for Slit $H = 15$ mm, $\lambda = 3$ mm and $W = 0.3$ mm, at $U_\infty = 30$ ms^{-1}.

in the form of $\eta_x/\Delta\tau$. Summary of the convection velocity as the fraction of the local freestream velocity U_∞ is provided in Table 5.3:

		U_c/U_∞
baseline	Pressure	0.86
	Suction	0.57
Slit	Pressure	0.86
	Suction	0.43

Table 5.3: Results of the convection velocities of the turbulent eddies for the baseline and slit TEs on the pressure and suction sides.

To some extents, the turbulent eddies described in the cross-correlation study share many similar characteristics as the turbulent spot, as the latter is sometimes called the "building block" of turbulent boundary layer. Gostelow *et al.* [55] compile the turbulent spot's convection velocity as a function of the pressure gradient parameter. They concluded that whilst the variation of the turbulent spot leading edge convection velocity with the pressure gradient is small, the TE convection velocity would reduce when the level of adverse pressure gradient increases. As demonstrated by the distribution of static pressure coefficient in Figure 6.8 of Chapter 6, the level of adverse pressure gradient near the aerofoil's TE suction side is significantly larger than that at the pressure side. This could explain the results in Table 5.3, which show that the convection

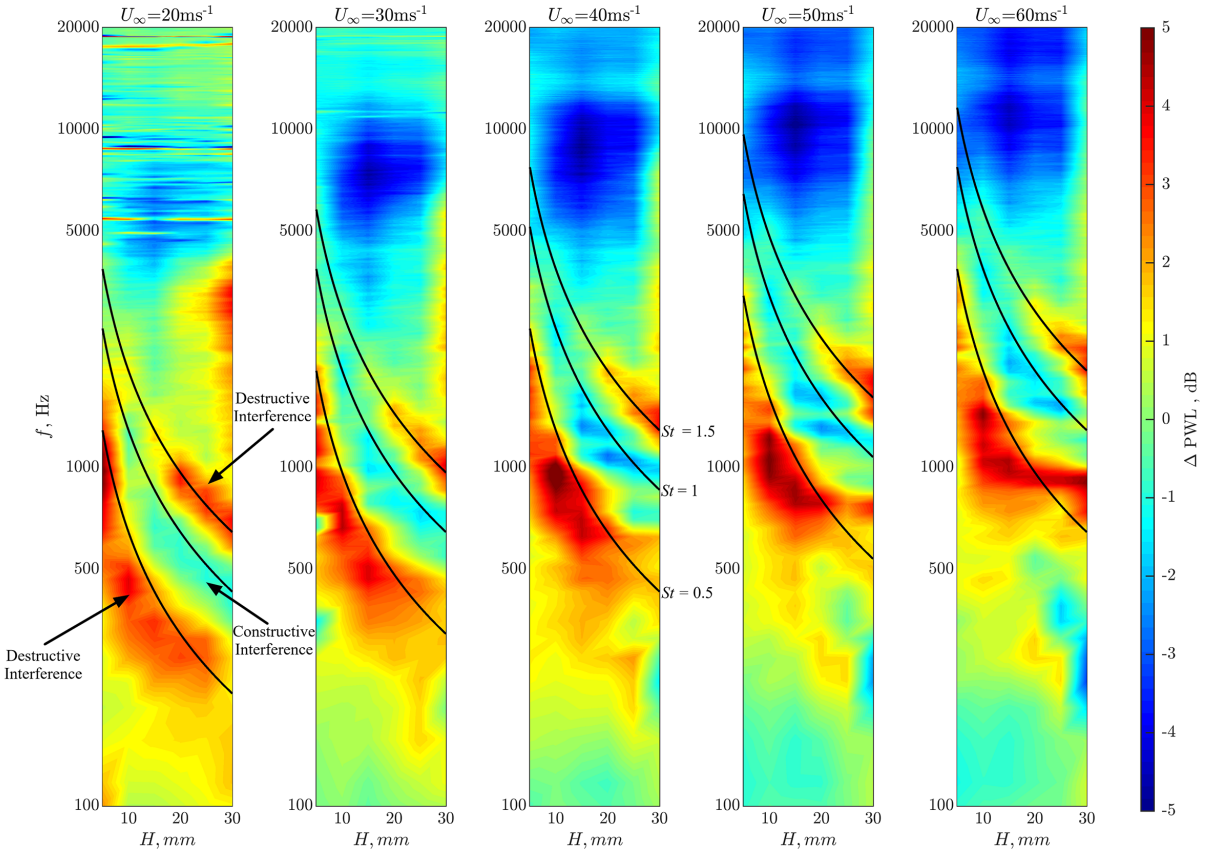

Figure 5.21: ΔPWL contour maps of the frequency, Hz, to slit amplitude (H) for the Slit TEs at 20 ms^{-1} $\leq U_\infty \leq$ 60 ms^{-1}.

velocities of the turbulent eddies at the suction side is generally slower than at the pressure side, regardless the type of TE investigated.

The effect of the secondary flow structure at the slit TE's suction side plays a further role in the convection velocity of the turbulent eddies locally. As discussed in Section 5.3.3.A, and the numerical results in Chapter 6, the secondary flow structure is transported along the edge of the serrations between the root and tip. The interaction between the secondary structures and the turbulent boundary layer and the rate at which they converge between the root and tip will be slower. This is manifested in Table 5.3 where the U_c/U_∞ between the baseline and slit TEs at the suction side are 0.57 and 0.43, respectively. In contrast, the pressure side convection velocity for both the baseline and slit TEs are similar at $U_c/U_\infty = 0.86$.

The next step to reconcile the velocity scaling for the Strouhal number in Eqn. 5.3, which pertains to the frequency–tuning capability of the slit TE, lies on the interpretation of the turbulent eddies convection velocities in Table 5.3. From the results discussed thus far, especially

referring to the streamwise coherences in Section 5.3.3.A, at first it seems logical to consider only the pressure side contribution because of the larger spatial coherence for the turbulence eddies there. However, a complete discard of the suction side contribution will be an incorrect approach. The smaller spatial extent of the streamwise coherence at the suction side could be due to the vertical displacement of the near wall turbulence between the mid and tip locations, as demonstrated in Figure 5.19 for the turbulence maxima. In this scenario, the reference signal at the root will naturally loss coherence with the signals from the mid location onwards when both the stationary and traverse hot wire probes are maintaining the same physical height relative to the slit wall surface. In summary, turbulent eddies traversing at the suction side slit TE will scatter noise at the root first, and while they continue to propagate downstream, the cross flow coming from the pressure side through the slit will displace them vertically from the mid location and downstream. The vertically displaced turbulence eddies are still capable of executing the second acoustic scattering at the tip, thus completing the acoustical interference mechanism. Based on the physics described above, a representative turbulent eddies convection velocity U_c to be used in the Strouhal number scaling can be the average between the suction side and pressure side values. The final version of the acoustical interference definition is now:

$$St = \frac{f \cdot l}{U_c} = \frac{1}{2}n \tag{5.10}$$

To remind again, the execution of the destructive interference between the root and tip of the slit TE should occur at odd numbers of n, which give St = 0.5, 1.5 and so on. The constructive interference, on the other hand, should occur at even number of n that gives St = 1.0, 2.0 and so on. Figure 5.21 shows the contours of the measured ΔPWL as a function of slit amplitudes H, and f at U_∞ = 20, 30, 40, 50 and 60 ms^{-1}. The results clearly demonstrate the co-existence of destructive interference (St = 0.5 and 1.5, noise reduction) and constructive interference (St = 1.0, noise increase) mechanisms across the large ranges of H and U_∞. The measured ΔPWL and their variations fit very well to the curves pertaining to the acoustical interference above, and most importantly, confirm the frequency-tuning capability of the slit TE. In what follows, an analytical effort will be discussed to derive a simple model for the prediction of noise reduction and noise increase by the slit TE based on the acoustical interference theory.

Analytical model for the noise produced by a slit TE

A. Noise Model

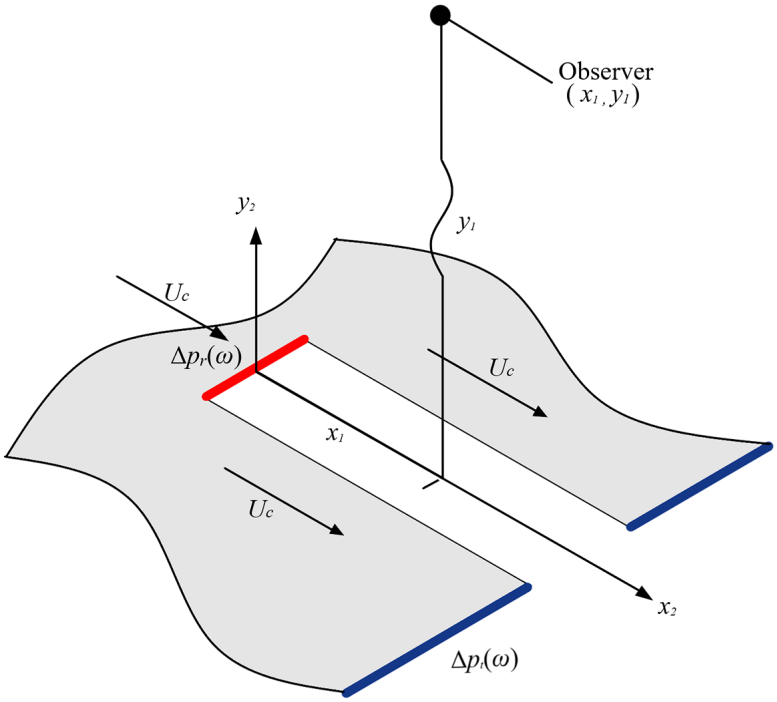

Figure 5.22: Topology of the assumption applied to the slit TE analytic model where the sources are defined as: red – root source and blue – tip source.

Figure 5.22 shows a schematic representing the geometry of the slit TE for the execution of the acoustic interference. The figure demonstrates two compact sources, at both end of the slit TE, where strong acoustical interference will take place between the sources. The incoming turbulent boundary layer flow interacts with the root of the slit first to produce a localised source at $y_1 = 0$, creating a pressure difference $\Delta p_r(\omega)$. The turbulent eddies continue to propagate over the TE surface with a convection velocity, U_c, the same parameter discussed previously in the Section 5.3.3.C. After some times, the turbulent eddies will then interact with the tip of the slit TE to produce another localised source, at $x_2 = H$, producing a local pressure difference $\Delta p_t(\omega)$. As a summary, the assumption of the model is that the source distribution along the slit is derived from two compact sources of strength, at the root and tip locations, defined as $\Delta p_r(\omega)$ (red line) and $\Delta p_t(\omega)$ (blue lines), respectively.

The two sources can be represented by Dirac delta function located at both the root and tip of the slit. Therefore, substituting this assumed source distribution into the radiation integral of the Amiet TE noise model [4] gives the following:

$$p(x_1, y_1, \omega) \sim \frac{x_1}{4\pi c_\infty \sigma} \int_0^H (\Delta p_r(\omega)\delta(0) + \Delta p_t(\omega)\delta(H)) e^{(-i(\omega/(c_\infty \beta^2)(\frac{M-x_1}{\sigma})x_2)} - dx_2; \tag{5.11}$$

$$\sigma^2 = x_1^2 + \beta^2 y_1^2; \tag{5.12}$$

$$\beta^2 = 1 - M^2. \tag{5.13}$$

A condition is made that the adjacent slits are further apart than the turbulence length scale, so interaction between the same eddies to multiple slits does not happen. The power spectrum density of the unsteady wall pressure for each slit can be summed up without regard to the phase difference. After performing the integration over the slit length H, the following expression can be obtained:

$$p(x_1, y_1, \omega) \sim \frac{x_1}{4\pi c_\infty \sigma} (\Delta p_r(\omega) + \Delta p_t(\omega)) \exp\Big(- i(\omega/(c_\infty \beta^2)(M - x_1/\sigma))H\Big). \tag{5.14}$$

Consider the power spectra density of far field pressure radiation,

$$\begin{aligned} &S_{pp}(x_1, y_1, \omega) = E[p(x_1, y_1, \omega)p^*(x_1, y_1, \omega)], \\ &S_{pp}(x_1, y_1, \omega) = \left(\frac{x_1}{4\pi c_\infty \sigma}\right)^2 \Bigg[S_{\Delta p_{rr}}(\omega) + S_{\Delta p_{tt}}(\omega) + E\left[\Delta p_r(\omega)\Delta p_t^*(\omega)\right] \\ &\exp\left(-\frac{i\omega\left(M - \frac{x_1}{\sigma}\right)H}{(c_\infty \beta^2)}\right) + E\left[\Delta p_r^*(\omega)\Delta p_t(\omega)\right] \exp\left(\frac{i\omega\left(M - \frac{x_1}{\sigma}\right)H}{(c_\infty \beta^2)}\right) \Bigg]. \end{aligned} \tag{5.15}$$

The term $E[\Delta p_r^*(\omega)\Delta p_t(\omega)]$ (and its conjugate) is the boundary layer streamwise cross spectrum, which may be expressed in complex form:

$$E\left[\Delta p_r^*(\omega)\Delta p_t(\omega)\right] = \sqrt{(S_{\Delta p_{rr}}(\omega)S_{\Delta p_{tt}}(\omega))}\gamma\left(\frac{\omega H}{l_1(\omega)}\right) \exp\left(-\frac{i\omega H}{U_c(\omega)}\right) \tag{5.16}$$

where $\gamma(\frac{\omega H}{l_1(\omega)})$ is the boundary layer streamwise (purely real) coherence function, assumed to be a function of the ratio of streamwise separation distance H to frequency-dependent coherence length $l_1(\omega)$. Note that the phase $\omega H/(U_c(\omega))$ of the cross spectrum is assumed to originate solely from the time taken for the turbulent eddies to convect over the slit length H, where $U_c(\omega)$ is the frequency-dependent convection velocity. Following Corcos:

$$\gamma\left(\frac{\omega H}{l_1(\omega)}\right) = \exp\left(-\frac{\eta\omega H}{2U_c(\omega)}\right) \tag{5.17}$$

provides an acceptable fit to the measured streamwise coherence function shown in Corcos [29, 30], where η is the empirical constant $\eta = 0.14$. The following Corcos empirical fit to the frequency-dependent convection velocity between two points separated by x_2 is given by,

$$\frac{U_c(\omega)}{U_\infty} = -9.6 \times 10^{-6} f + 0.5\left(1 + \frac{x_2}{\delta^*}\right)^{0.16}. \tag{5.18}$$

Combining the Eqn. 5.17, the far-field radiated pressure PSD may be expressed in the form:

$$\begin{aligned} S_{pp}(x_1, y_1, \omega) = &\left(\frac{x_1}{4\pi c_\infty \sigma}\right)^2 (S_{\Delta p_{rr}}(\omega) + S_{\Delta p_{tt}}(\omega)) \\ &+ 2\sqrt{S_{\Delta p_{rr}}(\omega) S_{\Delta p_{tt}}(\omega)} \exp\left(-\frac{\eta\omega H}{2U_c(\omega)}\right) \cos\left(\omega(\tau_H + \tau_A)\right) \end{aligned} \tag{5.19}$$

where τ_H is the time taken for the turbulent eddies to convect along the slit length,

$$\tau_H = \frac{H}{U_c(\omega)} \tag{5.20}$$

and τ_A is the difference in propagation times to the observer between sound radiation at the root of the slit and at the tip of the slit,

$$\tau_A = \frac{H}{c_\infty \beta^2}\left(\frac{M - x_1}{\sigma}\right) \tag{5.21}$$

which may be expressed in terms of observer angle θ by putting $x_1 = rcos(\theta)$ and $x_2 = rsin(\theta)$

$$\tau_A(\theta) = \frac{H}{(c_\infty \beta^2)}\left(\frac{M - \cos\theta}{\sqrt{(cos^2\theta + \beta^2 sin^2\theta)}}\right). \tag{5.22}$$

Note that at the peak frequency ω_0 where $\frac{(\omega_0 H)}{U_c} = \pi$.

$$\begin{aligned} S_{pp}(x_1, y_1, \omega_0) = &\left(\frac{x_1}{4\pi c_\infty \sigma}\right)^2 (S_{\Delta p_{rr}}(\omega_0) + S_{\Delta p_{tt}}(\omega_0)) \\ &+ 2\sqrt{S_{\Delta p_{rr}}(\omega_0) S_{\Delta p_{tt}}(\omega_0)} \exp\left(-\frac{\eta\omega H}{2U_c(\omega_0)}\right) \cos\left(\omega_0(\tau_H + \tau_A)\right). \end{aligned} \tag{5.23}$$

The evaluation of the analytic model to experimental results are shown in the next section. Readers should be aware that the analytic model should be used to predict the noise trends at which the peak frequency occurs, and not to predict the noise reduction. The prediction of the

noise reduction requires additional information to estimate the source strength located at the root and tip, $S_{\Delta prr}$ and $S_{\Delta ptt}$. The analytic results assume that the source strength between the root and tip are at the most effective interference. As a result, for the purpose of the comparison to the experimental results at various freestream velocity and slit amplitude, this assumption will be used.

The next investigation evaluated the coherence length obtained by a comparison of the Corcos empirical model to experimental coherence. The term 'coherence length' describes the rate of decay calculated using the square root coherence function [104]. The coherence length for two separate readings in the streamwise or spanwise direction, η_x and η_z respectively, was obtained by fitting an exponential to the square root coherence γ at $\eta_{x,z}$. Corcos [29, 30] proposed, subsequently modified by Finnveden *et al.* [49], the empirical model approach given as:

$$\gamma(\omega, \eta_x, \eta_z) = \exp\Big(-b_1\frac{\omega\eta_z}{U_c}\Big)\cdot\exp\Big(-b_3\frac{\omega\eta_x}{U_c}\Big)\cdot\exp i\Big(\frac{\omega\eta_z}{U_c}\Big), \tag{5.24}$$

$$\gamma(\omega, \eta_x) = \exp\left(-b_3\frac{\omega\eta_x}{U_c}\right), \tag{5.25}$$

$$\gamma(\omega, \eta_z) = \exp\left(-b_1\frac{\omega\eta_z}{U_c}\right) \tag{5.26}$$

where b_1 and b_3 are the decay factors for spanwise and streamwise respectively. The spanwise and streamwise coherence lengths are defined in Eqn. 5.24 as the first two exponential terms, and the third exponential term accounts for the mean pressure field [93]. The streamwise and spanwise coherence lengths are defined as Eqn. 5.25 and Eqn. 5.26, respectively.

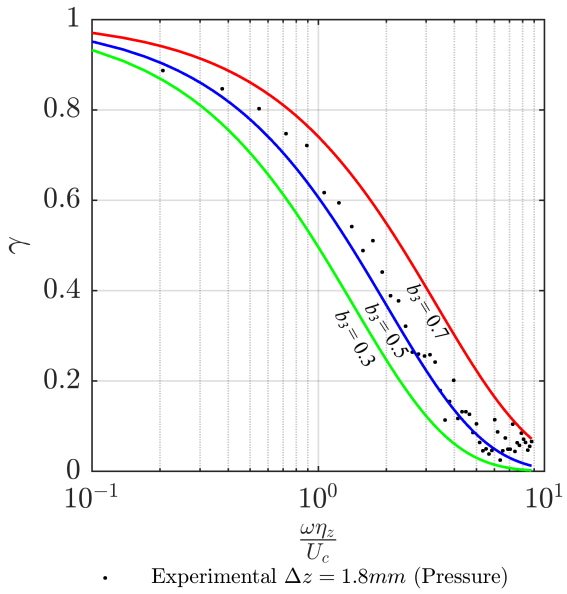

Figure 5.23: Comparison of the Corcos Empirical model for the coherence in the streamwise direction to the experimental streamwise coherence γ.

Figure 5.24 presents the sensitivity of the experimental coherence to the Corcos empirical model plotted against the non-dimensional frequency. The results showed good agreement between the experimental and empirical model at $\eta_x = 1.8$ mm with a decay constant $b_3 = 0.5$. Figures 5.25 and 5.26 demonstrated the updated analytical prediction based on the experimental decay constant which resembled similar trends to the experimental noise results.

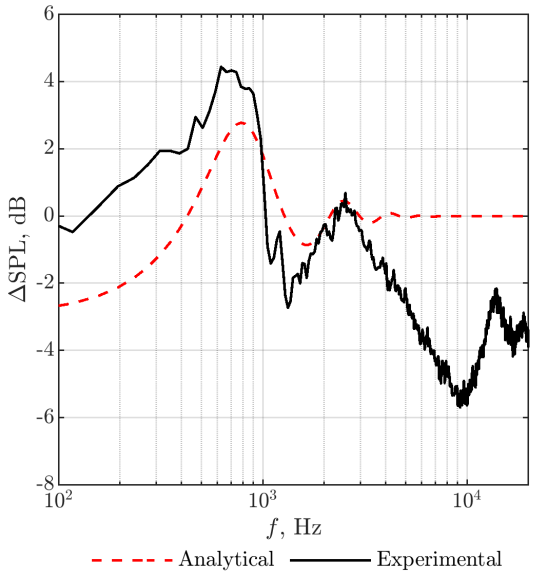

Figure 5.24: Comparison of experimental results to analytical prediction model against non-dimensional frequency at $U_\infty = 40$ ms^{-1} and $H = 15$ mm

B. Comparison between experimental and predicted noise performance by slit TEs

The noise model developed in the previous section will be validated against the measured results. Figure 5.24 shows the difference in the Sound Pressure Level ΔSPL (correspond to polar angle of 90°) measured at $U_\infty = 40$ ms^{-1}, with the slit amplitude $H = 15$ mm, wavelength $\lambda = 3$ mm and width $W = 0.3$ mm. The non-dimensional frequency $St = \frac{fH}{U_c}$ is in accordance to Eqn. 5.10 to describe the acoustical interference. The first peak is shown to occur at $St \sim 0.4$ and 0.5, and the second peak at $St = 1.5$. These correspond well to the destructive interference mechanisms. The first trough at $St = 0.8$, despite a slight deviation from the theoretical value of 1.0, still confirms the mechanism of constructive interference by the slit TE. Note that a large experimental dataset can support the frequency predicting capability as demonstrated in Figure 5.21.

The predicted ΔSPL is also shown in Figure 5.24, which exhibits an oscillatory behaviour in the frequency to exhibit the peaks (destructive interference) and troughs (constructive interference). The Corcos empirical constant $\eta = 0.14$ is used for the modelling of the streamwise coherence function. Note that the level of the predicted ΔSPL was offset so that it can be closer to the measured ΔSPL for comparison. As mentioned, the noise model cannot predict an accurate level of noise reduction/increase by the slit TE due to the negligence of the source strengths at the root and tip. As expected, the predicted ΔSPL demonstrates the occurrence of peaks at $St = 0.5$, 1.5 and so on, and the troughs at $St = 1.0$, 2.0 and so on. Overall, the predicted ΔSPL provides a respectable match to the experimental results at the primary frequencies. At $St > 2$, the analytic model's continual basis of the acoustical interference can no longer be replicated by the experimental results.

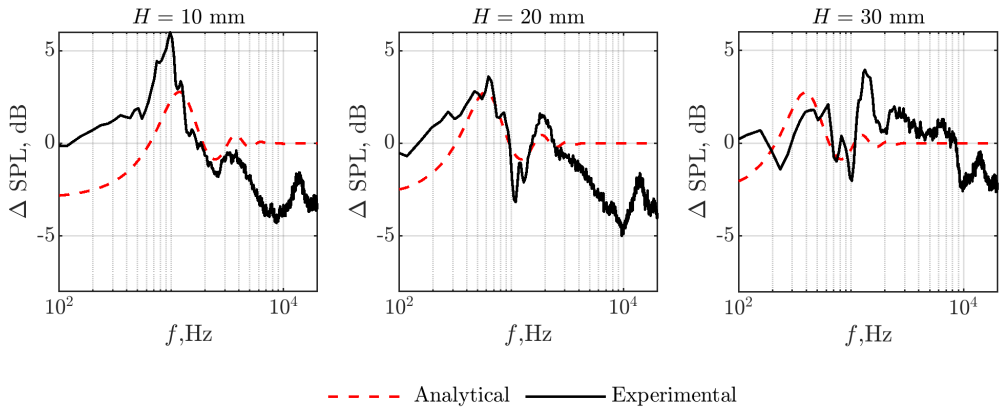

Figure 5.25: Comparison of the trend prediction of the analytic model to experimental results at various H and freestream velocity kept at $U_\infty = 40$ ms^{-1}.

To validate the analytical model further, more cases are compared. Figure 5.25 shows the ΔSPL achieved by the slit TE when H = 10, 20 and 30 mm, all of which with λ = 3 mm and W = 0.3 mm and subjected to U_∞ = 40 ms^{-1}. The comparison between the measured and predicted ΔSPL is made at dimensional frequency f. In all the cases shown here, the noise model, as a minimum, is capable of capturing the frequencies pertaining to the first and second peaks, as well as the first trough. As H increases, the peaks and troughs for both the measured and predicted ΔSPL will shift to lower frequencies, which is due to the larger wavelength between the two compact sources (root and tip).

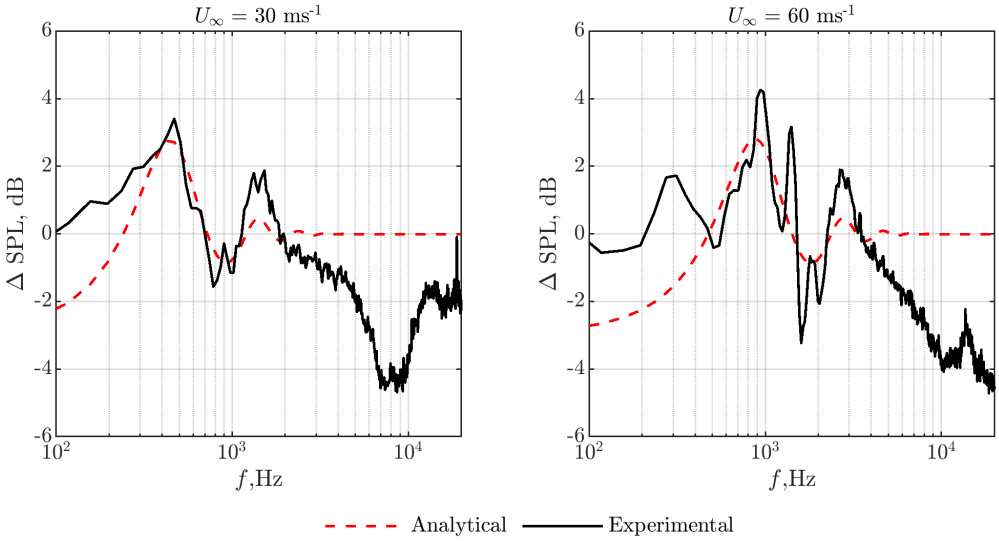

Figure 5.26: Comparison of the trend prediction of the analytic model to experimental results at various freestream velocities and slit amplitude kept at H = 20 mm.

Figure 5.26 shows the ΔSPL achieved by the slit TE when H = 20 mm, λ = 3 mm and W = 0.3 mm, but subjected to two inflow velocities at U_∞ = 30 ms^{-1} and 60 ms^{-1}. At U_∞ = 30 ms^{-1}, the noise model is also capable of capturing the frequencies pertaining to the first and second peaks, as well as the first trough. As expected, the measured ΔSPL cannot replicate the acoustical interference mechanism at higher order of the phase loop. At U_∞ = 60 ms^{-1}, a somewhat interesting phenomenon has been observed. Whilst the first peak, second peak and first trough in the measured ΔSPL can be captured accurately by the predicted ΔSPL, there seems to have another peak in the measured ΔSPL at a lower frequency of $f \approx$ 300 Hz, which is not predicted by the noise model. For identification purposes, this particular peak is named as the "peak 0". Since the noise model only considers the acoustical interference between two compact sources at phase angle $n\pi$, where n must be an integer, this means that the peak 0 is produced by two compact sources not necessary at the root and tip. Because the frequency pertaining to the peak 0 is lower than the first peak, it could either be that 1) the longitudinal

distance between the two sources must be greater than H, or 2) the convection velocity, U_c is significantly slower. A re-examination of the measured ΔPWL contour maps in Figure 5.21 reveals that, as the inflow velocity increases, there is a break-off from the first peak ($St = 0.5$), especially at higher H towards the lower frequency, to become what is known as the peak 0. The peak 0 is also followed by a prominent trough at lower frequency (called trough 0), especially towards the higher end of inflow velocity (50 and 60 ms^{-1}).

For the specific case when $H = 20$ mm and $U_\infty = 60$ ms^{-1} (the right hand side ΔSPL spectrum in Figure 5.26), an effective $^{H}/_{U_c}$ can be derived based on the assumption that the frequency pertaining to the measured peak 0 refers to $n' = 1$ from Eqn. 5.10. All the measured peaks are summarised in Table 5.4. The first and second columns of the table refers to the destructive interference mechanism of $n' = 1$, 3, 5, 7 & 9, and $St = 0.5$, 1.5, 2.5, 3.5 & 4.5, respectively. The third and fourth columns record the predicted (Eqn. 5.10) and measured peak frequencies, respectively. From the table, it is clear that the overall structure of the phase loop is better established if an effective $^{H}/_{U_c}$ is used. It is worth pointing out that the noise model described in Section 5.3.3.A can predict the peak frequencies well when $n' = 3$ and 9, which would otherwise correspond to $n = 1$ and 3 for a geometrical $^{H}/_{U_c}$. The same condition is also observed in other cases not discussed here. Hence, there seems to be a necessity to apply a correction factor of 3 when the slit TE is subjected to high inflow velocity. It is currently unknown what causes the physical property changes and the seemingly alteration in the phase loop structure. It could be related to a stronger cross flow component in the slit gap driven by high inflow velocity that results in a longer trajectory and a stronger secondary flow structure, which could lengthen the overall distance of the two scattering sources and a lower convection velocity, respectively, to cause a larger effective $^{H}/_{U_c}$. This remains to be investigated in the future.

n'	St	Predicted peak f (Hz)	Measured peak f (Hz)
1	0.5	300	300
3	1.5	900	938
5	2.5	1500	1406
7	3.5	2100	1800
9	4.5	2700	2700

Table 5.4: Summary of the predicted (Eqn. 5.10, using the effective $^{H}/_{U_c}$) and measured peak frequencies pertaining to the slit TE with $H = 20$ mm, $\lambda = 3$ mm and $W = 0.3$ mm at $U_\infty = 60$ ms^{-1}.

5.3.4 Double Rooted TE Serration (DRooTES)

This section presents a hybrid device *Double Rooted TE Serration*, or DRooTES, which exploits the dual-noise reduction mechanisms to reduce the aerofoil broadband noise radiation. The DRooTES combines the serration effect from the single-serrated TE, and the acoustical destructive interference mechanism from the slit TE. This device demonstrates further improvement in the level of broadband noise reduction, as well as the establishment of the frequency-tuning capability, simultaneously.

Noise performance by the DRooTES

A. Variation in the serration amplitude ($H \equiv h' + h''$)

To follow the same format as the previous geometries (single-serrated and slit TEs), the ΔPWL achieved by the DRooTES against the baseline aerofoil, in the first instance, could be based upon the different serration amplitude, H, which is the sum of h' (root_1–root_2) and h'' (root_2–tip) distances. Readers can refer to Figure 5.1 for the schematic that illustrates the geometries. Note that the h' and h'' can either be both equal to $H/2$ (i.e. $h' = h''$), or they are not equal ($h' \neq h''$), but the sum of which still gives the same H. It is necessary to point out that in order to examine specifically the acoustical interference mechanism in the DRooTES, the h' (root_1–root_2) is more relevant. Although the h'' (root_2–tip) is not expected to have a direct impact on the acoustical interference, it will be shown later that it can affect slightly the frequency scaling of the noise reduction, which will then have an impact on the frequency tuning for the DRooTES. In this section, both the ($h' = h''$) and ($h' \neq h''$) scenarios will be examined.

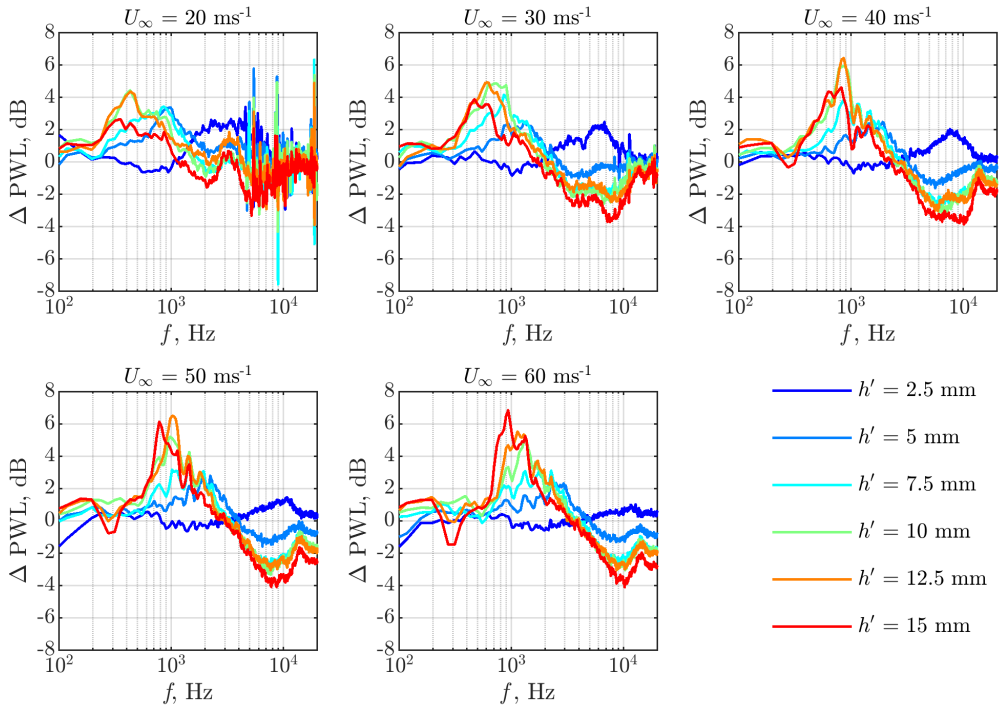

Figure 5.27: Comparison between the baseline and DRooTES (different h') TEs, ΔPWL, dB; where λ = 3 mm; at 20 ms^{-1} $\leq U_\infty \leq$ 60 ms^{-1}. Note that $h' = h''$.

The scenario of ($h' = h''$) will be considered first. Figure 5.27 presents a comparison of the ΔPWL achieved by the DRooTES of different h', where $h' = h''$, against the baseline aerofoil. Therefore the corresponding H will be $2h'$ for each case. The spectra are plotted in dimensional frequency, f. The best performer amongst all the DRooTES tested here tend to belong to those with the largest h'. For example, h' = 15 mm of the DRooTES is shown to achieve noise reduction of more than 7 dB at U_∞ = 60 ms^{-1}. Interestingly, the DRooTES with the smallest h' at 2.5 mm only begins to exhibit noise reduction capability against the baseline TE at high frequency. When h' increases to 5 mm, the peak ΔPWL frequency undergoes an abrupt drop. The peak frequency reduction rate, however, becomes steadier which is also accompanied by an increase level of ΔPWL when h' increases further. The DRooTES also causes noise increase against the baseline at high frequency, where the level of noise increase increases with h'. The overall trend witnessed for the DRooTES is similar to that of the single-serrated TE discussed in Section 5.3.2, albeit with a larger ΔPWL achieved by the former.

The next investigation is to establish whether those peak frequencies achieved by the DRooTES can be non-dimensionalised by the h' and U_c, thus producing the frequency–tuning capability equivalent to the slit TE. In this time, the non-dimensional frequency defined as below:

$$St = \frac{fh'}{u_c}\kappa, \tag{5.27}$$

U_c is the convection velocity of the turbulent eddies from h' to h'', which is obtained by the same experimental procedures as described in the slit TE case in Section 5.3.3.C. The empirical correction factor κ is defined as $\kappa = (\frac{h''}{h'})^m$, which is needed to compensate the scenario when $h' \neq h''$. Note that $\kappa = 1$ when $h' = h''$. Figure 5.28 re-plots the ΔPWL spectra when $h' = h''$, but against the above non-dimensional frequency St. It can observe that the maximum noise reduction (maximum ΔPWL) occurs at $St \approx 0.5$, which is very close to the values observed for the slit TE. This demonstrates that the same acoustical destructive mechanism is also valid for the DRooTES.

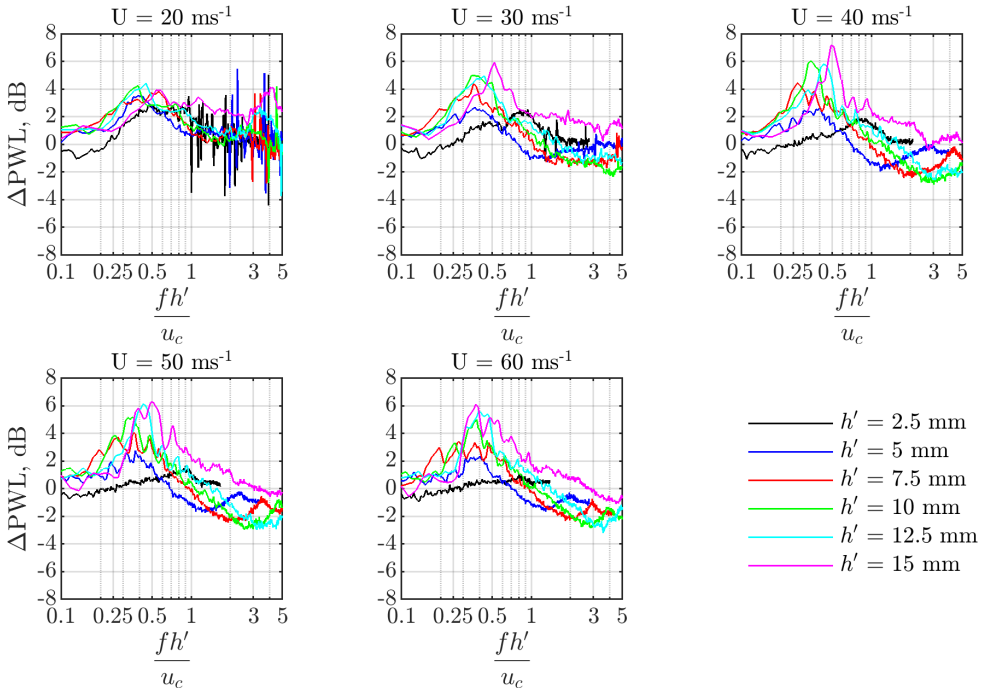

Figure 5.28: Non-Dimensional Frequency of the DRooTES when $h' = h''$, i.e. $\kappa = 1$, at various h', where $\lambda = 6$ mm, at 20 ms^{-1} $\leq U_\infty \leq$ 60 ms^{-1}.

The question now is whether the mechanism continues to be valid when $h' \neq h''$. In this scenario, κ is no longer a unity when $m \neq 1$. It is necessary to determine the power factor m in the expression of the κ, which is empirically determined to be 0.4 from the many dataset. Figure 5.29 shows the sensitivities of the broadband noise radiation at non-dimensional frequency at various h', where the corresponding h'' are then adjusted accordingly to produce a constant H at 30 mm. The results demonstrate that the different curves collapse reasonably well, and importantly, also at the new non-dimensional frequency of about 0.5. The increase of h' affects

the maximum noise reduction peak. The best performer was $h' = 20$ and 25 mm with 8 dB reduction in comparison to the $h' = 5$ mm which achieved only 5 dB at same freestream velocity of 60 ms^{-1}. This emphasises that, for a sufficiently large overall length H, a large longitudinal distance between the two scattering sources h' is preferred in order to achieve a better level of noise reduction, while retaining the frequency–tuning capability.

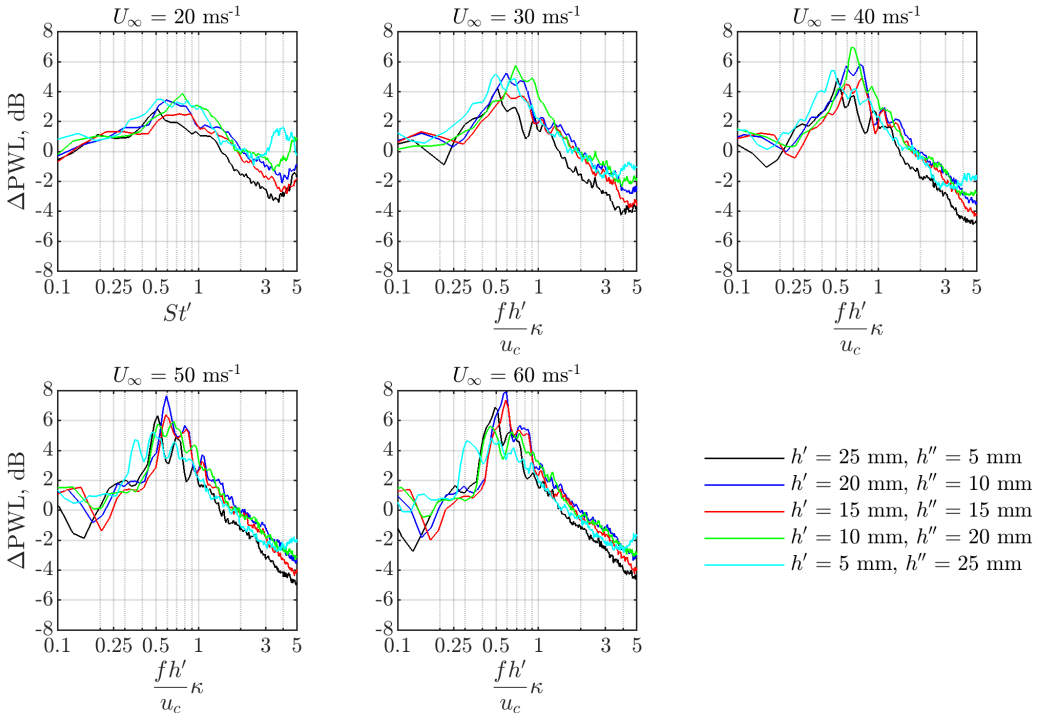

Figure 5.29: Non-Dimensional Frequency of the DRooTES when $h' \neq h''$, i.e. $\kappa \neq 1$, at various h', where $\lambda = 6$ mm, at 20 ms^{-1} $\leq U_\infty \leq$ 60 ms^{-1}.

There are two important observation that worth stating. First, in contrary to the slit TE, the acoustical constructive interference is non-existence for the DRooTES. This might be due to the geometrical nature of the oblique edge for the DRooTES that is unfavourable for the acoustical interference at higher frequency mode; second, the level of noise reduction by the DRooTES, notably at the peak ΔPWL, increases as the freestream velocity increases. This is an important improvement compared to the conventional single-serrated TE, which is known to deteriorate in performance as the freestream velocity increases.

B. Variation in the serration wavelength (λ) and angle of serration tip (Φ)

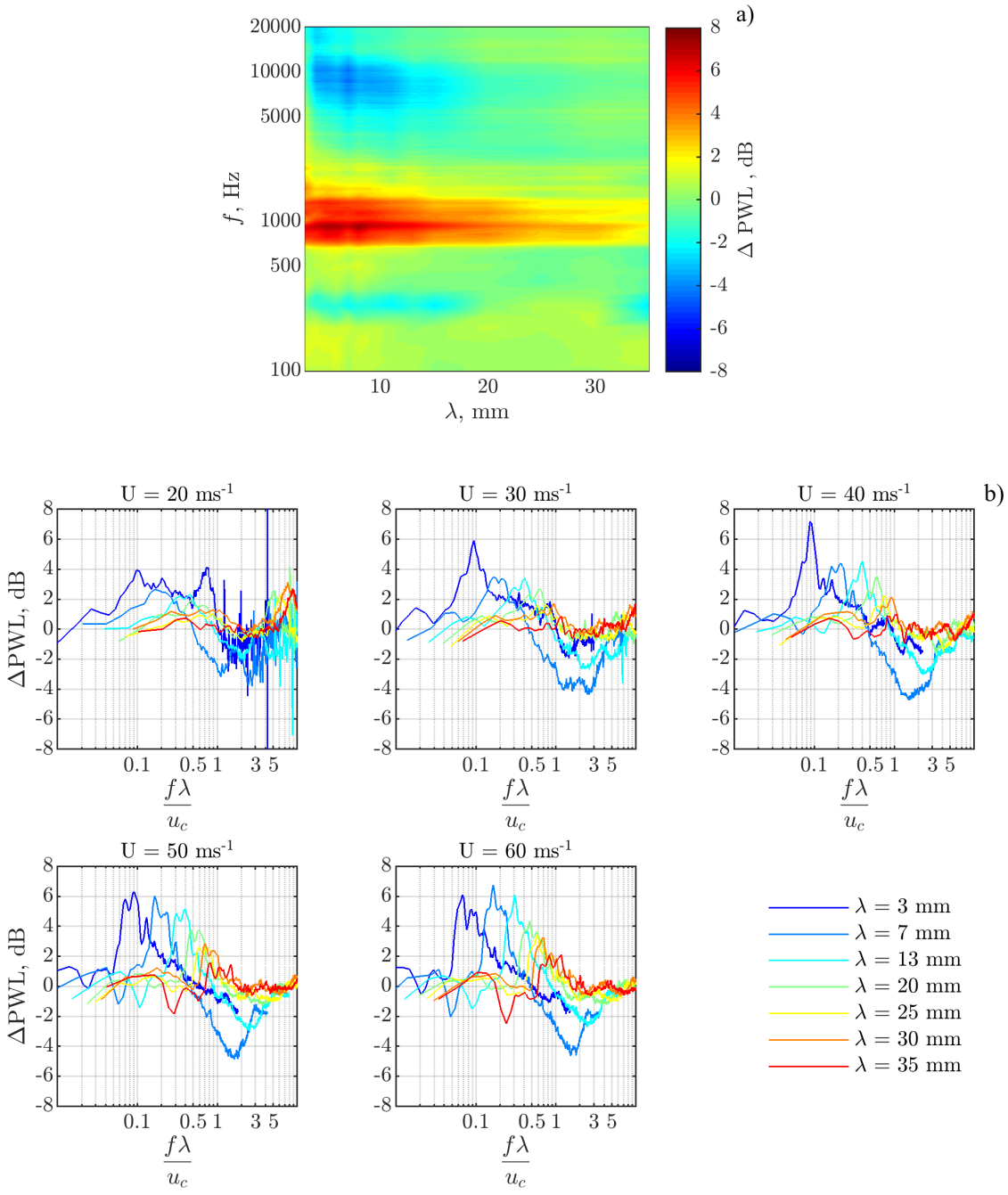

Figure 5.30: Comparison between the baseline and DRooTES (different λ) TEs, ΔPWL, dB, against (a) dimensional frequency, and (b) non-dimensional frequency. $H = 30$ mm for all ($h' = h'''$), where at 20 ms^{-1} $\leq U_\infty \leq$ 60 ms^{-1}.

Figure 5.30 shows the sensitivity of the broadband noise radiation by the DRooTES with different serration wavelength λ. From the ΔPWL contours in Figure 5.30a, the general trend is that the level of noise reduction increases as the λ decreases. The best performer amongst

the DRooTES is $\lambda = 3$ mm, where reduction up to 7.5 dB was observed. Note that this value is slightly lower than the reported 8 dB in the previous section because of the smaller h' used here. This emphasises that the h' is a slightly more important parameter than λ to achieve a high ΔPWL. The peak ΔPWL in Figure 5.30a is found to occur at a constant f. Again, this illustrates that the main geometrical parameter for the frequency tuning is the h', and insensitive to the λ. The overall characteristics in the variation of λ are similar to those of single-serrated TE discussed earlier. Figure 5.30b shows the spectra of ΔPWL, but the frequency is scaled with $f\lambda/U_c$. The results clearly demonstrate that λ has no effect on the non-dimensional frequency as the spectra do not collapse.

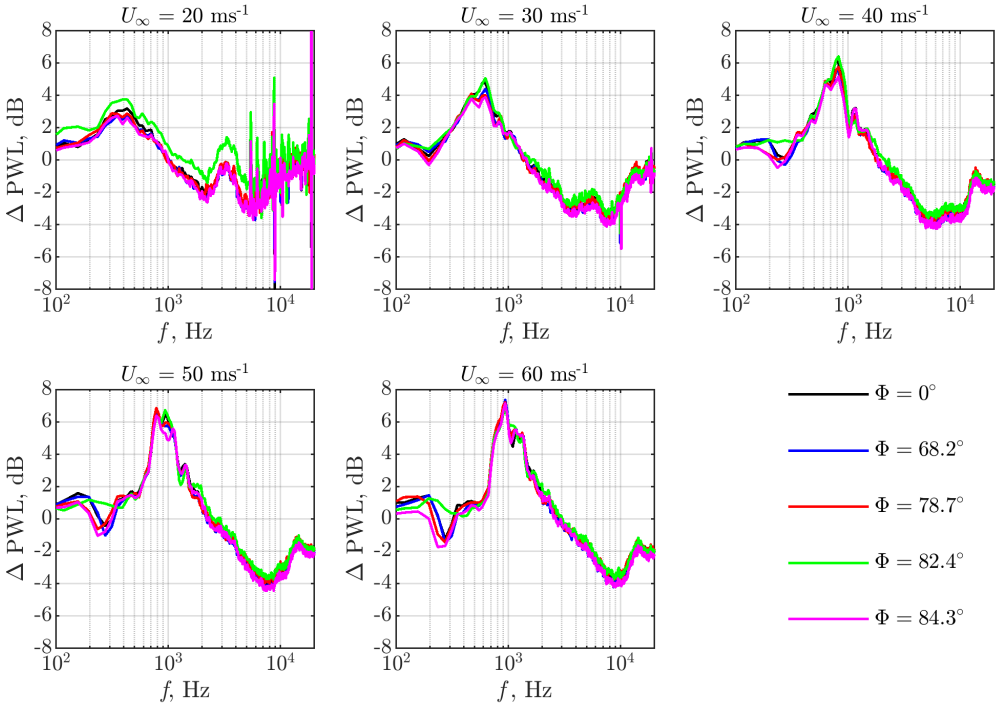

Figure 5.31: Comparison between the baseline and DRooTES (different Φ) TEs, ΔPWL, dB, against dimensional frequency. $H = 30$ mm ($(h' = h'' = 15$ mm) and $\lambda = 6$ mm, where at 20 ms^{-1} $\leq U_\infty \leq$ 60 ms^{-1}.

Finally, Figure 5.31 examines the effect of the angle of serration tip, Φ, on the broadband noise reduction of the DRooTES. Schematic illustration on the Φ can be referred to Figure 5.1. As shown in the graph, the effect of Φ offers little to no benefit to the ΔPWL across the range of freestream velocity investigated here. This represents another evidence that the main noise reduction mechanisms and the frequency–tuning are underpinned by the distance h', where it is found that a larger value of h' is beneficial for the noise reduction. On the other hand, the

region between the second root to the tip, h'', does not seem to have any effect on the overall performance of the DRooTES.

C. Overall Noise Performance of the DRooTES

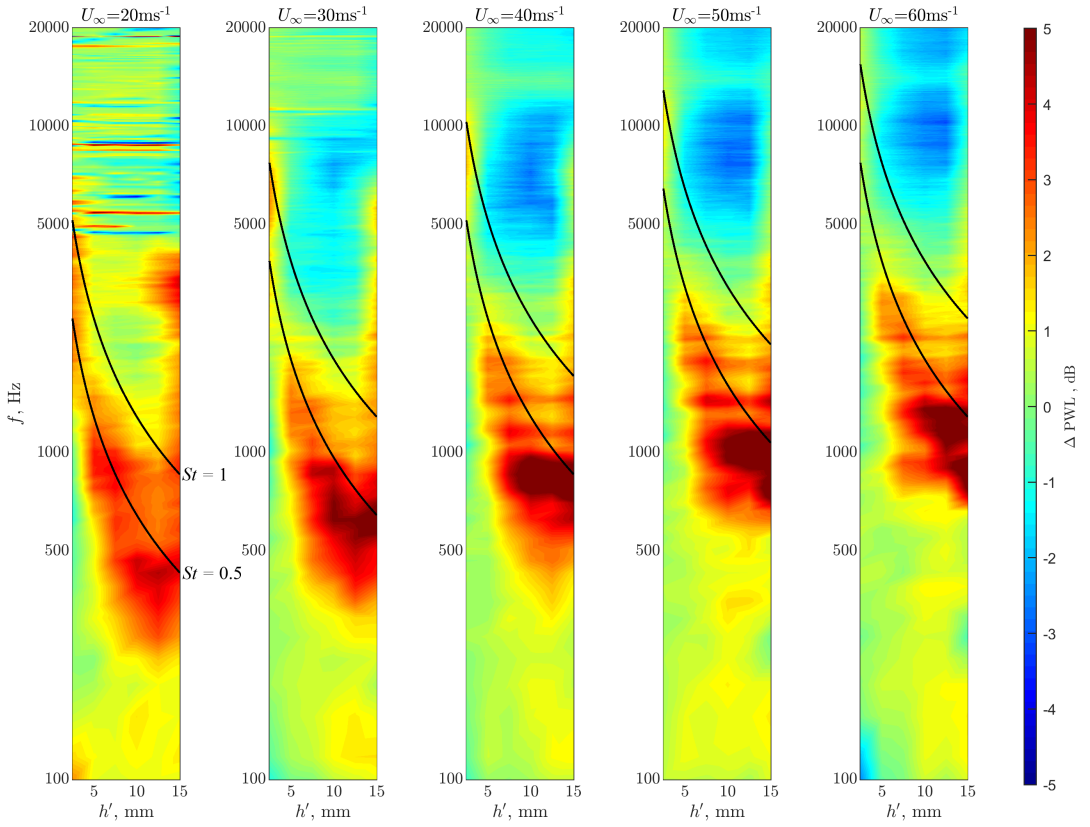

Figure 5.32: ΔPWL contour maps of frequency (f) against the root$_1$ – root$_2$ distance (h') for the DRooTES at 20 ms^{-1} $\leq U_\infty \leq$ 60 ms^{-1}.

Figure 5.32 shows several contours of ΔPWL as a function of f against h' at 20 ms^{-1} $\leq U_\infty \leq$ 60 ms^{-1}. Each contour is superimposed by two constant lines depicting the St = 0.5 and 1.0 that denote where the destructive interference and constructive interference should takes place, respectively, in the frequency–spatial domains. Indeed the noise reduction experimental results follows the St = 0.5 line pretty well across the entire freestream velocity range. However, unlike the slit TE, no noise increase (negative values of the ΔPWL) can be observed at the St = 1.0 line or regions surrounding it. This demonstrates that the while the DRooTES can exert the frequency–tuning capability, and possibly achieve further level of noise reduction by the

co-existence of the serration effect, it can also suppress the acoustical constructive interference. Furthermore, noise increase at the very high frequency is also much less than the slit TE case.

Flow field analysis of the DRooTES

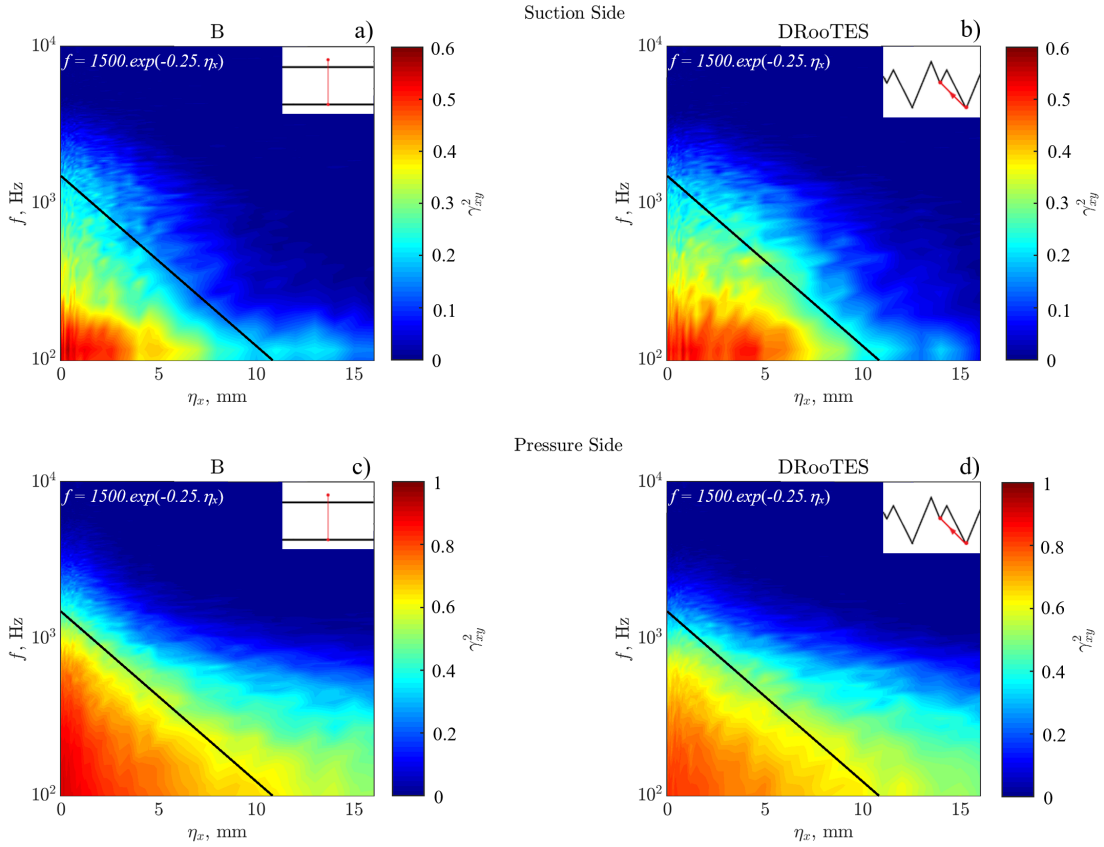

Figure 5.33: Comparison between the baseline and DRooTES for the γ^2_{xy} (streamwise coherence with obliqueness) between root$_1$ and root$_2$ where $H = 15$ mm and $\lambda = 3$ mm, at $U_\infty = 30$ ms^{-1}.

In this section, the analysis of the flow field pertaining to the DRooTES will be performed in the same way as in the Section 5.3.3 for the slit TE, but will be much condensed because the results here for the DRooTES are not too different. Figure 5.33 presents the streamwise coherence of the DRooTES between root$_1$ and root$_2$ for both the pressure and suction surfaces. Because of the obliqueness, the coherence will be represented by γ^2_{xy} for the DRooTES case. The γ^2_{xy} produced by the DRooTES on the suction side is different with the slit TE, as the latter would experience a larger spatial extent of the coherence level, which is attributed to the secondary flow structures. The overall similarity between the baseline TE and DRooTES in Figure 5.32 on the suction side thus suggests that such secondary flow structure is absence. A detailed examination reveals that the DRooTES produces considerable γ^2_{xy} level between the low and mid frequency, and undergoes a global exponential decay in the frequency against the streamwise distance,

$f \sim \exp(-0.25\eta_x)$ on the suction side. The DRooTES shows similar coherence strength to the baseline TE of $\gamma^2_{xy} \approx 0.6$ close to the root$_1$. Considerable level of the γ^2_{xy} can be observed up to the secondary root (root$_2$) of the DRooTES, at $\eta_{xy} = 8$ mm. This demonstrates a greater frequency range of the γ^2_{xy} achieved by the DRooTES in comparison to the baseline TE. This provides an evidence that the incoming turbulent eddies that scatter at the root$_1$ will also scatter effectively at the root$_2$, thereby producing an acoustical interference effect between the root$_1$ and root$_2$ of the DRooTES. On the pressure side, the DRooTES exhibit strong coherence similar to the baseline TE. The DRooTES also undergoes a slightly faster dissipation of the strength of the γ^2_{xy} downstream in comparison to the baseline TE. It is believed that the serrated feature of the DRooTES drives this particular characteristic of the faster dissipation of the turbulent eddy.

By comparing the γ^2_x and γ^2_{xy} results presented thus far between the slits TE and DRooTES, respectively, as well as the spanwise correlation length scale l_z presented earlier in Figure 5.11a, the following observations can be made:

- Significant level of γ^2_{xy} covers between the scattering roots for the DRooTES, which implies that the suction side of the DRooTES can also exert the frequency–tuning effect in a similar way the slit TE does in the γ^2_x.
- The difference in the γ^2_{xy} level between the baseline and DRooTES is larger than the difference in the γ^2_x level between the baseline and slit TE. This implies that an overall reduction in the turbulence coherence by the DRooTES has been exerted by the serration effect.
- The spanwise correlation length scale l_z presented in Figure 5.11a represents the extent of the incoming turbulent eddies at the vicinity of the root for the slit, and root$_1$ for the DRooTES. It is shown that, at the suction side, the l_z for the DRooTES is lower than the slit TE up to the mid frequency range, which can cause a direct consequence of lower TE noise radiation as in accordance to the analytical expression of Amiet [4]. This could represent another mechanism allowing the DRooTES to outperform the slit TE.
- As will be discussed in the next chapter, the secondary flow structures above the suction side contain high Lighthill stresses that might be responsible for the very high frequency noise increase. The lack of secondary flow structures on the suction side of the DRooTES can explain the relatively low level of very high frequency noise radiation.

5.3.5 Comparison among the single-serrated, slit and DRooTES TEs.

This section will now summarise the noise performance of the single-serrated, slit and DRooTES TEs at 20 ms^{-1} $\leq U_\infty \leq$ 60 ms^{-1}. To make a meaningful comparison, the amplitudes of the single-serrated and slit TEs are chosen at $H = 15$ mm, whilst the DRooTES is represented by $h' = 15$ mm, with $H = 30$ mm. All three have the same wavelength at $\lambda = 3$ mm. The reason to choose the DRooTES to be half of the overall amplitude of the single-serrated and slit TEs is due to the consideration of the scattering sources. As discussed previously, the dominant geometrical parameter for a DRooTES is the h', i.e. the distances between root$_1$ and root$_2$. The overall H will not affect much on the noise radiation.

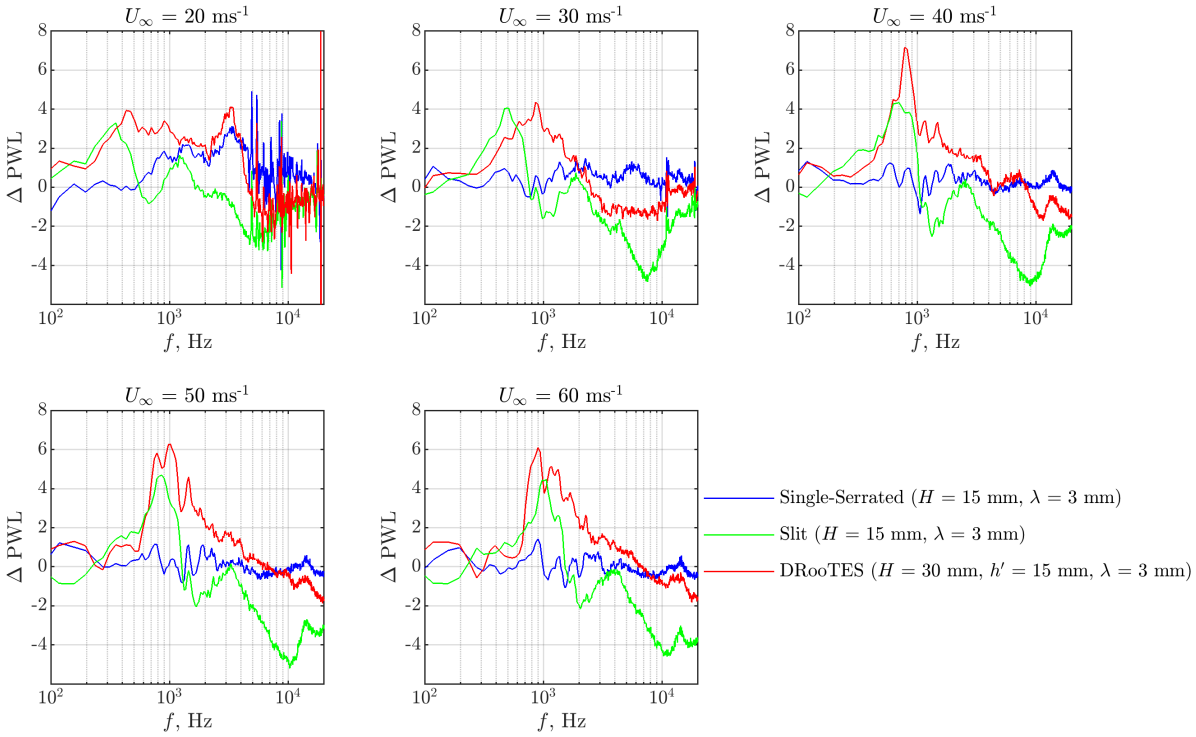

Figure 5.34: Comparison of the ΔPWL spectra achieved by the single-serrated, slit and DRooTES TEs at 20 ms^{-1}. $\leq U_\infty \leq$ 60 ms^{-1}.

The results in Figure 5.34 first show that the single-serrated TE is inefficient for the reduction of the broadband self-noise across much of the freestream velocities. This might be due to the insufficient serration amplitude, which is only 10% of the aerofoil chord. For the slit TE, significant improvement can already be observed where a dominant peak (by the destructive interference mechanism) appears in the spectra. This peak, however, will be followed by a trough because of the constructive interference. Prominent noise increase at very high frequency

can be observed due to the secondary flow structures on the suction side. The noise reduction mechanism by a slit TE is purely by the acoustical interference effect. When a DRooTES is used, significant improvements can be observed. The peaks achieved by the DRooTES are not only similar to those of the slits (demonstrating the destructive interference effect), but also 2–3 dB higher in the noise reduction. The DRooTES can also achieve noise reduction across a much wider frequency range without incurring any noise increase. This confirms that acoustical constructive interference mechanism is not existence, and most importantly, the DRooTES can exert the frequency–tuning capability and serration effect simultaneously. In other words, the DRooTES is a next-generation hybrid device that targets the source–radiation.

5.4 Summary

This chapter represents an experimental study on the aerofoil self-noise reduction by utilising the phase-cancellation of acoustical pressure waves between two scattering sources that are physically displaced in the longitudinal direction near the TE. The inspiration draws from one of the noise reduction mechanisms for TE serrations. However, the acoustical interference mechanism by a conventional TE serration, despite overwhelmingly proven by many researchers to be versatile in the reduction of the turbulence–TE broadband noise, still lacks the ability to target specific acoustical frequency. This is because there are multiple scattering sources along the oblique edges of a single-serrated TE where no distinct and characteristic phase angle can be established.

In this chapter, the otherwise oblique edge for a single-serration is modified to be a "slitted" geometry where the edges become parallel to the mean flow direction. In this geometry, acoustical scattering of the turbulent hydrodynamic sources along the edges will become minimal, while the main scattering sources are only restricted to the root and tip of the slit. Using a typical definition of a Strouhal number, and by forcing the condition of acoustical destructive interference to give the Strouhal number to be 0.5, 1.5 and so on, one could "choose" the peak frequency for the maximum noise reduction by adjusting the distance between the root and tip of the slitted TE. Another parameter that should be known a priori is the convection velocity of the turbulent eddies over the slit surfaces. The experimental and analytical results presented in this chapter both positively verify this noise reduction mechanism in what can be regarded as the frequency fine-tuning capability by a passive TE noise control device. Unfortunately, the slit TE can also produce the opposite effect quite prominently, namely the constructive interference that can radiate more efficiently than that of a straight TE at the Strouhal number of 1.0, 2.0 and so on.

Furthermore, secondary flow structures can be identified by the coherence measurement on the suction side. These structures, which will be discussed in more detail in the next chapter, can be a source of noise radiation at very high frequency.

A new device developed in this thesis is called the Double Rooted TE Serration, or DRooTES. It is capable of exerting the acoustical destructive interference, thereby retaining the frequency fine-tuning capability, but most importantly it also suppresses the acoustical constructive interference. By retaining an overall oblique edge, but also facilitating two longitudinal scattering roots, the DRooTES can establish both the serration and destructive interference mechanisms, respectively and cooperatively. It is also worth pointing out that a DRooTES does not radiate very high frequency noise. A comparison amongst the single-serrated, slit and DRooTES TEs indeed confirms that the DRooTES outperforms the two in many aspects.

Chapter 6

Qualitative Study of the Flow and Noise Mechanisms for a Slit Trailing Edge through CFD

6.1 Introduction

This chapter presents a numerical study into the flow mechanisms that resulted in the phase cancellation at the TE as introduced in Chapter 5. The numerical simulation maintained the same two geometries as presented in Chapter 5 which assessed an aerofoil with and without a slit TE, where the latter is referred to as the baseline TE. The streamwise sizes of the baseline and slit TEs were kept at $H = 15$ mm and the slit tip and root width were $a = 0.3$ mm and $W = 1.7$ mm. A two-dimensional RANS simulation was performed to assess the fluid dynamics of the NACA 65-(12)10 aerofoil, mounted in the acoustic facility at Brunel University London, against experiments, see Sec. 6.3.1. In Sec. 6.3.3 a detailed LES was carried out to examine the time-averaged and instantaneous three-dimensional fluid dynamics of turbulent boundary layer interactions at the slit and baseline TEs.

6.2 Methodology

6.2.1 Hotwire Anemometry

The near flow-field measurements were conducted using a freestream velocity of $U_\infty = 24$ ms^{-1} which corresponded to Re $= 2.4 \times 10^5$. The measurements were performed with a DANTEC miniature single hot-wire straight probe (55P11), where the wire was operated at an over-heat

ratio of 1.8 through CTA. The hot-wire probe was positioned parallel to the flow with the wire oriented in the z-direction (horizontal). The tip of the hotwire was positioned at $x = 0.1$ mm aligned with the lower lip of the open jet nozzle. The hot-wire signals were digitised by a 12-bit A/D convector (ADCPCI) at a sampling frequency of 20 kHz. The hot-wire measurements were carried out for a single component in the y-direction (vertical) from $y = -5$ mm to $y = 105$ mm at a resolution of 0.5 mm.

Post analyses of the near flow-field measurements were conducted to obtain the mean velocity, turbulence intensity and the turbulent integral length scale.

6.2.2 Static Pressure Distribution Measurements

The surface pressure distribution of the NACA 65-(12)10 aerofoil was determined at an AoA of 0° and a freestream velocity of $U_\infty = 24$ ms^{-1}. A pitot static tube was positioned within the freestream jet to obtain the static pressure, whilst the surface static pressure was obtained from eight positions across the pressure and suction surfaces of the aerofoil. The static pressure was measured with a FCO510 digital micro-manometer which has a built-in data logger at 1 Hz for 20 seconds for each static pressure tap. In addition, a Furness pressure scanner was used to change between each pressure tap on the aerofoil.

6.2.3 Computational Details

A. Description of the Simulation Cases

The geometry under investigation was that of the laminar camber NACA 65-(12)10 aerofoil which was previously used in experimental studies at Southampton University and Brunel University London. The measurements of the flow around the blade placed into an open wind tunnel system were performed at Brunel University London's acoustic facility, described in Sec. 3.1. The aerofoil was mounted at 3 cm from the inlet and at an AoA of 0°. In the current experiments, the blade aspect ratio was 1.99, the blade chord-length was 150.4 mm and its spanwise length was 300 mm. The experimental study investigated the effects of two flat plate TE add-ons: the baseline and the slit trailing edge. The three-dimensional numerical simulations were performed my assuming homogeneous flow conditions in the spanwise direction for the baseline TE, while for the representation of the slit TE non-homogeneous spanwise flow conditions needed to be employed. The RANS simulation was carried out using a free-stream velocity of $U_\infty = 24$ ms^{-1}, simulating the effects of the specific jet-like inflow conditions present in the experimental facility at Brunel University London on the flow around the aerofoil in order to be able to use exper-

imental results to validate the numerical results. The two LESs were carried out at $U_\infty = 30$ ms^{-1}, which corresponded to a Re $= 0.309 \times 10^6$, in an open jet system without the effects of the nozzle of the open-jet flow. In addition, to examine the flow characteristics, the boundary layer trip was applied to both sides of the aerofoil to ensure a turbulent flow was observed at the TE.

B. Numerical Method

The computational simulation was performed by a steady-state Reynolds-Average-Navier-Stokes (RANS) equation with a k-omega SST flow solver. Several additional models were applied to the flow solver to improve the result: Production Limiter, Production Kato-Launder, low-Re correction and curvature correction. Further information on the k-omega SST and additional models can be found in the ANSYS 20.2. Manual [112]. The computational method used the SIMPLE pressure-based solver, initially combined with a first-order and subsequently with a second-order upwind scheme. The final result was simulated for 40,000 iterations to obtain a converged solution.

C. Computational Domains, Grid and Boundary Conditions

The description of the computational domain, grid and boundary conditions is outlined in Sec. 3.5.3.

D. RANS k-omega shear stress transport

The computational domain used for the RANS simulation, illustrated in Figure 6.1, was a two-dimensional domain of 0.7 m width and 1.3 m height. The inlet and outlet were located on the left- and right-hand sides of the domain respectively, separated by a distance of $L_x = 4.67$C, where $c_0\_original = 0.15$ m was the aerofoil chord-length. The upper and lower walls were separated by a distance of $L_y = 8.67$C with the aerofoil positioned in the centre of the domain. The inlet was 0.1 m in height with 1 cm lips added across the upper and lower edges of the inlet which allowed the generation of the layers that would form in the experiment on the sides of the nozzle. The outlet was 1.1 m in height. The aerofoil leading edge was positioned at $0.27C$ downstream of the nozzle exit at the mid-point of the inlet, and the exit was positioned at $3.4C$ downstream of the aerofoil TE. To ensure similar flow characteristics to the experiment across the aerofoil, the inlet boundary condition was defined with a turbulence intensity $I = 0.2\%$ and a turbulence integer length scale of $\ell_z = 1 \times 10^{-5}$ m. The velocity profile was modelled by a 7^{th} order polynomial equation, used to interpolate the experimental hot-wire velocity measurements

from the exit of the experimental nozzle, using the user-defined function (UDF), shown in Figure 6.2. The outlet was defined as a pressure outlet with zero pressure gauge and the aerofoil surface and walls were defined with non-slip conditions.

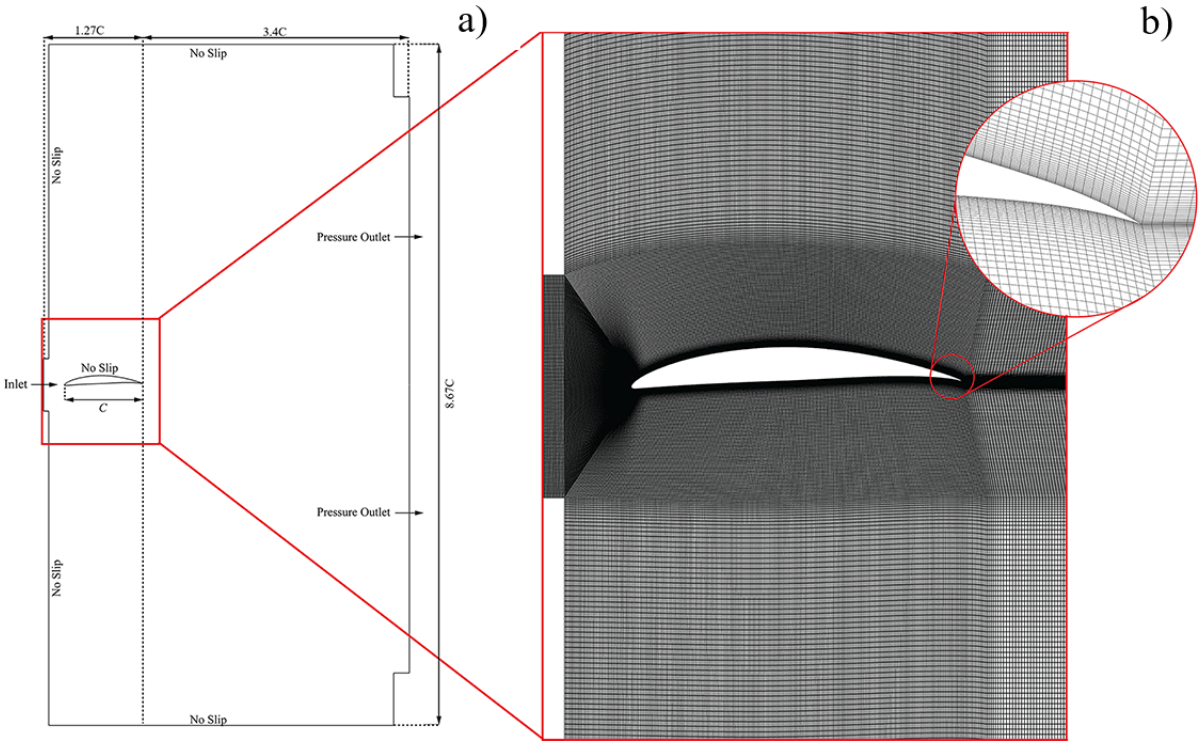

Figure 6.1: Computational domain of the two-dimensional RANS k-omega SST simulation where a) is the computational topology and b) computational mesh.

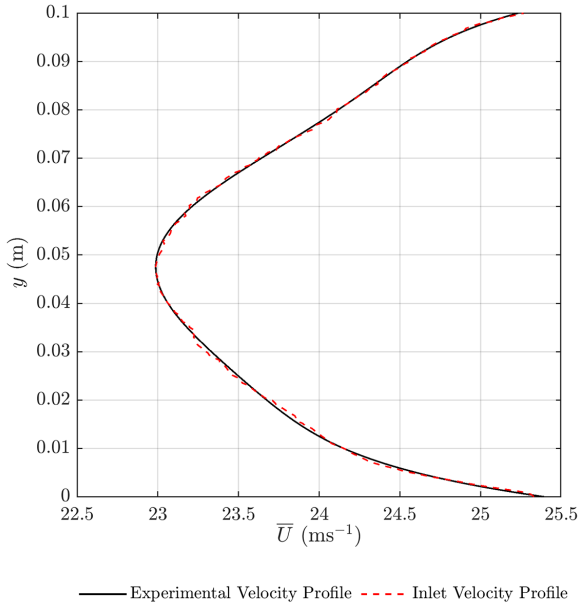

Figure 6.2: Mean streamwise velocity profile of the experimental to the modelled 7^{th} order polynomial curve of the inlet of the open jet wind tunnel nozzle.

The grid generation of a structured quadrilateral C-grid embedded into a H-grid was performed using the ANSYS ICEM CFD software, shown in Figure 6.1b). The structured quadrilateral grid had an orthogonal grid close to the aerofoil surface with a $y^+ = 3.1$, while in the streamwise direction the grid size varied between $x^+ = 50$. The total number of nodes was 453,322.

6.3 Results and Discussion

6.3.1 Experimental Angle for the NACA 65-(12)10 aerofoil

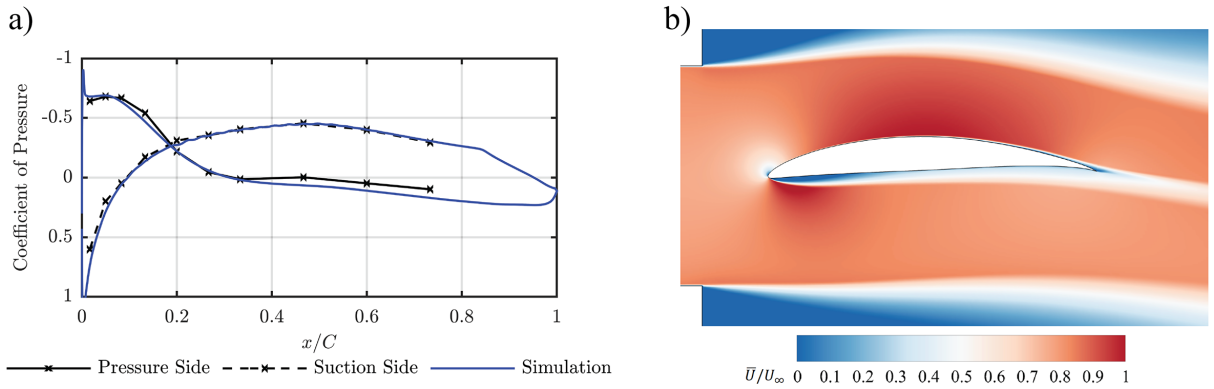

Figure 6.3: Numerical k - omega SST flow solver simulation of flow around the NACA65-(12)10 aerofoil at $U_\infty = 24$ ms^{-1} where a) shows the pressure distribution obtained in the experimental and the numerical results and b) presents the numerically obtained non-dimensional mean u velocity.

Figure 6.3 presents a comparison of the experimental to the numerical results of the NACA 65-(12)10 cambered aerofoil to validate the angle of incidence. The RANS employed a k - omega SST flow solver, as discussed in Sec. 6.2.3; this was set at geometrical AoA of $\alpha = -0.25°$. To match the experimental setup, readers should note that the boundary layer on the aerofoil was not tripped. Figure 6.3a) presents the static pressure distribution of the experimental against the numerical results across both surfaces of the aerofoil. It clearly shows that the numerical results match the experimental results quite well at an AoA of $\alpha = -0.25°$. Readers should note that the AoA relates between the chord line and the flow direction. However, a small increase in the difference between the experimental and numerical pressure coefficients towards the TE of the pressure surface was observed. This phenomenon was the result of the sensitivity of the shear layer of the freestream jet to external factors such as lack of recirculation in the free-stream, which affected the pressure distribution across the aerofoil. The strength of the recirculation

could have been increased by reducing the size of the pressure outlet; which in this study was chosen large enough to avoid any significant recirculation.

Figure 6.3b) shows non-dimensional mean u-velocity contours to illustrate the effects of the nozzle-induced free shear layer on the flow around the NACA 65-(12)10 aerofoil. The presence of a leading-edge separation bubble on the pressure side can be seen between $x/c_0\_original = 0$ to $x/c_0\_original = 0.3$, which can also be observed at the same location in Figure 6.3a). This aerofoil was originally designed as a laminar aerofoil which could explain the forming of the leading-edge bubble and the aerofoil was mounted with an off design angle. This phenomenon is thought to have been a result of a strong adverse pressure gradient induced on the leading edge pressure side resulting from the specific AoA employed. The pressure side boundary layer flow downstream of the leading edge was unable to overcome this strong adverse pressure gradient which resulted in the pressure side leading edge separation bubble. As a result of the separation, transition to fully turbulent flow occurred within the free shear layer with downstream reattachment of the now turbulent flow forming a thick, wake-like flow parallel to the pressure side. The phenomenon of the leading-edge separation bubble is illustrated in Figure 6.4. Furthermore, the presence of the leading-edge separation bubble could have contributed to aerofoil self-noise at the low-to-mid frequency range due to the shedding of large turbulent eddy structures.

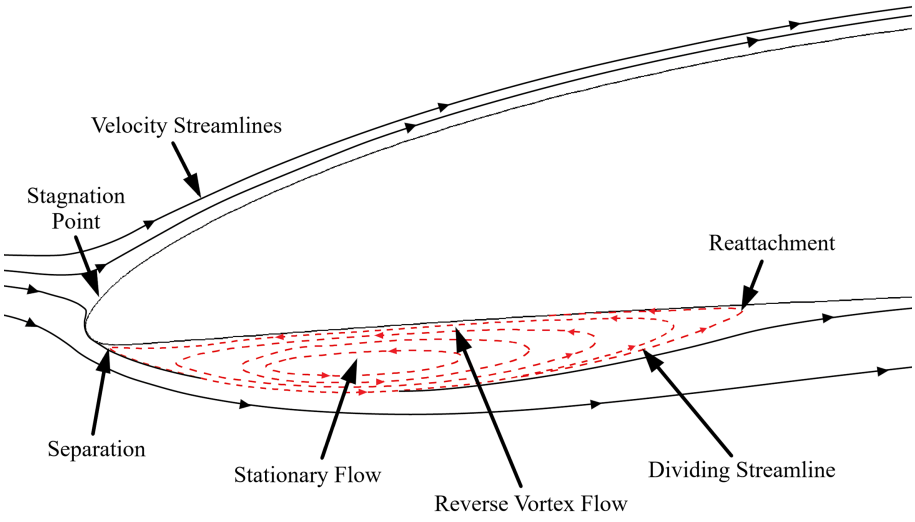

Figure 6.4: Illustration of the leading-edge separation bubble on the NACA 65-(12)10 aerofoil in the x-y plane.

The pressure side showed an increasing expansion angle towards the TE. This expansion angle experienced an adverse pressure gradient which caused the turbulent boundary layer, formed by the separation bubble, to increase in the boundary layer thickness. This phenomenon was confirmed in experimental results in Sec. 4.4. On the suction side, the thickest part of the

laminar aerofoil was at a considerable distance downstream at $x/c_0\_original = 0.5$ from the leading edge. Therefore, the downstream growth of the boundary layer was relatively slow due to the accelerating flow induced by the strong favourable pressure gradient over the first half of the aerofoil. Over the second half of the aerofoil, an adverse pressure gradient took over where the flow decelerated towards the TE and, as a result, the boundary layer became thicker. Figure 6.3b) shows that a separation region occurred at the TE as a result of the adverse pressure gradient.

6.3.2 Validation study of trip location

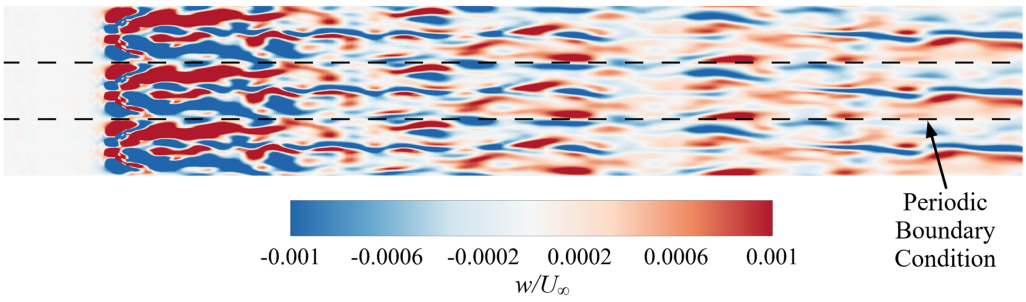

Figure 6.5: Contour map of the instantaneous non-dimensional w velocity component presenting the trip location and flow in the y-z plane on the suction side where the dash line represents the periodic boundary.

So far, the numerical results clearly demonstrated that the NACA 65-(12)10 aerofoil, without add-on flat plate TE and transition point (trip), generated two regions of separation as a result of strong adverse pressure gradients. The next investigation examined the effects of a trip on the suction side, located at 20% of the chord length ($x/c_0\_original = 0.2$), on the flow characteristics of NACA65-(12)10. The boundary layer trip was modelled based on a vortex generator where the blocks were positioned at 30° to the freestream flow at a vertical height of $y = 0.34$ mm corresponding to $y^+ = 31$. Figure 6.5 presents the LES numerical results of the instantaneous non-dimensional spanwise (w) velocity component across the upper surface of the NACA 65-(12)10 aerofoil. Figure 6.5 highlights that the boundary layer was successfully tripped across the upper surface (suction surface) as shown by the variations in the w velocity component downstream of the tripping location. Furthermore, an evaluation of the shape factor shown in Table 6.1 demonstrates that successful transition occurred from laminar to turbulent flow.

Boundary Parameters	Before the trip ($x/c_0 = 0.16$)	After the trip ($x/c_0 = 0.88$)
Displacement thickness (δ_1) (m)	3.48×10^{-4}	9.69×10^{-4}
Momentum thickness (δ_2) (m)	4.00×10^{-5}	5.69×10^{-4}
Shape factor	2.56	1.70

Table 6.1: Boundary layer parameters located before and after the trip on the suction surface at $U_\infty = 30$ ms^{-1}

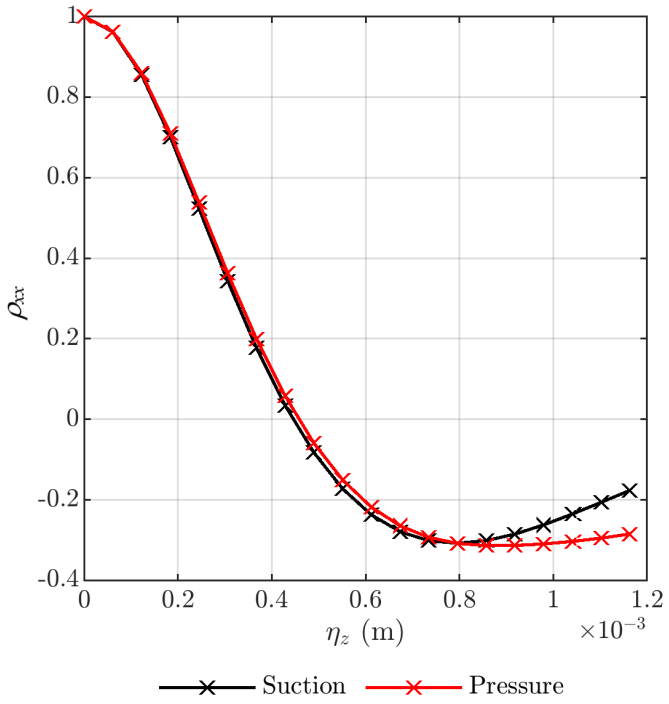

Figure 6.6: Time averaged two-point correlation of the turbulent boundary layer at $x/c_0 = 0.5$ on the suction and pressure surfaces.

Figure 6.6 presents the time-averaged two-point correlation of the turbulent boundary layer on both sides of the aerofoil at $x/c_0 = 0.5$. The results show that the turbulence was not isotropic in the spanwise direction, with the development a three-dimensional turbulent flow. The spanwise turbulent integral length scale, ℓ_z, can be determined from the two-point correlation, auto-correlation, function ρ_{xx} of a hydrodynamic quantity i.e.

$$\ell_z = \int_0^{\eta_x=0} \rho_{xx}(\eta_z) d\eta_z \tag{6.1}$$

In this case instantaneous velocity averaged over time over the span of the aerofoil near the TE. The spanwise turbulent integral length scale on the suction side was found to be $\ell_z = 2.482 \times 10^{-4}$ m , while on the pressure side it was $\ell_z = 2.547 \times 10^{-4}$ m.

6.3.3 Flow Patterns of the Slit Trailing Edge Case

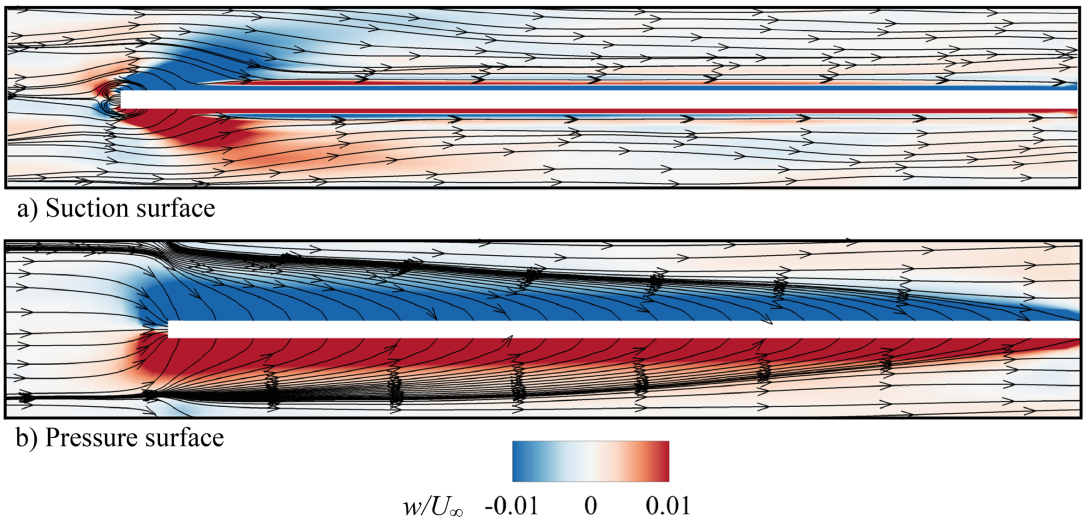

Figure 6.7: Time-averaged near-surface streamlines (friction lines) of the mean velocity combined with contours of the non-dimensional w-velocity on the a) suction surface and the b) pressure surface.

Figure 6.7 presents the time-averaged near-surface streamlines used to visualize the flow patterns on the slit TE where a) is the suction surface and b) is the pressure surface. Figure 6.7a) shows that the mean near-surface flow on the suction side remained parallel to the slit edge. Furthermore, it was unaffected by the influence of the slit gap across the TE apart from the areas near the root and the edge of the slit. Near the root a region of reverse flow can be seen, caused by the entrainment of flow entering through the slit immediately downstream of its root. Further downstream the effects of entrainment of flow through the slit on the near-surface flow pattern becomes much less pronounced and the streamlines become virtually parallel to the slit edge. The w velocity contours, however, do indicate that there still a small amount of entrainment of flow from the suction side, indicating upwash from the slit gap.

Figure 6.7b) shows that one the pressure surface, flow was drawn into the slit opening along the entire slit edge, a process that was driven by the large difference in pressure compared to the suction surface. However, as shown in Figure 6.8, the strength of this pressure difference could be seen weakening downstream along the slit with the direction of the near-surface streamline becoming more and more orientated towards the TE rather than the slit.

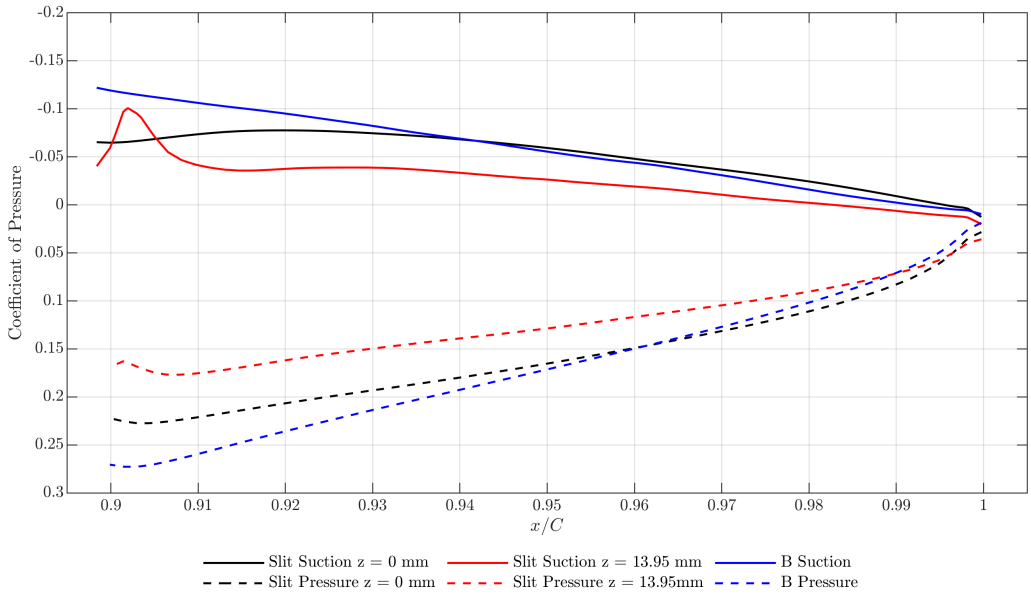

Figure 6.8: Mean coefficients of pressure at the suction and pressure surfaces for the baseline and slit TEs.

Figure 6.8 presents the mean pressure coefficient obtained on the pressure and suction surfaces for the baseline and slit TEs. The results show that the largest pressure difference at the TE occurred at the root location $x/c_0 = 0.9$ for the baseline, whereas for the slit the maximum pressure difference was found to be reduced and reached slightly downstream of the root, at $x/c_0 = 0.91$. As expected, the smallest pressure difference was obtained at the tip of the TE for both the baseline and slit TEs. However, compared to the baseline simulation, the pressure difference at the tip was slightly larger for the slit TE. The peak in the pressure obtained on the suction surface of the slit TE was a result of the initial adjustment to the presence of the slit causing a sudden change in flow conditions. This would explain the strong vertical flow at the root of the slit TE displayed in Figure 6.7, which weakens downstream towards the tip.

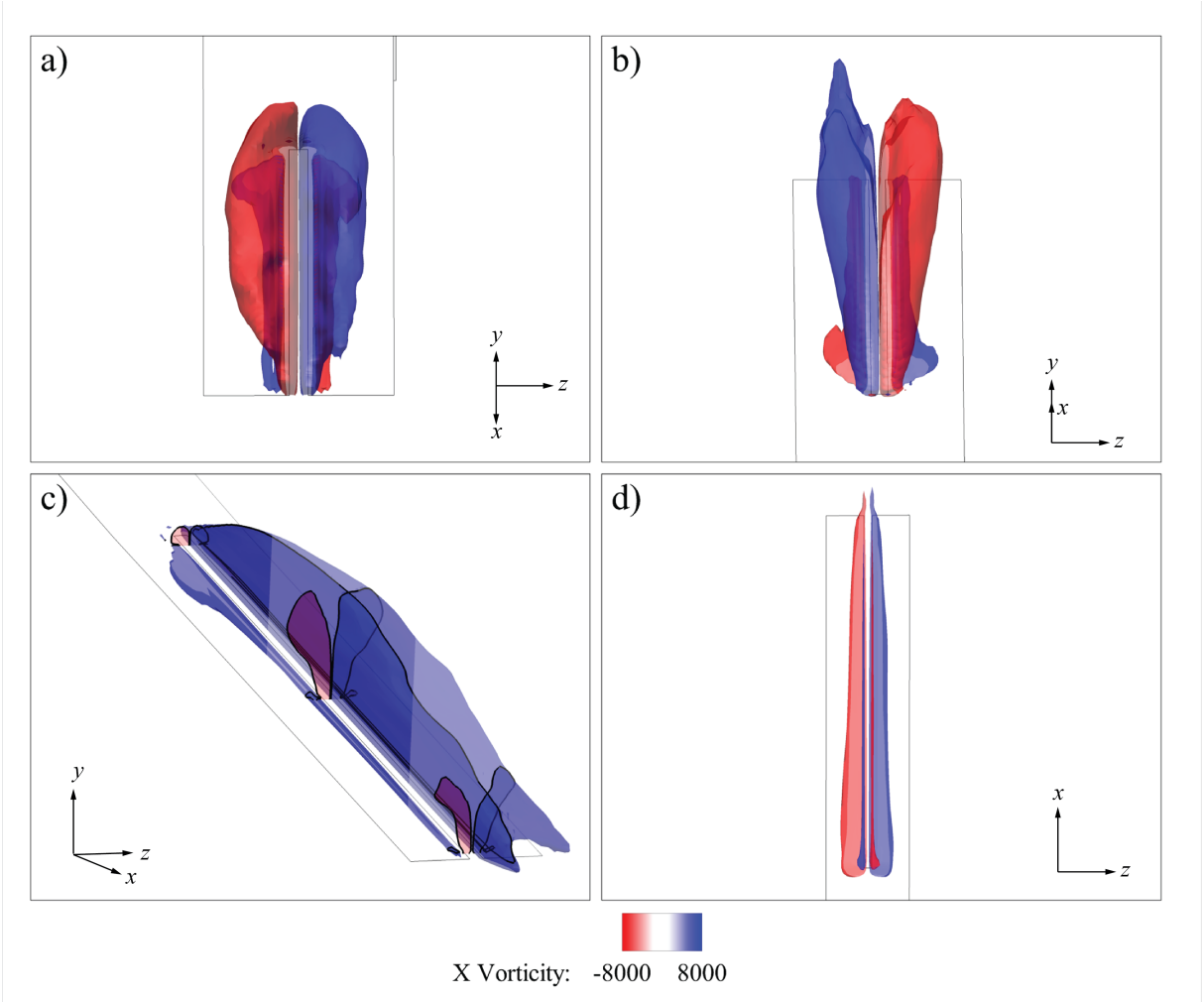

Figure 6.9: Iso-surfaces of the average streamwise vorticity at the slit TE on the suction and pressure surfaces, where a) view from the TE, b) view from the root of the slit, c) three-dimensional view and d) pressure surface streamwise vorticity.

Figure 6.9 shows iso-surfaces of the time-averaged streamwise vorticity located at the slit TE on both sides of the aerofoil. Figure 6.9 indicates two regions of strong streamwise vortices extending across the length of the slit edge from the root to the tip on the suction and pressure surfaces. The secondary streamwise vortices could be seen originating from the root as a result of the strong vertical flow generated by the pressure difference between the pressure and suction surfaces on both sides of the slit, as seen in Figure 6.8. Similar observations within experimental studies describe the phenomena as crossflow or leakage [11, 58, 130]. The vertical flow resulted in the formation of a mushroom shaped flow pattern, similar to a jet flow pattern where two vortices are formed on either side of the slit. These vortices formed on the surface of the TE draw in (entrain) boundary layer flow. Figure 6.9d) shows the strong elongated regions of streamwise vorticity at the pressure surface, along the edges of the slit. This streamwise vorticity was

generated as a result of the strong vertical jet through the slits emanating from the pressure surface.

The cross-sectional y-z plane shown in Figure 6.10 confirmed that the streamwise vortices were generated by the vertical jet flow at the root of the slit. At the mid location, shown in Figure 6.10b), the vortices increased in size in the vertical and spanwise direction as a result of surrounding fluid being entrained into the vortices. In addition, the vortices were seen to displace from the surface of the slits. At the tip location, the vortices reduced in size and returned to the surface of the slit TE, which can be seen in Figure 6.10c).

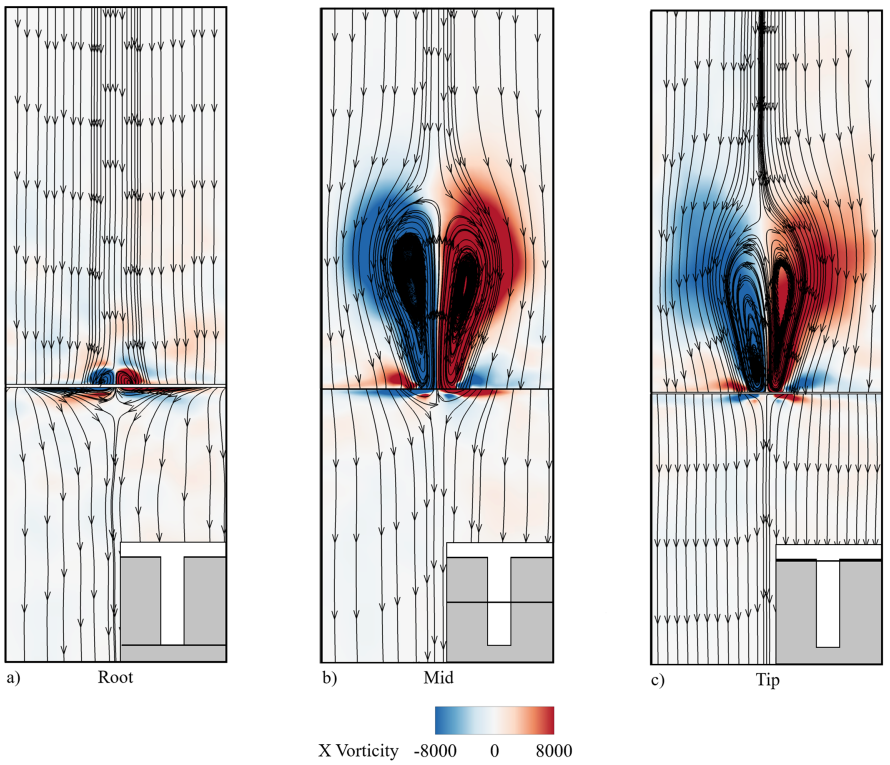

Figure 6.10: Contour map of the mean streamwise vorticity with pathlines of the flow at three locations: a) root, b) mid and c) tip of the slit TE.

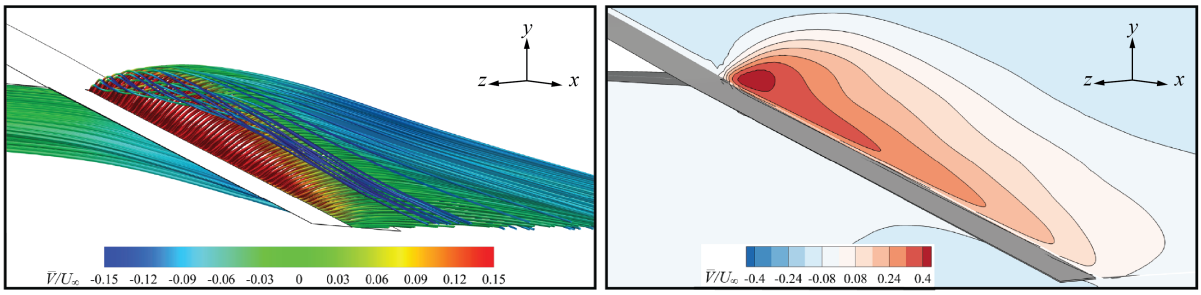

Figure 6.11: Secondary flow patterns generated by the vertical flow in-between the slit teeth on the NACA 65-(12)10 aerofoil with slit TE, where a) mean streamline pattern coloured by the non-dimensional mean v-velocity and b) contour map of non-dimensional mean v-velocity at z = 0.0015 m.

The next investigation examined the secondary flow patterns generated by flow interaction from the pressure to the suction side through the slit gaps. Figure 6.11a) presents the time-averaged pathlines of the flow occurring between both sides of the aerofoil. On the pressure side, the oncoming flow from the surface of the aerofoil main body and the freestream was drawn into the slits as a result of the large pressure gradient between the upper and lower surfaces of the flat plate TE. This was confirmed in Figure 6.8, showing that the pressure difference was maximum at the root and minimum at the tip. The friction velocity on the pressure surface was shown in Figure 6.7b), furthermore, analysis of the boundary layer profiles at three locations is discussed later in Figure 6.12. At the slit gap, the observation of a strong vertical velocity component was noted along the entire length of the slits, illustrated in the contour map of the mean v-component shown in Figure 6.11b). The strength of the vertical component was at its highest at the root and reduced towards the tip of the slits. Moreover, the effects of the vertical jet flow were greatest on the suction side, where the jet ensued orthogonally thereby entraining a significant amount of fluid. The vertical jet also offered additional benefits by introducing more energy into the boundary layer, while breaking up the large eddy structure within the flow. In addition, the vertical flow through the slit induced two counter-rotating streamwise vortices along the edges of the slit.

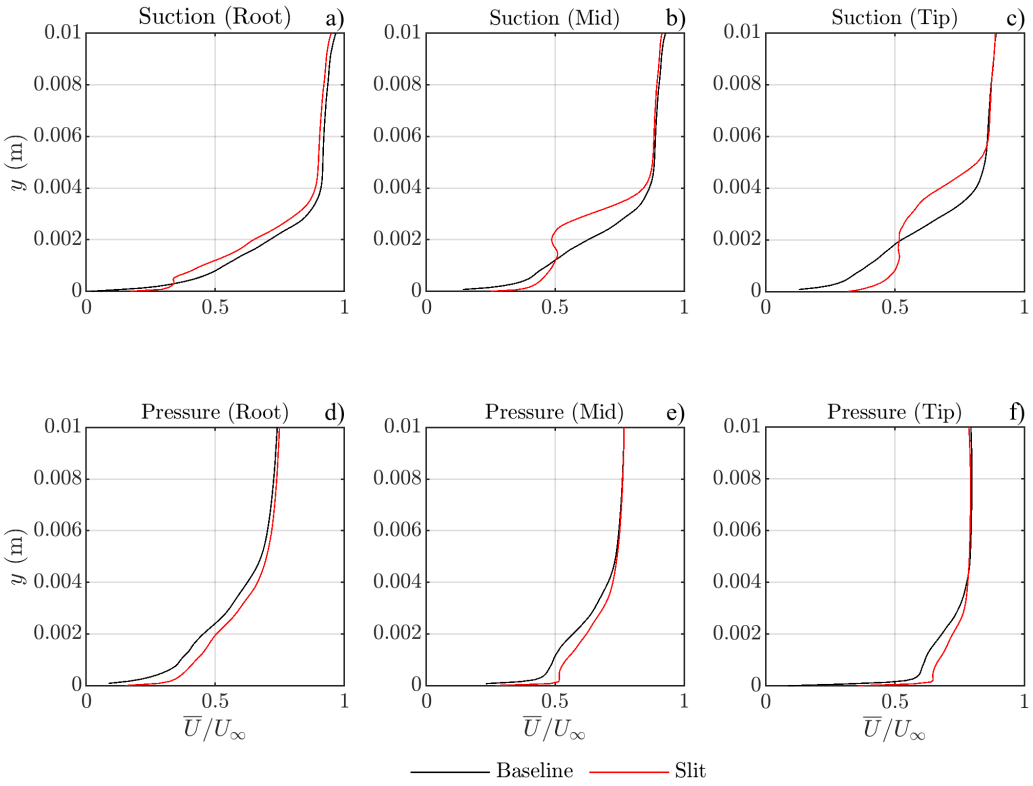

Figure 6.12: Comparison of the non-dimensional boundary layer profiles at the root, mid and tip locations on the slit TE with the corresponding profiles on the baseline TE for the suction surface and the pressure surface at $z = 0.001395$ m.

Figure 6.12 compares the boundary layer profiles for the baseline and slit TEs at the root, mid and tip locations for the suction surface and the pressure surface. The results compare well with the experimental results presented in Sec. 5.3.3.B. with similar profiles demonstrated on the suction and pressure surfaces. Upstream of the slit TE, the presence of the slit had no effect on the turbulent boundary layer profile. However, downstream of the slit TE the presence of the slit gave rise to complex flow patterns. Figure 6.12a) displays similar boundary layer profiles at the root for the baseline and slit TEs. However, close to the wall of the slit TE, evidence of a secondary flow structure was observed with an inflection profile. At the mid and tip locations, the baseline boundary layer became more fully developed with an increase in the momentum and displacement thicknesses. In comparison, the slit TE showed that the inflection profile became more pronounced while the thickness of the boundary layer increased. On the pressure side, seen in Figure 6.12b), the boundary layer profile exhibited a similar profile at the root location for both the baseline and slit TEs. At downstream locations, the baseline TE boundary layer became more fully developed towards the TE. In comparison, the slit TE boundary layer was

found to become thinner towards the tip of the slit TE. This reduction in the boundary layer thickness was the result of the surface flow being drawn into the slit gap, as discussed in Figure 6.7. In terms of acoustic performance, this reduction in the boundary layer thickness proves beneficial as it leads to a reduction of acoustic radiation at the TE.

Next, the convection velocity of the turbulent structures for the baseline and slit TE cases is investigated. A similar approach to obtain the convection velocity via cross-correlation of the velocity in the streamwise direction was performed in Sec. 5.3.3.C. The cross-correlation for the numerical study to acquire the convection velocity within the boundary layer on both sides of the aerofoil for the baseline and slit TEs, at $y = 0.001$ m. The following results were obtained:

		U_c/U_∞
Baseline	Pressure	0.4
	Suction	0.56
Slit	Pressure	0.73
	Suction	0.42

Table 6.2: Results of the cross-correlation for the baseline and Slit TEs on the pressure and suction sides.

The results shown in Table 6.2 confirmed similar observations to the experimental convection velocity found in Sec. 5.3.3C for the slit TE. The baseline TE exhibited similar convection on the suction surface, however, it was noted that on the pressure surface the convection velocity differed in comparison to the experimental results. Readers should be mindful that the numerical simulation was performed without the presence of the jet shear layer generated by the open jet nozzle, or the leading-edge separation bubble. Therefore, the boundary layer characteristics for baseline and slit TEs would be significantly different, which can be confirmed by the experimental results shown in Sec. 5.3.3.B. However, for the slit TE, similar convection velocities were obtained in the numerical simulation and the experiments, indicating that the mechanisms that drive the flow over the slit TE are similar.

Figure 6.13 presents the TKE in x-y planes at three spanwise locations for the slit TE. The results show regions of high TKE at all spanwise locations. These regions were partly generated by production of TKE in the free shear layer that results from the interaction of crossflow through the slit driven by the pressure difference between the pressure and suction sides combined with the secondary flow (vorticity) structures generated at the root, seen in Figure 6.13 b) and c). The shear stress driving the TKE production is likely to be a source of high frequency noise. At the centreline of the slit at $z = 0$ mm (Figure 6.13a) the region of high TKE is the result of the shedding of the secondary vortical structure from the slit into a wake-like flow, which

is subsequently dissipated downstream of the TE. Further information into the shedding of the secondary structure is discussed in Figure 6.16.

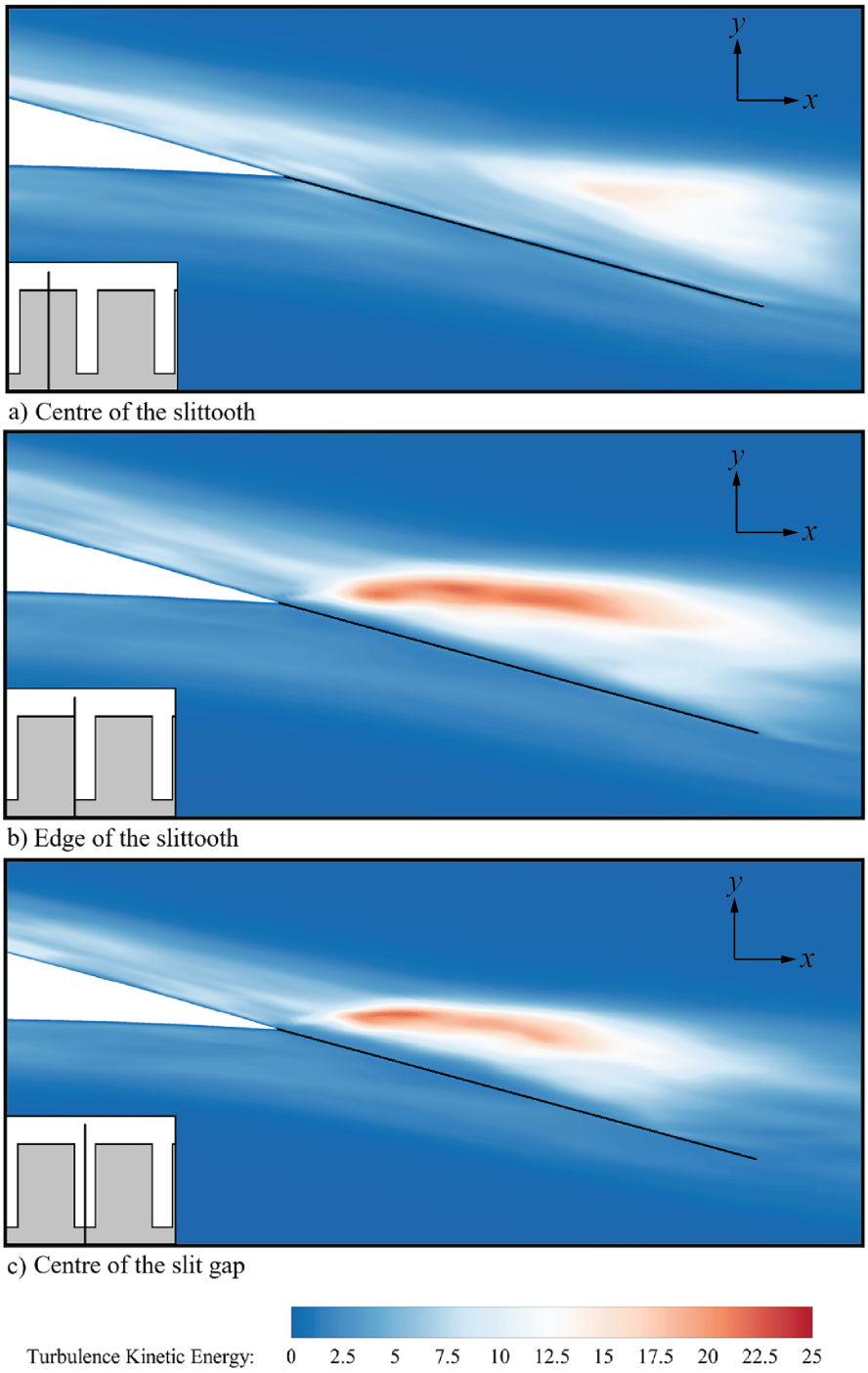

Figure 6.13: TKE contour maps at various x-y planes for the slit TE (–) refers to the TE, where (a) $z = 0$ mm (centre of the slittooth), (b) $z = 1.395$ mm (edge of the slittooth), (c) $z = 1.5$ mm (centre of slit gap), at $U_\infty = 30$ ms^{-1}.

Figure 6.13 presents the TKE at three locations in the x-y planes for the slit TE. The results

indicated the presence high TKE region observed on the suction side at various spanwise locations. These regions of high TKE were generated along the free shear layer and the region of the vortical structures which associated with high shear stress relating to the vertical flow in between the slit, seen in Figure 6.13a) and b). Figure 6.13c) observed a region of high TKE which was the result of the shedding of the secondary structure into a wake-like flow and dissipated downstream of the TE. A comparison of the TKE at three streamwise locations, represent by the black lines in Figure 6.13, are presented Figure 6.14.

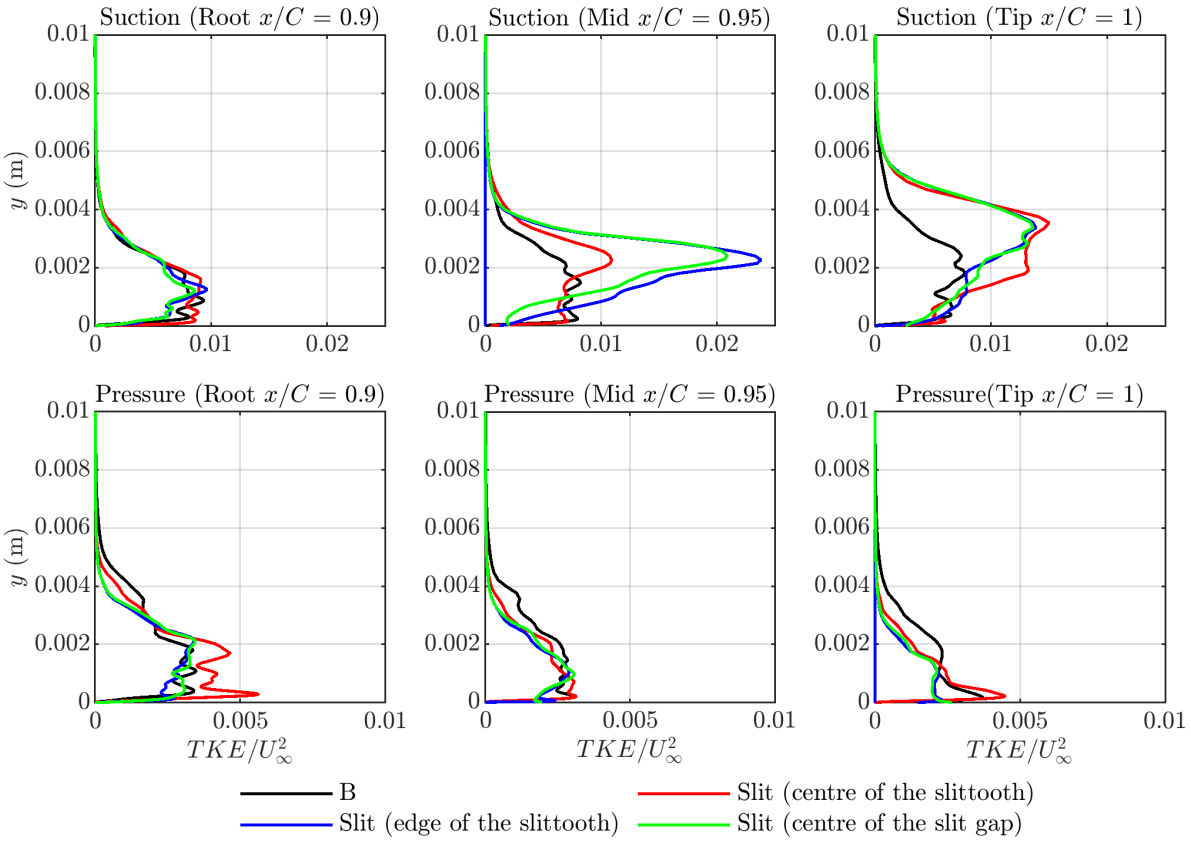

Figure 6.14: Comparison of the non-dimensional TKE ($^{TKE}/_{U_\infty^2}$) across on both sides of the aerofoil at various locations in the streamwise direction at the root ($x = 0.1395$ m), mid ($x = 0.147$ m) and tip ($x = 0.155$ m) the spanwise locations are at $z = 0$ mm (centre of the slit tooth), $z = 1.35$ mm (edge of the slit) and $z = 1.5$ mm (centre of the slit gap).

Figure 6.14 presents a comparison of the non-dimensional turbulence kinetic energy (TKE) across the suction and pressure surfaces. For the baseline TE, the results demonstrated that the suction surface had high levels of TKE of 0.008 in comparison to the pressure surface with a TKE of about 0.003. Furthermore, the TKE levels at the mid and tip remained consistent with the TKE levels observed at the root on the suction surface. In contrast, at the pressure surfaces the TKE levels were redistributed closer to the wall towards the TE. The slit TE exhibited similar

TKE to the baseline at the root for both surfaces. However, at $z = 0$ mm on the pressure surface an additional increase in TKE of 0.006 at the root was shown; this was due to the flow being funneled. At the mid location, high TKE of secondary flow structures was observed at z = 1.35 mm and z = 1.5 mm at the same location as seen in Figure 6.12b. On the pressure surface, the TKE near to the surface was significantly reduced by 0.001 in comparison to $z = 0$ mm, which remained similar to the baseline. This reduction in TKE at $z = 1.35$ mm and $z = 1.5$ mm was a result of the flow being drawn into the slits as shown in Figure 6.7 of the surface flow patterns. At the TE, secondary structures, generated by the vertical flow, were found across the slit TE. However, the TKE witnessed at the mid location reduced towards the TE where it redistributed the energy to the vertical and spanwise components. Also, the pressure surface showed an increase in the TKE for all streamwise locations, where $z = 0$ mm produced high intensity TKE compared to the baseline.

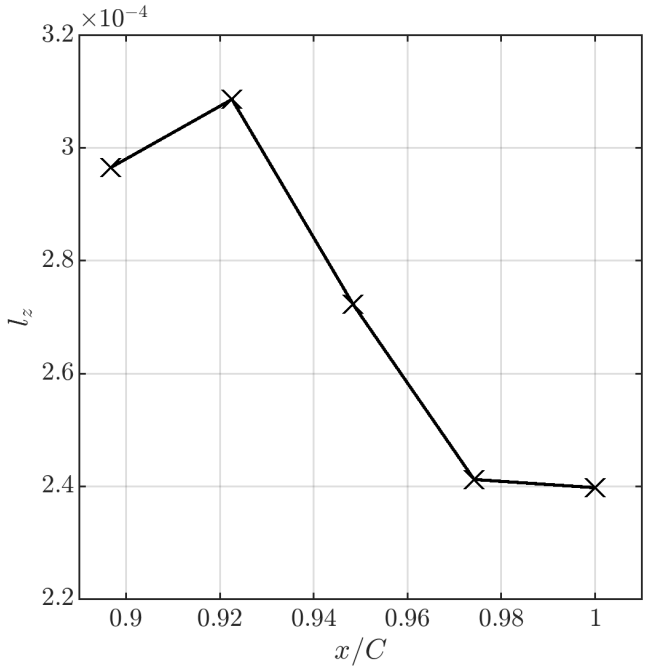

Figure 6.15: Time-averaged spanwise integral length scale, ℓ_z, at various locations downstream of the slit TE.

Figure 6.15 presents the spanwise integral length scale at five downstream locations of the slit TE. The results show that the spanwise integral length scale initially increased to $\ell_z = 3.09 \times 10^{-4}$ at $x/c_0 = 0.925$. Thereafter the spanwise integral length scale became increasingly smaller until it reached a value of $\ell_z = 2.39 \times 10^{-4}$ at $x/c_0 = 1$. This final reduction in spanwise integral length scale towards the TE observed in the present simulations using a slit TE, differs from earlier studies of serrated TEs, where the spanwise integral length scale was found to keep

on increasing towards the tip of the serrations. This different behaviour is attributed to the continuous widening of the serrations towards the TE which possibly gave rise to the continuous increase in spanwise integral length scale. In the slit case, the spanwise integral length scale possibly initially increased to adjust to the presence of the slit and subsequently became smaller due to the loss in spanwise coherence.

6.3.4 Study of Instantaneous Flow Patterns

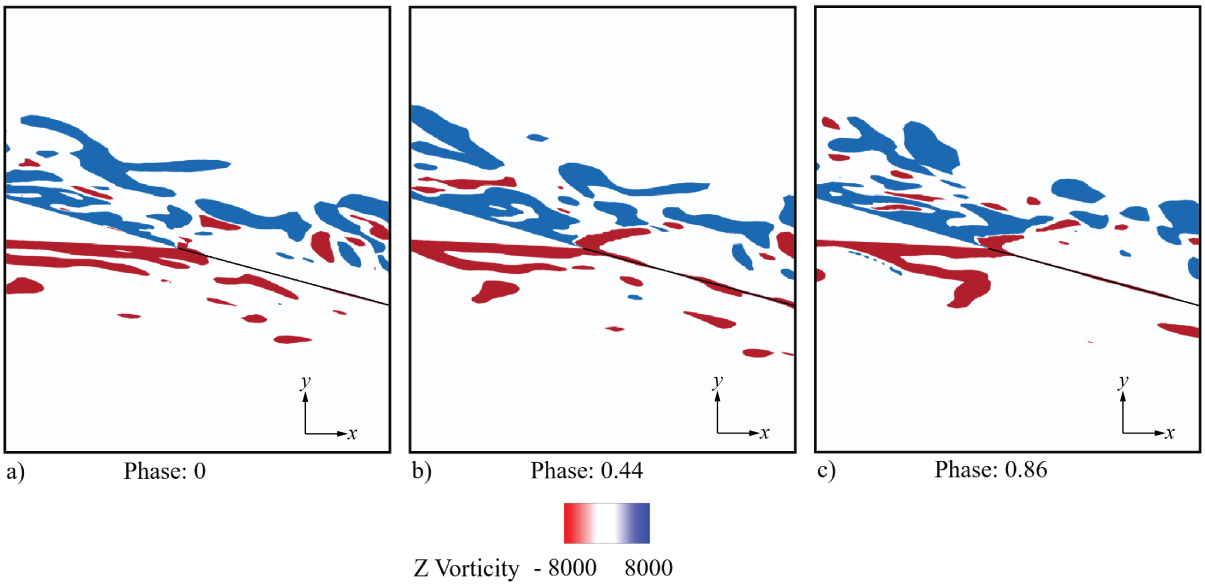

Figure 6.16: Contour maps of the spanwise vorticity as a sequence of timesteps, $0 \leq \psi \leq 1$, in the x-y plane for the slit TE at $z = 1.5$ mm (centre of the slit gap), where complete phase angle, $\psi = 1$, is $t = 3.44 \times 10^{-4}$ seconds.

Figure 6.16 presents the instantaneous spanwise vorticity in the x-y plane for the slit TE at z = 1.5 mm. The results demonstrate two distinct regions of spanwise vorticity of mainly counter-clockwise and mainly clockwise rotating vorticity on the suction and pressure sides respectively. The results in phase one shows the spanwise vorticity structures on the pressure surface being convected by the free-stream towards the root of the slit. As the vorticity interacts with the root of the slit, spanwise vorticity is drawn upwards through the slit to the suction side. As stated previously in Figure 6.11 the vertical velocity through the slit, drawing vorticity from the pressure side upwards, was due to a pressure imbalance between both sides of the aerofoil. The jet of air through the slit also pushes the vorticity originating upstream from the suction surface towards the free stream (as seen in Phase 2). After some time, parts of the elongated vorticity structures are shed and washed downstream. A wake-like turbulent boundary layer is formed, which can be seen in Phase three. The flow patterns described in these three phases tend to

repeat in time and result in the fluctuation and breakdown of the spanwise vorticity originating from both sides of the aerofoil. In addition, Figure 6.13 results also showed that part of the pressure side spanwise vortical structures are transported downstream along the slit from the root to the tip.

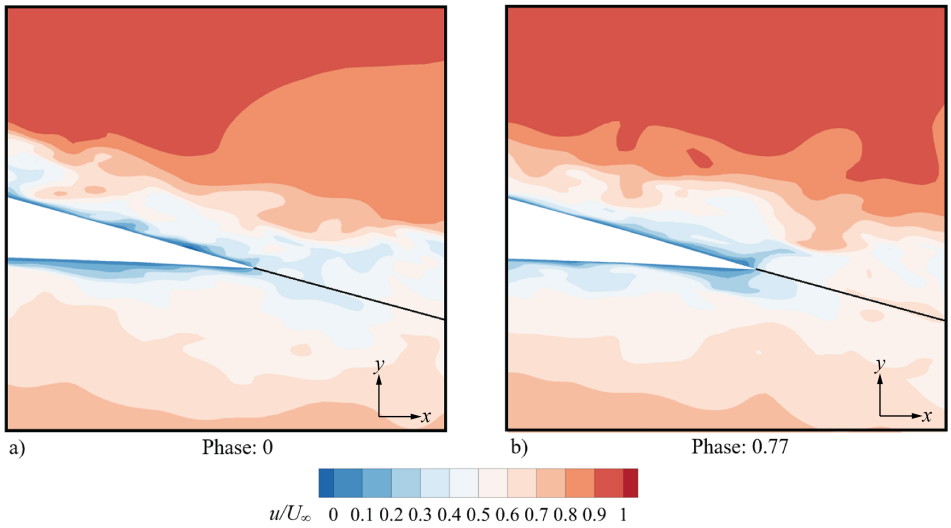

Figure 6.17: Sequence of contour maps in time, $0 \leq \psi \leq 1$, of the non-dimensional u component in the x-y plane at $z = 1.5$ mm for the slit TE, where complete phase angle, $\psi = 1$, is $t = 5.2 \times 10^{-4}$ seconds.

Figure 6.17 shows a sequence in time of u velocity contours in the x-y plane at $z = 1.5$ mm for the slit TE to study the interaction of small regions of separated flow close to the surface on both sides of the aerofoil body. These small areas of recirculating flow are convected along the main aerofoil towards the root of the slit TE. On the suction surface, these structures interact with the root of the slit and are drawn upwards by the vertical jet through the slit as also seen in Figure 6.16. In contrast, on the pressure surface, these structures are either drawn upwards through the slit or transported along the slit while decaying downstream.

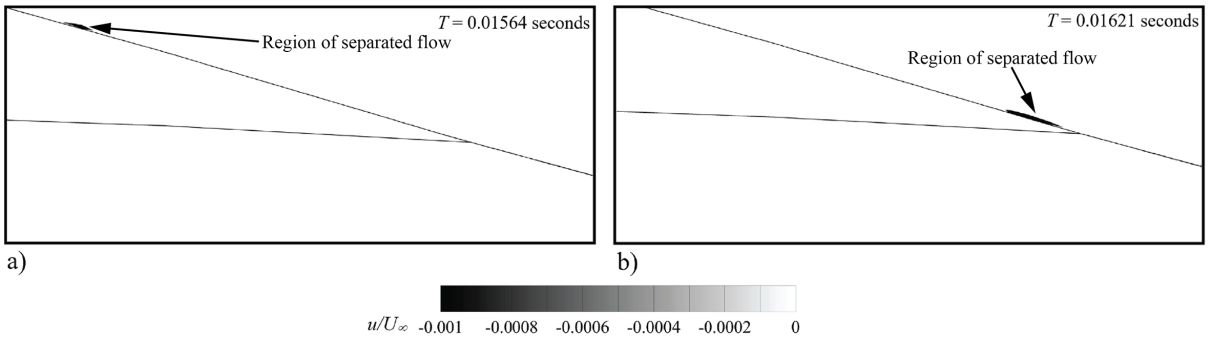

Figure 6.18: Instantaneous time shots of separated flow at the surface of the baseline main aerofoil body of the non-dimensional u velocity component.

Figure 6.18 presents two instances of time showing regions of instantaneous flow separation in the baseline TE case. The results represent two time instances where instantaneous flow at the surface of the main aerofoil has a negative streamwise velocity component. These structures were observed at mid chord towards the TE on the suction surface and at the add-on TE device on the pressure surfaces. This instantaneous separation indicates that the flow was unstable and was likely to separate if sudden changes occurred in flow conditions such as changes in geometries and flow parameters. Figure 6.19 illustrates the NACA 65-(12)10 aerofoil with a flat plate introducing a slight change made to the geometry that immediately leads to the formation of a separation bubble on the suction side at the start of the insertion of the flat plate TE.

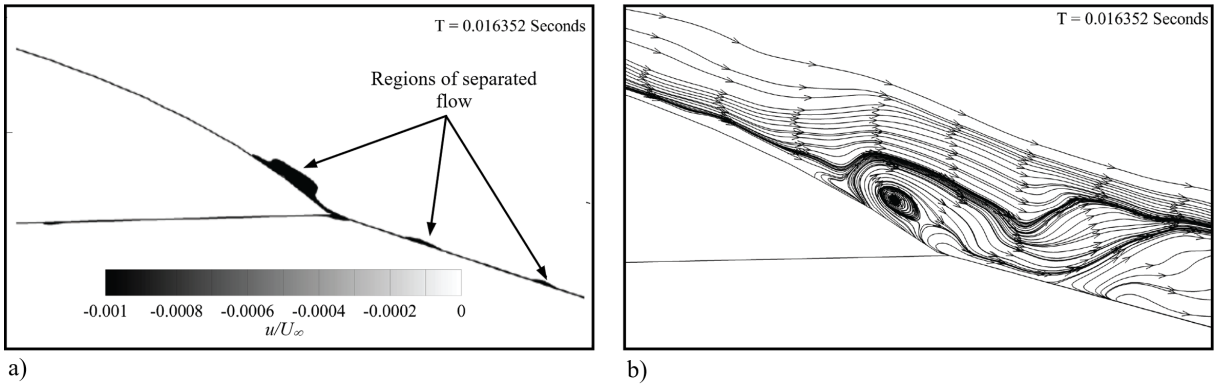

Figure 6.19: Snapshot of (a) the non-dimensional u velocity component and (b) velocity streaklines at mid span showing a region of separated flow at the suction surface of the main baseline aerofoil body.

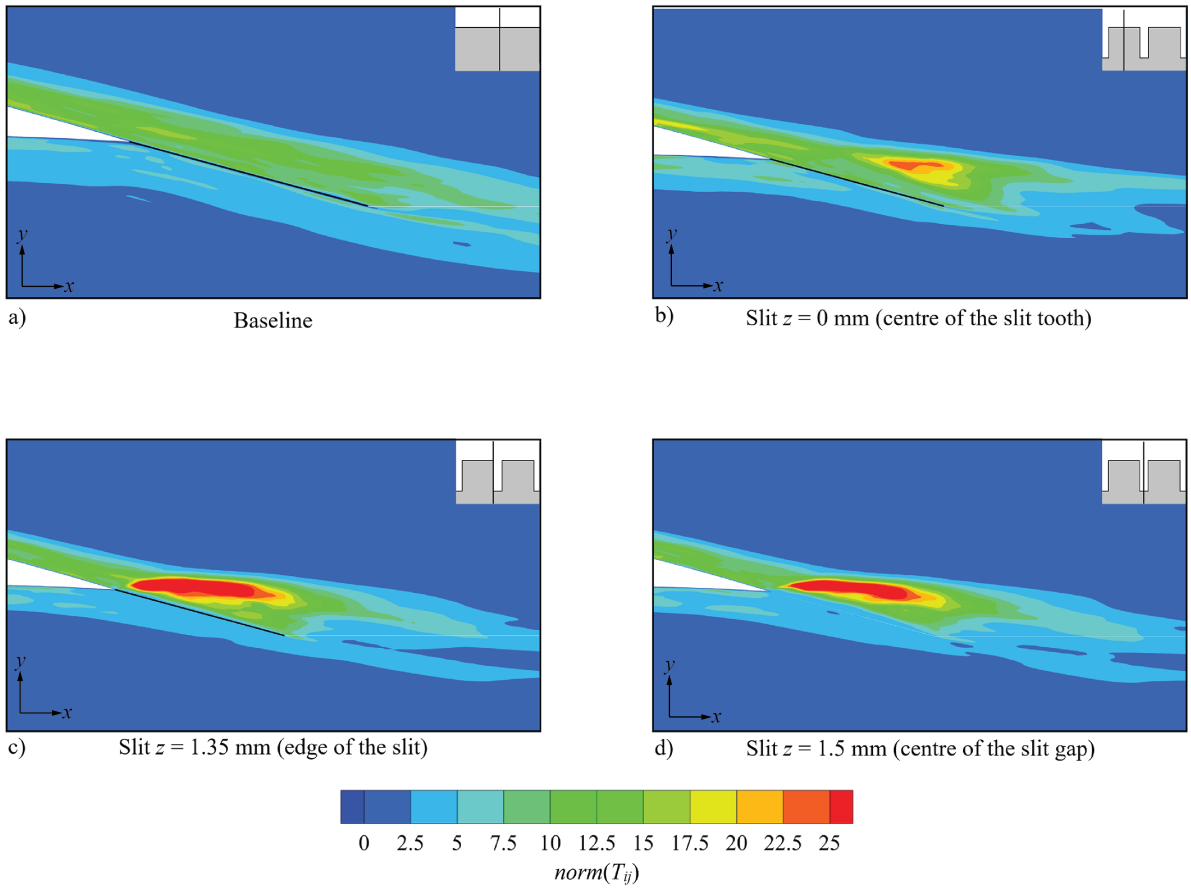

Figure 6.20: Comparison of the Lighthill stress tensor norm of the baseline and slit TEs, where a) baseline, b) slit $z = 0$ mm, c) slit $z = 1.35$ mm and d) slit $z = 1.5$ mm.

Next, the Lighthill stress tensor norm was analysed for the baseline aerofoil against the slit TE at $z = 1.35$ mm and $z = 1.5$ mm. The The Lighthill stress tensor has been defined in Eqn. 6.2. The simulation assumes the flow to be incompressible, therefore the majority of the velocity fluctuations is turbulence and the viscous terms can be ignored. In addition, the flow could be assumed to be homentropic where $(p - p_\infty) = (\rho - \rho_\infty)c_\infty^2$, and that $\rho' \ll \rho_\infty = const$ and $v_i^2 \ll c_\infty^2$. For further information refer to Glegg and Devenport [54]. Therefore, incompressible flow the Lighthill stress tensor norm was defined as:

$$norm(T_{ij}) = \rho \cdot ||u_i u_j|| = \rho \cdot \sqrt{\overline{u'u'}^2 + \overline{v'v'}^2 + \overline{w'w'}^2 + 2 \cdot (\overline{u'v'}^2 + \overline{u'w'}^2 + \overline{v'w'}^2)} \tag{6.2}$$

The results in Figure 6.20 clearly identified the turbulent boundary layer across the suction and pressure surfaces as a potential source of noise. Furthermore, it was noted that the noise emanated from the TE and within the wake. For the slit TE case, the results in Figure 6.20b) showed the highest Lighthill stress tensor values, corresponding to the location of the free shear

layer generated by the interaction between the vertical jet from the slit and the suction side boundary layer. In addition, the counter-rotating vortices were identified as a source of acoustic radiation due to the high shear stress. However, the free shear layer was seen to shed vorticity and was found to dissipate into a wake-like turbulent flow downstream of the slit TE, which in comparison to the baseline case resulted in a reduction of the levels of the Lighthill stress tensor norm.

6.4 Summary

The numerical study that was performed by employing LES examined the flow mechanisms that resulted in phase-cancellation at the TE. The LES assessed two TE geometries from Chapter 5: the baseline and the slit TE, where the amplitude, slit tip and root width were kept at H = 15 mm, a = 0.3 mm and W = 1.7 mm, respectively. A two-dimensional RANS simulation was carried out to assess the flow dynamics around the NACA 65-(12)10 aerofoil in the acoustic facility.

The RANS simulation indicated the presence of a separation bubble on the pressure side at the leading edge. The results showed that the separation bubble resulted in the transition of the laminar to turbulent flow and developed a wake-like flow structure across the pressure side of the aerofoil. The resultant effect led to a thicker boundary layer on the pressure side in comparison to the suction side.

The LES results found the presence of two streamwise counter-rotating vorticial structures on the surface, laying on either side of the slits. Furthermore, the formation of the streamwise vortical structures was caused by the vertical flow through the slits that was generated by the pressure imbalance between the pressure and suction surfaces. The pressure imbalance modified the flow patterns at the surfaces. Furthermore, after an initial increase, the spanwise integral length scale downstream of the root of the slits was observed to gradually reduce in the downstream direction, indicating the reduction in spanwise coherence due to the presence of slits.

Chapter 7

Summary and Future works

This chapter presents a summary of the key findings of the three research projects presented within this thesis. Section 7.1. presents a brief outline of the overall thesis including its aims, objectives and applications. The following sections 7.2 to 7.4. present a description of the experimental setup and the key findings of each individual project. Finally, section 7.5 discusses potential future works.

7.1 Thesis Overview

The thesis entailed investigation into add-on flat plate TEs to ascertain which add-on achieved the largest reduction in TBL-TE noise. It also explored differences in fluid dynamical mechanisms in the near flow field, compared to conventional TE geometry, that could help to explain reductions in noise. The thesis aimed to address the growing issue of noise pollution in the aviation and wind energy sectors, due to increasingly strict noise regulations. Passive flow control devices, such as serrations, have been put in place on the TE of turbine rotors to reduce TBL-TE noise. Despite this, further optimisation of sawtooth devices through new noise mechanisms and geometrical parameters was yet to be investigated.

This research presented an experimental study into aerofoil self-noise radiation obtained by adding variable flap angles to the TE and discussed the flow mechanisms responsible for it. In addition, for the first time, the experimental study investigated an acoustic mechanism known as phase cancellation between two sources physically displaced in a longitudinal direction. Flow and acoustic measurements were obtained, and a new analytical noise prediction model was derived which predicts acoustic trends for a slit TE. Finally, a numerical study investigated the slit TE and discussed the flow mechanisms responsible for the reduction in noise levels.

7.2 Chapter 4 - Exploiting the Misalignment of the Flat Plate Trailing Edge Devices

In Chapter 4 experimental results are presented studying the effect of flap angle misalignment on the self-noise of an aerofoil and its near wake flow field. The main findings of this study are that:

- Serrated and non-serrated TE cases showed a reduction in self-noise at low-to-mid frequencies of up to 7 dB and 4 dB respectively, while at mid-to-high frequencies the self-noise was found to increase. For both serrated and non-serrated TE cases, the largest amplitude of H = 35 mm was found to result in the highest broadband noise reduction.
- The misaligned TE cases produced different noise characteristics when compared to the conventional baseline and SS TEs. It was also experimentally verified that the noise characteristics observed for f $<$ 0.5 kHz and f $>$ 7 kHz for both single- and multi-flapped cases were a result of the TE misalignment for both serrated and non-serrated TEs (Objective: 2). It was suggested that misalignment resulted in a noise increase at high frequencies, especially for negative flap angle (flap down) cases, due to altering the flow condition along the TE (Objective: 2).
- The sawtooth geometry was most effective for the reduction of noise between 500 Hz and 7 kHz for all flapped TE cases. Furthermore, for the single-flapped cases it was found that:
  - for 500 Hz $<$ f $<$ 2 kHz, the noise performance degraded for positive flap angles due to a reduction in crossflow (Objective: 2).
  - for 2 kHz $<$ f $<$ 7 kHz positive flap angles resulted in noise reduction. It was suggested that the positive flap angle 1) reduced the interaction of the crossflow in-between the serrations and secondary flow structures and 2) altered the flow characteristics, such as the blade loading, upstream of the TE (Objective: 2).
  - For 500 Hz $<$ f $<$ 7 kHz, the noise performance degraded for negative flap angles. It was suggested that 1) the increase in strength of the crossflow resulted in cross-contamination and also increased the strength of the secondary flow structures, and 2) the negative flap angle led to an alteration in the blade loading through pressure erosion (Objective: 2).
- Using Single-Flapped-Serrations, IFS, it was found that positive flap angles were most effective for broadband noise reduction at mid-to-high frequencies and less so for low-to-mid frequencies. At negative flap angles, the opposite was found to be true and noise

increases were observed across all frequencies. It was identified that the best configurations of IFS flap-up and flap-down has the smallest flap angles (Objective 1).

- Multi-Flapped-Serration, MFS, and Split-Flapped-Serration, SFS, cases were found to suppress the vortex shedding generated at 800 Hz $<$ f $<$ 2 kHz, by the multi-flapped TEs caused by scattering turbulent structures along the discontinuous edge (Objective: 2).

- Compared to the SS TE, the MFS and SFS TE cases were found to reduce broadband noise for mid-to-high frequencies, while noise increases were observed for the low-to-mid frequencies. The optimum configuration had the smallest flap angles (Objective: 1).

- Superior broadband noise reduction amongst the misaligned TE cases was found for spanwise-wavy- serrations, SWS. The SWS TE produced similar levels of noise reduction as the SS TE across the low-to-mid frequency range. At mid-to-high frequencies, the SWS TE outperformed the SS TE, but was not as good as the MFS and SFS TEs. At high frequencies, the SWS produced slight increases in noise compared to the baseline TE (Objective: 1).

- Flow measurements confirmed the presence of a crossflow/leakage flow in between the serrations. It was suggested that this was caused by the pressure imbalance between both sides of the aerofoil. It was shown that the crossflow strength reduced significantly for positive flap angles and increased for negative flap angles (Objective: 2).

7.3 Chapter 5 - Trailing Edge Geometrical Modification to Achieve Frequency Targeted Self-Noise Reduction by Acoustical Destructive Interference Mechanism

Chapter 5 reports on an extensive experimental study on aerofoil self-noise reduction by phase-cancellation of acoustical pressure waves between two scattering sources that were displaced in the longitudinal direction near the trailing edge. The main results are that:

- That conventional serrated TE exhibited no evidence of target-specific acoustic frequencies due to the multiple scattering sources along the oblique edges of the serrated TE. Therefore, no distinct and characteristic phase angle could be identified. For the slit trailing edge cases it was found that:

- Destructive acoustic interference could be successfully demonstrated for Strouhal numbers of 0.5, 1.5 and so on. Unfortunately, also constructive interference was found for Strouhal

number of 1.0, 2.0 and so on, resulting in noise increases compared to a straight trailing edge (Objective: 3).

- the acoustical scattering of the turbulent hydrodynamic sources along the edge was minimum, while the main scattering sources are only restricted to the root and tip of the slit (Objective: 3).

- For the first time, by tuning the peak frequency, maximum noise reduction can be achieved by adjusting the distance between the root and tip of the slit TE. Furthermore, the experimental and analytical results both positively verify this noise reduction mechanism in what can be regarded as the frequency fine-tuning capability by a passive trailing edge noise control device (Objective: 3).

- Secondary flow structures, that were suggested to be a source of noise radiation at very high frequencies, can be identified by the coherence measurement on the suction side (Objective: 3). For the newly developed so-called Double-Rooted-Trailing-Edge-Serration (DRooTES) device the following results were found:

- It was proven to be capable of exerting acoustical destructive interference, thereby retaining the frequency fine-tuning capability. Moreover, the device suppresses the acoustical constructive interference, by retaining an overall oblique edge and by facilitating two longitudinal scattering roots (Objective: 3).

- Therefore, DRooTES the noise-reduction effects of both the serration and destructive interference mechanisms are combined, without radiating very high frequency noise. A comparison between the single-serrated, the slit and the DRooTES trailing edges indeed confirms that the DRooTES outperforms the other two in many aspects (Objective: 3).

7.4 Chapter 6 - Qualitative Study of the Flow and Noise Mechanisms for a Slit Trailing Edge through CFD

Chapter 6 reports on a qualitative study examining the flow mechanisms of the baseline and slit TE cases that resulted in the phase-cancellation discussed in Chapter 5. The RANS simulation of the flow around a NACA 65-(12)10 aerofoil generated by a jet-like inflow produced a two-dimensional flow field with the following characteristics:

- A separation bubble was found at the leading edge on the pressure surface of the aerofoil, which resulted in laminar-to-turbulent boundary layer transition and the downstream de-

velopment of a thick, wake-like boundary layer flow. The LES of flow over a trailing edge with slits, presented a three-dimensional flow field with the following characteristics::

- Two streamwise counter-rotating vortical structures that were aligned on either side of the slits were identified on the suction surface (Objective: 4).
- The formation of the two streamwise vortical structures was attributed to the pressure imbalance between the pressure and suction surfaces of the aerofoil, resulting in a jet-like flow through the slits from the pressure side to the suction side; thereby modifying the flow patterns at the surfaces (Objective: 4).
- Moving from the root of the slit downstream, after an initial increase, the spanwise integral length gradually reduces, indicating the reduction in spanwise coherence due to the presence of slits (Objective: 4).

The wind tunnel experiments reported in this thesis demonstrate the feasibility of TE devices to reduce aerodynamic noise. Employing such TE devices in real-life applications, such as those presented in Chapter 1, could result in further reductions in noise.

7.5 Future Work

Suggestions for future works are presented below:

1. To investigate the effects of the TE geometries, presented within this thesis, on the aerodynamic performance using a force balance.
2. To carry out detailed DNS or LES simulations, using an acoustic model, of the slit and double-rooted serrated TEs.
3. To perform flow and acoustic measurements for the TE geometries presented in Chapter 5 on a symmetrical aerofoil such as NACA 0012.
4. To further develop an acoustic interference analytical model to improve the accuracy of the noise emission prediction generated from TE self-noise.

References

[1] C. Acre León, D. Ragni, S. Pröbsting, F. Scarano, and J. Madsen. "Flow topology and acoustic emissions of trailing edge serrations at incidence". In: *Experiments in Fluids* 57.5 (2016), pp. 1–17. DOI: 10.1007/s00348-016-2181-1.

[2] Airbus. *Airbus Global market forecast 2010-2029*. Tech. rep. 2010.

[3] R. K. Amiet. "Acoustic radiation from an airfoil in a turbulent stream". In: *Journal of Sound and Vibration* 41.4 (1975), pp. 407–420. DOI: 10.1016/s0022-460x(75)80105-2.

[4] R. K. Amiet. "Noise due to turbulent flow past a trailing edge". In: *Journal of Sound and Vibration* 47.3 (1976), pp. 387–393. ISSN: 0022-460X. DOI: 10.1016/0022-460X(76)90948-2.

[5] F. Anselmet and P. O. Mattei. "A Bit of History". In: *Acoustics, Aeroacoustics and Vibrations*. John Wiley & Sons, Ltd, 2016. Chap. 1, pp. 1–8. ISBN: 9781119178361. DOI: 10.1002/9781119178361.ch1. URL: https://onlinelibrary.wiley.com/doi/abs/10.1002/9781119178361.ch1.

[6] H. Arbey and J. Bataille. "Noise generated by airfoil profiles placed in a uniform laminar flow". In: *Journal of Fluid Mechanics* 134 (1983), pp. 33–47. DOI: 10.1017/S0022112083003201.

[7] New Zealand Wind Energy Association. *How Wind Energy Works: Improvements in Technology*. URL: http://www.windenergy.org.nz/improvements-in-technology. accessed: 30.03.2020.

[8] Air Transport Action Group (ATAG). *The economic and social benefits of air transport 2008*. Tech. rep.

[9] Civil Aviation Authority. *Aviation noise and health | UK Civil Aviation Authority*. URL: https://www.caa.co.uk/Consumers/Environment/Noise/Aviation-noise-and-health/. accessed: 30.03.2020.

[10] F. Avallone, C. A. Leon, S. Pröbsting, K. P. Lynch, and D. Ragni. "Tomographic-PIV investigation of the flow over serrated trailing-edges". In: *54th AIAA Aerospace Sciences Meeting*. American Institute of Aeronautics and Astronautics, 2016. DOI: 10.2514/6.2016-1012.

[11] F. Avallone, S. Pröbsting, and D. Ragni. "Three-dimensional flow field over a trailing-edge serration and implications on broadband noise". In: *Physics of Fluids* 28.11 (2016).

[12] F. Avallone, W. C. P. van der Velden, D. Ragni, and D. Casalino. "Noise reduction mechanisms of sawtooth and combed-sawtooth trailing-edge serrations". In: *Journal of Fluid Mechanics* 848 (2018), pp. 560–591. DOI: 10.1017/jfm.2018.377.

[13] F. Avallone, W.C.P. van der Velden, and D. Ragni. "Benefits of curved serrations on broadband trailing-edge noise reduction". In: *Journal of Sound and Vibration* 400 (2017), pp. 167–177. DOI: 10.1016/j.jsv.2017.04.007.

[14] T. W. Bachmann. "Anatomical, morphometrical and biomechanical studies of barn owls' and pigeons' wings". PhD thesis. RWTH Aachen University, 2010. URL: http://publications.rwth-aachen.de/record/51750/files/3251.pdf.

[15] R. E. Berg. *Acoustics*. 2019. URL: https://www.britannica.com/science/acoustics.

[16] L. Bertsch, M. Snellen, L. Enghardt, and C. Hillenherms. "Aircraft noise generation and assessment: executive summary". In: *CEAS Aeronautical Journal* 10.1 (2019), pp. 3–9. DOI: 10.1007/s13272-019-00384-3.

[17] T. M. Biedermann, T. P. Chong, F. Kameier, and C. O. Paschereit. "Statistical–Empirical Modeling of Airfoil Noise Subjected to Leading-Edge Serrations". In: *AIAA Journal* 55.9 (2017), pp. 3128–3142. DOI: 10.2514/1.J055633. URL: https://doi.org/10.2514/1.J055633.

[18] K. Braun, N. Van der Borg, A. Dassen, F. Doorenspleet, A. Gordner, J. Ocker, and R. Parchen. "Serrated trailing edge noise (STENO)". In: *Proceedings of the European Wind Energy Conference*. Nice, France, James & James (Science Publishers) Ltd., London, UK., 1999.

[19] T.F. Brooks and T.H. Hodgson. "Trailing edge noise prediction from measured surface pressures". In: *Journal of Sound and Vibration* 78.1 (1981), pp. 69–117. ISSN: 0022-460X. DOI: https://doi.org/10.1016/S0022-460X(81)80158-7. URL: http://www.sciencedirect.com/science/article/pii/S0022460X81801587.

[20] M. Cannard, P. Joseph, J. Turner, J. W. Kim, and P. Chaitanya. "Physical mechanisms and performance of slitted leading-edge profiles for the reduction of broadband aerofoil interaction noise". In: *Journal of Sound and Vibration* 473 (2020), p. 115214. ISSN: 0022-460X. DOI: 10.1016/j.jsv.2020.115214.

[21] J. T. Cannon and S. Dostrovsky. "Taylor (1713)". In: *Studies in the History of Mathematics and Physical Sciences*. Springer New York, 1981, pp. 15–22. DOI: 10.1007/978-1-4613-9461-7_3.

[22] P. Chaitanya and P. Joseph. "Slitted leading edge profiles for the reduction of turbulence-aerofoil interaction noise". In: *The Journal of the Acoustical Society of America* 143.6 (2018), pp. 3494–3504. DOI: 10.1121/1.5040972. URL: https://doi.org/10.1121/1.5040972.

[23] K. L. Chandiramani. "Diffraction of evanescent waves, with applications to aerodynamically scattered sound and radiation from unbaffled plates". In: *The Journal of the Acoustical Society of America* 55.1 (1974), pp. 19–29. DOI: 10.1121/1.1919471. URL: https://doi.org/10.1121/1.1919471.

[24] D. M. Chase. "Noise Radiated from an Edge in Turbulent Flow". In: *AIAA Journal* 13.8 (1975), pp. 1041–1047. ISSN: 0001-1452. DOI: 10.2514/3.60502.

[25] D. M. Chase. "Sound Radiated by Turbulent Flow off a Rigid Half-Plane as Obtained from a Wavevector Spectrum of Hydrodynamic Pressure". In: *The Journal of the Acoustical Society of America* 52.3B (1972), pp. 1011–1023. DOI: 10.1121/1.1913170. URL: https://doi.org/10.1121/1.1913170.

[26] Tze Pei Chong, Alexandros Vathylakis, Archie McEwen, Foster Kemsley, Chioma Muhammad, and Saarim Siddiqi. "Aeroacoustic and Aerodynamic Performances of an Aerofoil Subjected to Sinusoidal Leading Edges". In: *21st AIAA/CEAS Aeroacoustics Conference*. American Institute of Aeronautics and Astronautics, 2015. DOI: 10.2514/6.2015-2200. URL: https://arc.aiaa.org/doi/abs/10.2514/6.2015-2200.

[27] European Commission. *Communication from the Commission to The European Parliament, The Council, The European Economic And Social Committee And The Committee Of The Regions: A Roadmap for moving to a competitive low carbon economy in 2050*. Tech. rep. European Environment Agency, 2011. URL: http://eur-lex.europa.eu/LexUriServ/LexUriServ.do?uri=COM:2011:0112:FIN:EN:PDF.

[28] G. Corbetta, European Wind Energy Association, A. Ho, and I. Pineda. *Wind energy scenarios for 2030*. Tech. rep. European Wind Energy Association, 2015.

[29] G. M. Corcos. "Resolution of Pressure in Turbulence". In: *The Journal of the Acoustical Society of America* 35.2 (1963), pp. 192–199. DOI: 10.1121/1.1918431. URL: https://doi.org/10.1121/1.1918431.

[30] G.M Corcos. *Pressure fluctuations in shear flows*. 183 2. University of California, Institute of Engineering Research, 1962.

[31] T. Corke and R. Nelson. *Wind Energy Design*. 1st ed. Vol. 1. Taylor & Francis Ltd, Apr. 12, 2018. 326 pp. ISBN: 1138096024. DOI: 10.1201/b22301. URL: https://www.ebook.de/de/product/33213221/thomas_corke_robert_nelson_wind_energy_design.html.

[32] D. G. Crighton and F. G. Leppington. "Radiation properties of the semi-infinite vortex sheet: the initial-value problem". In: *Journal of Fluid Mechanics* 64.2 (1974), pp. 393–414. DOI: 10.1017/S0022112074002461.

[33] D. G. Crighton and F. G. Leppington. "Scattering of aerodynamic noise by a semi-infinite compliant plate". In: *Journal of Fluid Mechanics* 43.4 (1970), pp. 721–736. DOI: 10.1017/S0022112070002690.

[34] D. G. Crighton and M. J. Lighthill. "Radiation properties of the semi-infinite vortex sheet". In: *Proceedings of the Royal Society of London. A. Mathematical and Physical Sciences* 330.1581 (1972), pp. 185–198. DOI: 10.1098/rspa.1972.0139. URL: https://royalsocietypublishing.org/doi/abs/10.1098/rspa.1972.0139.

[35] N. Curle and M. J. Lighthill. "The influence of solid boundaries upon aerodynamic sound". In: *Proceedings of the Royal Society of London. Series A. Mathematical and Physical Sciences* 231.1187 (1955), pp. 505–514. DOI: 10.1098/rspa.1955.0191.

[36] T. Dassen, R. Parchen, J. Bruggeman, and F. Hagg. "Results of a wind tunnel study on the reduction of airfoil self-noise by the application of serrated blade trailing edges". In: *Proceedings of the European Wind Energy Conference*. NLR-TP-1996-350. 1996, pp. 800–803. URL: http://hdl.handle.net/10921/1359.

[37] S. S. Davis. "Theory of Discrete Vortex Noise". In: *AIAA Journal* 13.3 (1975), pp. 375–380. DOI: 10.2514/3.49707. URL: https://doi.org/10.2514/3.49707.

[38] L. Debnath. "A short biography of Joseph Fourier and historical development of Fourier series and Fourier transforms". In: *International Journal of Mathematical Education in Science and Technology* (2011), pp. 1–24. DOI: 10.1080/0020739X.2011.633712.

[39] G. Desquesnes, M. Terracol, and P. Sagaut. "Numerical investigation of the tone noise mechanism over laminar airfoils". In: *Journal of Fluid Mechanics* 591 (2007), pp. 155–182. DOI: 10.1017/S0022112007007896.

[40] EASA. *EASA certification noise levels*. Tech. rep. 2018.

[41] EASA. *European Aviation Environmental Report 2019*. Tech. rep. 2019. DOI: 10.2822/309946. URL: https://www.easa.europa.eu/eaer/system/files/usr_uploaded/219473_EASA_EAER_2019_WEB_HI-RES_190311.pdf.

[42] MTU Aero Engines. *On the horizon: Whispering jets*. Tech. rep. 2012. URL: https://www.mtu.de/fileadmin/EN/7_News_Media/2_Media/2_MTU_Report/PDFs/Report_2012_2.pdf.

[43] Department of the Environment. *Draft Planning Policy Statement 18 Renewable Energy*. Tech. rep. 2007. URL: https://www.planningni.gov.uk/de/index/policy/planning_statements_and_supplementary_planning_guidance/pps18-draft-renewable-energy.pdf.

[44] Association of European Airlines. *Delivering a bright future for European Aviation and Passengers. 5 year Strategic Plan 2010-2014*. Tech. rep. 2010.

[45] J. H. Ferziger and M. Perić. *Computational Methods for Fluid Dynamics*. Berlin New York: Springer Berlin Heidelberg, 2002. ISBN: 9783540420743. DOI: 10.1007/978-3-642-56026-2.

[46] J. E. Ffowcs Williams and L. H. Hall. "Aerodynamic sound generation by turbulent flow in the vicinity of a scattering half plane". In: *Journal of Fluid Mechanics* 40.4 (1970), pp. 657–670. DOI: 10.1017/s0022112070000368.

[47] A. Finez, M. Jacob, E. Jondeau, and M. Roger. "Broadband Noise Reduction with Trailing Edge Brushes". In: *16th AIAA/CEAS Aeroacoustics Conference*. American Institute of Aeronautics and Astronautics, 2010. DOI: 10.2514/6.2010-3980.

[48] M. R. Fink and D. A. Bailey. *Airframe noise reduction studies and clean-airframe noise investigation*. Tech. rep. NASA, 1980.

[49] S. Finnveden, F. Birgersson, U. Ross, and T. Kremer. "A model of wall pressure correlation for prediction of turbulence-induced vibration". In: *Journal of Fluids and Structures* 20.8 (2005), pp. 1127–1143. ISSN: 0889-9746. DOI: https://doi.org/10.1016/j.jfluidstructs.2005.05.012. URL: http://www.sciencedirect.com/science/article/pii/S0889974605000885.

[50] D. H. Geiger. "Comparative Analysis of Serrated Trailing Edge Designs on Idealized AircraftEngine Fan Blades for Noise Reduction". MA thesis. Virginia Tech, 2004.

[51] T Gerhard, S Erbslöh, and T Carolus. "Reduction of airfoil trailing edge noise by trailing edge blowing". In: *Journal of Physics: Conference Series* 524 (2014), p. 012123. DOI: 10.1088/1742-6596/524/1/012123. URL: https://doi.org/10.1088%2F1742-6596%2F524%2F1%2F012123.

[52] M. Germano, U. Piomelli, P. Moin, and W. H. Cabot. "A dynamic subgrid-scale eddy viscosity model". In: *Physics of Fluids A: Fluid Dynamics* 3.7 (1991), pp. 1760–1765. DOI: 10.1063/1.857955.

[53] T. Geyer, E. Sarradj, and C. Fritzche. "Measuring owl flight noise". In: *Institute of NoiseControl Engineering*. 2014, pp. 183–198.

[54] S. Glegg and W. Devenport. "Chapter 4 - Lighthill's acoustic analogy". In: *Aeroacoustics of Low Mach Number Flows*. Ed. by Stewart Glegg and William Devenport. Academic Press, 2017, pp. 73–93. ISBN: 978-0-12-809651-2. DOI: https://doi.org/10.1016/B978-0-12-809651-2.00004-7. URL: http://www.sciencedirect.com/science/article/pii/B9780128096512000047.

[55] J. P. Gostelow, N. Melwani, and G. J. Walker. "Effects of Streamwise Pressure Gradient on Turbulent Spot Development". In: *Journal of Turbomachinery* 118.4 (1996), pp. 737–743. ISSN: 0889-504X. DOI: 10.1115/1.2840929. URL: https://doi.org/10.1115/1.2840929.

[56] R. R. Graham. "The Silent Flight of Owls". In: *The Journal of the Royal Aeronautical Society* 38.286 (1934), pp. 837–843. DOI: 10.1017/S0368393100109915.

[57] M. Gruber. "Airfoil noise reduction by edge treatments". PhD Thesis. University of Southampton, 2012. URL: https://eprints.soton.ac.uk/349012/.

[58] M. Gruber, P. F. Joseph, and T. P. Chong. "On the mechanisms of serrated airfoil trailing edge noise reduction". In: *17th AIAA/CEAS Aeroacoustics Conference*. AIAA Paper No. 2011-2781. June 2011. DOI: 10.2514/6.2011-2781.

[59] M. Gruber, P. Joseph, and T. P. Chong. "Experimental Investigation of Airfoil Self Noise and Turbulent Wake Reduction by the use of Trailing Edge Serrations". In: *16th AIAA/CEAS Aeroacoustics Conference*. American Institute of Aeronautics and Astronautics, 2010. DOI: 10.2514/6.2010-3803.

[60] F. Hagg, G. A. M. Van Kuik, R. Parchen, N. J. C. M. Van de Borg, and R. Watson. "Noise reduction on a 1 MW size wind turbine with a serrated trailing edge, European wind energy conference". In: *EWEC -CONFERENCE-, European wind energy conference*. Irish Wind Energy Association; 1998, pp. 165–168. ISBN: 0953392201. URL: https://www.tib.eu/de/suchen/id/BLCP%3ACN027427470.

[61] K. L. Hansen, R. M. Kelso, and B. B. Dally. "Performance Variations of Leading-Edge Tubercles for Distinct Airfoil Profiles". In: *AIAA Journal* 49.1 (2011), pp. 185–194. DOI: 10.2514/1.J050631. URL: https://doi.org/10.2514/1.J050631.

[62] M. Herr. "Design Criteria for Low-Noise Trailing-Edges". In: *13th AIAA/CEAS Aeroacoustics Conference (28th AIAA Aeroacoustics Conference)*. American Institute of Aeronautics and Astronautics, 2007. DOI: 10.2514/6.2007-3470.

[63] M. Herr and W. Dobrzynski. "Experimental Investigations in Low-Noise Trailing Edge Design." In: *AIAA Journal* 43.6 (2005), pp. 1167–1175. DOI: 10.2514/1.11101.

[64] M. S. Howe. "Contributions to the theory of aerodynamic sound, with application to excess jet noise and the theory of the flute". In: *Journal of Fluid Mechanics* 71.4 (1975), pp. 625–673. DOI: 10.1017/S0022112075002777.

[65] M. S. Howe. "Noise produced by a sawtooth trailing edge". In: *The Journal of the Acoustical Society of America* 90.1 (1991), pp. 482–487. DOI: 10.1121/1.401273. URL: https://doi.org/10.1121/1.401273.

[66] M. S. Howe. "The effect of forward flight on the diffraction radiation of a high speed jet". In: *Journal of Sound and Vibration* 50.2 (1977), pp. 183–193. ISSN: 0022-460X. DOI: 10.1016/0022-460x(77)90353-4. URL: http://www.sciencedirect.com/science/article/pii/0022460X77903534.

[67] M. S. Howe. "The influence of vortex shedding on the generation of sound by convected turbulence". In: *Journal of Fluid Mechanics* 76.4 (1976), pp. 711–740. DOI: 10.1017/S0022112076000864.

[68] M.S. Howe. "A review of the theory of trailing edge noise". In: *Journal of Sound and Vibration* 61.3 (1978), pp. 437–465. ISSN: 0022-460X. DOI: 10.1016/0022-460x(78)90391-7. URL: http://www.sciencedirect.com/science/article/pii/0022460X78903917.

[69] M.S. Howe. "Aerodynamic noise of a serrated trailing edge". In: *Journal of Fluids and Structures* 5.1 (1991), pp. 33–45. ISSN: 0889-9746. DOI: 10.1016/0889-9746(91)80010-B. URL: http://www.sciencedirect.com/science/article/pii/088997469180010B.

[70] J. Hurault, A. Gupta, E. Sloth, N. Nielsen, A. Borgoltz, and P. Ravetta. "Aeroacoustic wind tunnel experiment for serrated design optimisation and its application to a wind turbine rotor". In: *6th International Meeting on Wind Turbine Noise*. Vol. 39. 2015, pp. 651–660. DOI: 10.1260/0309-524x.39.6.651.

[71] ICAO. *Report of the Second CAEP Noise Technology Independent Expert Panel — Novel Aircraft-NoiseTechnology Review and Medium- and Long-term Noise Reduction Goals, Doc 10017*. Tech. rep. International Civil Aviation Organization, 2014.

[72] WindEurope Business Intelligence, Daniel. Fraile, and Ariola Mbistrova. *Wind in power 2017 - Annual combined onshore and offshore wind energy statistics*. Tech. rep. WindEurope, 2018. URL: https://windeurope.org/wp-content/uploads/files/about-wind/statistics/WindEurope-Annual-Statistics-2017.pdf.

[73] H. Johari, C. Henoch, D. Custodio, and A. Levshin. "Effects of Leading-Edge Protuberances on Airfoil Performance". In: *AIAA Journal* 45.11 (2007), pp. 2634–2642. DOI: 10.2514/1.28497. URL: https://doi.org/10.2514/1.28497.

[74] M. A. Johnstone. "Aristotle on Sounds". In: *British Journal for the History of Philosophy* 21.4 (2013), pp. 631–648. DOI: 10.1080/09608788.2013.792239. URL: https://doi.org/10.1080/09608788.2013.792239.

[75] D. S. Jones. "Aerodynamic Sound Due to a Source Near a Half-Plane". In: *IMA Journal of Applied Mathematics* 9.1 (1972), pp. 114–122. ISSN: 0272-4960. DOI: 10.1093/imamat/9.1.114. URL: https://doi.org/10.1093/imamat/9.1.114.

[76] L. Jones and R. Sandberg. "Numerical Investigation of Airfoil Self-Noise Reduction by Addition of Trailing-Edge Serrations". In: *16th AIAA/CEAS Aeroacoustics Conference*. Stockholm, Sweden, 2010. DOI: 10.2514/6.2010-3703. URL: https://arc.aiaa.org/doi/abs/10.2514/6.2010-3703.

[77] A. Juknevicius and T. P. Chong. "On the spatial-temporal development of synthetic turbulent boundary layer on a serrated trailing edge". In: *25th AIAA/CEAS Aeroacoustics Conference*. Delft, The Netherlands: American Institute of Aeronautics and Astronautics, 2019. DOI: 10.2514/6.2019-2457.

[78] T. Kellner. *How Loud is a Wind Turbine?* 2014. URL: https://www.ge.com/reports/post/92442325225/how-loud-is-a-wind-turbine/. accessed: 30.03.2020.

[79] J. W. Kim, S. Haeri, and P. F. Joseph. "On the reduction of aerofoil–turbulence interaction noise associated with wavy leading edges". In: *Journal of Fluid Mechanics* 792 (2016), pp. 526–552. DOI: 10.1017/jfm.2016.95.

[80] A. M. Knepper. "Examination of three candidate technologies for high-lift devices on an aircraft wing". PhD thesis. Cranfield University, 2005. URL: http://hdl.handle.net/1826/1058.

[81] L. D. Knopper and C. A. Ollson. "Health effects and wind turbines: A review of the literature". In: *Environmental Health* 10.1 (2011), pp. 78–88. DOI: 10.1186/1476-069x-10-78.

[82] R. A. Kroeger, H. D. Grushka, and T. C Helvey. "Low speed aerodynamics for ultra-quiet flight." In: *Technical Report TR* (1971), pp. 971–75.

[83] C. Arce León, R. Merino-Martínez, S. Pröbsting, D. Ragni, and F. Avallone. "Acoustic Emissions of Semi-Permeable Trailing Edge Serrations". In: *Acoustics Australia* 46.1 (2017), pp. 111–117. DOI: 10.1007/s40857-017-0093-8.

[84] H. Levine. "Acoustical Diffraction Radiation". In: *The Journal of the Acoustical Society of America* 52.4A (1972), pp. 1092–1092. DOI: 10.1121/1.1913217. URL: https://doi.org/10.1121/1.1913217.

[85] M. J. Lighthill. "On sound generated aerodynamically II. Turbulence as a source of sound". In: *Proceedings of the Royal Society of London. Series A. Mathematical and Physical Sciences* 222.1148 (1954), pp. 1–32. DOI: 10.1098/rspa.1954.0049. URL: https://royalsocietypublishing.org/doi/abs/10.1098/rspa.1954.0049.

[86] M. J. Lighthill and M. H. A. Newman. "On sound generated aerodynamically I. General theory". In: *Proceedings of the Royal Society of London. Series A. Mathematical and Physical Sciences* 211.1107 (1952), pp. 564–587. DOI: 10.1098/rspa.1952.0060.

[87] G.M. Lilley. "A study of the silent flight of the owl". In: *4th AIAA/CEAS Aeroacoutics Conference*. Vol. 1998-2340. Toulouse,France, 1998.

[88] X. Liu, M. Azarpeyvand, and R. Theunissen. "Aerodynamic and Aeroacoustic Performance of Serrated Airfoils". In: *21st AIAA/CEAS Aeroacoustics Conference*. American Institute of Aeronautics and Astronautics, 2015, pp. 1–16. DOI: 10.2514/6.2015-2201.

[89] E. Llorente and D. Ragni. "Trailing edge serrations effects on the aerodynamic performance of a NACA 643418". In: *Wind Energy* 22.3 (2019), pp. 392–406. DOI: 10.1002/we.2293.

[90] T. S. Lund. "The use of explicit filters in large eddy simulation". In: *Computers & Mathematics with Applications* 46.4 (2003), pp. 603–616. DOI: 10.1016/s0898-1221(03)90019-8.

[91] B. Lyu, M. Azarpeyvand, and S. Sinayoko. "Prediction of noise from serrated trailing edges". In: *Journal of Fluid Mechanics* 793 (2016), pp. 556–588. DOI: 10.1017/jfm.2016.132.

[92] J. F. Manwell, J. G. McGowan, and A. L. Rogers. *Wind Energy Explained*. 2nd ed. Wiley, Jan. 1, 2010. 704 pp. ISBN: 0470015004. URL: https://www.ebook.de/de/product/6597132/james_f_manwell_jon_g_mcgowan_anthony_l_rogers_wind_energy_explained.html.

[93] S. Meloni, J. LT Lawrence, A. R. Proença, R. H Self, and R. Camussi. "Wall pressure fluctuations induced by a single stream jet over a semi-finite plate". In: *International Journal of Aeroacoustics* (2020). DOI: 10.1177/1475472x20930650. URL: https://doi.org/10.1177/1475472X20930650.

[94] H. M. E. Miedema and H. Vos. "Exposure-response relationships for transportation noise". In: *The Journal of the Acoustical Society of America* 104.6 (1998), pp. 3432–3445. DOI: 10.1121/1.423927.

[95] D. S. Miklosovic, M. M. Murray, L. E. Howle, and F. E. Fish. "Leading-edge tubercles delay stall on humpback whale (Megaptera novaeangliae) flippers". In: *Physics of Fluids* 16.5 (2004), pp. L39–L42. DOI: 10.1063/1.1688341. URL: https://doi.org/10.1063/1.1688341.

[96] D. Moreau and C. J. Doolan. "Tonal Noise from Trailing Edge Serration at Low Reynolds Numbers". In: *19th AIAA/CEAS Aeroacoustics Conference*. American Institute of Aeronautics and Astronautics, 2013. DOI: 10.2514/6.2013-2010.

[97] J. D. Morgan. "THE INTERACTION OF SOUND WITH A SEMI-INFINITE VORTEX SHEET". In: *The Quarterly Journal of Mechanics and Applied Mathematics* 27.4 (1974), pp. 465–487. ISSN: 0033-5614. DOI: 10.1093/qjmam/27.4.465. URL: https://doi.org/10.1093/qjmam/27.4.465.

[98] NATS. *Noise*. 2020. URL: https://www.nats.aero/environment/aircraft-noise/. (accessed: 28.04.2020).

[99] M. A. Nissenbaum, J. J. Aramini, and C. D. Hanning. "Effects of industrial wind turbine noise on sleep and health". In: *Noise and Health* 14.60 (2012), p. 237. DOI: 10.4103/1463-1741.102961.

[100] S. Oerlemans, M. Fisher, T. Maeder, and K. Kogler. "Reduction of Wind Turbine Noise Using Optimized Airfoils and Trailing-Edge Serrations". In: *AIAA Journal* 47.6 (2009), pp. 1470–1481. ISSN: 0001-1452. DOI: 10.2514/1.38888.

[101] S. Oerlemans and P. Fuglsang. "Low-noise wind turbine design". In: *Siemens Wind Power A/S* (2012), p. 11. URL: http://www.ewea.org/events/workshops/wp-content/uploads/2012/12/EWEA-Noise-Workshop-Oxford-2012-1-1-Stefan-Oerlemans.pdf.

[102] International Civil Aviation Organization. *Annual Report 2018: The World of Air Transport in 2018*. Tech. rep. 2018.

[103] J. Ortmann and J. Wild. "Effect of Acoustic Slat Modifications on Aerodynamic Properties of High-Lift Systems". In: *24th AIAA Applied Aerodynamics Conference*. American Institute of Aeronautics and Astronautics, 2006. DOI: 10.2514/6.2006-3842.

[104] D. Palumbo. "Determining correlation and coherence lengths in turbulent boundary layer flight data". In: *Journal of Sound and Vibration* 331.16 (2012), pp. 3721–3737. DOI: 10.1016/j.jsv.2012.03.015.

[105] R. Parchen. *Progress report DRAW: A prediction scheme for trailing-edge noise based on detailed boundary-layer characterisitics*. Tech. rep. The Netherlands: TNO Rept. HAGRPT-980023, TNO Institute of Applied Physics, 1998.

[106] R. W. Paterson, R. K. Amiet, and L. C. Munch. "Isolated Airfoil-Tip Vortex Interaction Noise". In: *Journal of Aircraft* 12.1 (1975), pp. 34–40. DOI: 10.2514/3.59798. URL: https://doi.org/10.2514/3.59798.

[107] E. Pedersen and W. K. Persson. "Wind turbine noise, annoyance and self-reported health and well-being in different living environments". In: *Occupational and Environmental Medicine* 64 (2007), pp. 480–486.

[108] K Persson Waye, E Öhrström, and M. Björkman. "Pleasant and unpleasantcharacteristics in wind turbine sounds". In: *Proceedings of Internoise*. Nice, France, 2000, pp. 2327–2330.

[109] K. Persson Waye, E Öhrström, and M Björkman. "Sounds from wind turbines-can they be made more pleasant?" In: *Proceedings of 7th International Congress on Noise as a Public Health Problem*. Sydney, Australia, 1998, pp. 531–534.

[110] J. N. Pinder. "Mechanical Noise from Wind Turbines". In: *Wind Engineering* 16.3 (1992), pp. 158–168. ISSN: 0309524X, 2048402X. URL: http://www.jstor.org/stable/43750324.

[111] A. Powell. "On the Aerodynamic Noise of a Rigid Flat Plate Moving at Zero Incidence". In: *The Journal of the Acoustical Society of America* 31.12 (1959), pp. 1649–1653. DOI: 10.1121/1.1907674.

[112] Ansys® Academic ANSYS Fluent 2020 R2. *Fluent Theory Guide*. Vol. Release 20.2, Help System. 2020. Chap. 4. Turbulence.

[113] D. Ragni, F. Avallone, W. C. P. van der Velden, and D. Casalino. "Measurements of near-wall pressure fluctuations for trailing-edge serrations and slits". In: *Experiments in Fluids* 60.1 (2018). DOI: 10.1007/s00348-018-2654-5.

[114] M. G. Reyes. "The rhetoric in mathematics: Newton, Leibniz, the calculus, and the rhetorical force of the infinitesimal". In: *Quarterly Journal of Speech* 90.2 (2004), pp. 163–188. DOI: 10.1080/0033563042000227427.

[115] O. Rodriguez. "Base drag reduction by control of the three-dimensional unsteady vortical structures". In: *Exp. Fluids* 11.218 (1991), pp. 218–226. ISSN: 0723-4864. DOI: 10.1007/bf00192747.

[116] R. D. Sandberg and L. E. Jones. "Direct numerical simulations of airfoil self-noise". In: *Procedia Engineering* 6 (2010), pp. 274–282. DOI: 10.1016/j.proeng.2010.09.029.

[117] R. D. Sandberg and N. D. Sandham. "Direct numerical simulation of turbulent flow past a trailing edge and the associated noise generation". In: *Journal of Fluid Mechanics* 596 (2008), pp. 353–385. DOI: 10.1017/S0022112007009561.

[118] J. G. Schepers et al. *SIROCCO. Silent rotors by acoustic optimisation.* 2007.

[119] M. A. El-Sharkawi. *Wind Energy: an introduction.* Boca Raton: CRC Press, Taylor & Francis Group, 2016. ISBN: 1482263998.

[120] A. Skillen, A. Revell, A. Pinelli, U. Piomelli, and J. Favier. "Flow over a Wing with Leading-Edge Undulations". In: *AIAA Journal* 53.2 (2015), pp. 464–472. DOI: 10.2514/1.J053142.

[121] J. Smagorinsky. "GENERAL CIRCULATION EXPERIMENTS WITH THE PRIMITIVE EQUATIONS". In: *Monthly Weather Review* 91.3 (1963), pp. 99–164. DOI: 10.1175/1520-0493(1963)091.

[122] J. W. Strutt. *The Theory of Sound.* Vol. 1. Cambridge Library Collection - Physical Sciences. Cambridge University Press, 2011. DOI: 10.1017/CBO9781139058087.

[123] J. W. Strutt. *The Theory of Sound.* Vol. 2. Cambridge Library Collection - Physical Sciences. Cambridge University Press, 2011. ISBN: 9781139058094. DOI: 10.1017/CBO9781139058094.

[124] C. K. W. Tam. "Discrete tones of isolated airfoils". In: *The Journal of the Acoustical Society of America* 55.6 (1974), pp. 1173–1177. DOI: 10.1121/1.1914682. URL: https://doi.org/10.1121/1.1914682.

[125] D. Pope T.F. Brooks and M.A. Marcolini. "Airfoil Self-noise and Prediction". In: *NASA Reference Publication Number 1218* (1989).

[126] N. Thomaries and G. Papadakis. "Numerical Analysis of a Trailing Edge with Triangular Serrations Using Dynamic Mode Decomposition". In: *54th AIAA Aerospace Science Meeting*. Vol. 2016-2084. San Diego, California, USA: American Institute of Aeronautics and Astronautics, 2016. DOI: 10.2514/6.2016-2084.

[127] W. Tong. *Wind power generation and wind turbine design*. Southampton Boston: WIT Press, 2010. ISBN: 9781845642051.

[128] UNFCCC. *COP 21 Paris Agreement*. Tech. rep. 2015.

[129] A. Vathylakis, T. P. Chong, and J. H. Kim. "Design of a low-noise aeroacoustic wind tunnel facility at Brunel University". In: *20th AIAA/CEAS Aeroacoustics Conference*. American Institute of Aeronautics and Astronautics, 2014. DOI: 10.2514/6.2014-3288.

[130] A. Vathylakis, T. P. Chong, C. Paruchuri, and P. Joseph. "Sensitivity of aerofoil self-noise reductions to serration flap angles". In: *22nd AIAA/CEAS Aeroacoustics Conference*. AIAA Paper No. 2016-2837. 2016. DOI: 10.2514/6.2016-2837.

[131] W. C. van der Velden, Francesco Avallone, and Daniele Ragni. "Numerical analysis of noise reduction mechanisms of serrated trailing edges under zero lift condition". In: *23rd AIAA/CEAS Aeroacoustics Conference*. American Institute of Aeronautics and Astronautics, 2017. DOI: 10.2514/6.2017-4173.

[132] *Vincenzo Viviani*. 2016. DOI: 10.1063/pt.5.031191. URL: https://physicstoday.scitation.org/do/10.1063/pt.5.031191/full/.

[133] S Wagner. *Wind Turbine Noise*. Berlin, Heidelberg: Springer Berlin Heidelberg, 1996. ISBN: 978-3-642-88710-9.

[134] P. C. Woodhead, T. P. Chong, and J. Wissink. "Exploiting the Misalignment of the Serrated Trailing Edge for Improved Aerofoil Broadband Noise Reduction". In: *23rd AIAA/CEAS Aeroacoustics Conference*. AIAA Paper No. 2017-4175. 2017. DOI: 10.2514/6.2017-4175. URL: https://arc.aiaa.org/doi/abs/10.2514/6.2017-4175.

[135] X Zhang. "Airframe Noise – High Lift Device Noise". In: *Encyclopedia of Aerospace Engineering*. Ed. by R. Blockley and W. Shyy. 2010. ISBN: 9780470686652. DOI: 10.1002/9780470686652.eae338. URL: https://onlinelibrary.wiley.com/doi/abs/10.1002/9780470686652.eae338.